TECHNISCHE UNIVERSITÄT MÜNCHEN

Ingenieurfakultät Bau Geo Umwelt

Lehrstuhl für Statik

Variation of Reference Strategy

Generation of Optimized Cutting Patterns for Textile Fabrics

Armin Michael Widhammer

Vollständiger Abdruck der von der Ingenieurfakultät Bau Geo Umwelt der Technischen Universität München zur Erlangung des akademischen Grades eines

Doktor-Ingenieurs

genehmigten Dissertation.

Vorsitzender:

Univ.-Prof. Dr.-Ing. habil. Fabian Duddeck

Prüfer der Dissertation:

1. Univ.-Prof. Dr.-Ing. Kai-Uwe Bletzinger
2. Univ.-Prof. Dr.-Ing. Wolfgang A. Wall
3. Prof. Dr.-Ing. Kurt Maute,
   University of Colorado, Boulder, Colorado/USA

Die Dissertation wurde am 17.06.2015 bei der Technischen Universität München eingereicht und durch die Ingenieurfakultät Bau Geo Umwelt am 05.11.2015 angenommen.

Abstract

Over the last couple of decades the application of lightweight design concepts in combination with high performance textiles has become very common in various fields of engineering (aeronautic/aerospace, automotive, civil, biomedical). In general, lightweight structures are characterized by a geometrically driven load bearing behavior. This leads to complex and double-curved surfaces and geometries, whose feasibility is directly linked to the high shear flexibility of the material. However, in almost all cases the wrought materials (textile fabrics or foils) are delivered in a plane way contradicting the non-developable characteristics of the target structure. Within the scope of this thesis, an innovative numerical methodology for the generation of optimized cutting patterns for lightweight structures made of highly nonlinear orthotropic/anisotropic materials (e.g. CFRPs, textile fabrics) is developed, implemented and evaluated. In addition, a novel approach for modeling the structural response of textile fabrics on a macroscopic level is elaborated.

A novel approach for the generation of optimized cutting patterns including nonlinear anisotropic material behavior is presented. The developed *Variation of Reference Strategy* (VaReS) is based on an unconstrained optimization problem which minimizes the total elastic potential energy within the target structure. The core concept of VaReS is the definition of the design variables: the global nodal position in the material configuration. This guarantees a stress-free state in the (optimized) cutting pattern. Two numerical approaches (variational principle and method of steepest descent) for solving the stated optimization problem are presented. Both approaches are based on an isoparametric finite element approach resulting in a novel 3-parameter membrane VaReS element. Finally, both numerical approaches are benchmarked by means of a ruled surface (cylindrical shell) and applied to both synclastic and anticlasitc surfaces (spherical shell and generic rib) in combination with isotropic as well as orthotropic strain-energy functions.

The mathematical description of textile fabrics on a mesoscopic scale proves to be quite complex. The presented novel nonlinear surrogate (material) model is based on a hyperelastic approach capturing the nonlinear structural response of the textile fabric on a macroscopic level. Therefore, the fabric's strain-energy function is represented in terms of Bézier surfaces/curves. The required sample points of the Bézier surfaces/curves are based on experimental data gained by velocity driven biaxial tensile tests (raw data). The full workflow, i.e. generating the response surface based strain-energy functions out of the raw data, is established and applied to three different types of textile fabrics.

The presented industrial applications (parts of a textile car seat cover and a complete CFRP roof crossrail for a car) underline the generality and potential of both the *Variation of Reference Strategy* and the *response surface based material model.*

Zusammenfassung

Die Entwicklung und Umsetzung von Leichtbaustrategien gewinnt über die letzten Jahrzehnte hinweg stetig an Bedeutung. Hierbei spielt der Einsatz von textilen Hochleistungswerkstoffen eine zentrale Rolle. Ihre Anwendungen sind vielschichtig und reichen von Strukturbauteilen in der Luft- und Raumfahrt und im Automobilbau bis hin zu medizintechnischen Produkten und Membrantragwerken. Charakteristisch für derartige Strukturen ist ihr Lastabtragungsverhalten. Dieses ist durch die geometrische Steifigkeit dominiert und führt zu komplexen und meist doppelt gekrümmten (antiklastisch und synklastisch) Formen. Die Realisierbarkeit dieser Formen hängt stark von der Schubsteifigkeit des verwendeten Materials ab. In den meisten Fällen, steht der Rohstoff als ebenes Halbzeug zur Verfügung und wird mittels eines Tiefziehverfahrens in Form gebracht. Diese Prozesskette zeigt deutlich die Notwendigkeit geeigneter Zuschnittsmuster, da es aus mathematischer Sicht nicht möglich ist doppelt gekrümmte Flächen eindeutig zu Verebnen. Im Rahmen dieser Dissertation wird eine neuartige und leistungsfähige numerisches Methode zur Ermittlung von optimalen Zuschnittsmustern unter Berücksichtigung des nichtlinearen und anisotropen/orthotropen Materialverhaltens textiler Werkstoffe entwickelt, umgesetzt und bewertet. Des Weiteren wird eine neuartige Methode zur Modellierung des nichtlinearen Materialverhaltens textiler Werkstoffe auf Makroebenen vorgestellt.

Der erarbeitete Ansatz zur Ermittlung optimaler Zuschnittsmuster (*Variation of Reference Strategy*) basiert auf der Lösung eines unbeschränkten Optimierungsproblems. Die durch den Umformprozess entstehende elastische potentielle Energie innerhalb der Zielstruktur wird hierbei minimiert. Der gewählte Ansatz ermöglicht die Berücksichtigung des nichtlinearen und anisotropen Materialverhaltens bei der Zuschnittsermittlung. Die zentrale Idee hierbei ist die Wahl der Optimierungsvariablen, welche die globalen Knotenpositionen bezüglich der Ausgangsgeometrie darstellen, und somit die Spannungsfreiheit innerhalb des (optimierten) Zuschnittsmusters sicherstellt. Zur Lösung des Optimierungsproblems werden zwei unterschiedliche Lösungsstrategien, ein Variationsprinzip und ein gradientenbasiertes Verfahren (Method of steepest descent), verfolgt. Ein im Zuge dessen neuartig entwickeltes Membran-Element liefert hierfür die Grundlage. Beide Lösungsstrategien werden anschließend mittels geeigneter Beispiele (Zylinderschale, Kugelschale und Segment einer generischen Rippe) getestet.

Da sich aus mathematischer Sicht die mesoskopische Beschreibung des Materialverhaltens textiler Werkstoffe als äußerst aufwendig und komplex darstellt, wird im Rahmen dieser Dissertation ein makroskopisches Meta-Model basierend auf der Theorie der Hyperelastizität gewählt. Die zugrunde liegenden Dehnungsenergiefunktionen werden hierbei mit Hilfe von Bézier Flächen/Kurven (Antwortflächen) beschrieben. Eine Reihe von geschwindigkeitsgesteuerten Biaxial-Zugversuchen liefern die Rohdaten für die hierfür benötigten Stützstellen. Im Rahmen dieser Dissertation wird der gesamte Workflow, d.h. die Ermittlung der Antwortflächen aus den Rohdaten, vorgestellt und wird anschließend für drei unterschiedliche Arten von Textilien exemplarisch eingesetzt.

Abschließend werden die entwickelten Methoden auf Fragestellungen aus der Industrie (Teile eines textilen Autositzbezuges und ein vollständiger Carbon-Dachspriegel) angewandt. Die hierbei erzielten Ergebnisse belegen die Robustheit, Leistungsfähigkeit und unterstreichen das breite Anwendungsspektrum der entwickelten *Variation of Reference Strategy* und des *antwortflächenbasierten Materialmodels.*

Acknowledgments

This dissertation is the result of the research activities which I have been conducting at the *Chair of Structural Analysis* (Lehrstuhl für Statik) at the Technische Universität München, Munich, Germany.

First of all, I want to say ”Thank you very much” to Univ.-Prof. Dr.-Ing. Kai-Uwe Bletzinger. Not only for guiding me through my time as a doctoral candidate, but also for providing me with the second chance to be part of the Chair of Structural Analysis again.

Furthermore, I would like to thank Univ.-Prof. Dr.-Ing. Wolfgang A. Wall, Prof. Dr.-Ing. Kurt Maute and Univ.-Prof. Dr.-Ing. habil. Fabian Duddeck for completing my board of examiners. Their interest in my research and their comments on my dissertation are gratefully appreciated.

I also want to thank Arnulf A. Lipp, Sebastian Kreissl and Thomas Senner from the BMW Group for the fruitful cooperation, the inspiring discussions and their trust placed in my person and work.

Moreover, I want to thank Prof. Dr.-Ing. habil. Sybille Krzywinski and Dipl.-Ing. Ellen Wendt from the Institute of Textile Machinery and High Performance Material Technology (ITM) at the Dresden University of Technology for making available comprehensive experimental data.

I would like to say ”Thank you” to all my coworkers at the Chair of Structural Analysis. Very special thanks goes to Benedikt Philipp, Ann-Kathrin Goldbach, Michael Breitenberger, Falko Dieringer, Stefan Sicklinger, Helmut Masching, Andreas Mini and Altuğ Emiroğlu who were always open for inspiring discussions.

Beyond that, I want to thank Dr.-Ing. Roland Wüchner for his advice and his office door which was always open to me.

At this point I would like to express my deepest gratitude to my parents Georg and Annemarie. Without their absolute support and full confidence in my abilities, it would not have been possible for me to successfully conclude the project ”Dr.-Ing. Armin Widhammer”.

Last but not least, I would like to thank my dear girlfriend Gaby for her patience and the shoulder to lean on during the time I was finalizing my thesis and preparing for my doctoral viva.

Munich, November 2015
Armin Michael Widhammer

Contents

Abbreviations

BVP	Boundary Value Problem
BCs	Boundary Conditions
CFRPs	Carbon Fiber Reinforced Plastics
CAD	Computer Aided Design
CM	Center Mark
CSM	Computational Structural Mechanics
cf.	confer
DFG	Deutsche Forschungsgemeinschaft
DOF	Degree Of Freedom
e.g.	exempli gratia
et al.	et alii
FE	Finite Element
FEA	Finite Element Analysis
FEM	Finite Element Method
GFRPs	Glass Fiber Reinforced Plastics
i.e.	id est
LTE	Linear Triangular Finite Element
NCF	Non-Crimp Fabric
NeoHook	Neo-Hookean material model
NURBS	NonUniform Rational B-Spline
NVP	Natural Variational Principle
PDE	Partial Differential Equation
PTFE	Polytetrafluoroethylene (Teflon)
PVC	Polyvinyl chloride
PVW	Principle of Virtual Work
Ph.D.	Doctor of Philosophy
rrk	interlock jersey
RVE	Representative Volume element or unit cell
SoE	System of Equations
StVenKir	St. Venant-Kirchhoff material model
TLF	Total-Lagrangian Formulation
TPE	Total Potential Energy
UD	unidirectional
VaReS	Variation of Reference Strategy

vs.	versus
w.r.t.	with respect to

Symbols

Roman: Tensors

$\mathbf{C}$	right Cauchy-Green tensor or Green deformation tensor
$\mathbf{E}$	Green-Lagrange strain tensor
$\mathbf{F}$	deformation gradient
$\mathbf{I}$	metric tensor
$\mathbf{K}$	curvature tensor
$\mathbf{M}_i$	i-th structural tensor
$\mathbf{P}$	1^{st} Piola-Kirchhoff stress tensor
$\mathbf{S}$	2^{nd} Piola-Kirchhoff stress tensor

$\mathbf{b}$	left Cauchy-Green tensor or Finger deformation tensor
$\mathbf{e}$	Euler-Almansi strain tensor

Roman: Vectors and Matrices

$\mathbf{A}_i$, $\mathbf{A}^i$	i-th material mid-surface base vectors
$\mathbf{B}$	material body force (vector)
$\mathbf{G}_i$, $\mathbf{G}^i$	f-th material base vectors
$\mathbf{J}$	Jacobian matrix (short Jacobian)
$\mathbf{N}$	material normal vector
$\mathbf{P}_i$	i-th B-Spline/NURBS control point (curve)
$\mathbf{P}_{ij}$	(i,j)-th B-Spline/NURBS control point (surface)
$\mathbf{R}$	material position vector
$\mathbf{T}_{\mathbf{N}}$	material traction vector
$\mathbf{U}\left(\mathbf{X}, t\right)$	displacement field
$\mathbf{X} = X_i \mathbf{e}_i$	material (nodal) position

$\mathbf{a}$	covariant spatial mid-surface base vectors
$\mathbf{b}$	spatial body force (vector)
$\mathbf{e}_i$	i-th Euclidean base vectors

$\mathbf{f}_k$	vector of forces measured at t_i
$\mathbf{f}_{\text{eff}}$	effective force vector
$\mathbf{g}$	contra-variant spatial base vectors
$\mathbf{n}$	spatial normal vector
$\mathbf{r}$	spatial position vector
$\mathbf{s}^i$	search direction
$\mathbf{t}_{\mathbf{n}}$	spatial traction vector
$\mathbf{u}\left(\mathbf{X},t\right)$	displacement field
$\mathbf{u}_k$	vector of displacements measured at t_i
$\mathbf{x} = x_i\mathbf{e}_i$	spatial (nodal) position

Roman: Scalars

A	cross-sectional area
$B_{i,p}\left(\xi\right)$	i-th p-th degree Bernstein polynomial
$B_{j,q}\left(\eta\right)$	j-th q-th degree Bernstein polynomial
$C_i\left(\mathbf{P}_{(\bullet)}\right)$	i-th scalar vector-valued constraint
E	Young's modulus of elasticity
$I_i\left(\mathbf{C}\right)$	Principal invariant ($i = 1\dots 3$)
$I_j\left(\mathbf{C}\right)$	structural invariant ($j > 3$)
J	volume ratio (determinant of the deformation gradient)
$K_1,\ K_2$	principal curvature
M_k	shear moments at t_i
$O\left(\mathbf{P}_{(\bullet)}\right)$	scalar vector-valued objective function
P	arbitrary point within a body
V	volume

$f_{\mathrm{K_i}}$	measured forces ($i = 1\dots 4$)
$f_{\mathrm{K}_{13}},\ f_{\mathrm{K}_{24}}$	arithmetic mean: measured forces
$f_{\parallel}^{\text{pre}},\ f_{\perp}^{\text{pre}}$	predefined (compensation) force
n_{exp}	total number of samples per experiment
p_{surf}	effective surface pressure
t_i	instant of time for measurements ($i = 1\dots n_{\text{exp}}$)
thk	thickness
$u_{\mathrm{M_i}}$	measured displacements ($i = 1\dots 4$)
$u_{\mathrm{M}_{13}},\ u_{\mathrm{M}_{24}}$	arithmetic mean: measured displacements

Greek: Vectors, Matrices and Tensors

$\boldsymbol{\sigma}$	Cauchy stress tensor
Φ_i	i-th fiber directions (warp/weft)

Greek: Scalars

$\Gamma^{(\bullet)}_{(\bullet)a}$	Christoffel symbol associated to the a-th DOF
$\Gamma^{(\bullet)}_{(\bullet)b}$	Christoffel symbol associated to the b-th DOF

$\Pi\left(\mathbf{C}\right)$	Total elastic energy
$\Psi\left(\mathbf{C}\right)$	strain-energy function or stored energy function

α_k	shear angles measured at t_i
α^i	step size for i-th iteration step
$\chi\left(\mathbf{X}, t\right)$	motion of a point
$\lambda_{\parallel}$, $\lambda_{\perp}$	fiber stretch (warp/weft)
κ	Gaussian curvature
ν	Poisson's ratio
ϕ_α	fiber orientation (angle)
$\cos\phi$, ϕ	fiber twist, fiber twist angle (degree)
σ	normal stress
τ	shear stress

θ^i	surface/curve parameters → Lagrangian polynomials
ξ, η	surface/curve parameters → B-Splines or NURBS

ζ_i	unknowns of a nonlinear system of equation

Symbols and Operators

$\mathbb{D}$	elasticity tensor
$\mathbb{R}^2$	2 dimensional (2D) vector space
$\mathbb{R}^3$	3 dimensional (3D) vector space
$\mathbb{U}_{\text{norm}}$, $\mathbb{U}_{\text{shear}}$	normal-/shear-set
$\mathbb{V}_{\text{norm}}$, $\mathbb{V}_{\text{shear}}$	normal-/shear-campaign (samples per experiment)

$\mathcal{C}$	curve
$\mathcal{S}$	surface
$\mathcal{B}$	continuum body (short body)
$\partial\mathcal{B}$	boundary of a continuum body (short boundary)
$\mathcal{K}^3$, $\mathcal{K}^2$	body of an Euclidean vector space (3D, 2D)
$\mathcal{V}_{\text{norm}}$, $\mathcal{V}_{\text{shear}}$	subset of an Euclidean vector space (3D, 2D)
$\mathcal{F}\left(\bullet\right)$	scalar-, vector-, or tensor-valued functional
$\mathcal{L}\left(\mathbf{P}_{(\bullet)}, \lambda_i\right)$	Lagrangian function
$\boldsymbol{\mathcal{R}}$, $\mathcal{R}_a$	residual vector, a-th (discrete) residual
$\boldsymbol{\mathcal{K}}$, $\mathcal{K}_{ab}$	tangential stiffness matrix, (a-th,b-th) coefficient

Γ_0	boundary of the material domain
Γ	boundary of the spatial domain
Ω_0	material domain
Ω	spatial domain
$\delta W_{\text{int}}\left(\mathbf{u}, \delta\mathbf{u}\right)$	internal virtual work
$\delta W_{\text{ext}}\left(\mathbf{u}, \delta\mathbf{u}\right)$	external virtual work
$\Pi_{\text{int}}\left(\mathbf{u}\right)$	internal potential energy
$\Pi_{\text{ext}}\left(\mathbf{u}\right)$	external potential energy

$\Pi_{\text{total}}(\mathbf{u})$	total potential energy

$\delta(\bullet)$	1^{st} Variation of $(\bullet)$
$\Delta(\bullet)$	linearization of $(\bullet)$
$\square(\mathbf{X}, t)$	material scalar, vector or tensor-valued quantity
$\diamondsuit(\mathbf{x}, t)$	spatial scalar, vector or tensor-valued quantity

$\veebar$	exclusive disjunction or XOR
$D_{(\bullet)}$	Gâteaux operator
$\pounds_{(\bullet)}$	Lie operator
$\Delta_{(\bullet)}$	Linearization operator
ϵ_{ijk}	Levi-Civita symbol
$\nabla_{(\bullet)}$	Nabla operator
$\lvert(\bullet)\rvert$	absolute value
$\lVert(\bullet)\rVert_{\infty}$	supremum norm or Chebyshev norm
$\lVert(\bullet)\rVert$	L^2-norm

Subscripts

$\parallel$	quantity in warp direction
$\perp$	quantity in weft direction
$\sharp$	quantity w.r.t. shear
χ	quantity resulting from an elastic deformation
a	a-th degree of freedom
$,a$	partial derivative w.r.t. the a-th degree of freedom
b	b-th degree of freedom
$,b$	partial derivative w.r.t. the b-th degree of freedom
conv	converged solution
exact	analytical solution
init	initial guess
iso	isochoric motion
iter	solution of i-th iteration step
max	upper bound of a specified range
min	lower bound of a specified range
norm	fiber-parallel biaxial tensile tests
pre	quantity resulting from predefined state
ps	plane stress state
rel	relative value
SF	stress-free state
shear	45° biaxial tensile tests
vol	volumetric motion
0.5	arithmetic mean of a specified range

Superscripts

$\flat$	covariant vector/tensor
$\sharp$	contra-variant vector/tensor
$\parallel$	in-plane component of a vector/tensor
$\perp$	out-of-plane component of a vector/tensor
σ	prescribed stresses (Neumann BCs)
u	prescribed displacements (Dirichlet BCs)
$\mathcal{S}$	quantity related to the body's mid-surface

1

Introduction

"I never saw a wild thing sorry for itself. A small bird will drop frozen dead from a bough without ever having felt sorry for itself."

— David Herbert Lawrence, 1885 - 1930
English novelist

1.1 Motivation

Over the last couple of decades the application of lightweight design concepts in combination with high performance textiles has become very common in various fields of engineering, e.g. aeronautics/aerospace engineering (stringer and ribs), automotive engineering (frame components and car body panels), civil engineering (pneumatic structures and architectural membranes), etc. Reasons for this evolution are on the one hand the development/manufacturing of advanced high-tensile materials (carbon/glass/aramid fibers) and on the other hand the availability of better and better numerical simulation techniques (better especially in speed and accuracy).

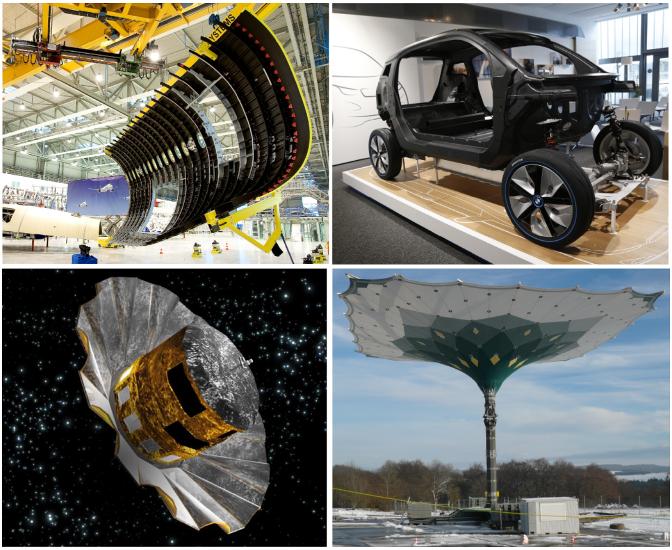

Figure 1.1: Widespread applications: A350 CFRP fuselage segment [111] (upper left), BMW i3 CFRP passenger cell [94] (upper right), foldable solar array and sunshild of the GAIA satellite [38] (lower left), foldable umbrella in unfolded state [91] (lower right)

Despite their widespread applications (cf. Figure 1.1) all these structures follow the basic rule of lightweight design: the load carrying behavior is dominated by the geometrical stiffness (i.e. loads are mostly carried by *normal forces*). A special type of lightweight structures are the so-called *tensile* or *membrane* structures. Due to the missing bending stiffness of the applied materials (textile fabrics or foils), the load transfer within these structures is done exclusively through in-plane tensile forces. The two most effective ways manipulating the geometrical stiffness of membrane-like structures are either increasing the curvature or incorporating a predefined stress state (so-called *prestress*). This leads to double-curved surfaces and geometries whose feasibility is directly linked to the high shear flexibility of the material.

In almost all cases, the wrought materials are delivered as either plane textile[1] fabrics or plane foils. In case of textile fabrics, the wrought material is either dry or resin coated. Hence, in order to realize a spatial structure the wrought material has to undergo some forming process, regardless of the application (e.g. car seat cover, car body panel, architectural membrane, etc.). The forming or manufacturing process bringing a tailored patch of plane wrought material into the desired shape of the spatial structure (*target*) is known as *drape process* or short *draping*. The tailored patch itself is called *cutting pattern* or *blank*. However, the fact that the cutting pattern is plane highly contradicts with the non-developable characteristic of the final structure. Thus, it is not possible to drape the textile fabric or foil without generating residual stresses within the target structure. In case of a free-standing structure (architectural membranes) such residual stresses directly effect its shape, i.e. a change of its curvature or the occurrence of wrinkles can be observed. Similar problems are well-known in the apparel industry. But in contrast, here the design of the cloth is of importance, not the load carrying behavior. In case of a curred structure (CFRPs or GFRPs) such residual stresses result in a reorientation or an additional marcelling of the fibers. Furthermore, wrinkles or gaps might occur. In case of supported structures (car seat) a combination of all described defects can be observed. Bottom line, such residual stresses have a more or less significant effect on the load carrying behavior and/or manufacturing quality depending on the chosen textile fabric or foil. Hence, a design engineer is faced with the following questions:

- → How should the cutting pattern of the textile fabric be such that the final draped shape has minimal deviation from the desired product?
- → What are the residual stresses and how do they affect the structural behavior?

REMARK I: Due to similar questions regarding optimized cutting patterns for lightweight designs, the need for innovative numerical methods and adequate material models is not only apparent in the sector of garment production technology anymore but has spread to various fields of engineering, e.g. automotive, aeronautic, civil engineering, etc.

1.2 Terminology and Classification

The intention of this section is to introduce a common wording as well as a classification of the most common used textile fabrics with respect to

---

[1] braided/knitted/woven fabrics made of synthetic (carbon/glass/aramid/etc.) or natural fibers (cotton/etc.)

their production process. For a more detailed classification and for further information on draping/manufacturing related topics the author refers to Cherif et al. [33], Flemming et al. [42] and Gutowski [54].

1.2.1 Terminology

Within the scope of this dissertation the following terms are stated as follows[2]:

Fiber: A one-dimensional flexible structure exhibiting only tensile stiffness. Depending on the material they are grouped in either natural fibers (cotton, hemp, wood, etc.) or synthetic fibers (carbon, fiberglass, polymer, etc.). Fibers are further classified with respect to their length: *filaments* (endless or $> 1000[mm]$), *staple fibers* (finite but processable), *flock fibers* (too short for further processing).

Yarn: A one-dimensional textile structure made of either filaments (*filament yarn*) or staple fibers (*spun yarn*). The single filaments/staple fibers are joint together in either a form-fit or a bonded connection.

Roving: A bundle of several filaments made of high performance materials (e.g. carbon, fiber-glass, aramid, etc.). The single filaments are either aligned in a parallel way (*single-end roving*) or an assembly of multiple fiber bundles (*multi-end roving*). Their cross-section areas are either rectangular or elliptical. A roving can be seen as a filament yarn used for textile lightweight structures.

Textile fabric: A plane (2D) structure which is generated due to a textile manufacturing process (sewing, knitting, braiding, weaving, etc.) using either yarns or rovings. A more detailed classification of textile fabrics is provided in Section 1.2.2.

3D textiles: A spatial (3D) structure which is generated due to a textile manufacturing process (sewing, knitting, braiding, weaving, etc.) using either yarns or rovings. It is important to note that 3D textiles are different to draped textile fabrics. 3D textiles are not further discussed in this dissertation.

Fiber direction: The direction of the yarns, rovings, wales, stitches, i.e. the direction of the ansiotropy within the fabric. For woven, knitted or braided fabrics the two orthogonal fiber directions are called *warp direction* and *weft direction*. More details are given in Section 1.2.2.

Fiber orientation: The orientation of the textile fabric within the structure of investigation.

Cutting pattern or blank: A tailored patch of plane wrought material. The term blank is mostly used within the context of sheet-metal forming.

Drape process or draping: The forming or manufacturing process bring-

---

[2] this summary does not claim to be complete

ing a tailored patch of plane wrought material into its final shape. In general, this is done by means of a deep-drawing tool where the mold defines the target shape of the spatial structure.

Drape simulation: The numerical simulation of the draping process considering all aspects of the chosen manufacturing technology, e.g. friction between mold and cutting pattern, restraining beadings, closing pressure, etc. State of the art commercial explicit FE-Codes for drape simulation: LS-DYNA [44], PAM-FORM [49], ABAQUS [104].

Cutting pattern analysis: The generation of the developed view of the target structure. In general, no unique solution exists (only in case of ruled surfaces, cf. Figure 2.3). Hence, some sort of iterative scheme or optimization technique is required which is either based on a geometric or an energetic problem formulation. Up to now, the common approaches for cutting pattern analysis do not consider any aspects of the chosen manufacturing technique.

1.2.2 Classification of textile fabrics

Due to the fact that the production process primarily dictates the structural response of a textile fabric on a macroscopic scale, textile fabrics can be generally subdivided in three different groups:

- → nonwoven materials (not covered)
- → non-stich-forming materials
- → stitch-forming materials

The focus of this thesis lies on the non-stich-forming materials (non-crimp fabrics, woven fabrics, braided fabrics) and stitch-forming materials (knitted fabrics). Therefore, the mentioned textile fabrics are discussed in more detail in Section 1.2.2.1 - Section 1.2.2.4. For further information on these textile fabrics applied to lightweight design concepts, the author refers to Cherif et al. [33], Flemming et al. [42] and Gutowski [54].

1.2.2.1 Non-crimp fabrics

Non-crimp fabrics (NCFs) are patches of parallel aligned rovings. For a better handling, the rovings are either glued together by means of a special fleece or sewed together by means of synthetic yarns. The simplest non-crimp fabric is the so-called *unidirectional ply* (UD-ply) where the single rovings are aligned in only one direction (cf. left picture in Figure 1.2). Several UD-plies may be combined to so-called *multi-axial non-crimp fabrics* (cf. right picture in Figure 1.2). In case of two orthogonal fiber directions they are called *biaxial plies*. In order to increase their manageability during manufacturing, the single plies are either glued or sewed together by means of a special flees or synthetic yarns, respectively. With an increasing number of UD-plies, multi-axial non-crimped fabrics might already be considered as 3D textiles.

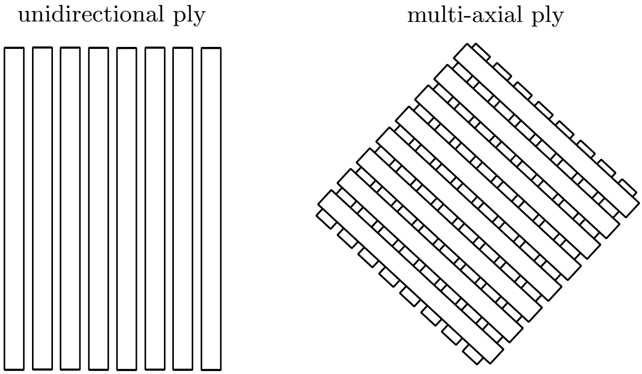
unidirectional ply

multi-axial ply

Figure 1.2: Non-crimp fabric: single UD-ply (left), multi-axial non-crimp fabric (right)

The major advantage of non-crimp fabrics is the fact that they are the only type of textile fabric where the yarns/rovings are not undulated and/or bent during their production process. This results in an optimum utilization of the material's tensile strength due to the spatial straight alignment of the rovings.

1.2.2.2 Woven fabrics

Woven fabrics consist of at least two orthogonal and intersecting rovings (yarns) leading to a bi-directional plane fabric. The rovings (yarns) which are aligned with the axis of the loom are called *warp* or *warp rovings (yarns)*. The rovings (yarns) aligned in the perpendicular direction are called *weft* or *weft rovings (yarns)*. Due to lifting and lowering of individual warp rowings (yarns) during the weft insertion, different weave constructions can be realized. The most common used weave types for lightweight structures are the *plain weave*, *twill weave*, *satin weave* and *Scheindreher weave*. Their different weave constructions are shown in Figure 1.3.

In contrast to non-crimp fabrics, the material's tensile and shear strength as well as the drape property of woven fabrics strongly depend on the underlying weave construction. The reasons for this are on the one hand the introduced undulations of the yarns/rovings and on the other hand the arising contact pressure at the intersection points, cf. Figure 1.3.

REMARK I: For woven fabrics the following naming convention for the fiber directions is used: The *warp direction* and *weft direction* are aligned with the warp rovings (yarns) and weft rovings (yarns), respectively.

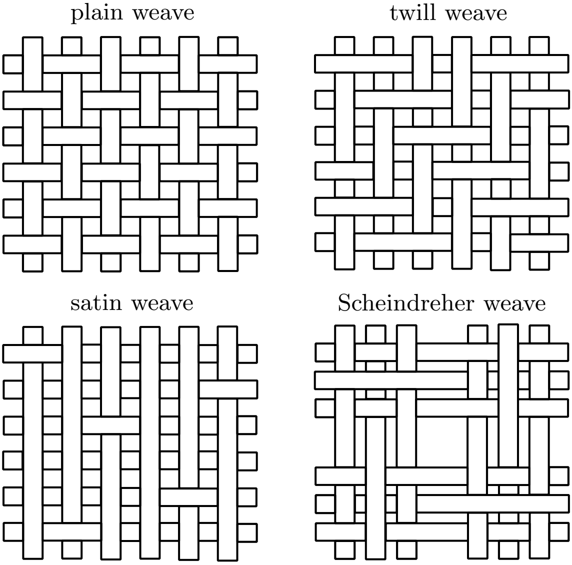

Figure 1.3: Woven fabrics: plain weave (upper left), twill weave (upper right), satin weave (lower left), Scheindreher weave (lower right) [*source*: Figure 4.3.6 in FLEMMING ET AL. [42]]

1.2.2.3 Knitted fabrics

Knitted fabrics are bi-directional textile fabrics based on a network of stitches[3]. In contrast to woven fabrics, the roving (yarns) are formed to interlacing stitches (cf. Figure 1.4). This leads to two distinct material directions: the row of stitches called *stitch course* and the vertical alignment of the stitches called *wales course* (cf. Figure 1.4).

There are two perspectives of the single stitches along the wales course which directly depend on the production process (i.e. if the vertical neighboring stitches are connected to each other either from below or above[4]). A stitch is called *knit stitch* if its legs are in the front (cf. Figure 1.4). It is called *purl* if its head and foot is in the front (cf. Figure 1.4). Depending on the combination of knit stitch and purl within the fabric the following four basic types of knitted fabrics can be identified: *single jersey*, *double jersey*, *interlock jersey* and *purl stitch*. Their different weave constructions are shown in Figure 1.5.

---

[3] stitches are not the only but the most dominant interlacing elements for knitted fabrics, see CHERIF ET AL. [33]

[4] for a fixed perspective, e.g. the top view of a knitter

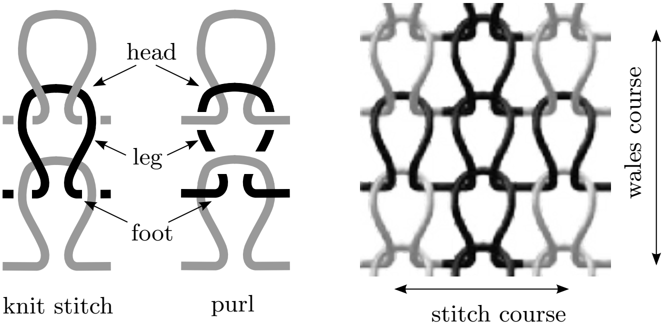

Figure 1.4: Knitted fabric: knit stitch vs. purl (left), definition of stitch and wales course (right) [*source*: Figure 6.3 and Figure 6.8 in Cherif et al. [33]]

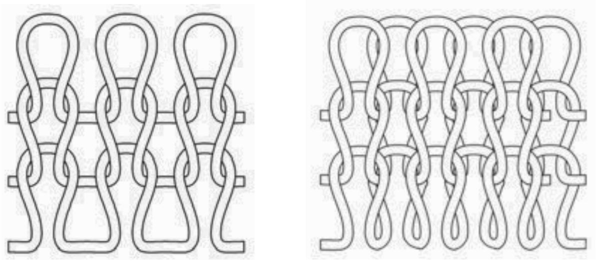
single jersey

double jersey

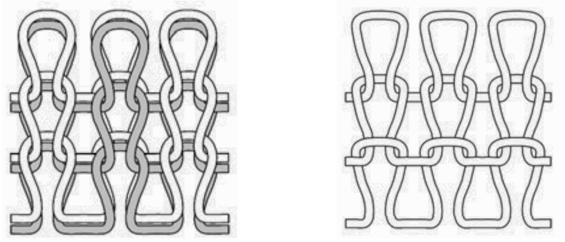
interlock jersey

purl stitch

Figure 1.5: Knitted fabrics: single jersey (upper left), double jersey (upper right), interlock jersey (lower left), purl stitch (lower right) [*source*: Figure 6.11 - 6.14 in Cherif et al. [33]]

In general, knitted fabrics exhibit good drape properties due to their network of stitches. In contrast to non-crimp and woven fabrics, in knitted fabrics the rovings are highly bent leading to a significant drop in their tensile stiffness. Therefore, additional yarns for reinforcement may be introduced.

REMARK II: For knitted fabrics the following naming convention for the fiber directions is used: The *warp direction* is aligned with the wales course and the *weft direction* is aligned with the stitch course.

1.2.2.4 Braided fabrics

Braided fabrics consist of at least 3 different rovings (yarns) which are interlaced with each other in a regular but not orthogonal way. Additional rovings (yarns) for reinforcement may be introduced. Depending on the production process (cf. Figure 1.6), braided fabrics can be grouped in *band-shaped* and *tube-shaped* fabrics.

Figure 1.6: Braided fabrics: schematics of a band-shaped fabric (left), radial braiding machine (center), schematics of a tube-shaped fabric (right) [*source*: Figure 8.4 in Cherif et al. [33], Figure 4.4.1 - 4.4.2 in Flemming et al. [42], [43]]

In general, braided fabrics exhibit good drape properties due to their skew-angled alignment of the rovings. The major advantage of braided fabrics is the possibility of incorporating either an out-of-plane contour (band-shaped) or an in shape and/or diameter varying cross-section (tube-shaped). This reduces the need of further forming steps since the semi-finished patches already show a higher contour accuracy.

1.3 State of the art

The *method of finite elements* (FEM) or *finite element analysis* (FEA) has become a state of the art simulation tool providing deep insight in the static or dynamic (nonlinear) response of elastic structures subjected to external loads and/or body forces, e.g. pressure loads, displacements, temperature, gravitation etc. *Material* or *constitutive models* play an important role since they establish the link between the mathematical model (*kinematics* and *strains*) on the one hand and the structure's physical response (*stress*) on the other. Over the past decades, a lot of research has been done for isotropic or anisotropic but homogeneous materials such as metallic material (cold-rolled steels, high resistance steels, non-iron alloys, etc.) and technical plastics or rubber-like materials (elastomer materials, thermoplastics, thermoset materials). These activities have resulted in substantial and highly detailed data bases as well as in powerful and accurate mechanical models capturing various aspects of material behavior, e.g. elasticity, plasticity, visco-elasticity, etc.

Carbon fiber reinforced plastics (CFRPs) are more and more utilized for series components of modern cars and aircrafts, e.g. BMW i3, BMW i8, Boing 787, A350 XWB, etc. High performance *textile fabrics* made of natural or plastic fibers are not only used for functional clothes such as waterproof jackets or bandages, but also for architectural membranes such as membrane rooftops or pneumatic structures. All these materials are characterized by a highly anisotropic behavior on a macroscopic level, i.e. a very high tensional fiber/yarn stiffness in combination with a comparably low shear stiffness. It is important to mention that due to their manufacturing process (braiding, knitting, weaving, etc.) textile fabrics cannot be seen as homogeneously distributed materials as it is the case for metals, technical plastics and rubber-like materials. In addition, their production process is primarily responsible for their structural response. In more detail, the fiber/yarn or roving itself might show a linear elastic behavior (mesoscopic scale) but on a macroscopic scale the fabric does not automatically behave linear elastically[5]. The reason for this is the load-induced kinematic of the underlying micro-structure which might lead to a sudden increase in *inter-fiber friction* or *collisions* between the single fiber/yarns or rovings. The characteristics of the inter-fiber friction is mainly depending on the material and type of the fibers/yarns or rovings as well as their additional thermal treatment or coating. A similar effect can be observed for biological tissues. Despite their increasing prominence in various fields of engineering (e.g. aeronautic and automotive, civil, clothing, biomedical etc.), when it comes to numerical simulations the availability of detailed data bases characterizing high performance textiles is very limited. The development of adequate material models is still in its infancy. An overview of the current available material models and ongoing research activities is given in Chapter 1.3.1.

With the invention of high performance textile fabrics a new level of realizing complex shaped geometries was reached. A lot of research has been conducted on the development of efficient finite element formulations for the static and dynamic analysis of membrane-type (e.g. architectural membranes) and shell-type (e.g. car body panels) structures. However, the available simulation/optimization tools focusing on manufacturing are only a few. Especially for series components made of carbon fibers, the high

---

[5] e.g. a single carbon roving is considered as linear elastic but a bi-directional plane weave does not show a linear elastic behavior

material costs have to be taken into account. The use of optimized cutting patterns does not only influence the quality and the structural behavior but also reduces the overall costs of the part and is therefore of considerable interest. Another aspect for reducing the costs is a reliable prediction of the draping process. The number of production trails can be tremendously decreased by means of numerical drape simulations. Consequently, the raising popularity of lightweight design concepts in combination with textile fabrics leads to an increasing demand on more sophisticated simulation tools dealing with manufacturing and production issues. An overview of the current available numerical methods for generating optimized cutting patterns and ongoing research activities is given in Chapter 1.3.2.

1.3.1 Fundamental work: Anisotropic material models (textile fabrics)

Over the past decades various research groups have worked on the development of mathematical models for anisotropic inhomogeneous materials. Their broad range of applications reaches from simple linear *homogenized models* for basket weaves up to complex *multi-scale approaches* for 3D knitted fabrics. A summary of the milestones is given below.

KARWARTH ET AL. [63] and MÜNSCH AND REINHARDT [86] focused on orthotropic materials for architectural membranes such as PVC coated woven polyester-fabrics or PTFE coated woven glass-fabrics. Their published material models are based on a linear strain-stress relation.

A more mechanically motivated approach for modeling plain weaves focuses on the forces acting on the rovings/yarns at their crossover points. Due to the geometry of the crossover points such models are also-called *"Dreiecks-Modelle"*. KAWABATA ET AL. [64] presented such a mechanically motivated model for describing the structural response of plain weaves under biaxial tensile loads. Their model is based on a nonlinear elastic behavior of the yarns/rovings. The effect of the undulated roving/yarns (i.e. the arising compressive forces acting on the yarns/rovings due to tensile forces acting on the fabric) is also incorporated into their model. In KAWABATA ET AL. [65] [66] their model is extended to uniaxial load cases and shear load cases, respectively. BLUM AND BIDMON [18] introduced a hyperelastic model for coated plain weaves, whereat a truncated power series defines the underlying strain-energy function (cf. BLUM [17]). A set of *"Dreiecks-Modelle"*, which represents the kinematics of a characteristic cell[6] of nonlinear but incompressible yarns/rovings, is used for evaluating the required elasticity constants. In the work of BÖGNER [21] an extension to BLUM is presented accounting for the compressibility of the yarns/rovings. More information on the evaluation of the required material parameters and the corresponding biaxial tensile tests is given in BLUM ET AL. [19] and BLUM ET AL. [20]. PARSONS ET AL. [90] enhanced the model presented by KAWABATA ET AL. towards the application within an explicit FE framework.

---

[6] i.e. a representative volume element (RVE) or unit cell

Due to the fact that computation power is less of an issue these days, fully FE-modeled RVEs for woven or knitted fabrics are nowadays more feasible. Ballhause [7] and Ballhause et al. [8] developed a meso-scale model which is based on discrete elements (DE). Their model is primarily designed for capturing the failure behavior of fabric reinforced membranes. Over the past couple of years various research groups have worked on the development of powerful and reliable finite element based RVEs for knitted fabrics (e.g. Fillep et al. [39] [40]), non-crimp or woven fabrics (e.g. Bednarcyk et al. [10], Charmetant [31], Gatouillat [45], Simon et al. [102]) and 3D fabrics (e.g. Sonon and Massart [103]).

Instead of considering highly abstracted models (beams, trusses, springs) or very detailed models (FE, DE) on a meso-level, Raible et al. [95] and Reese et al. [97] published a hyperelastic material model for fiber reinforced pneumatic membranes considering them as a three dimensional continuum. Therefore, the elongations of the yarns/rovings are described by means of *structural invariants* embedded in an isotropically acting matrix described by means of the *principal invariants*. A complete list of possible polyconvex strain-energy functions for modeling hyperelastic transverse isotropy is presented in Schröder and Neff [100]. Based on this work, Balzani et al. [9] and Schröder et al. [99] presented a polyconvex strain-energy function for architectural membranes made of textile fabrics. Aimène et al. [1] and Vidal-Sallé et al. [107] came up with a hyperelastic model for uncoated non-crimp and woven fabrics. The corresponding strain-energy function is only formulated in terms of the structural invariants, i.e. an energy contribution due to an isotropically acting matrix is neglected.

In contrast, Ruiz and Gonzáles [98] tested several isotropic strain-energy functions and compared their applicability to textile fabrics.

Less specialized orthotropic and transversely isotropic hyperelastic material models are published by Bonet and Burton [22] and Lürdig et al. [82]. Holzapfel and Ogden [59] discussed the possibilities and limits of plane biaxial tests within the context of anisotropic hyperelastic material models.

Instead of considering a hyperelastic material behavior, Badel et al. [5] presented a model for non-crimp and woven fabrics based on a rate constitutive equation.

A completely different approach for modeling the structural response of textile fabrics was chosen by Gosling and Bridgens [50] and Bridgens and Gosling [24], [25], [26], [27]. They presented a meta model (response surface model) which represents the nonlinear stress-strain relations by means of either polynomial based surfaces or NURBS surfaces. In more detail, two surfaces are established describing the stresses in warp and weft direction subjected to a strain pair (warp and weft strains). The required sample points are achieved by means of biaxial tensile tests (Gosling and Bridgens [23], [28]). Hirokazu [58] came up with a similar approach which is also based on biaxial tensile tests. But instead of interpolating all sample points by means of surfaces, he used spatial curves. The space between each curve is then interpolated in a linear fashion. COELHO ET AL. [34] used NURBS based response surfaces in order to describe the stress-strain relations of isotropic materials. Their response surfaces are spanned within a principal strain-stress space.

1.3.2 Fundamental work: Cutting patterns and Inverse approaches

A well-known example for lightweight design concepts in civil engineering is the roof of the Olympic stadium in Munich (1972). Frei Otto (consulting architect) designed that pioneering tensile structure based on a cable-net covered with patches made of acrylic glass. In order to realize Frei Ottos' ideas LINKWITZ and his co-workers developed numerical methods for both the form finding of cable-net structures (*Force Density Method*) and the generation of corresponding cutting patterns based on geodesic lines, e.g. LINKWITZ [77], LINKWITZ [78], LINKWITZ AND PREUSS [79], LINKWITZ AND SCHEK [80] and LINKWITZ ET AL. [81].

GRÜNDIG ET AL. [53] came up with the idea of using an affine map between the plane configuration (2D) and the spatial configuration (3D) defining the element edges as design variables. Other kinematically based approaches are summarized in TOPPING AND IVÁNYI [105]. The major drawback of these approaches is the disregard of the material behavior. In order to circumvent this, MAURIN AND MOTRO [83] developed the so-called *Stress Compensation Method*. In a first step, an orthogonal projection of the spatial configuration (3D) into a plane leads to a non stress-free intermediate configuration (2D). Followed by the second step, a least squares approach minimizes the sum of the differences between these residual stresses and a predefined stress state by varying the contour of the intermediate configuration. The approach published by KIM AND LEE [68] is based on the *stress compensation method*. But in contrast to MAURIN AND MOTRO [83], not only the displacements of the contour of the intermediate configuration, but also the internal displacements are defined as design variables.

The methodology for optimized cutting patterns published by HAUG ET AL. [55], [56] is based on solving a standard problem in structural mechanics. In a first step, the desired material characteristics are assigned to a not necessarily pre-stressed structure by means of the so-called *metric retrieval method*. In a second step, the structure is divided into different subdomains defined by geodesic boundaries, also called geodesic gores. In a next step, each gore is separately forced into an appropriate plane. Finally, the optimized cutting patterns are found by finding the equilibrium state of the statically determinant supported flat gores allowing only in-plane motions of the nodes.

Within the context of Computer Aided Design (CAD) and visualization strategies, this problem[7] is known as *texture mapping.* A purely geometrical but well-established method is the so-called *angle based flattening* strategy published by Sheffer and de Sturler [101]. McCartney et al. [85] presented a flattening algorithm which is based on the elastic deformation of the element edges. With a strong focus on garment design, an extension to orthotropic materials is presented in McCartney et al. [84]. Wang et al. [108] came up with the idea of introducing a spring-mass system for considering the elastic effects of the underlying material.

A more general approach for finding the stress-free (unloaded) configuration of a target structure subjected to a given set of boundary conditions (displacements and tractions) was published by Govindee and Mihalic [51] [52]. According to the theory of finite deformations, the mapping of a point in the material configuration to the corresponding point in the spatial configuration is defined by a so-called motion. Govindee and Mihalic came up with the idea of defining the inverse motion of a point as primary unknown. Their work was extended to anisotropy by Germain [48]. Similar questions are arising in biomechanical applications. Gee et al. [46] and Vaillant and Glaunés [106] addressed the problem of finding the unloaded configuration when patient-specific geometries are directly reconstructed out of in vivo imaging data.

Linhard et al. [74], [75] introduced two also mechanically motivated approaches[8] for solving the optimization problem. In accordance to Maurin and Motro, Linhard et al. minimize the differences between a predefined stress state and the residual stresses in an integral sense choosing either a least squares or a Galerkin approach. But instead of using an intermediate configuration, Linhard et al. directly used the spatial configuration for computing the residual and predefined stresses. Additionally, Bletzinger and Linhard [15] and Bletzinger et al. [16] incorporated their approaches into an overall design strategy for architectural membranes. Further enhancements on the design of membrane structures considering cutting patterns has been published by Dieringer et al. [36] and Dieringer [37].

1.4 Objectives

The analysis of the currently available material models for textile fabrics and their manufacturing related numerical simulation techniques clearly shows room for improvement. Quite a lot of research has been conducted on material models for woven fabrics and UD-plies. But when it comes to knitted or braided fabrics powerful models are less available. Furthermore, the arrival of fiber reinforced materials in the series production leads to an increased demand on powerful simulation tools dealing with issues related to manufacturing, e.g. cutting pattern generation, draping, infiltration, etc.

---

[7] i.e. the generation of optimized cutting patterns

[8] *Least Squares Optimization* and *Minimization of the stress difference energy*

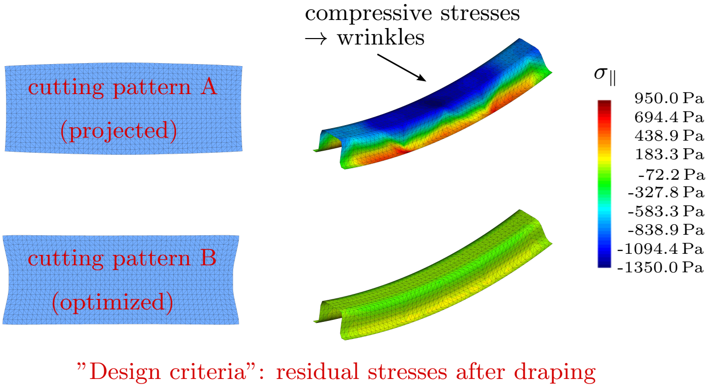

Figure 1.7: Well-known challenge → plane shape (cutting pattern - left) of a double-curved surface (target structure -right) for a mechanically driven problem (e.g. Cauchy stresses $\sigma_{||}$ in warp direction)

The objective of this dissertation is the development of innovative *numerical methods for the generation of optimized cutting patterns while taking into consideration the highly nonlinear material behavior of the underlying textile fabric* (cf. Figure 1.7). Within that framework, the following two milestones are defined:

- → The development of a novel **nonlinear elastic anisotropic material model** for textile fabrics which is independent of their production process, i.e. a common model for woven, knitted and braided fabrics. Its range of application is primarily the generation of cutting patterns.
- → The development of a **robust numerical method for the generation of optimized cutting patterns** where the occurring large deformations (nonlinear kinematics) as well as the finite strains (nonlinear material models) are consistently taken into account.

1.5 Concept

This thesis is organized as follows:

CHAPTER 2 introduces a set of mathematical operators, concepts and principles providing the mathematical framework for solving partial differential equations and nonlinear optimization problems. Furthermore, the concept of differential geometry is introduced providing a powerful mathematical tool box for describing an arbitrary structure (solid, surface, line) in a 3 dimensional space.

Chapter 3 introduces the concept of nonlinear continuum mechanics which provides a powerful theoretical framework for modeling continuous bodies on a macroscopic scale. Within the scope of this chapter all important aspects (strains, stresses and equilibrium) are addressed and their mathematical descriptions are provided.

Chapter 4 shows a novel approach for modeling the structural response of either knitted, braided or woven fabrics based on a nonlinear (hyperelastic) surrogate model. The required strain-energy function is represented in terms of Bézier surfaces/curves. The sampling points of the Bézier surfaces/curves are based on a set of experimental data which is achieved due to a series of velocity-driven biaxial tensile tension tests. Besides the theoretical framework, this chapter introduces strategies for data processing and data fitting. Finally, the response surfaces for three different textile fabrics are presented.

Chapter 5 shows a novel approach for the generation of optimized cutting patterns. The so-called *Variation of Reference Strategy* (VaReS) is based on a variational energy principle (*Minimum of total elastic potential energy*) in combination with a nonlinear Lagrangian description of motion. But in contrast to a *Total Lagrangian Formulation*, the global positions of the nodes in the undeformed configuration are the design variables for the unconstrained optimization problem. Several numerical examples are presented, showing the power, robustness and stability of the Variation of Reference Strategy.

Chapter 6 presents two different industrial applications of the presented method and material model. The first example deals with the generation of optimized cutting patterns for selected parts of a textile car seat cover. The second example deals with the generation of optimized cutting patterns for structures made of CFRP (roof crossrail for cars).

Chapter 7 concludes this dissertation with a summary of the introduced response surface material model and the developed *Variation of Reference Strategy*. Based on the achieved results and identified drawbacks further applications and ideas for future research projects are discussed.

2

Fundamentals

"Since the fabric of the universe is most perfect and the work of a most wise Creator, nothing at all takes place in the universe in which some rule of maximum or minimum does not appear."

— Leonhard Euler, 1707 - 1783
Swiss Mathematician and Physicist

2.1 Mathematics

In general, problems within the field of structural mechanics are mathematically described in terms of partial differential equations (PDE) based on unknown scalar, vector or tensor fields (primary variables), e.g. displacement field, temperature field. In case of a so-called *conservative system* there exists a potential functional[1] or short potential describing the internal stress state and the external loading of the system. More details on conservative systems are given in BELYTSCHKO ET AL. [11] or HOLZAPFEL [60]. Since in nature all systems tend to a state where their energy is on a minimum level, the equilibrium state is described by the system's *stationary point* of the underlying potential functional (extremum principle). In a more mathematical fashion, such problems are called *natural variational principles* (NVP) (ZIENKIEWICZ [113]). A more general approach for such problems is based on the boundary value problem describing the balance of momentum (dynamics) or the static equilibrium (statics). A very common strategy for obtaining an approximate solution for the boundary value problem (BVP) is based on the method of weighted residuals (Galerkin method).

This chapter provides and discusses the basic mathematical concepts for handling and solving problems described in terms of either a natural variational principle or a boundary value problem (i.e. strong forms and weak forms of PDEs). Additionally, the concept of differential geometry providing a powerful tool for describing spatial surfaces will be introduced. For comprehensive information on these topics, the author refers to a broad variety of literature: BAŞAR AND KRÄTZIG [4], GEKELER [47], HOLZAPFEL [60], KIELHÖFER [67], WRIGGERS [112], ZIENKIEWICZ [113].

2.1.1 Nabla operator

In the following, two fundamental concepts are discussed describing the change of arbitrary scalar, vector or tensor-valued fields[2]. But before doing this, the so-called *Nabla operator* $\nabla_{(\bullet)}$ defining a column vector of partial derivatives w.r.t. all components of an arbitrary vector $(\bullet)$ needs to be introduced:

$$\nabla_{(\bullet)} = \begin{bmatrix} \dfrac{\partial}{\partial (\bullet)_1} \\ \vdots \\ \dfrac{\partial}{\partial (\bullet)_n} \end{bmatrix} \quad \text{with} \quad (\bullet) = \begin{bmatrix} (\bullet)_1 \\ \vdots \\ (\bullet)_n \end{bmatrix} \tag{2.1}$$

---

[1] according to BRONSTEIN ET AL. [29], a function is called functional if it assigns a scalar, vector or tensor-valued field $\mathbf{a}(\mathbf{x})$ to a scalar function $\Pi(\mathbf{a})$, e.g. $\Pi(\mathbf{a}) = \int_\Omega \mathbf{a}(\mathbf{x})\,\mathrm{d}\Omega$

[2] e.g. level set field, displacement or velocity field, strain or stress field

In case of a n-dimensional Euclidean space $\mathbb{R}^n$, Equation (2.1) can be redefined as follows:

$$\nabla = \nabla_{\mathbf{x}} = \frac{\partial}{\partial x_i}\,\mathbf{e}_i = \frac{\partial}{\partial x_1}\mathbf{e}_1 + \ldots + \frac{\partial}{\partial x_n}\mathbf{e}_n \tag{2.2}$$

2.1.2 Gradient and Directional derivative

Consider an arbitrary domain Ω embedded within an Euclidean space $\mathbb{R}^3$. A scalar, vector or tensor-valued quantity depending on the position $\mathbf{x}$ inside the domain Ω is called a scalar field $\alpha\left(\mathbf{x}\right)$, vector field $\mathbf{a}\left(\mathbf{x}\right)$ or tensor-valued field $\mathbf{A}\left(\mathbf{x}\right)$, respectively. A very important characteristic of such a field is its change in the direction of each Euclidean basis $\mathbf{e}_i$. Therefore, the so-called *gradient* is defined as follows:

$$\mathrm{grad}\alpha = \nabla\alpha = \frac{\partial\alpha}{\partial x_i}\mathbf{e}_i \tag{2.3a}$$

$$\mathrm{grad}\mathbf{a} = \nabla\otimes\mathbf{a} = \frac{\partial a_i}{\partial x_j}\mathbf{e}_i\otimes\mathbf{e}_j \tag{2.3b}$$

$$\mathrm{grad}\mathbf{A} = \nabla\otimes\mathbf{A} = \frac{\partial A_{ij}}{\partial x_k}\mathbf{e}_i\otimes\mathbf{e}_j\otimes\mathbf{e}_k \tag{2.3c}$$

REMARK I: In addition to the gradient of scalar, vector or tensor-valued fields, especially in fluid mechanics their divergence[3] and curl may be of interest. For further information the author refers to CHAVES [32], GEKELER [47] and HOLZAPFEL [60].

The concept of the directional derivative or *Gâteaux derivative* is a powerful tool obtaining information on the change of a scalar, vector or tensor-valued field w.r.t. an arbitrary direction $(\bullet)$ at a fixed position $\mathbf{x}$. Therefore, consider a scalar field $\alpha\left(\mathbf{x}\right)$. By means of a local parameter ϵ, the increase/decrease of the scalar field along a straight line $L : \bar{\mathbf{x}} = \mathbf{x} + \epsilon\left(\bullet\right)$ can be measured. Looking at $\epsilon = 0$ leads to the increase/decrease of the scalar field at the point $\mathbf{x}$ in the direction of $(\bullet)$:

$$D_{(\bullet)}\alpha\left(\mathbf{x}\right) = \frac{\mathrm{d}}{\mathrm{d}\epsilon}\Big(\alpha\left(\mathbf{x} + \epsilon\ (\bullet)\right)\Big)\Big|_{\epsilon=0} \tag{2.4}$$

with $D_{(\bullet)}$ being the so-called *Gâteaux operator*. A closer look at Equation (2.4) reveals that the directional derivative is equivalent to the orthogonal projection of the gradient of the scalar field in the specified direction. Finally, the Gâteaux derivative does not only apply to scalar fields but also

---

[3] see Equation (A.42) in Appendix A

to vector and tensor-valued fields as well:

$$D_{(\bullet)}\alpha\left(\mathbf{x}\right) = \frac{\partial\alpha\left(\mathbf{x}\right)}{\partial\mathbf{x}} \cdot (\bullet) = \mathrm{grad}\alpha \cdot (\bullet) \tag{2.5a}$$

$$D_{(\bullet)}\mathbf{a}\left(\mathbf{x}\right) = \frac{\partial\mathbf{a}\left(\mathbf{x}\right)}{\partial\mathbf{x}} \cdot (\bullet) = \mathrm{grad}\mathbf{a} \cdot (\bullet) \tag{2.5b}$$

$$D_{(\bullet)}\mathbf{A}\left(\mathbf{x}\right) = \frac{\partial\mathbf{A}\left(\mathbf{x}\right)}{\partial\mathbf{x}} \cdot (\bullet) = \mathrm{grad}\mathbf{A} \cdot (\bullet) \tag{2.5c}$$

2.1.3 Natural variational principles

Let $\mathcal{F}\left(\mathbf{a}\right)$ be an arbitrary potential functional over a domain Ω where its input argument is again an arbitrary function of an underlying vector field $f\left(\mathbf{a}\right) = f\big(\mathbf{a}\left(\mathbf{x}\right)\big)$:

$$\min \longrightarrow \mathcal{F}\left(\mathbf{a}\right) = \int\limits_{\Omega} f\left(\mathbf{a}\right)\ \mathrm{d}\Omega \tag{2.6}$$

The goal is now to find that vector field $\mathbf{a}\left(\mathbf{x}\right)$, which minimizes the functional $\mathcal{F}\left(\mathbf{a}\right)$, i.e. which leads to a *stationary point*. Therefore, an infinitesimal ($\epsilon \to 0$) small and *virtual* vector field $\delta\mathbf{a}$ is introduced yielding a slightly modified vector field $\bar{\mathbf{a}}$:

$$\delta\mathbf{a} = \bar{\mathbf{a}} - \mathbf{a} \tag{2.7}$$

where $\tilde{\mathbf{a}}$ is an arbitrary and independent vector field vanishing at the portions of the boundary $\partial\Omega$ where $\mathbf{a}$ is prescribed (*essential boundary conditions*). Applying the Gâteaux derivative (2.4) in the direction of the virtual vector field leads to the so-called 1^{st} *Variation* of the functional:

$$\delta\mathcal{F}\left(\mathbf{a},\delta\mathbf{a}\right) = D_{\delta\mathbf{a}}\mathcal{F}\left(\mathbf{a},\delta\mathbf{a}\right) = \frac{\mathrm{d}}{\mathrm{d}\epsilon}\Big(\mathcal{F}\left(\mathbf{a}+\epsilon\ \delta\mathbf{a}\right)\Big)\bigg|_{\epsilon=0} \tag{2.8}$$

According to the rules of *Variational Calculus*, a stationary point of a functional is reached when its first variation vanishes[4], i.e. $\delta\mathcal{F}\left(\mathbf{a},\delta\mathbf{a}\right) = 0$. By means of the permutability property (A.18), this leads to:

$$\begin{aligned}
\delta\mathcal{F}\left(\mathbf{a},\delta\mathbf{a}\right) &= \delta\int\limits_{\Omega} f\left(\mathbf{a},\delta\mathbf{a}\right)\ \mathrm{d}\Omega = \int\limits_{\Omega} \delta f\left(\mathbf{a},\delta\mathbf{a}\right)\ \mathrm{d}\Omega \\
&= \int\limits_{\Omega} \frac{\mathrm{d}}{\mathrm{d}\epsilon}\Big(f\left(\mathbf{a}+\epsilon\ \delta\mathbf{a}\right)\Big)\bigg|_{\epsilon=0}\ \mathrm{d}\Omega \\
&= \int\limits_{\Omega} \frac{\partial f\left(\mathbf{a}\right)}{\partial\mathbf{a}} \cdot \delta\mathbf{a}\ \mathrm{d}\Omega = \delta\mathbf{a}\int\limits_{\Omega} \frac{\partial f\left(\mathbf{a}\right)}{\partial\mathbf{a}}\ \mathrm{d}\Omega = 0
\end{aligned} \tag{2.9}$$

According to the 1^{st} *Fundamental Lemma of Variational Calculus* (i.e. $\delta\mathbf{a} \neq 0$), Equation (2.9) is only fulfilled if the integral vanishes. Finally,

---

[4] this is analog to the definition of a stationary point in *Calculus*

the following in general nonlinear system of equations (SoE) for the optimization problem stated in Equation (2.6) can be established:

$$\boldsymbol{\mathcal{R}}\left(\mathbf{a}\right) = \int\limits_{\Omega} \frac{\partial f\left(\mathbf{a}\right)}{\partial \mathbf{a}}\ \mathrm{d}\Omega = 0 \tag{2.10}$$

REMARK II: The intent of this section is to introduce the basic tools for this type of problem. For further information on the topic of *Variational Calculus* the author refers to BAŞAR AND KRÄTZIG [4], GEKELER [47], HOLZAPFEL [60] and KIELHOFER [67].

2.1.4 Method of weighted residuals: Galerkin approach

Consider the following arbitrary boundary value problem:

$$f\left(\mathbf{a}_{,\mathbf{x}}\left(\mathbf{x}\right), \mathbf{a}\left(\mathbf{x}\right)\right) + g\left(\mathbf{x}\right) = 0 \qquad \text{on} \quad \Omega \tag{2.11a}$$

$$\mathbf{a}\left(\mathbf{x}\right) = \bar{\mathbf{a}}\left(\mathbf{x}\right) \qquad \text{on} \quad \partial\Omega^{\mathrm{Dir}} \tag{2.11b}$$

$$\mathbf{a}_{,\mathbf{x}}\left(\mathbf{x}\right) = \bar{\mathbf{a}}_{,\mathbf{x}}\left(\mathbf{x}\right) \qquad \text{on} \quad \partial\Omega^{\mathrm{Neu}} \tag{2.11c}$$

with Equation (2.11b) and (2.11c) representing the Dirichlet boundary conditions and Neumann boundary conditions, respectively.

$$\partial\Omega = \partial\Omega^{\mathrm{Dir}} \cup \partial\Omega^{\mathrm{Neu}} \quad \text{and} \quad \partial\Omega^{\mathrm{Dir}} \cap \partial\Omega^{\mathrm{Neu}} = \emptyset \tag{2.12}$$

Equation (2.11a) is also known as *strong form.* In general, there exists no closed form solution for such boundary value problems. In order to find that vector field $\mathbf{a}\left(\mathbf{x}\right)$ which satisfies Equation (2.11a), an approximation technique called *method of weighted residual* is applied. Therefore, the vector field $\mathbf{a}\left(\mathbf{x}\right)$ is approximated by a so-called *trail field.* A very common choice for the trail field is stated below:

$$\mathbf{a}\left(\mathbf{x}\right) \approx \tilde{\mathbf{a}}\left(\mathbf{x}\right) = \sum_{i=1}^{n} N_i\left(\mathbf{x}\right) \cdot \mathbf{a}_i \tag{2.13}$$

with $N_i\left(\mathbf{x}\right)$ representing the so-called *trail functions*[5]. Inserting Equation (2.13) in (2.11a) leads to the following *residual equation*:

$$R\left(\tilde{\mathbf{a}}\left(\mathbf{x}\right)\right) = f\left(\tilde{\mathbf{a}}_{,\mathbf{x}}\left(\mathbf{x}\right), \tilde{\mathbf{a}}\left(\mathbf{x}\right)\right) + g\left(\mathbf{x}\right) \neq 0 \tag{2.14}$$

The strategy is now to minimize the inner product of the residual equation and a *test field* $\boldsymbol{\eta}\left(\mathbf{x}\right)$ in an integral sense:

$$\boldsymbol{\mathcal{R}}\left(\mathbf{a}\right) =< \boldsymbol{\eta}\left(\mathbf{x}\right), R\left(\tilde{\mathbf{a}}\left(\mathbf{x}\right)\right) >= \int\limits_{\Omega} \boldsymbol{\eta}\left(\mathbf{x}\right) \cdot R\left(\tilde{\mathbf{a}}\left(\mathbf{x}\right)\right) \mathrm{d}\,\Omega = 0 \tag{2.15}$$

---

[5] within the scope of finite elements the trail functions are the shape function

The test field $\boldsymbol{\eta}\left(\mathbf{x}\right)$ can be chosen arbitrarily but has to meet the Dirichlet BCs defined in Equation (2.11b). In case of the *Galerkin method* the test and trial functions are identical, i.e.

$$\boldsymbol{\eta}\left(\mathbf{x}\right) = \sum_{j=1}^{n} N_j\left(\mathbf{x}\right) \cdot \boldsymbol{\eta}_j \tag{2.16}$$

Finally, Equation (2.15) results in a system of n independent (nonlinear) equations with the goal of finding the unknown coefficients $\mathbf{a}_i$. Equation (2.15) is also called the *weak form* of the stated boundary value problem (2.11a).

REMARK III: For further information on the *method of weighted residuals* and the *Galerkin approach* the author refers to GEKELER [47], HUGHES [61], KIELHOFER [67] and ZIENKIEWICZ [113].

2.1.5 Linearization

The concept of linearization is similar to the variational concept introduced in the previous Section 2.1.3. But instead of considering a virtual vector field, a finite vector field called increment $\Delta\mathbf{a}$ is used. Again, applying the Gâteaux derivative (2.4) in the direction of the increment vector field $\Delta\mathbf{a}$ yields the linearization of $\boldsymbol{\mathcal{R}}\left(\mathbf{a}\right)$:

$$\Delta\boldsymbol{\mathcal{R}}\left(\mathbf{a}, \Delta\mathbf{a}\right) = D_{\Delta\mathbf{a}}\boldsymbol{\mathcal{R}}\left(\mathbf{a}, \Delta\mathbf{a}\right) = \left.\frac{\mathrm{d}}{\mathrm{d}\epsilon}\left(\boldsymbol{\mathcal{R}}\left(\mathbf{a} + \epsilon\,\Delta\mathbf{a}\right)\right)\right|_{\epsilon=0} \tag{2.17}$$

with $\Delta\left(\bullet\right)$ being the so-called *Linearization operator*.

2.2 Iterative schemes: nonlinear (optimization) problems

2.2.1 Newton-Raphson scheme

Consider the following nonlinear system of equations:

$$\boldsymbol{\mathcal{R}}\left(\mathbf{a}\right) = \int_{\Omega} \frac{\partial f\left(\mathbf{a}\right)}{\partial \mathbf{a}}\ \mathrm{d}\Omega = 0 \tag{2.18}$$

where the vector field $\mathbf{a}$ represents the field of primary variables. A common approach for solving such a nonlinear system is the so-called *Newton-Raphson scheme*. It is an iterative procedure for finding the roots of a nonlinear problem based on its *consistent linearization*.

Considering an arbitrary point $\mathbf{a}^i$ of $\boldsymbol{\mathcal{R}}\left(\mathbf{a}\right)$, the vicinity of the point $\mathbf{a}^i$ can be approximated in a linear fashion by means of a truncated sum (Taylor-Series - see BRONSTEIN ET AL. [29]):

$$\boldsymbol{\mathcal{R}}\left(\mathbf{a}^{i+1}\right) = \boldsymbol{\mathcal{R}}\left(\mathbf{a}^{i}\right) + \Delta\boldsymbol{\mathcal{R}}\left(\mathbf{a}^{i}, \Delta\mathbf{a}\right) + \mathcal{O}\left(\Delta\mathbf{a}^2\right) \tag{2.19}$$

with $\Delta\boldsymbol{\mathcal{R}}\left(\mathbf{a}^i, \Delta\mathbf{a}\right)$ being the directional derivative of $\boldsymbol{\mathcal{R}}(\mathbf{a})$ at $\mathbf{a}^i$ pointing towards $\mathbf{a}^{i+1}$. According to Equation (2.17), the directional derivative can be expressed as follows:

$$D_{\Delta\mathbf{a}}\boldsymbol{\mathcal{R}}\left(\mathbf{a}^i, \Delta\mathbf{a}\right) = \left.\frac{\partial\boldsymbol{\mathcal{R}}(\mathbf{a})}{\partial\mathbf{a}}\right|_{a^i} \cdot \Delta\mathbf{a} = \left.\frac{\partial\boldsymbol{\mathcal{R}}(\mathbf{a})}{\partial\mathbf{a}}\right|_{a^i} \cdot \left(\mathbf{a}^{i+1} - \mathbf{a}^i\right) \tag{2.20}$$

Keeping in mind that the function value has to vanish, for each iteration step the following statement holds:

$$\boldsymbol{\mathcal{R}}\left(\mathbf{a}^{i+1}\right) = \boldsymbol{\mathcal{R}}\left(\mathbf{a}^i\right) + \Delta\boldsymbol{\mathcal{R}}\left(\mathbf{a}^i, \Delta\mathbf{a}\right) = 0 \tag{2.21}$$

More precisely, the new vector $\mathbf{a}^{i+1}$ is assumed to represent the root, whereat $\Delta\mathbf{a}$ represents the update of the unknown vector field $\mathbf{a}$ from the i to the i+1 iteration step. Consequently, applying Equation (2.20) to Equation (2.21) leads to the governing equation of the Newton-Raphson scheme:

$$\mathbf{a}^{i+1} = \mathbf{a}^i - \left[\left.\frac{\partial\boldsymbol{\mathcal{R}}(\mathbf{a})}{\partial\mathbf{a}}\right|_{a^i}\right]^{-1} \cdot \boldsymbol{\mathcal{R}}\left(\mathbf{a}^i\right) \tag{2.22}$$

REMARK I: Over the past decades various variations of the Newton-Raphson scheme have been developed dealing with problems arising due to the linearization. For further information on the so-called *Newton type* iterations schemes, the author refers to DEUFLHARD [35].

2.2.2 Method of steepest descent

Consider the following arbitrary but unconstrained minimization problem:

$$\min_{\mathbf{a}\in\mathbb{R}^n} \longrightarrow f(\mathbf{a}) \tag{2.23}$$

with $\mathbf{a}$ being the vector of n design variables. In contrast to a natural variational principle (see Section 2.1.3), the *method of steepest decent* directly works on the objective function itself. Considering an arbitrary iteration step i, the negative gradient information of the objective function $f(\mathbf{a})$ at a given point $\mathbf{a}^i$

$$\mathbf{s}^i = -\nabla_{\mathbf{a}} f\left(\mathbf{a}^i\right) \tag{2.24}$$

is used for the design update

$$\mathbf{a}^{i+1} = \mathbf{a}^i + \alpha\,\mathbf{s}^i \tag{2.25}$$

with α being the *step-size* and $\mathbf{s}^i$ being the *search direction.* In case of a non-fixed step-size, a *line search technique* needs to be applied additionally, e.g. *Armijo step-size rule* or *polynomial approximation.* In general, the gradient does not point towards the optimum. This effect is reflected in a *zig-zagging* characteristic.

REMARK II: For further information on the method of steepest descent the author refers to Baldick [6].

2.3 The concept of differential geometry

The mathematical description of a structure in space provides the basis for investigating its structural response. Depending on their overall dimensions (l_1, l_2, l_3), spatial structures can be categorized in three different groups, namely trusses/beams (1D), shells/membranes (2D) and solids (3D), cf. Figure 2.1.

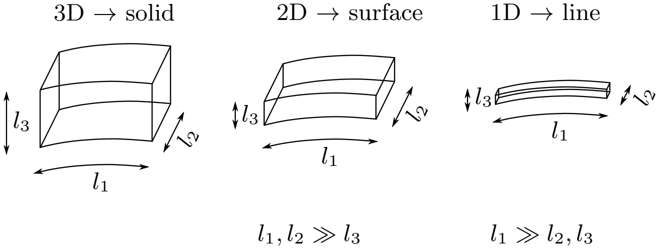

Figure 2.1: Categories of structures in space: solid (left), surface (center), line (right)

All structures investigated in this thesis are characterized by their in-plane dimensions being significantly larger than their out-of-plane dimension, i.e. $l_1, l_2 \gg l_3$. Hence, they are considered as 2D surfaces, see Figure 2.1. Furthermore, in case of a constant thickness ($l_3 =$ const.), the corresponding volume integral can be reduced to a product of thickness and an integral over a 2D surface representing the structure's mid-plane. The mathematical description, i.e. the geometry and properties, can therefore be reduced to their mid-plane. Hence, two independent in-plane parameters, the so-called surface parameters, are sufficient. This leads to a dimensional reduction by 1, i.e. 3D → 2D. All required mathematical tools for this task are provided by the theory of differential geometry and will be presented in the following. For a comprehensive and circumstantial compendium on these topics the author refers to various literature: Başar and Krätzig [4], Chapelle and Bathe [30], Krätzig and Başar [72].

2.3.1 Surfaces: Description of Geometry

Consider a body $\mathcal{B}$ representing a thin structure within a 3-dimensional Euclidean space $\mathbb{R}^3$, as illustrated in Figure 2.2. If $l_1, l_2 \gg l_3$ holds, the body $\mathcal{B}$ can be reduced to a surface $\mathcal{S}$. The goal is now to describe the

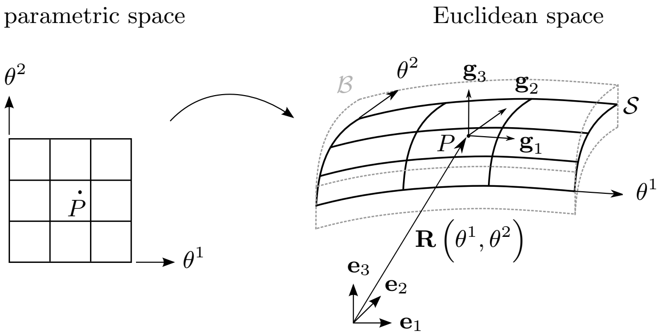

Figure 2.2: Description of a thin structure in space

position of an arbitrary point located on this surface $P \in \mathcal{S}$ in terms of the two independent surface parameters θ^1 and θ^2. Therefore, a two dimensional coordinate frame spanned by an orthonormal basis θ^i $(i = 1 \ldots 2)$ is introduced. The resulting coordinate space $\mathbb{R}^2$ is also referred to as parametric space, see Figure 2.2. The orthonormal surface parameters within the parametric space are then mapped onto the surface $\mathcal{S}$ defined within the Euclidean space $\mathbb{R}^3$:

$$\begin{aligned} \mathcal{S} : \left(\theta^1,\theta^2\right) &\in \mathbb{R}^2 \to \mathbb{R}^3 \, , \\ \left(\theta^1,\theta^2\right) &\to \mathbf{R}\left(\theta^1,\theta^2\right) = x_j\left(\theta^1,\theta^2\right)\mathbf{e}_j \quad \text{with} \quad j = 1\ldots 3 \end{aligned} \tag{2.26}$$

This leads to a unique parametric description of each point $P \in \mathcal{S}$ due to its position vector $\mathbf{R}$. A closer look on the corresponding map reveals the structure of its linear operator, the *Jacobian matrix* $\mathbf{J}$:

$$\begin{bmatrix} \mathrm{d}x_1 \\ \mathrm{d}x_2 \\ \mathrm{d}x_3 \end{bmatrix} = \left[\frac{\partial\left(x_1,x_2,x_3\right)}{\partial\left(\theta^1,\theta^2\right)}\right] \cdot \begin{bmatrix} \mathrm{d}\theta^1 \\ \mathrm{d}\theta^2 \end{bmatrix} \quad \text{with} \quad \mathbf{J} = \left[\frac{\partial\left(x_1,x_2,x_3\right)}{\partial\left(\theta^1,\theta^2\right)}\right] \tag{2.27}$$

With the parametric description (2.26) on hand, for each point $P \in \mathcal{S}$ a *convective coordinate frame* spanned by its *covariant* base vectors $\mathbf{g}_i$ $(i = 1 \ldots 3)$ can be established as follows:

$$\mathbf{g}_1 = \frac{\partial\mathbf{R}\left(\theta^1,\theta^2\right)}{\partial\theta^1} \, , \quad \mathbf{g}_2 = \frac{\partial\mathbf{R}\left(\theta^1,\theta^2\right)}{\partial\theta^2} \, , \quad \mathbf{g}_3 = \frac{\mathbf{g}_1 \times \mathbf{g}_2}{\|\mathbf{g}_1 \times \mathbf{g}_2\|} \tag{2.28}$$

In addition to the general basis defined by Equation (2.28) the *dual basis* of the convective coordinate frame can be introduced. The corresponding *contra-variant* base vectors $\mathbf{g}^i$ $(i = 1 \ldots 3)$ are defined as follows:

$$\mathbf{g}^1 = \mathbf{g}_2 \times \mathbf{g}_3 \;, \quad \mathbf{g}^2 = \mathbf{g}_3 \times \mathbf{g}_1 \;, \quad \mathbf{g}^3 = \mathbf{g}_3 \tag{2.29}$$

A second glance on Equation (2.29) clearly shows the relation between the covariant and contra-variant base vectors. Each of the two in-plane base vectors of one basis is orthogonal to the other in-plane base vector and the out-of-plane base vector of the dual basis, see equation $(2.29)_1$ and $(2.29)_2$. The out-of-plane base vectors coincide, see equation $(2.29)_3$.

REMARK I: Due to their definition, the out-of-plane base vectors $\mathbf{g}_3$ and $\mathbf{g}^3$ only capture the orientation of the surface in space but exhibit no information on the inner geometry of the surface in space w.r.t. its normal direction. If the kinematics of a shell-type body is described by means of its mid-surface[6], this effect has to be taken into account (see Section 3.1.1).

REMARK II: Throughout this thesis scalars, vectors and tensor-valued quantities with subscripts or superscripts are called covariant or contra-variant, respectively.

The determinant of the Jacobian matrix (2.27) or short *Jacobian* plays an important role. This is due to the fact that it provides detailed information on the behavior of the map in the nearby neighborhood. Consider the map defined by Equation (2.26). A closer look on the absolute value of the Jacobian $\det\mathrm{J} = |\det \mathbf{J}|$ reveals that it exhibits a measure for the shrinkage or dilatation of the area in the vicinity of $P \in \mathcal{S}$. Looking at Equation (2.27), the evaluation of the determinant is not straightforward. Due to the rectangular structure of $\mathbf{J}$ the so-called *Gram determinant* or short *Gramian*[7] has to be established. By means of the in-plane covariant base vectors $(2.28)_1$ and $(2.28)_2$ the Gramian results in:

$$\begin{aligned} \mathrm{Gram}\,(\mathbf{J}) = \det\left(\mathbf{J}^T\mathbf{J}\right) &= \begin{bmatrix} <\mathbf{g}_1 \,,\, \mathbf{g}_1> & <\mathbf{g}_1 \,,\, \mathbf{g}_2> \\ <\mathbf{g}_2 \,,\, \mathbf{g}_1> & <\mathbf{g}_2 \,,\, \mathbf{g}_2> \end{bmatrix} \\ &= \|\mathbf{g}_1 \times \mathbf{g}_2\|^2 \end{aligned} \tag{2.30}$$

Thus, the Gramian represents the square of the area of the parallelogram spanned by the in-plane covariant base vectors. This leads to

$$\det\mathrm{J} = \sqrt{\mathrm{Gram}\,(\mathbf{J})} = \|\mathbf{g}_1 \times \mathbf{g}_2\| \tag{2.31}$$

Applying the substitution rule of calculus, a differential surface element in the parametric space $\mathrm{d}\theta^1\,\mathrm{d}\theta^2$ is mapped into a differential surface element $\mathrm{d}a$ in the Euclidean space as follows:

$$\mathrm{d}a = \det\mathrm{J}\;\, \mathrm{d}\theta^1\,\mathrm{d}\theta^2 \tag{2.32}$$

---

[6] 3-, 5-, 6-parameter formulation, see page 36f

[7] for additional information the author refers to BEUTELSPACHER [12]

Finally, by means of Equation (2.32) the area of a spatial surface can now be established in terms of its surface parameters:

$$\int_a (\bullet)\ \mathrm{d}a = \int_{\theta^1}\int_{\theta^2} (\bullet)\ \det\mathrm{J}\ \mathrm{d}\theta^1\,\mathrm{d}\theta^2 \tag{2.33}$$

REMARK III: Within the scope of finite elements, Equation (2.33) appears to be very useful for evaluating the system matrices within the element's parametric space.

2.3.2 Surfaces: 1$^{\mathrm{st}}$ and 2$^{\mathrm{nd}}$ fundamental form

The convective coordinate frames defined by Equation (2.28) and (2.29) prove to be very useful for evaluating the properties of a surface in the vicinity of a point $P \in \mathrm{S}$. Therefore, the following two so-called *fundamental forms* will be introduced.

2.3.2.1 1$^{\mathrm{st}}$ fundamental form

The 1$^{\mathrm{st}}$ *fundamental form* provides detailed information on the inner geometry of a surface at a point $P \in \mathrm{S}$. In terms of mathematics, all this information is achieved due to the so-called *metric-tensor* **I**:

$$\mathbf{I} = g_{ij}\ \mathbf{g}^i \otimes \mathbf{g}^j = g^{ij}\ \mathbf{g}_i \otimes \mathbf{g}_j \quad \text{with} \quad i,j = 1\ldots 3 \tag{2.34}$$

where the coefficients are either the inner products of the covariant base vectors (2.35a) or contra-variant base vectors (2.35b).

$$g_{ij} =< \mathbf{g}_i\ ,\ \mathbf{g}_j >= \mathbf{g}_i \cdot \mathbf{g}_j \tag{2.35a}$$

$$g^{ij} =< \mathbf{g}^i\ ,\ \mathbf{g}^j >= \mathbf{g}^i \cdot \mathbf{g}^j \tag{2.35b}$$

Due to the definition of the third base vector $(2.28)_3$ or $(2.29)_3$, the corresponding inner products posses no additional geometric information, i.e. $g_{33} = g^{33} = 1$ and $g_{i3} = g_{3j} = 0$ or $g^{i3} = g^{3j} = 0$, respectively. The remaining coefficients of the metric-tensor $(i, j = 1\ldots 2)$ exhibit a measure for the length of the basis vectors (diagonal terms), the angle between two basis vector (off-diagonal terms) and the area of the parallelogram spanned by two base vectors (square root of the determinant).

Since the covariant and contra-variant metric tensors are defined at the same point $P \in \mathrm{S}$, they describe the same inner geometry. Hence, the following relation holds:

$$g_{ij} = \left[g^{ij}\right]^{-1} \tag{2.36}$$

Additionally, the covariant and contra-variant coefficients of the metric tensor provide the possibility to switch between the dual basis:

$$\mathbf{g}^i = g^{ij}\ \mathbf{g}_j \tag{2.37a}$$

$$\mathbf{g}_i = g_{ij}\ \mathbf{g}^j \tag{2.37b}$$

Finally, by means of Equation (2.37) and the *Kronecker delta* defined in Equation (A.8) the metric tensor can be expressed as the dyadic product of the covariant and contra-variant base vectors:

$$\mathbf{I} = \mathbf{g}_i \otimes \mathbf{g}^i = \mathbf{g}^j \otimes \mathbf{g}_j \quad \text{with} \quad i, j = 1 \ldots 3 \tag{2.38}$$

2.3.2.2 2nd fundamental form

The 2nd *fundamental form* provides detailed information on the shape of a surface. Introducing the so-called *curvature-tensor* **K** leads to a measure for the curvature and twist of a surface at a point $P \in \mathrm{S}$:

$$\mathbf{K} = -\frac{\partial \mathbf{x}}{\partial \theta^i} \cdot \frac{\partial \mathbf{g}_3}{\partial \theta^j}\, \mathbf{g}^i \otimes \mathbf{g}^j \quad \text{with} \quad i, j = 1 \ldots 2 \tag{2.39}$$

The inverse of the diagonal terms K_{11} and K_{22} represent the radii of the circles of curvature within the planes spanned by the corresponding in-plane contra-variant base vectors $\mathbf{g}^1$ and $\mathbf{g}^2$ and the surface outward normal vector $\mathbf{n} = \mathbf{g}^3$, respectively. The sign of the respective coefficient shows the location of its center of curvature. If the sign is positive/negative the center of curvature is said to be outside/inside[8] the surface. Furthermore, the off-diagonal coefficients K_{12} and K_{21} exhibit a measure for the twist of the surface. Solving the eigenvalue problem of Equation (2.39) leads to the so-called *principal curvatures*:

$$\mathbf{K} = \mathrm{K}_i\, \hat{\mathbf{n}}_i \otimes \hat{\mathbf{n}}_i \quad \text{with} \quad i = 1 \ldots 2 \tag{2.40}$$

with K_i being the i-th eigenvalue and $\hat{\mathbf{n}}_i$ being the i-th eigenvector. The inverse of K_i are called *principal radii of curvature* R_i.

The product of the principal curvatures K_i leads to the so-called *Gaussian curvature* κ:

$$\kappa = \mathrm{K}_1 \cdot \mathrm{K}_2 = \frac{1}{\mathrm{R}_1} \cdot \frac{1}{\mathrm{R}_2} = \det(\mathbf{K}) \tag{2.41}$$

The Gaussian curvature allows a categorization of the surface at each point $P \in \mathrm{S}$ within the following three groups (cf. Figure 2.3):

- → $\kappa < 0$: anticlastic or hyperbolic
- → $\kappa = 0$: parabolic or ruled
- → $\kappa > 0$: synclastic or elliptic

REMARK IV: If and only if a surface consists exclusively of parabolic points ($\forall P \in S : \kappa = 0$), the surface is said to be developable. Hence, there exists a stress-free coextensive planar configuration of the surface, e.g. a coextensive rectangle for a cylindrical surface.

---

[8] this is defined by the so-called outward normal vector **n**

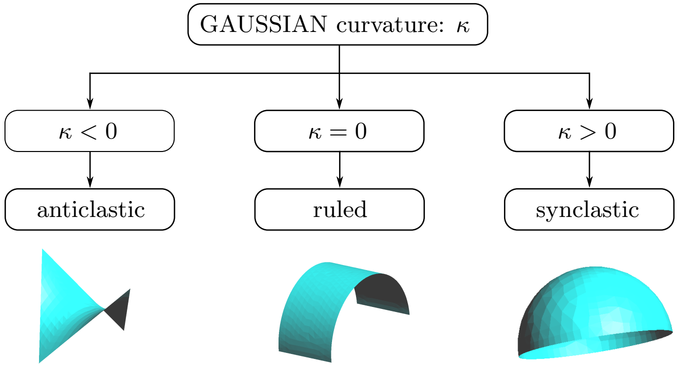

Figure 2.3: Categories of surfaces: anticlastic/hyperbolic (left), ruled/parabolic (center), synclastic/elliptic (right)

3

Nonlinear continuum mechanics

"Fest gemauert in der Erden steht die Form, aus Lehm gebrannt. Heute muß die Glocke werden. Frisch Gesellen, seid zur Hand."

— Friedrich Schiller, 1759 - 1805
German poet, philosopher and historian

Consider an arbitrary structure (body) made of either steel, concrete, CFRP, textile fabric or any other material. Several millions of individual particles composed of a set of different molecules are combined, forming its physical shape and being responsible for its physical behavior. In contrast to a physicist or a chemist, for a structural engineer results gained on an atomistic level are quite time consuming and in the most cases of little interest. Considering a bridge for example, a design engineer is more interested in the overall physical behavior, the so-called macroscopic scale, instead of the single motion of each concrete particle, the so-called microscopic scale. On a macroscopic level, the structure to investigate is considered as a continuous body or continua approximating its internal microscopic structure. As a result of this assumption, every single point within the continuous body is not directly related to a specific particle or molecule anymore. The theory of nonlinear continuum mechanics provides a powerful theoretical framework for modeling a continuous body on a macroscopic scale. This chapter introduces the mathematical descriptions for the kinematic (strains), structural response (stresses) and state (equilibrium) of a body based on a continuum mechanical approach.

3.1 Nonlinear kinematics of a continuum

Starting from a macroscopic[1] point of view, a continuous body or simple continuum $\mathcal{B}$ is defined as a body where the mass and the volume is continuously distributed over itself. For the following considerations such a continuous body $\mathcal{B}$ is located within an Euclidean space $\mathbb{R}^3$ spanned by an orthonormal basis $\mathbf{e}_i$ $(i = 1, 2, 3)$. The geometrical domain Ω engaged by the continuous body $\mathcal{B}$ is defined as configuration.

This section will introduce the basic concepts of describing the motion of a point inside a continuum (see Section 3.1.2) followed by some strategies describing the deformation state of a continua (see Section 3.1.3). The intent of this section is to provide the reader with all necessary definitions and equations regarding nonlinear kinematics within the scope of this thesis. For comprehensive information on these topics, the author refers to a broad variety of literature: ALTENBACH [2], BELYTSCHKO ET AL. [11], CHAVES [32], HAUPT [57], HOLZAPFEL [60], ITSKOV [62], OGDEN [88], PARISCH [89], WRIGGERS [112].

3.1.1 Degenerated solids: shell-like bodies

Consider a thin continuous body $\mathcal{B}$ (cf. Figure 2.1). As already discussed in Section 2.3, the description of its geometry can be reduced to a surface (in general either the lower/upper surface or mid-surface). Unfortunately, when it comes to energy related questions this reduction is not applicable in most of the cases. The reason for this is the fact that information distributed over the whole volume of the body needs to be taken into account for capturing the entire strain and stress state of the thin continuous body $\mathcal{B}$.

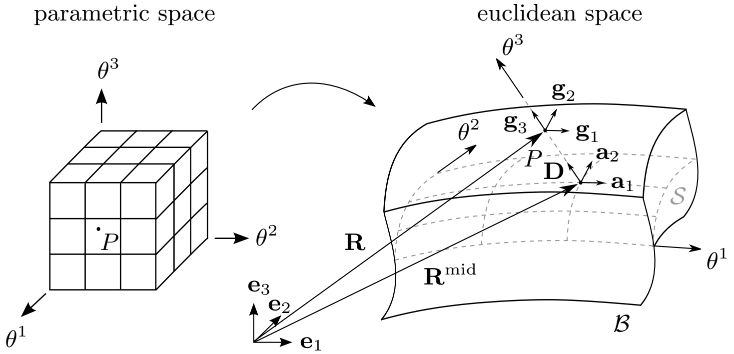

Figure 3.1: Degenerated solid approach

---

[1] a more detailed definition of the different scales is given in CHAVES [32]

Therefore, the so-called *degenerated solid* approach is introduced. A point within a thin continuous body $\mathcal{B}$ is described by its mid-surface $\mathbf{R}^{\mathrm{mid}}$ and a so-called *director* $\mathbf{D}$ pointing towards this point (cf. Figure 3.1).

$$\begin{aligned} &\mathcal{B} : \left(\theta^1, \theta^2, \theta^3\right) \in \mathbb{R}^3 \to \mathbb{R}^3 \, , \\ &\left(\theta^1, \theta^2, \theta^3\right) \to \mathbf{R}\left(\theta^1, \theta^2, \theta^3\right) = \mathbf{R}^{\mathrm{mid}}\left(\theta^1, \theta^2\right) + \theta^3 \cdot \mathbf{D}\left(\theta^1, \theta^2\right) \end{aligned} \tag{3.1}$$

Due to the fact that the degenerated solid approach is a mixture between the description of a solid and a surface, the concepts of differential geometry[2] can directly be applied. Consequently, the set of covariant base vectors can be established by means of Equation (2.28):

$$\mathbf{g}_1 = \frac{\partial \mathbf{R}\left(\theta^1, \theta^2, \theta^3\right)}{\partial \theta^1} = \mathbf{a}_1 + \theta^3 \cdot \frac{\partial \mathbf{a}_3}{\partial \theta^1} \qquad \text{for} \quad -\frac{l_3}{2} \leq \theta^3 \leq \frac{l_3}{2} \tag{3.2a}$$

$$\mathbf{g}_2 = \frac{\partial \mathbf{R}\left(\theta^1, \theta^2, \theta^3\right)}{\partial \theta^2} = \mathbf{a}_2 + \theta^3 \cdot \frac{\partial \mathbf{a}_3}{\partial \theta^2} \qquad \text{for} \quad -\frac{l_3}{2} \leq \theta^3 \leq \frac{l_3}{2} \tag{3.2b}$$

$$\mathbf{g}_3 = \frac{\partial \mathbf{R}\left(\theta^1, \theta^2, \theta^3\right)}{\partial \theta^3} = \mathbf{a}_3 \qquad \text{for} \quad -\frac{l_3}{2} \leq \theta^3 \leq \frac{l_3}{2} \tag{3.2c}$$

with $\mathbf{a}_i$ $(i = 1 \ldots 2)$ being the covariant in-plane base vectors of the mid-surface:

$$\mathbf{a}_1 = \frac{\partial \mathbf{R}^{\mathrm{mid}}\left(\theta^1, \theta^2\right)}{\partial \theta^1} \quad \text{and} \quad \mathbf{a}_2 = \frac{\partial \mathbf{R}^{\mathrm{mid}}\left(\theta^1, \theta^2\right)}{\partial \theta^2} \tag{3.3}$$

and $\mathbf{D}\left(\theta^1, \theta^2\right)$ being the scaled orthonormal covariant out-of-plane base vector $\mathbf{a}_3$ of the mid-surface:

$$\mathbf{D}\left(\theta^1, \theta^2\right) = \mathbf{a}_3 = \frac{\mathbf{a}_1 \times \mathbf{a}_2}{\|\mathbf{a}_1 \times \mathbf{a}_2\|} \quad \text{for} \quad -\frac{l_3}{2} \leq \theta^3 \leq \frac{l_3}{2} \tag{3.4}$$

Furthermore, the dual basis (i.e. the set of contra-variant base vectors) is defined as follows:

$$\mathbf{g}^1 = \mathbf{g}_2 \times \mathbf{g}_3 \, , \quad \mathbf{g}^2 = \mathbf{g}_3 \times \mathbf{g}_1 \, , \quad \mathbf{g}^3 = \mathbf{g}_3 \tag{3.5}$$

Analogously to Equation (2.32), the determinant of the Jacobian is used for mapping a differential volume element $\mathrm{d}\theta^1 \, \mathrm{d}\theta^2 \, \mathrm{d}\theta^3$ within the parametric space into a differential volume element $\mathrm{d}v$ within an Euclidean space:

$$\mathrm{d}v = \det\mathrm{J} \; \mathrm{d}\theta^1 \, \mathrm{d}\theta^2 \, \mathrm{d}\theta^3 \tag{3.6}$$

---

[2] i.e. co- and contra-variant base vectors, 1st and 2nd fundamental forms, etc.

where detJ is defined as follows:

$$\det J = \det\left(\left[\frac{\partial\left(x_1, x_2, x_3\right)}{\partial\left(\theta^1, \theta^2, \theta^3\right)}\right]\right) = \left(\mathbf{g}_1 \times \mathbf{g}_2\right) \cdot \mathbf{g}_3 \tag{3.7}$$

REMARK I: For further information on *degenerated solids* the author refers to Bischoff [13] and Bischoff et al. [14].

3.1.2 Description of motion

In order to describe the motion of a continuous body $\mathcal{B}$, two different frames need to be introduced. These frames can then be used for capturing the so-called *configurations* of the body $\mathcal{B}$ at different times, see Figure 3.2. The first frame is called *material* configuration[3] and refers to an initial time $t = 0$ where the body $\mathcal{B}$ is considered as undeformed. Within the *material* configuration each point $P \in \mathcal{B}$ is described by its position vector $\mathbf{X} = \mathbf{X}\left(t = 0\right) = X_i \mathbf{e}_i$ and $\mathbf{X} \in \Omega_0$. The second frame is called *spatial* configuration[4] and refers to a subsequent time $t > 0$ where the body $\mathcal{B}$ has moved and deformed. Within the *spatial* configuration each point $P \in \mathcal{B}$ is described by its position vector $\mathbf{x} = \mathbf{x}\left(t\right) = x_i \mathbf{e}_i$ and $\mathbf{x} \in \Omega$.

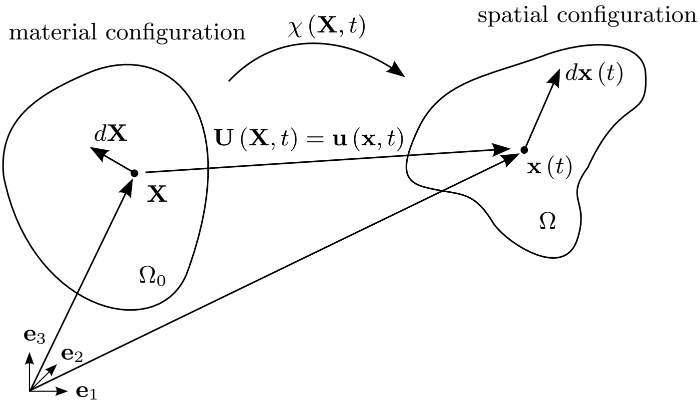

Figure 3.2: Motion of a continuum body

With these two configurations at hand, the *motion* of a point $P \in \mathcal{B}$ at a time $t > 0$ is defined as follows (cf. Figure 3.2):

$$\mathbf{X} \xrightarrow{\chi} \mathbf{x}: \quad \mathbf{x} = \chi\left(\mathbf{X}, t\right) \tag{3.8}$$

---

[3] also called reference or initial configuration

[4] also called deformed or current configuration

As stated in Equation (3.8), the set of independent variables are the so-called *material* coordinates $\mathbf{X}$ and the time t. Hence, all observed scalars, vectors and tensor-valued quantities are described w.r.t. the material frame, i.e. all dependent variables are functions of the material coordinate $\mathbf{X}$ and time. This approach is also known as *Lagrangian* description of motion.

For every point $P \in \mathcal{B}$ Equation (3.8) implies a unique relation between its material and spatial configuration at all times $t > 0$. Therefore, the inverse of Equation (3.8) straightforwardly leads to the *inverse motion* of a point $P \in \mathcal{B}$ at time $t > 0$:

$$\mathbf{x} \xrightarrow{\chi^{-1}} \mathbf{X}: \quad \mathbf{X} = \chi^{-1}(\mathbf{x}, t) \tag{3.9}$$

As stated in Equation (3.9), the set of independent variables are the so-called *spatial* coordinates $\mathbf{x}$ and the time t. Hence, all observed scalars, vectors and tensor-valued quantities are described w.r.t. the spatial frame, i.e. all dependent variables are functions of the spatial coordinate $\mathbf{x}$ and time. This approach is also known as *Eulerian* description of motion.

The material position $\mathbf{X}$ and spatial position $\mathbf{x}$ of a point $P \in \mathcal{B}$ are linked by the so-called *displacement field*. Depending on the point of view, the displacement field can either be defined in the Lagrangian (3.10a) or in the Eulerian (3.10b) form:

$$\mathbf{U}(\mathbf{X}, t) = \mathbf{x}(\mathbf{X}, t) - \mathbf{X} = \chi(\mathbf{X}, t) - \mathbf{X} \tag{3.10a}$$

$$\mathbf{u}(\mathbf{x}, t) = \mathbf{x} - \mathbf{X}(\mathbf{x}, t) = \mathbf{x} - \chi^{-1}(\mathbf{x}, t) \tag{3.10b}$$

Since both equations in (Equation (3.10)) describe the same displacement field, Equation (3.10a) is linked to Equation (3.10b) due to the inverse motion (3.9):

$$\mathbf{U}(\mathbf{X}, t) = \mathbf{U}\left[\chi^{-1}(\mathbf{x}, t), t\right] = \mathbf{u}(\mathbf{x}, t) \tag{3.11}$$

The derivative of the displacement field (3.10) w.r.t. the time leads to the *velocity field*. Again, depending on the point of view, the velocity field can be established either in the Lagrangian (3.12a) or the Eulerian (3.12b) form:

$$\mathbf{V}(\mathbf{X}, t) = \frac{\partial \mathbf{U}(\mathbf{X}, t)}{\partial t} = \frac{\partial \chi(\mathbf{X}, t)}{\partial t} \tag{3.12a}$$

$$\mathbf{v}(\mathbf{x}, t) = \frac{\partial \mathbf{u}(\mathbf{x}, t)}{\partial t} = -\frac{\partial \chi^{-1}(\mathbf{x}, t)}{\partial t} \tag{3.12b}$$

Again, both equations in (3.12) describe the same velocity field:

$$\mathbf{V}(\mathbf{X}, t) = \mathbf{V}\left[\chi^{-1}(\mathbf{x}, t), t\right] = \mathbf{v}(\mathbf{x}, t) \tag{3.13}$$

Consider an infinitesimal line element $\mathrm{d}\mathbf{X} = \mathrm{d}\mathbf{X}(t = 0)$ defined within the material frame at $t > 0$. By means of a linear operator, the so-called deformation gradient[5] $\mathbf{F}(\mathbf{X},t)$, this infinitesimal line element $\mathrm{d}\mathbf{X}$ is mapped to its corresponding spatial configuration $\mathrm{d}\mathbf{x} = \mathrm{d}\mathbf{x}(t)$ as follows:

$$\mathrm{d}\mathbf{x} = \mathbf{F}(\mathbf{X},t)\ \mathrm{d}\mathbf{X} \tag{3.14}$$

Inserting the motion defined in Equation (3.8) into Equation (3.14) leads to the definition of the deformation gradient $\mathbf{F}$:

$$\mathbf{F}(\mathbf{X},t) = \frac{\partial \chi(\mathbf{X},t)}{\partial \mathbf{X}} = \mathrm{Grad}\,\mathbf{x}(\mathbf{X},t) \tag{3.15}$$

In case of a degenerated solid approach (see Section 3.1.1) the material and spatial position vector of a point $P \in \mathcal{B}$ are anchored within the same parameter space:

$$\mathbf{R} = \mathbf{R}^{\mathrm{mid}}\left(\theta^1,\theta^2\right) + \theta^3 \cdot \mathbf{D}\left(\theta^1,\theta^2\right) = X_i\left(\theta^1,\theta^2,\theta^3\right)\ \mathbf{e}_i \tag{3.16a}$$

$$\mathbf{r} = \mathbf{r}^{\mathrm{mid}}\left(\theta^1,\theta^2\right) + \theta^3 \cdot \mathbf{d}\left(\theta^1,\theta^2\right) = x_i\left(\theta^1,\theta^2,\theta^3\right)\ \mathbf{e}_i \tag{3.16b}$$

Applying Equation (3.2) to (3.16a) and (3.16b) leads to the set of covariant material base vectors

$$\mathbf{G}_1 = \mathbf{A}_1 + \theta^3 \cdot \frac{\partial \mathbf{A}_3}{\partial \theta^1}\,, \quad \mathbf{G}_2 = \mathbf{A}_2 + \theta^3 \cdot \frac{\partial \mathbf{A}_3}{\partial \theta^2}\,, \quad \mathbf{G}_3 = \mathbf{A}_3 \tag{3.17}$$

and the set of covariant spatial base vectors:

$$\mathbf{g}_1 = \mathbf{a}_1 + \theta^3 \cdot \frac{\partial \mathbf{a}_3}{\partial \theta^1}\,, \quad \mathbf{g}_2 = \mathbf{a}_2 + \theta^3 \cdot \frac{\partial \mathbf{a}_3}{\partial \theta^2}\,, \quad \mathbf{g}_3 = \mathbf{a}_3 \tag{3.18}$$

Considering the *spatial director* $\mathbf{d}$, its definition is crucial when it comes to describing the out-of-plane shear deformations of the degenerated solid. Furthermore, it directly dictates the link between the stress state of a 3D continuum and the kinematics of a degenerated solid, i.e. if the change in thickness direction l_3 is directly captured by the director (*extensible director*) or has to be treated separately (*inextensible director*)[6]. Depending on the number of parameters, i.e. the dimension of the underlying displacement field $\mathbf{u}(\mathbf{X},t)$ of the mid-surface, the following director formulations are presented and discussed in numerous scientific publications and textbooks (e.g. Bischoff et al. [14]):

→ *3 parameter*: The spatial director remains orthonormal to the spatial in-plane base vectors. Consequently, neither the change in thickness (*inextensible*) nor the out-of-plane shear deformations can be captured by this formulation.

$$\mathbf{d} = \mathbf{a}_3 = \frac{\mathbf{a}_1 \times \mathbf{a}_2}{\|\mathbf{a}_1 \times \mathbf{a}_2\|} \quad \text{and} \quad \mathbf{u}(\mathbf{X},t) = \begin{bmatrix} u_1 & u_2 & u_3 \end{bmatrix}^{\mathrm{T}} \tag{3.19}$$

---

[5] in some textbooks $\mathbf{F}(\mathbf{X},t)$ and $\mathbf{F}^{-1}(\mathbf{x},t)$ are called *material* and *spatial* deformation gradient, respectively (e.g. Chaves [32])

[6] i.e. plane stress or plane strain

- → *5 parameter*: The spatial director is still inextensible but is able to rotate. Hence, the out-of-plane shear deformations can be captured. The rotation of the director is controlled by means of additional degrees of freedom acting on the displacement field $\mathbf{u}(\mathbf{X},t)$ of the mid-surface:

$$\mathbf{u}(\mathbf{X},t) = \begin{bmatrix} u_1 + \theta^3 u_1^{\mathrm{dir}} & u_2 + \theta^3 u_2^{\mathrm{dir}} & u_3 \end{bmatrix}^{\mathrm{T}} \tag{3.20}$$

- → *6 parameter*: The spatial director is completely controlled by means of additional degrees of freedom acting on the displacement field $\mathbf{u}(\mathbf{X},t)$ of the mid-surface. Consequently, the out-of-plane shear deformations as well as the change in thickness direction can be captured.

$$\mathbf{u}(\mathbf{X},t) = \begin{bmatrix} u_1 + \theta^3 u_1^{\mathrm{dir}} & u_2 + \theta^3 u_2^{\mathrm{dir}} & u_3 + \theta^3 u_3^{\mathrm{dir}} \end{bmatrix}^{\mathrm{T}} \tag{3.21}$$

REMARK II: It is quite obvious that the choice of the director formulation has to fit the physics of the underlying structural problem. Throughout this thesis a *3-parameter formulation* is sufficient and adequate, see Section 4.1.2 and Section 5.2.

REMARK III: It is important to mention that the 5-parameter formulation as well as the 6-parameter formulation lead to the so-called *poisson thickness locking.* For further information the author refers to BISCHOFF [13] and BISCHOFF ET AL. [14] and KOSCHNICK [71].

Applying (3.16) to (3.15), the deformation gradient can be rearranged to a dyadic product of the convective base vectors (3.2) and (3.5):

$$\mathbf{F}(\mathbf{X},t) = \frac{\partial x_i}{\partial \theta^r}\frac{\partial \theta^r}{\partial X_j}\,\mathbf{e}_i \otimes \mathbf{e}_j = \mathbf{g}_k \otimes \mathbf{G}^k \tag{3.22}$$

Consequently, the inverse of that linear operator (3.15) defines the mapping of an infinitesimal line element in the spatial configuration $\mathrm{d}\mathbf{x}$ to its corresponding material configuration $\mathrm{d}\mathbf{X}$ at time $t > 0$. Hence, inserting the inverse motion defined in Equation (3.9) into Equation (3.14) leads to the inverse of the deformation gradient $\mathbf{F}^{-1}(\mathbf{x},t)$:

$$\mathbf{F}^{-1}(\mathbf{x},t) = \frac{\partial \chi^{-1}(\mathbf{x},t)}{\partial \mathbf{x}} = \operatorname{grad}\mathbf{X}(\mathbf{x},t) \tag{3.23}$$

Analogously to Equation (3.22), the inverse of the deformation gradient can be expressed in terms of the convective base vectors (3.2) and (3.5):

$$\mathbf{F}^{-1}(\mathbf{x},t) = \frac{\partial X_i}{\partial \theta^r}\frac{\partial \theta^r}{\partial x_j}\,\mathbf{e}_i \otimes \mathbf{e}_j = \mathbf{G}_k \otimes \mathbf{g}^k \tag{3.24}$$

REMARK IV: Throughout this thesis scalars, vectors and tensor-valued quantities depending on material coordinates are called material quantities and are described by capital letters. Scalars, vectors and tensor-valued quantities depending on spatial coordinates are called spatial quantities and are described by lower-case letters.

The linear operators introduced by Equation (3.15) and (3.23) do not only apply to an infinitesimal line element but also to vectors and tensor-valued quantities defined in a material or spatial convective coordinate frame (introduced by Equation (3.17) and (3.18)). Hence, a vector or tensor-valued quantity anchored in one configuration is transfered to the other by means of either a so-called *push-forward* operation $\chi_* (\bullet)$ or a *pull-back* operation $\chi_*^{-1} (\bullet)$:

$$\Diamond (\mathbf{x}, t) = \chi_* \left(\Box (\mathbf{X}, t)\right) \tag{3.25a}$$

$$\Box (\mathbf{X}, t) = \chi_*^{-1} \left(\Diamond (\mathbf{x}, t)\right) \tag{3.25b}$$

In more detail, the push-forward operation (3.25a) maps a material vector or tensor-valued quantity $\Box (\mathbf{X}, t)$ to the corresponding spatial vector or tensor-value quantity $\Diamond (\mathbf{x}, t)$. Consequently, the pull-back operation (3.25b) maps a spatial vector or tensor-valued quantity $\Diamond (\mathbf{x}, t)$ to the corresponding material vector or tensor-valued quantity $\Box (\mathbf{X}, t)$.

REMARK V: The structure of $\chi_* (\bullet)$ and $\chi_*^{-1} (\bullet)$ strongly depends on the structure of $(\bullet)$. For the most common cases, the push-forward and pull-back operators are listed in Appendix A.5.

However, the operators defined in Equation (3.25a) and (3.25b) are not suitable for the mapping of infinitesimal volume and surface elements. Starting with an infinitesimal material volume element

$$\mathrm{d}V = (\mathrm{d}\mathbf{X}_1 \times \mathrm{d}\mathbf{X}_2) \cdot \mathrm{d}\mathbf{X}_3 = \epsilon_{ijk}\ \mathrm{d}X_{1i}\ \mathrm{d}X_{2j}\ \mathrm{d}X_{3k} \tag{3.26}$$

with ϵ_{ijk} being the so-called Levi-Civita symbol. By means of the equations (3.14), (3.23) and (A.39), the following relations can be established:

$$\mathrm{d}v = \det \mathbf{F} (\mathbf{X}, t)\ \mathrm{d}V \tag{3.27a}$$

$$\mathrm{d}V = \det \mathbf{F}^{-1} (\mathbf{x}, t)\ \mathrm{d}v \tag{3.27b}$$

According to Equation (3.27), the volume ratio $J (\mathbf{X}, t) = \det \mathbf{F} (\mathbf{X}, t)$ and its inverse $J^{-1} (\mathbf{x}, t) = \det \mathbf{F}^{-1} (\mathbf{x}, t)$ provide a measure for the change in volume occurring during the motion χ and χ^{-1}, respectively. In analogy with Equation (3.26), an infinitesimal material surface element $\mathrm{d}\mathbf{S}$ can be defined as:

$$\mathrm{d}\mathbf{S} = \mathrm{d}\mathbf{X}_1 \times \mathrm{d}\mathbf{X}_2 \quad \text{with} \quad \mathrm{d}S_i = \epsilon_{ijk}\ \mathrm{d}X_{1j}\ \mathrm{d}X_{2k} \tag{3.28}$$

By means of Equation (3.14) and (3.23), the following relations, the so-called *Nanson's formula*[7], can be established:

$$\mathrm{d}\mathbf{s} = J (\mathbf{X}, t)\ \mathbf{F}^{-T} (\mathbf{x}, t)\ \mathrm{d}\mathbf{S} \tag{3.29a}$$

$$\mathrm{d}\mathbf{S} = J^{-1} (\mathbf{x}, t)\ \mathbf{F}^{T} (\mathbf{X}, t)\ \mathrm{d}\mathbf{s} \tag{3.29b}$$

---

[7] for further information the author refers to: HOLZAPFEL [60] and CHAVES [32]

If, however, a vector or tensor-valued quantity is directly related to the volume, the volume ratio $J(\mathbf{X}, t)$ has to be incorporated in the push-forward or pull-back operation, respectively. Hence, combining Equation (3.27b) with Equation (3.25a) and Equation (3.27a) with Equation (3.25b) leads to the so-called *Piola transformations*:

$$\diamondsuit(\mathbf{x}, t) = J^{-1}(\mathbf{x}, t)\, \chi_*\left(\square(\mathbf{X}, t)\right) \tag{3.30a}$$

$$\square(\mathbf{X}, t) = J(\mathbf{X}, t)\, \chi_*^{-1}\left(\diamondsuit(\mathbf{x}, t)\right) \tag{3.30b}$$

The total derivative of fields is an important concept of differential calculus, since it describes their overall change w.r.t. all independent variables. In case of a time-dependent field, the total derivative is also known as *material time derivative* or *total time derivative.* Of course, the material time derivative applies to both material and spatial fields of some scalar, vector or tensor-valued quantity. Considering a material field $\mathcal{F}(\mathbf{X}, t)$ of some scalar, vector or tensor-valued quantity $\square(\mathbf{X}, t)$, its total material time derivative at a fixed position $\mathbf{X}$ is defined as:

$$\frac{\mathrm{D}\mathcal{F}(\mathbf{X}, t)}{\mathrm{D}t} = \left.\frac{\partial \mathcal{F}(\mathbf{X}, t)}{\partial t}\right|_{\mathbf{X}} \tag{3.31}$$

By means of Equation (3.9), Equation (3.12) and the chain rule, the material time derivative of a material quantity $\square(\mathbf{X}, t)$ at a fixed postion $\mathbf{X}$ can be expressed as the directional derivative towards the corresponding velocity vector $\mathbf{v}(\mathbf{x}, t)$:

$$\frac{\mathrm{D}\square(\mathbf{X}, t)}{\mathrm{D}t} = \mathrm{Grad}\square(\mathbf{X}, t) \cdot \mathbf{v}(\mathbf{x}, t) = \mathrm{D}_{\mathbf{v}}\,\square(\mathbf{X}, t) \tag{3.32}$$

According to Equation (2.8) and Equation (2.17), replacing the velocity vector field either with a virtual field $\delta(\bullet)$ or an increment of a vector field $\Delta(\bullet)$ straightforwardly leads to the variation (3.33*a*) or the linearization (3.33*b*) of the material quantity $\square(\mathbf{X}, t)$ at a fixed position $\mathbf{X}$:

$$\delta\square(\mathbf{X}, t) = \mathrm{D}_{\delta(\bullet)}\,\square(\mathbf{X}, t) \tag{3.33a}$$

$$\Delta\square(\mathbf{X}, t) = \mathrm{D}_{\Delta(\bullet)}\,\square(\mathbf{X}, t) \tag{3.33b}$$

Next, a spatial field $f(\mathbf{x}, t)$ of some scalar, vector or tensor-valued quantity $\diamondsuit(\mathbf{x}, t)$ will be considered. For a fixed position $\mathbf{X}$, the total material time derivative of a spatial field $f(\mathbf{x}, t)$ is defined as:

$$\frac{\mathrm{D}f(\mathbf{x}, t)}{\mathrm{D}t} = \chi_*\left[\frac{\mathrm{D}}{\mathrm{D}t}\chi_*^{-1}\left(f(\mathbf{x}, t)\right)\right] = \left.\frac{\partial f\left(\chi(\mathbf{X}, t), t\right)}{\partial t}\right|_{\chi^{-1}(\mathbf{x}, t)} \tag{3.34}$$

In more detail, Equation (3.34) shows that the material time derivative of a spatial field is defined as the material time derivative of the corresponding material field in combination with a push-forward operation (defined by

Equation (3.25a)). By means of Equation (3.12) and the chain rule, the material time derivative of a spatial field can be expressed in terms of the spatial gradient grad$\diamondsuit(\mathbf{x}, t)$ and the corresponding velocity vector $\mathbf{v}(\mathbf{x}, t)$:

$$\frac{\mathrm{D}\diamondsuit(\mathbf{x}, t)}{\mathrm{D}t} = \frac{\partial\diamondsuit(\mathbf{x}, t)}{\partial t} + \mathrm{grad}\diamondsuit(\mathbf{x}, t) \cdot \mathbf{v}(\mathbf{x}, t) \tag{3.35}$$

As already shown in Equation (3.32), the material time derivative of a material field is equivalent to its directional derivative towards the corresponding velocity vector. Instead of considering the velocity vector $\mathbf{v}(\mathbf{x}, t)$, in various cases the total derivative of a spatial field $f(\mathbf{x}, t)$ directing towards an arbitrary vector $(\bullet)$ is of interest. Following the strategy introduced by Equation (3.34) leads to:

$$\pounds_{(\bullet)} f(\mathbf{x}, t) = \chi_* \left[D_{(\bullet)} \chi_*^{-1} \left(f(\mathbf{x}, t) \right) \right] = \chi_* \left(D_{(\bullet)} \mathcal{F}(\mathbf{X}, t) \right) \tag{3.36}$$

with $\pounds_{(\bullet)}$ being the so-called *Lie-operator*. Hence, applying either a virtual field $\delta(\bullet)$ or an increment of a vector field $\Delta(\bullet)$ leads to the variation (3.37a) or the linearization (3.37b) of a spatial quantity $\diamondsuit(\mathbf{x}, t)$:

$$\delta\diamondsuit(\mathbf{x}, t) = \pounds_{(\delta\bullet)}\diamondsuit(\mathbf{x}, t) = \chi_* \left[D_{(\delta\bullet)}\square(\mathbf{X}, t) \right] \tag{3.37a}$$

$$\Delta\diamondsuit(\mathbf{x}, t) = \pounds_{(\Delta\bullet)}\diamondsuit(\mathbf{x}, t) = \chi_* \left[D_{(\Delta\bullet)}\square(\mathbf{X}, t) \right] \tag{3.37b}$$

REMARK VI: If a velocity vector $\mathbf{v}(\mathbf{x}, t)$ is chosen, Equation (3.36) is equivalent to the material time derivative for spatial fields. Thus, Equation (3.38) is also called *Lie Time Derivative*

$$\pounds_{\mathbf{v}}\diamondsuit(\mathbf{x}, t) = \chi_* \left[D_{\mathbf{v}}\square(\mathbf{X}, t) \right] = \frac{\mathrm{D}\diamondsuit(\mathbf{x}, t)}{\mathrm{D}t} \tag{3.38}$$

REMARK VII: For the sake of simplicity and if not stated otherwise, these arguments will not be explicitly mentioned: $\mathbf{x} = \mathbf{x}(\mathbf{X}, t)$, $\chi = \chi(\mathbf{X}, t)$, $\mathbf{F} = \mathbf{F}(\mathbf{X}, t)$, $J = J(\mathbf{X}, t)$ and $\chi^{-1} = \chi^{-1}(\mathbf{x}, t)$, $\mathbf{F}^{-1} = \mathbf{F}^{-1}(\mathbf{x}, t)$, $J^{-1} = J^{-1}(\mathbf{x}, t)$.

3.1.3 Finite strain theory

Consider the deformation of an infinitesimal line element at a point $P \in \mathcal{B}$ introduced in the previous section. A closer look reveals that the introduced deformation process is basically a combination of a rigid body rotation and a pure stretch / shrinkage of the line element, shown in Figure 3.3. This leads to a fundamental theorem called *Polar decomposition.* It states that the deformation gradient $\mathbf{F}$ can be separated into the so-called rotation tensor $\mathbf{R}$ and the right (material) stretch tensor $\mathbf{U}$ or left (spatial) stretch tensor $\mathbf{v}$:

$$\mathbf{F} = \mathbf{R}\,\mathbf{U} = \mathbf{v}\,\mathbf{R} \tag{3.39}$$

where $\mathbf{U}$ and $\mathbf{v}$ describe the stretch / shrinkage either from a material or a spatial point of view. Due to the orthogonal property of the rotation tensor[8], the dot-product of the transpose of the deformation gradient with itself acts like a filter returning the so-called *right Cauchy-Green tensor* $\mathbf{C}$:

$$\mathbf{C} = \mathbf{F}^T\mathbf{F} = \mathbf{U}^T\mathbf{R}^T\mathbf{R}\,\mathbf{U} = \mathbf{U}^T\mathbf{I}\,\mathbf{U} = \mathbf{U}^2 \tag{3.40}$$

Applying Equation (3.22) leads to the right Cauchy-Green tensor $\mathbf{C}$ in terms of the 1st fundamental form (see Section 2.3.2):

$$\mathbf{C} = \left(\mathbf{g}_i \otimes \mathbf{G}^i\right)^T \left(\mathbf{g}_j \otimes \mathbf{G}^j\right) = \mathbf{g}_i \cdot \mathbf{g}_j\, \mathbf{G}^i \otimes \mathbf{G}^j = g_{ij}\, \mathbf{G}^i \otimes \mathbf{G}^j \tag{3.41}$$

Hence, the right Cauchy-Green tensor $\mathbf{C}$ measures the inner geometry in the vicinity of $P \in \mathcal{B}$ at its spatial position $\mathbf{x}$ from a material point of view $\mathbf{X}$.

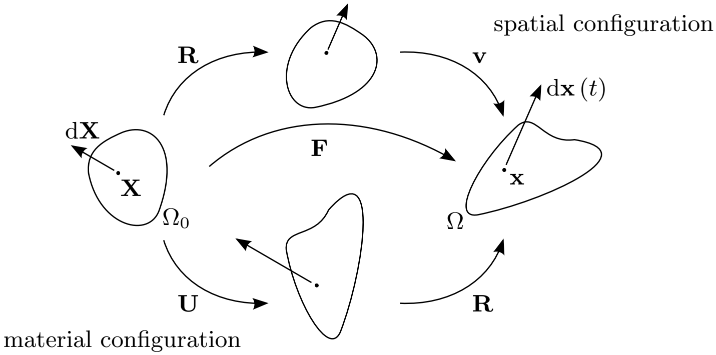

Figure 3.3: Deformation of an infinitesimal line element at $P \in \mathcal{B}$: polar decomposition

REMARK VIII: Consider the left stretch tensor $\mathbf{v}$. The dot product $\mathbf{F}^T\mathbf{F}$ yields an alternative formulation of the right Cauchy-Green tensor:

$$\mathbf{C} = \mathbf{F}^T\mathbf{F} = \mathbf{R}^T\mathbf{v}^T\,\mathbf{v}\,\mathbf{R} = \mathbf{R}^T\mathbf{v}^2\,\mathbf{R} = \mathbf{R}^T\mathbf{b}\,\mathbf{R} \tag{3.42}$$

with $\mathbf{b} = \mathbf{v}^2$ being the so-called *left Cauchy-Green tensor*. Hence, the following relation can be derived:

$$\mathbf{b} = \mathbf{F}\,\mathbf{F}^T = \mathbf{R}\,\mathbf{C}\,\mathbf{R}^T \tag{3.43}$$

A common approach for measuring the strain state of a body is the comparison between the material inner geometry and spatial inner geometry

---

[8] i.e. $\mathbf{R}^T\,\mathbf{R} = \mathbf{I}$ and $\det\mathbf{R} = 1$

in the vicinity of a point $P \in \mathcal{B}$. Depending on the point of view, different *strain measures* can be defined. The so-called *Green-Lagrange strain tensor* **E** only considers information anchored in the material configuration, i.e information provided by the material metric tensor (2.34) and the right Cauchy-Green tensor (3.41):

$$\mathbf{E} = \frac{1}{2}\left(\mathbf{C} - \mathbf{I}\right) = \frac{1}{2}\left(g_{ij} - G_{ij}\right)\mathbf{G}^i \otimes \mathbf{G}^j \tag{3.44}$$

The so-called *Euler-Almansi strain tensor* **e** is exclusively based on information provided by the spatial metric tensor (2.34) and the left Cauchy-Green tensor (3.42):

$$\mathbf{e} = \frac{1}{2}\left(\mathbf{b} - \mathbf{I}\right) = \frac{1}{2}\left(g_{ij} - G_{ij}\right)\mathbf{g}^i \otimes \mathbf{g}^j \tag{3.45}$$

REMARK IX: An alternative approach to Equation (3.44) and Equation (3.45) are the so-called *Logarithmic strain measures*. Instead of using the right or left Cauchy-Green tensor, these measures are based on either the right or left stretch tensor depending on the point of view:

$$\mathbf{E}^0 = \ln\mathbf{U} \quad \text{and} \quad \mathbf{e}^0 = \ln\mathbf{v} \tag{3.46}$$

REMARK X: A more general definition for both the material and spatial strain measures is stated in HOLZAPFEL [60] and WRIGGERS [112]:

$$\mathbf{E}^\alpha = \frac{1}{\alpha}\left(\mathbf{U}^\alpha - \mathbf{I}\right) \quad \text{and} \quad \mathbf{e}^\alpha = \frac{1}{\alpha}\left(\mathbf{v}^\alpha - \mathbf{I}\right) \quad \text{for} \quad \alpha \neq 0, \alpha \in \mathbb{R} \tag{3.47}$$

3.2 The concept of stress

Consider a simple but deformable continuum body $\mathcal{B}$ undergoing a certain motion $\chi\left(\mathbf{X}, t\right)$. On a macroscopic level, every point $P \in \mathcal{B}$ is subjected to a resistance force (also called *internal force*) caused by the interaction of particles within the underlying microscopic structure. In order to quantify these resistance forces a so-called *stress tensor* field will be introduced in following. Since these resistance forces strongly depend on the underlying microscopic structure, the stress tensor is directly linked to the applied *material model* (see Section 3.3). In the following, the most commonly used stress tensors, namely the *Cauchy stress tensor*, the 1st *Piola-Kirchhoff stress tensor* and the 2nd *Piola-Kirchhoff stress tensor*, are discussed in more detail.

The so-called *Cauchy stress tensor* field $\boldsymbol{\sigma}\left(\mathbf{x}, t\right)$ measures the stresses within the spatial configuration, i.e. the internal forces are measured w.r.t. the deformed area. Therefore, for every single point $P \in \mathcal{B}$ at $\mathbf{x}\left(t\right)$ a symmetric tensor is provided measuring the so-called *true stresses*. The Cauchy stress tensor is fully anchored in the spatial configuration.

The so-called 1st *Piola-Kirchhoff stress tensor* field $\mathbf{P}\,(\mathbf{X}, t)$ measures the stresses within the material configuration, i.e. the internal forces are measured w.r.t. the undeformed area. For every single point $P \in \mathcal{B}$ at $\mathbf{X}$ a non-symmetric tensor is provided measuring the so-called *nominal stresses.* Since the forces are only occurring in the spatial configuration, the 1st Piola-Kirchhoff stress tensor is anchored in both the spatial and the material configuration.

By means of Nanson's formula (3.29) the following relations between both stress tensors can be established:

$$\mathbf{P} = J\,\boldsymbol{\sigma}\,\mathbf{F}^{-T} \quad \text{and} \quad \boldsymbol{\sigma} = J^{-1}\,\mathbf{P}\,\mathbf{F}^{T} \tag{3.48}$$

A further tensor field which is fully anchored in the material configuration is the so-called 2nd *Piola-Kirchhoff stress tensor* field $\mathbf{S}\,(\mathbf{X})$. It describes the Cauchy stresses $\boldsymbol{\sigma}\,(\mathbf{x}, t)$ from a material point of view. Therefore, applying the Piola transformation (3.30) leads to the following symmetric second-order tensor:

$$\mathbf{S} = J\,(\mathbf{X}, t)\,\chi_*^{-1}\big(\boldsymbol{\sigma}\,(\mathbf{x}, t)\big) = J\,\mathbf{F}^{-1}\,\boldsymbol{\sigma}\,\mathbf{F}^{-T} \tag{3.49}$$

REMARK I: It is important to mention that due to its definition the 2nd Piola-Kirchhoff stress tensor exhibits no explicit physical meaning. Nevertheless, due to its symmetry the 2nd Piola-Kirchhoff stress tensor is an important quantity within the context of computational mechanics and the theory of hyperelasticity (see Section 3.3.2).

Following a standard approach in elastostatics, the body is cut by a plane running through a given point $P \in \mathcal{B}$ (dashed line in Figure 3.4). This leads to the corresponding *stress resultants* $\mathrm{d}\mathbf{f}$:

$$\mathrm{d}\mathbf{f} = \mathbf{t}\,(\mathbf{x}, t, \mathbf{n})\,\mathrm{d}a = \mathbf{T}\,(\mathbf{X}, t, \mathbf{N})\,\mathrm{d}A \tag{3.50}$$

where $\mathbf{t}\,(\mathbf{x}, t, \mathbf{n})$ and $\mathbf{T}\,(\mathbf{X}, t, \mathbf{N})$ represent the so-called *surface traction vectors.* Depending on the point of view, the *Cauchy traction vector* $\mathbf{t}\,(\mathbf{x}, t, \mathbf{n})$ and 1st *Piola-Kirchhoff traction vector* $\mathbf{T}\,(\mathbf{X}, t, \mathbf{N})$ describe the stresses within the spatial configuration and material configuration, respectively. Therefore, they are also called *true traction vector* and *nominal traction vector*, respectively. According to *Cauchy's stress theorem*, the traction vectors are directly linked to the Cauchy stress tensor or 1st Piola-Kirchhoff stress tensor by means of the corresponding cutting plane's normal vector $\mathbf{n}\,(\mathbf{x})$ or $\mathbf{N}\,(\mathbf{X})$, respectively:

$$\mathbf{t}\,(\mathbf{x}, t, \mathbf{n}) = \mathbf{t}_{\mathbf{n}} = \boldsymbol{\sigma}\,(\mathbf{x}, t)\;\mathbf{n}\,(\mathbf{x}) \tag{3.51a}$$

$$\mathbf{T}\,(\mathbf{X}, t, \mathbf{N}) = \mathbf{T}_{\mathbf{N}} = \mathbf{P}\,(\mathbf{X}, t)\;\mathbf{N}\,(\mathbf{X}) \tag{3.51b}$$

Finally, the Cauchy traction vector $\mathbf{t}_{\mathbf{n}} = \mathbf{t}\,(\mathbf{x}, t, \mathbf{n})$ is additively split into its in-plane $\mathbf{t}_{\mathbf{n}}^{\parallel}$ and out-of-plane components $\mathbf{t}_{\mathbf{n}}^{\perp}$

$$\mathbf{t}_{\mathbf{n}} = \mathbf{t}_{\mathbf{n}}^{\parallel} + \mathbf{t}_{\mathbf{n}}^{\perp} = \sigma\,\mathbf{n} + \tau\,\mathbf{m} \tag{3.52}$$

where σ and τ represents the well-known *normal* and *shear* stresses acting on a differential surface da (cf. Figure 3.4):

$$\sigma = \mathbf{n} \cdot \boldsymbol{\sigma}\, \mathbf{n} \quad \text{and} \quad \tau = \mathbf{m} \cdot \boldsymbol{\sigma}\, \mathbf{n} \quad \text{with} \quad \mathbf{m} \cdot \mathbf{n} = 0 \tag{3.53}$$

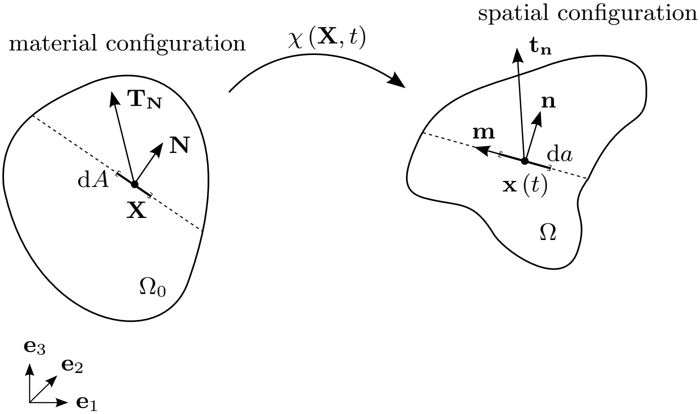

Figure 3.4: The concept of stress: traction vectors

REMARK II: For further information on the introduced concept of stress and additional stress tensors the author refers to ALTENBACH [2], BELYTSCHKO ET AL. [11], CHAVES [32], HAUPT [57], HOLZAPFEL [60], OGDEN [88], PARISCH [89], WRIGGERS [112].

3.3 The concept of hyperelasticity

Up to now, in the previous Sections (3.1) and (3.2) the kinematic and energetic quantities (strains and stresses) were addressed independently. In contrast to the kinematics, the energetic quantities are not unique for different materials, i.e. a certain motion will not lead to the same stresses (e.g. steel, rubber, CFRP, textiles, etc.). Hence, an additional mathematical relation, the so-called *constitutive relation*, has to be considered. It establishes the link between the kinematic and energetic quantities. Over the past decades various research groups focused on the modeling of different materials dealing with all kind of aspects such as nonlinearity, anisotropy, time-dependency, inelasticity, incompressibility, etc. All these specific material models are derived from one of the four basic theories: elasticity, plasticity, visco-elasticity, visco-plasticity. A general overview on the mathematical treatment of these categories is given by HAUPT [57].

In case of the so-called *phenomenological models*, the underlying mathematical function represents the macroscopic material response. Therefore, the *characteristics* and the corresponding *material parameters* are identified by means of appropriate experiments.

The materials throughout this thesis are assumed to be *homogeneously distributed* over a continuous body $\mathcal{B}$. Therefore, the material response only depends on the strain state[9] acting on the continuous body $\mathcal{B}$ and is independent of the position within the continuous body $\mathcal{B}$ (further details in CHAVES [32] or HOLZAPFEL [60]).

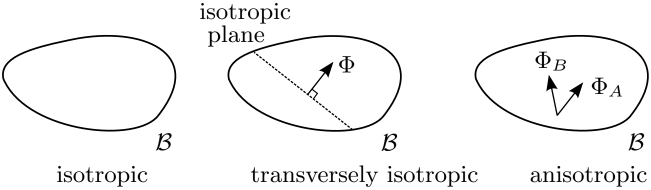

Figure 3.5: Material response: isotropic (left), transversely isotropic (center), anistropic (right)

A *Cauchy-elastic* material behavior is characterized by a reversible material response which is independent of the load history and load velocity. In general, the stress-strain response during loading may differs from the stress-strain response during unloading. However, both (i.e. loading and unloading) must lead to the same stress-free and strain-free state.

The focus of this thesis is on the so-called *hyperelastic* material behavior. Constitutive models of this type are more restrictive w.r.t. the loading and unloading. In contrast to Cauchy-elastic materials, in case of a hyperelastic behavior the stress-strain response during loading coincides with the stress-strain response during unloading. This additional requirement leads to a scalar potential functional $\Psi(\mathbf{C})$, the so-called *strain-energy function* or *stored-energy function*, describing the elastic potential energy $\Pi(\mathbf{C})$:

$$\Pi(\mathbf{C}) = \int\limits_{\Omega_0} \Psi(\mathbf{C})\, \mathrm{d}\Omega_0 \tag{3.54}$$

In the most simple case Equation (3.54) describes an *isotropic* material response, e.g. steel, rubber, etc. (HOLZAPFEL [60] or OGDEN [88]). Considering composite materials, textile fabrics or biological tissues, at least one material direction is reinforced by a single fiber or a bundle of fibers. Therefore, the so-called *anisotropic* material response strongly depends on the fiber direction within a homogeneously distributed matrix. A special group of anisotropic materials are the so-called *transversely isotropic* materials. Materials belonging to this group only consist of one fiber direction

---

[9] from a material point of view the strain state is described by the right Cauchy-Green tensor (3.40)

for reinforcement in combination with an isotropic behavior within the plane perpendicular to that (see Figure 3.5 (center)). A detailed list of suitable polyconvex[10] strain-energy functions is given by SCHRÖDER AND NEFF [100].

The intent of this section is to provide the reader with all necessary equations regarding the modeling of anisotropic and isotropic nonlinear elastic materials based on a strain-energy function. For a comprehensive and circumstantial compendium on these topics the author refers to a broad variety of literature: BELYTSCHKO ET AL. [11], CHAVES [32], HAUPT [57], HOLZAPFEL [60], OGDEN [88], SCHRÖDER AND NEFF [100], WRIGGERS [112].

3.3.1 Theory of Invariants

As already mentioned in the introduction of this chapter, the response of a homogeneously distributed hyperelastic material solely depends on the strain state. By means of the *representation theorem for invariants* [11], the strain-energy function w.r.t. a material point of view can then be reformulated in terms of *invariants* of the right Cauchy-Green tensor.

In case of an isotropic material behavior, the so-called three *principal invariants* provide all required information, i.e. the normal stretches $I_1(\mathbf{C})$, the shear deformation $I_2(\mathbf{C})$ and the change in volume $I_3(\mathbf{C})$.

$$I_1(\mathbf{C}) = \mathrm{tr}\mathbf{C} \tag{3.55a}$$

$$I_2(\mathbf{C}) = \frac{1}{2}\left((\mathrm{tr}\mathbf{C})^2 - \mathrm{tr}\mathbf{C}^2\right) \tag{3.55b}$$

$$I_3(\mathbf{C}) = \det\mathbf{C} \tag{3.55c}$$

Hence, for an isotropic material the elastic potential energy defined by Equation (3.54) can be reformulated as follows:

$$\Pi(\mathbf{C}) = \int\limits_{\Omega_0} \Psi\left(I_1(\mathbf{C}), I_2(\mathbf{C}), I_3(\mathbf{C})\right) \mathrm{d}\Omega_0 \tag{3.56}$$

REMARK I: In order to describe the stress-free state $\Pi(\mathbf{C}) = 0$, Equation (3.56) has to vanish under the following conditions: $I_1(\mathbf{C}) = 3$, $I_2(\mathbf{C}) = 3$ and $I_3(\mathbf{C}) = 1$.

REMARK II: In case of an incompressible material such as rubber, the following condition has to be enforced: $I_3(\mathbf{C}) = 1$ (OGDEN [88]).

---

[10] the concept of polyconvexity is very important for strain-energy functions since it guarantees the existence of a global minimum, see BALZANI ET AL. [9] or SCHRÖDER AND NEFF [100]

[11] a scalar-valued tensor function may be expressed in terms of invariants of its arguments, if it is invariant under rotation (HOLZAPFEL [60], OGDEN [88])

In case of an anisotropic or transversely isotropic material behavior, additional *structural invariants* have to be introduced providing a supplementary measure for the strains related to the i-th fiber direction Φ_i:

$$I_{4+2(i-1)}\left(\mathbf{C},\mathbf{M}_i\right) = \Phi_i \cdot \mathbf{C}\,\Phi_i = \operatorname{tr}\left(\mathbf{C}\,\mathbf{M}_i\right) \tag{3.57a}$$

$$I_{5+2(i-1)}\left(\mathbf{C},\mathbf{M}_i\right) = \Phi_i \cdot \mathbf{C}^2\,\Phi_i = \operatorname{tr}\left(\mathbf{C}^2\,\mathbf{M}_i\right) \tag{3.57b}$$

These new invariants are based on the concept of the so-called *structural tensors* $\mathbf{M}_i$

$$\mathbf{M}_i = \Phi_i \otimes \Phi_i \tag{3.58}$$

with Φ_i being the i-th fiber direction. A closer look on the introduced *structural tensor* reveals that it acts like a filter on the right Cauchy-Green tensor $\mathbf{C}$: it isolates the deformations w.r.t. the i-th fiber direction Φ_i.

Finally, the elastic potential energy defined by Equation (3.55) can be extended to a general anisotropic formulation:

$$\Pi\left(\mathbf{C},\mathbf{M}_i\right) = \int\limits_{\Omega_0} \Psi\left(I_1, I_2, I_3, I_{4+2(i-1)}, I_{5+2(i-1)}\right) \mathrm{d}\Omega_0 \tag{3.59}$$

with $i = 1 \ldots n$ and n defining the total number of fiber directions Φ. For the sake of clarity the arguments of I_i are skipped, if not stated otherwise $I_i = I_i\left(\mathbf{C}\right)$ holds.

REMARK III: In order to describe the stress-free state, Equation (3.59) has to vanish under the following conditions: $I_1 = 3$, $I_2 = 3$, $I_3 = 1$, $I_{4+2(i-1)} = 1$ and $I_{5+2(i-1)} = 1$.

3.3.2 Constitutive relations

In general, the *constitutive equation* serves as a link between the kinematic and energetic quantities, whereby the combination of these quantities is restricted to the so-called *work conjugate pairs*. These pairs guarantee a consistent formulation of the internal work meaning that the considered strains and stresses are sharing the same point of view. A list of the most commonly used work conjugate pairs is given in Table 3.1.

strain measure	stress measure	point of view
Deformation Gradient	1^{st} Piola-Kirchhoff	material/spatial
Green-Lagrange	2^{nd} Piola-Kirchhoff	material
Euler-Almansi	Cauchy	spatial

Table 3.1: Selected work conjugate pairs

Within the context of the theory of hyperelasticity, the 2^{nd} Piola-Kirchhoff stress tensor introduced in Section 3.2 is directly correlated to the underlying strain-energy function. In more detail, the 2^{nd} Piola-Kirchhoff stress tensor $\mathbf{S}(\mathbf{E})$ is defined as the first derivative of the strain-energy function $\Psi(\mathbf{C})$ w.r.t. the Green-Lagrange strain tensor $\mathbf{E}(\mathbf{C})$:

$$\mathbf{S}(\mathbf{E}) = \frac{\partial \Psi(\mathbf{C})}{\partial \mathbf{E}(\mathbf{C})} = \frac{\partial \Psi(\mathbf{C})}{\partial \mathbf{C}} \cdot \frac{\partial \mathbf{C}}{\partial \mathbf{E}} = 2\, \frac{\partial \Psi(\mathbf{C})}{\partial \mathbf{C}} \tag{3.60}$$

with $\mathbf{C} = 2\mathbf{E} + \mathbf{I}$. Finally, incorporating the principal (3.55) and structural (3.57) invariants into Equation (3.60) leads to the 2^{nd} Piola-Kirchhoff stress tensor $\mathbf{S}(\mathbf{E})$ for a general anisotropic material:

$$\mathbf{S}(\mathbf{E}) = 2 \sum_{k=1}^{3+2i} \frac{\Psi(I_1 \dots I_k)}{\partial I_k} \frac{\partial I_k}{\partial \mathbf{C}} \tag{3.61}$$

with the first derivatives of the principal invariants (3.55):

$$\frac{\partial I_1}{\partial \mathbf{C}} = \mathbf{I} \quad \text{and} \quad \frac{\partial I_2}{\partial \mathbf{C}} = I_1 \mathbf{I} - \mathbf{C} \quad \text{and} \quad \frac{\partial I_3}{\partial \mathbf{C}} = I_3 \mathbf{C}^{-1} \tag{3.62}$$

and the first derivatives of the structural invariants (3.57):

$$\frac{\partial I_{4+2(i-1)}}{\partial \mathbf{C}} = \mathbf{M}_i \quad \text{and} \quad \frac{\partial I_{5+2(i-1)}}{\partial \mathbf{C}} = \mathbf{C}\,\mathbf{M}_i + \mathbf{M}_i\,\mathbf{C} \tag{3.63}$$

In case of a gradient based solution technique like the Newton-Raphson scheme, the linearization of the constitutive equation is of importance (more details on this topic are given in Section 3.4.2). Applying the Gâteaux derivative (2.17) to Equation (3.60) leads to:

$$D_{(\bullet)}\mathbf{S}(\mathbf{E}) = \frac{\partial \mathbf{S}(\mathbf{E})}{\partial \mathbf{E}} : D_{(\bullet)}\mathbf{E} = \mathbb{D} : D_{(\bullet)}\mathbf{E} \tag{3.64}$$

with $\mathbb{D}$ being a fourth-order tensor called *elasticity tensor*. A closer look at the elasticity tensor shows that in case of a hyperelastic material the elasticity tensor $\mathbb{D}$ is exactly the second derivative of the strain-energy function $\Psi(\mathbf{C})$ w.r.t. the right Cauchy-Green tensor $\mathbf{C}$:

$$\mathbb{D} = \frac{\partial \mathbf{S}(\mathbf{E})}{\partial \mathbf{E}} = \frac{\partial}{\partial \mathbf{E}} \left(\frac{\partial \Psi(\mathbf{C})}{\partial \mathbf{E}} \right) = 4\, \frac{\partial^2 \Psi(\mathbf{C})}{\partial \mathbf{C}\, \partial \mathbf{C}} \tag{3.65}$$

Again, incorporating the principal (3.55) and structural (3.57) invariants into (3.65) leads to the elasticity tensor $\mathbb{D}$ for a general anisotropic material:

$$\mathbb{D} = 4 \sum_{k=1}^{3+2i} \frac{\partial I_k}{\partial \mathbf{C}} \otimes \frac{\partial^2 \Psi(I_1 \dots I_k)}{\partial \mathbf{C}\, \partial I_k} + \frac{\partial \Psi(I_1 \dots I_k)}{\partial I_k} \frac{\partial^2 I_k}{\partial \mathbf{C}\, \partial \mathbf{C}} \tag{3.66}$$

with the second derivatives of the principal invariants (3.55):

$$\frac{\partial^2 I_1}{\partial \mathbf{C} \partial \mathbf{C}} = \mathbf{0} \tag{3.67a}$$

$$\frac{\partial^2 I_2}{\partial \mathbf{C} \partial \mathbf{C}} = \mathbf{I} \otimes \mathbf{I} - \mathbf{I} \odot \mathbf{I} \tag{3.67b}$$

$$\frac{\partial^2 I_3}{\partial \mathbf{C} \partial \mathbf{C}} = I_3 \left(\mathbf{C}^{-1} \otimes \mathbf{C}^{-1} - \mathbf{C}^{-1} \odot \mathbf{C}^{-1} \right) \tag{3.67c}$$

and the second derivatives of the structural invariants (3.57):

$$\frac{\partial^2 I_{4+2(i-1)}}{\partial \mathbf{C} \partial \mathbf{C}} = \mathbf{0} \tag{3.68a}$$

$$\frac{\partial^2 I_{5+2(i-1)}}{\partial \mathbf{C} \partial \mathbf{C}} = \mathbf{I} \odot \mathbf{M}_i + \mathbf{M}_i \odot \mathbf{I} \tag{3.68b}$$

REMARK IV: Due to the symmetry of the right Cauchy-Green tensor $\mathbf{C}$, the first derivative of the strain-energy function $\Psi(\mathbf{C})$ results again in a symmetric second order tensor. This correlates with the symmetry requirement for the 2nd Piola-Kirchhoff stress tensor $\mathbf{S}$ stated in Section 3.2: $S^{ij} = S^{ji}$

REMARK V: Due to its properties of a potential function, the elasticity tensor possesses both the *minor symmetry* $(3.69)_1$ and the *major symmetry* $(3.69)_2$:

$$\mathbb{D}^{ijkl} = \mathbb{D}^{jikl} = \mathbb{D}^{ijlk} \quad \text{and} \quad \mathbb{D}^{ijkl} = \mathbb{D}^{klij} \tag{3.69}$$

3.3.3 Plane stress problem in hyperelasticity

Consider an inextensible director kinematic (i.e. 3 parameter and 5 parameter formulation - see page 36f) for describing the motion of a shell-like body (see Section 3.1.1). A closer view reveals that due to the definition of the material and spatial director a change in thickness direction cannot be captured. In terms of Green-Lagrange strains this results in the following intrinsic kinematic constraints:

$$\text{3 parameter:} \quad E_{13} = E_{23} = E_{31} = E_{32} = E_{33} = 0 \tag{3.70a}$$

$$\text{5 parameter:} \quad E_{33} = 0 \tag{3.70b}$$

In order to circumvent this lack of information and incorporate lateral shrinkage, the strains related to the thickness direction have to be treated independently of the in-plane kinematics. Therefore, additional assumptions on the stresses acting in thickness direction have to be made - called *plane stress assumptions*. In case of a Total Lagrangian Formulation the plane stress assumptions result in the following requirements on the contravariant 2nd Piola-Krichhoff stresses:

$$\text{3 parameter:} \quad S^{13} = S^{23} = S^{31} = S^{32} = S^{33} = 0 \tag{3.71a}$$

$$\text{5 parameter:} \quad S^{33} = 0 \tag{3.71b}$$

In general, strain-energy functions based on the 3 principal invariants (3.55) describe the behavior of a 3D continuum, i.e. due to the *Poisson effect* (Poisson's ratio: $-1 < \nu < 0.5$) in-plane deformations also result in out-of-plane strains (lateral shrinkage). Assigning such a material to an inextensible director kinematic (i.e. 3-parameter and 5-parameter formulation - see p. 36) leads to unrealistic stress results due to the intrinsic kinematic constraints. In more detail, due to the definition of the material and spatial directors only the rigid body rotations but not the changes in thickness direction are captured by the deformation gradient $\mathbf{F}$. Keeping in mind that the deformation gradient is indirectly linked to the principal invariants via the right Cauchy-Green tensor $\mathbf{C}$, the strain-energy function does not account for the lateral shrinkage (i.e. the thin body is forced to a constant thickness). Hence, the resulting stress tensor does not fulfill the plane stress conditions.

In order to circumvent this effect additional information regarding the director rotation (3 parameter) and extension (3 and 5 parameter) are required. BALZANI ET AL. [9], KLINKEL AND GOVINDJEE [69] and KLINKEL ET AL. [70] came up with an iterative scheme for updating the corresponding out-of-plane strains. Depending on the underlying director kinematic (3 or 5 parameter), the corresponding coefficients of the strain tensor are modified in a way that the respective plane stress assumptions (3.71) are met (3 parameter: normal and shear strains such that (3.71a) - 5 parameter: normal strain such that (3.71b)).

Consider the 3 parameter formulation. Instead of enforcing the plane stress state on strain level, the presented approach directly updates the 3rd covariant spatial base vector $\mathbf{g}_3$. Thus, the three coefficients of the 3rd covariant spatial base vector are defined as unknowns ζ_b, $b = 1 \ldots 3$:

$$\mathbf{g}_3 = \overset{3}{g_i}\, \mathbf{e}_i = \zeta_b\, \mathbf{e}_b \tag{3.72}$$

According to Equation (3.60) and taking into account the symmetry of the 2nd Piola-Kirchhoff stress tensor (i.e. $S^{ij} = S^{ji}$), the following three residual equations for a fixed displacement field $\mathbf{u}(\mathbf{X}, t)$ can be established:

$$R_1^{ps} = S^{13} = 2 \left. \frac{\partial \Psi\left(\mathbf{C}\left(\boldsymbol{\zeta}\right)\right)}{\partial C_{13}} \right|_{\mathbf{u}(\mathbf{X},t)} = 0 \tag{3.73a}$$

$$R_2^{ps} = S^{23} = 2 \left. \frac{\partial \Psi\left(\mathbf{C}\left(\boldsymbol{\zeta}\right)\right)}{\partial C_{23}} \right|_{\mathbf{u}(\mathbf{X},t)} = 0 \tag{3.73b}$$

$$R_3^{ps} = S^{33} = 2 \left. \frac{\partial \Psi\left(\mathbf{C}\left(\boldsymbol{\zeta}\right)\right)}{\partial C_{33}} \right|_{\mathbf{u}(\mathbf{X},t)} = 0 \tag{3.73c}$$

with $\mathbf{S} = S^{ij}\, \mathbf{G}_i \otimes \mathbf{G}_j$ and $\mathbf{C} = \mathbf{g}_i \cdot \mathbf{g}_j\, \mathbf{G}^i \otimes \mathbf{G}^j$. In general, Equation (3.73) results in a nonlinear system of equations which requires an iterative solution scheme. The method of choice is the Newton-Raphson scheme introduced in Section 2.2.1. Applying Equation (2.21) to (3.73) leads to the linearized system of equations:

$$\mathbf{R}^{ps}\left(\boldsymbol{\zeta}^{i+1}\right) = \mathbf{R}^{ps}\left(\boldsymbol{\zeta}^{i}\right) + D_{\Delta\boldsymbol{\zeta}}\mathbf{R}^{ps}\left(\boldsymbol{\zeta}^{i}, \Delta\boldsymbol{\zeta}\right) = 0 \tag{3.74}$$

with

$$\boldsymbol{\zeta}^{i+1} = \boldsymbol{\zeta}^{i} + \Delta\boldsymbol{\zeta} \tag{3.75}$$

A closer view on the linearization operator (2.20) reveals the structure of the required partial derivatives for a fixed displacement field $\mathbf{u}\left(\mathbf{X}, t\right)$:

$$\frac{\partial R_a^{ps}}{\partial \zeta_b} = \frac{\partial S^a}{\partial \zeta_b} = 4 \left. \frac{\partial^2 \Psi\left(\mathbf{C}\left(\boldsymbol{\zeta}\right)\right)}{\partial C_a \partial C_a} \frac{\partial C_a}{\partial \zeta_b} \right|_{\mathbf{u}(\mathbf{X},t)} = \mathbb{D}^{aa} \frac{\partial C_a}{\partial \zeta_b} \tag{3.76}$$

with the indexes $a = 13, 23, 33$ and $b = 1 \ldots 3$.

REMARK VI: If a *Gaussian quadrature*[12] is applied for numerical integration, the presented procedure directly acts on *Gauss point level.* Therefore, it has to be performed at each *Gauss point* while the required integrals (i.e. residual force vector and tangential stiffness matrix) are established.

REMARK VII: The presented procedure shows its major advantage when information on the strain-energy function under plane stress conditions is required. This issue will be addressed in Section 5.

Finally, the effect of the updated out-of-plane strains needs to be incorporated in the elasticity tensor. More precisely, the link between the inplain strains and out-of-plane stress via Poisson's ratio has to be corrected. Therefore, the linearized 2nd Piola-Krichhoff stress tensor (3.64) is separated into its in-plane ($k = 11, 22, 12$) and out-of-plane ($o = 33, 13, 23$) proportions:

$$D_{(\Delta\mathbf{u})}\mathbf{S}_k^{\mathrm{V}} = \mathbb{D}_{kk}^{\mathrm{V}} \cdot D_{(\Delta\mathbf{u})}\mathbf{E}_k^{\mathrm{V}} + \mathbb{D}_{ko}^{\mathrm{V}} \cdot D_{(\Delta\mathbf{u})}\mathbf{E}_o^{\mathrm{V}} \tag{3.77a}$$

$$D_{(\Delta\mathbf{u})}\mathbf{S}_o^{\mathrm{V}} = \mathbb{D}_{ok}^{\mathrm{V}} \cdot D_{(\Delta\mathbf{u})}\mathbf{E}_k^{\mathrm{V}} + \mathbb{D}_{oo}^{\mathrm{V}} \cdot D_{(\Delta\mathbf{u})}\mathbf{E}_o^{\mathrm{V}} = 0 \tag{3.77b}$$

with $\mathbf{E}^{\mathrm{V}} = \mathbf{E}^{\mathrm{V}}\left(\mathbf{u}\right)$, $\mathbf{S}^{\mathrm{V}} = \mathbf{S}^{\mathrm{V}}\left(\mathbf{E}\right)$ and $\mathbb{D}^{\mathrm{V}} = \mathbb{D}^{\mathrm{V}}\left(\mathbf{E}\right)$ are the vector/matrix representations[13] of the strain, stess and elasticity tensor, respectively[14]. By means of Equation (3.77b) the out-of-plane strains $\mathbf{E}_o^{\mathrm{V}}$ can be eliminated in Equation (3.77a):

$$D_{(\Delta\mathbf{u})}\tilde{\mathbf{S}}^{\mathrm{V}} = \tilde{\mathbb{D}}^{\mathrm{V}} \cdot D_{(\Delta\mathbf{u})}\tilde{\mathbf{E}}^{\mathrm{V}} \tag{3.78}$$

---

[12] for further information the author refers to BELYTSCHKO ET AL. [11], HUGHES [61], ZIENKIEWICZ [113], etc.

[13] also known in the literature as *Voigt notation*, see BELYTSCHKO ET AL. [11]

[14] all vectors/matrices are explained in more detail in Appendix B

with $\tilde{\mathbb{D}}^{\mathrm{V}}$ being the modified elasticity tensor:

$$\tilde{\mathbb{D}}^{\mathrm{V}} = \mathbb{D}^{\mathrm{V}}_{kk} - \mathbb{D}^{\mathrm{V}}_{ko} \left[\mathbb{D}^{\mathrm{V}}_{oo} \right]^{-1} \mathbb{D}^{\mathrm{V}}_{ok} \tag{3.79}$$

as well as $\tilde{\mathbf{E}}^{\mathrm{V}} = \mathbf{E}^{\mathrm{V}}_{k}$ and $\tilde{\mathbf{S}}^{\mathrm{V}} = \mathbf{S}^{\mathrm{V}}_{k}$ being the in-plane strains and stresses.

REMARK VIII: The presented procedure directly incorporates the director strains into the stress and elasticity tensor. Thus, the dimension of the modified stress tensor $\tilde{\mathbf{S}}$ and modified elasticity tensor $\tilde{\mathbb{D}}$ can be reduced $(i, j, k, l = 1 \ldots 2)$:

$$\tilde{\mathbf{S}} = \tilde{S}^{ij}\, \mathbf{G}_i \otimes \mathbf{G}_j \quad \text{and} \quad \tilde{\mathbb{D}} = \tilde{D}^{ijkl}\, \mathbf{G}_i \otimes \mathbf{G}_j \otimes \mathbf{G}_k \otimes \mathbf{G}_l$$

REMARK IX: The procedure represented by Equation (3.79) is known in the literature as *static condensation*. For further information the author refers to HUGHES [61].

3.3.4 Plane strain problem in hyperelasticity

In case of *plane strain conditions* ($E_{33} = 0$ and $E_{3i} = E_{i3} = 0$ with $i = 1 \ldots 2$) the mentioned constraints are directly enforced by the inextensible director. Therefore, no further treatment regarding the Poisson effect is required.

3.4 Variational principles in elastostatics

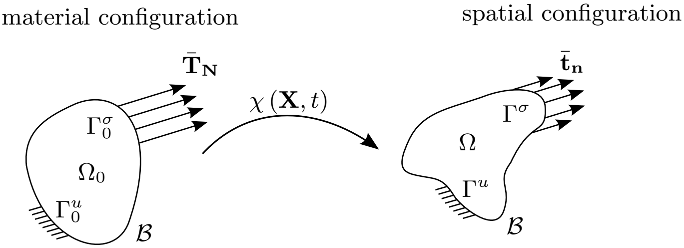

Figure 3.6: The boundary value problem (BVP): elastostatics

This section will focus on the *principle of Minimum Total Potential Energy* as well as on the general *boundary value problem of elastostatics*. Therefore, consider a continuum body $\mathcal{B}$ subjected to a set of prescribed conditions acting on the boundary of the body $\partial\mathcal{B}$. As depicted in Figure 3.6, there exist two different types of boundary conditions (BCs) prescribing either the displacements $\bar{\mathbf{U}} = \bar{\mathbf{u}}$ (*Dirichlet BCs*) or the surface tractions $\bar{\mathbf{T}}_{\mathbf{N}}$ and

$\bar{\mathbf{t}}_{\mathbf{n}}$ (*Neumann BCs*), respectively. Finally, depending on the point of view the boundary of the body $\mathcal{B}$ can be decomposed as follows:

$$\partial\mathcal{B} = \partial\mathcal{B}^u \cup \partial\mathcal{B}^\sigma \quad \text{and} \quad \partial\mathcal{B}^u \cap \partial\mathcal{B}^\sigma = \emptyset \tag{3.80}$$

where $\partial\mathcal{B}^u$ and $\partial\mathcal{B}^\sigma$ describe either the material boundary Γ_0^u and Γ_0^σ or the spatial boundary Γ^u and Γ^σ, respectively.

REMARK I: For the sake of simplicity and if not stated otherwise the arguments of the material and spatial fields are omitted, e.g.:

$$\mathbf{U} = \mathbf{U}\,(\mathbf{X}, t) \quad \text{and} \quad \mathbf{u} = \mathbf{u}\,(\mathbf{x}, t)$$

3.4.1 Principle of Virtual Work

Consider a general non-conservative *static* mechanical system, e.g. hypoelastic material behavior, follower loads etc. According to *Cauchy's first equation of motion*[15], the so-called *strong from* of the boundary value problem of elastostatics (i.e. neglecting all time-dependent terms) can be stated as follows (cf. Figure 3.6):

$$\begin{aligned} \operatorname{div}\boldsymbol{\sigma} + \mathbf{b} &= \mathbf{0} && && \text{(3.81a)} \\ \mathbf{u} &= \bar{\mathbf{u}} && \text{on} \quad \Gamma^u && \text{(3.81b)} \\ \mathbf{t} = \boldsymbol{\sigma}\,\mathbf{n} &= \bar{\mathbf{t}} && \text{on} \quad \Gamma^\sigma && \text{(3.81c)} \end{aligned}$$

with $\mathbf{b}$ being a body force acting inside the spatial domain Ω. Furthermore, (3.81b) and (3.81c) represent the Dirichlet BCs and Neumann BCs w.r.t. the spatial configuration, respectively. The structure of Equation (3.81a) does not only require information on the boundary provided by Equation (3.81b) and (3.81c) but also information on the interior of the body. In general, this information is not available for arbitrary structures. In order to circumvent the mentioned lack of information, Equation (3.81a) needs to be transformed to its *weak form.* The major advantage of the weak form is the fact that it only requires information which is provided by the set of Dirichlet BCs and Neumann BCs. Depending on the chosen trail and test fields, only an approximate solution of the balance equation Equation (3.81a) may be provided.

The weak form of the static equilibrium (3.81a) is achieved by means of the *Galerkin approach*, see Section 2.1.4. Therefore, an infinitesimal small and virtual displacement field $\delta\mathbf{u}$ is introduced leading to a *virtual spatial configuration* (cf. Figure 3.7):

$$\delta\mathbf{u} = \epsilon\,\tilde{\mathbf{u}} = \bar{\mathbf{u}} - \mathbf{u} \quad \text{with} \quad \delta\mathbf{u} = \mathbf{0} \quad \text{on} \quad \Gamma^u \tag{3.82}$$

According to the requirements of a virtual field (see page 20), the virtual displacement field $\delta\mathbf{u}$ vanishes on the Dirichlet boundary Γ^u. Recalling

---

[15] for further information the author refers to HOLZAPFEL [60]

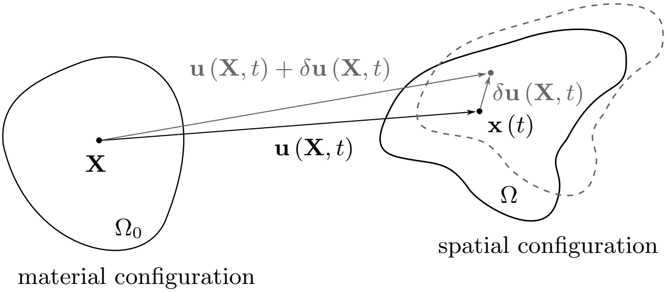

Figure 3.7: Virtual displacement field $\delta\mathbf{u}$

Equation (2.15), the integral form of the static equilibrium (3.81a) can be established as the domain integral over the inner product between (3.81a) and (3.82) whereat the introduced virtual displacement field $\delta\mathbf{u}$ serves as the test field $\boldsymbol{\eta}$.

$$\int\limits_{\Omega} (\operatorname{div}\boldsymbol{\sigma} + \mathbf{b}) \cdot \delta\mathbf{u} \; \mathrm{d}\Omega = 0 \tag{3.83}$$

By means of the identity stated in Equation (A.43) and the symmetry of the Cauchy stress tensor $\boldsymbol{\sigma} = \boldsymbol{\sigma}\big(\mathbf{e}(\mathbf{u})\big)$

$$\operatorname{div}(\boldsymbol{\sigma}\,\delta\mathbf{u}) = \operatorname{div}\boldsymbol{\sigma}\cdot\delta\mathbf{u} + \boldsymbol{\sigma} : \delta\mathbf{e} \tag{3.84}$$

and applying the *divergence theorem*[16] (A.44)

$$\int\limits_{\Omega} \operatorname{div}(\boldsymbol{\sigma}\,\delta\mathbf{u}) \; \mathrm{d}\Omega = \int\limits_{\Gamma} \boldsymbol{\sigma}\,\mathbf{n}\cdot\delta\mathbf{u} \; \mathrm{d}\Gamma \tag{3.85}$$

Equation (3.83) can be rearranged to

$$\int\limits_{\Gamma} \boldsymbol{\sigma}\,\mathbf{n}\cdot\delta\mathbf{u} \; \mathrm{d}\Gamma - \int\limits_{\Omega} \boldsymbol{\sigma} : \delta\mathbf{e} \; \mathrm{d}\Omega + \int\limits_{\Omega} \mathbf{b}\cdot\delta\mathbf{u} \; \mathrm{d}\Omega = 0 \tag{3.86}$$

with $\delta\mathbf{e} = \delta\mathbf{e}(\mathbf{u})$ being the 1st Variation of the Euler-Almansi strain tensor[17]:

$$\delta\mathbf{e}(\mathbf{u}) = \frac{1}{2}\left(\delta\mathbf{u}\otimes\nabla + \nabla\otimes\delta\mathbf{u}\right) = \operatorname{sym}(\nabla\otimes\delta\mathbf{u}) \tag{3.87}$$

Due to the fact that from a physical perspective each integral represents a work term, Equation (3.86) is called the *Principle of Virtual Work*:

$$\delta W(\mathbf{u},\delta\mathbf{u}) \equiv \delta W_{\text{int}}(\mathbf{u},\delta\mathbf{u}) - \delta W_{\text{ext}}(\mathbf{u},\delta\mathbf{u}) = 0 \tag{3.88}$$

---

[16] also known in literature as *Gauss's theorem* - see Bronstein et al. [29]

[17] a detailed derivation is given in Holzalpfel [60]

with the *internal virtual work* δW_{int} in spatial description

$$\delta W_{\text{int}}\left(\mathbf{u}, \delta\mathbf{u}\right) = \int\limits_{\Omega} \boldsymbol{\sigma}\big(\mathbf{e}\left(\mathbf{u}\right)\big) : \delta\mathbf{e}\left(\mathbf{u}\right)\, \mathrm{d}\Omega \tag{3.89}$$

and the *external virtual work* δW_{ext} in spatial description

$$\delta W_{\text{ext}}\left(\mathbf{u}, \delta\mathbf{u}\right) = \int\limits_{\Gamma^{\sigma}} \bar{\mathbf{t}} \cdot \delta\mathbf{u}\, \mathrm{d}\Gamma^{\sigma} + \int\limits_{\Omega} \mathbf{b} \cdot \delta\mathbf{u}\, \mathrm{d}\Omega \tag{3.90}$$

Since the virtual displacement field vanishes on the Dirichlet boundary (3.82), only the traction vector (3.51a) acting on the Neumann boundary has to be taken into account in the external virtual work.

REMARK II: Inserting Equation (3.89) and (3.90) into (3.88) leads to the *updated Lagrangian formulation* of the *Principle of Virtual Work.*

By means of the Lie Time derivative (3.37a), the 1$^{\text{st}}$ Variation of the Euler-Almansi strain tensor can be expressed in terms of the Green-Lagrange strain tensor:

$$\delta\mathbf{e}\left(\mathbf{u}\right) = \pounds_{\delta\mathbf{u}}\mathbf{e}\left(\mathbf{u}\right) = \chi_{*}\left[D_{\delta\mathbf{u}}\mathbf{E}\left(\mathbf{u}\right)\right] \tag{3.91}$$

Additionally, applying Equation (3.27a) to the spatial differential volume $\mathrm{d}\Omega$ leads to the *internal virtual work* δW_{int} in material description:

$$\begin{aligned} \delta W_{\text{int}}\left(\mathbf{u}, \delta\mathbf{u}\right) &= \int\limits_{\Omega_0} \boldsymbol{\sigma}\big(\mathbf{e}\left(\mathbf{u}\right)\big) : \mathbf{F}^{-T}\delta\mathbf{E}\left(\mathbf{u}\right)\mathbf{F}^{-1}\, J\, \mathrm{d}\Omega_0 \\ &= \int\limits_{\Omega_0} \mathbf{S}\big(\mathbf{E}\left(\mathbf{u}\right)\big) : \delta\mathbf{E}\left(\mathbf{u}\right)\, \mathrm{d}\Omega_0 \end{aligned} \tag{3.92}$$

According to Holzapfel [60], the spatial body force $\mathbf{b}$ is mapped into the material space as follows:

$$\mathbf{b} = J^{-1}\,\mathbf{B} \tag{3.93}$$

By means of the identity stated in Equation (3.50) and (3.93), the *external virtual work* δW_{ext} in material description can be established:

$$\delta W_{\text{ext}}\left(\mathbf{u}, \delta\mathbf{u}\right) = \int\limits_{\Gamma_0^{\sigma}} \bar{\mathbf{T}} \cdot \delta\mathbf{u}\, \mathrm{d}\Gamma_0^{\sigma} + \int\limits_{\Omega_0} \mathbf{B} \cdot \delta\mathbf{u}\, \mathrm{d}\Omega_0 \tag{3.94}$$

REMARK III: Inserting Equation (3.92) and (3.94) into (3.88) leads to the *Lagrangian formulation* of the *Principle of Virtual Work.*

3.4.2 Principle of Minimum Total Potential Energy

Consider a conservative *static* mechanical system, i.e. there exists a potential function for both the internal potential energy $\Pi_{\text{int}}(\mathbf{u})$ and external potential energy $\Pi_{\text{ext}}(\mathbf{u})$. From a Lagrangian perspective, the internal and external potential energies can be stated as follows:

$$\Pi_{\text{int}}(\mathbf{u}) = \int\limits_{\Omega_0} \Psi\big(\mathbf{E}(\mathbf{u})\big)\ \mathrm{d}\Omega_0 \tag{3.95a}$$

$$\Pi_{\text{ext}}(\mathbf{u}) = -\int\limits_{\Omega_0} \mathbf{B}\cdot\mathbf{u}\ \mathrm{d}\Omega_0 - \int\limits_{\Gamma_0^\sigma} \bar{\mathbf{T}}\cdot\mathbf{u}\ \mathrm{d}\Gamma_0^\sigma \tag{3.95b}$$

with $\mathbf{B}$ being a body force acting inside the material domain Ω_0 and $\bar{\mathbf{T}}$ being a prescribed traction acting on the material boundary Γ_0^σ of the continuum body $\mathcal{B}$ (cf. Figure 3.6). The goal is now to find the static equilibrium, i.e. that point where the sum of the internal and external potential energy is at its minimum. In terms of mathematics, the static equilibrium can be stated as the following optimization problem - known as Minimum Total Potential Energy:

$$\min_{\mathbf{u}\in\Omega_0} \rightarrow \Pi(\mathbf{u}) = \Pi_{\text{int}}(\mathbf{u}) + \Pi_{\text{ext}}(\mathbf{u}) \tag{3.96a}$$

$$\mathbf{U} = \bar{\mathbf{U}} \qquad \text{on} \quad \partial\Gamma_0^u \tag{3.96b}$$

$$\mathbf{T} = \mathbf{P}\,\mathbf{N} = \bar{\mathbf{T}}_{\mathbf{N}} \qquad \text{on} \quad \partial\Gamma_0^\sigma \tag{3.96c}$$

where (3.96b) and (3.96c) represent the Dirichlet BCs and Neumann BCs w.r.t. the material configuration, respectively. Recalling the concept of natural variational principles introduced in Section 2.1.3, the static equilibrium is reached, if the 1^{st} Variation of the total potential energy functional vanishes (i.e. in its stationary point). Applying Equation (2.8) in combination with the virtual displacement field (3.82) to (3.96a) leads to the stationary point of the total potential energy functional:

$$\delta\Pi(\mathbf{u},\delta\mathbf{u}) = \delta\Pi_{\text{int}}(\mathbf{u},\delta\mathbf{u}) + \delta\Pi_{\text{ext}}(\mathbf{u},\delta\mathbf{u}) = 0 \tag{3.97}$$

Consider the 1^{st} Variation of the internal potential energy. Applying the Gâteaux derivative (2.4) in the direction of the virtual displacement field to Equation (3.95a) leads to the *internal virtual work* δW_{int}:

$$\begin{aligned} \delta W_{\text{int}}(\mathbf{u},\delta\mathbf{u}) &= \delta\Pi_{\text{int}}(\mathbf{u},\delta\mathbf{u}) = D_{\delta\mathbf{u}}\Pi_{\text{int}}(\mathbf{u}) \\ &= \int\limits_{\Omega_0} \mathbf{S}\big(\mathbf{E}(\mathbf{u})\big) : \delta\mathbf{E}(\mathbf{u})\ \mathrm{d}\Omega_0 \end{aligned} \tag{3.98}$$

In more detail, by means of the chain rule and Equation (3.60) the 1^{st} Variation of the strain-energy can be established:

$$\delta\Psi\big(\mathbf{E}(\mathbf{u})\big) = \frac{\partial\Psi\big(\mathbf{E}(\mathbf{u})\big)}{\partial\mathbf{E}(\mathbf{u})} : \delta\mathbf{E}(\mathbf{u}) = \mathbf{S}\big(\mathbf{E}(\mathbf{u})\big) : \delta\mathbf{E}(\mathbf{u}) \tag{3.99}$$

Consider the 1^{st} Variation of the external potential energy. Applying the Gâteaux derivative (2.4) in the direction of the virtual displacement field to Equation (3.95b) leads to the *external virtual work* $-\delta W_{\text{ext}}$:

$$\begin{aligned} -\delta W_{\text{ext}}\left(\mathbf{u},\delta\mathbf{u}\right) &= \delta\Pi_{\text{ext}}\left(\mathbf{u},\delta\mathbf{u}\right) = D_{\delta\mathbf{u}}\Pi_{\text{ext}}\left(\mathbf{u}\right) \\ &= -\int\limits_{\Omega_0} \mathbf{B}\cdot\delta\mathbf{u}\ \mathrm{d}\Omega_0 - \int\limits_{\Gamma_0^\sigma} \bar{\mathbf{T}}\cdot\delta\mathbf{u}\ \mathrm{d}\Gamma_0^\sigma \end{aligned} \tag{3.100}$$

Finally, Equation (3.97) can be reformulated to the well-known *Principle of Virtual Work* (3.88):

$$\int\limits_{\Omega_0} \mathbf{S}\left(\mathbf{E}\left(\mathbf{u}\right)\right) : \delta\mathbf{E}\left(\mathbf{u}\right)\ \mathrm{d}\Omega_0 - \int\limits_{\Omega_0} \mathbf{B}\cdot\delta\mathbf{u}\ \mathrm{d}\Omega_0 - \int\limits_{\Gamma_0^\sigma} \bar{\mathbf{T}}\cdot\delta\mathbf{u}\ \mathrm{d}\Gamma_0^\sigma = 0 \tag{3.101}$$

REMARK IV: It is important to mention that both the *Principle of Virtual Work* in material description and the principle of Minimum Total Potential Energy lead to the same governing equation for hyperelastic materials.

3.4.3 Linearization of the Principle of Virtual Work

In general Equation (3.88) exhibits a nonlinear characteristic. In order to find the unknown displacement field $\mathbf{u} = \mathbf{u}\left(\mathbf{X}, t\right)$ that meets the static equilibrium under a given set of Dirichlet and Neumann BCs, an iterative scheme is required. The most common technique in structural mechanics is the Newton-Raphson scheme introduced in Section 2.2.1.

Applying Equation (2.21) to Equation (3.88) leads to the *linearized Principle of Virtual Work*:

$$\delta W\left(\mathbf{u}^{i+1},\delta\mathbf{u}\right) = \delta W\left(\mathbf{u}^{i},\delta\mathbf{u}\right) + \Delta\delta W\left(\mathbf{u}^{i},\delta\mathbf{u},\Delta\mathbf{u}\right) = 0 \tag{3.102}$$

with the displacement increment $\Delta\mathbf{u}$

$$\mathbf{u}^{i+1} = \mathbf{u}^{i} + \Delta\mathbf{u} \tag{3.103}$$

Consider the *Principle of Virtual Work* in material description. According to Equation (2.17), the second term in Equation (3.102) $\Delta\delta W\left(\mathbf{u},\delta\mathbf{u},\Delta\mathbf{u}\right)$ can be expressed as a sum of Gâteaux derivatives in direction of the displacement increment $\Delta\mathbf{u}$ (3.103):

$$\Delta\delta W\left(\mathbf{u},\delta\mathbf{u},\Delta\mathbf{u}\right) = D_{\Delta\mathbf{u}}\delta W_{\text{int}}\left(\mathbf{u},\delta\mathbf{u}\right) - D_{\Delta\mathbf{u}}\delta W_{\text{ext}}\left(\mathbf{u},\delta\mathbf{u}\right) \tag{3.104}$$

By means of the product rule the *linearized internal virtual work* in material description can be established as follows:

$$\begin{aligned} D_{\triangle\mathbf{u}}\delta W_{\text{int}}\left(\mathbf{u},\delta\mathbf{u}\right) = &\int\limits_{\Omega_0}\Big(\mathbb{D}\big(\mathbf{E}\left(\mathbf{u}\right)\big) : D_{\triangle\mathbf{u}}\mathbf{E}\left(\mathbf{u}\right)\Big) : \delta\mathbf{E}\left(\mathbf{u}\right)\,\mathrm{d}\Omega_0 \\ &+\int\limits_{\Omega_0}\mathbf{S}\big(\mathbf{E}\left(\mathbf{u}\right)\big) : D_{\triangle\mathbf{u}}\delta\mathbf{E}\left(\mathbf{u}\right)\,\mathrm{d}\Omega_0 \end{aligned} \tag{3.105}$$

with $D_{\triangle\mathbf{u}}\mathbf{S}\big(\mathbf{E}\left(\mathbf{u}\right)\big)$ being the linearization of the 2^{nd} Piola-Krichhoff stress tensor (3.64):

$$D_{\triangle\mathbf{u}}\mathbf{S}\big(\mathbf{E}\left(\mathbf{u}\right)\big) = \frac{\partial\mathbf{S}\big(\mathbf{E}\left(\mathbf{u}\right)\big)}{\partial\mathbf{E}\left(\mathbf{u}\right)} : D_{\triangle\mathbf{u}}\mathbf{E}\left(\mathbf{u}\right) = \mathbb{D}\big(\mathbf{E}\left(\mathbf{u}\right)\big) : D_{\triangle\mathbf{u}}\mathbf{E}\left(\mathbf{u}\right) \tag{3.106}$$

The *linearized external virtual work* in material description can be established as follows:

$$D_{\triangle\mathbf{u}}\delta W_{\text{ext}}\left(\mathbf{u},\delta\mathbf{u}\right) = -\int\limits_{\Omega_0} D_{\triangle\mathbf{u}}\mathbf{B}\cdot\delta\mathbf{u}\,\mathrm{d}\Omega_0 - \int\limits_{\Gamma_0^\sigma} D_{\triangle\mathbf{u}}\bar{\mathbf{T}}\cdot\delta\mathbf{u}\,\mathrm{d}\Gamma_0^\sigma \tag{3.107}$$

REMARK V: In case of a conservative system, the external virtual work does not depend on the displacement field $\mathbf{u}\left(\mathbf{X},t\right)$. Hence, the linearization of the external virtual work vanishes:

$$D_{\triangle\mathbf{u}}\delta W_{\text{ext}}\left(\mathbf{u},\delta\mathbf{u}\right) = 0 \quad \text{with} \quad D_{\triangle\mathbf{u}}\bar{\mathbf{T}} = D_{\triangle\mathbf{u}}\mathbf{B} = 0 \tag{3.108}$$

4

A novel hyperelastic material model for textile fabrics

"Du kannst! So wolle nur!"

— Johann Wolfgang von Goethe, 1749 - 1832
German poet and politician

The mathematical description of textile fabrics (such as canvas, velvet, curtain, knitted fabrics, etc.) proves to be quite complex. Their structural response is composed of the rovings'/yarn's elongation, friction between their single rovings/yarns and some intrinsic rigid body motions of the micro structure. This chapter will show a novel approach for modeling the structural response of a textile fabric based on a nonlinear surrogate model. Therefore, Bézier surfaces/curves are introduced representing the fabric's strain-energy function. In more detail, several campaigns of velocity-driven biaxial tensile tests lead to a set of experimental (raw) data. In a second step, the gained set of data is transformed into adequate continuum mechanical quantities. Finally, the processed data are approximated by means of either a surface or curve depending on the experimental set-up (i.e. if the specimens are either mounted in fiber direction or under 45°). Within the scope of this thesis, three different fabrics have been tested. The corresponding response surfaces are presented at the end of this chapter.

4.1 Response surface based strain-energy functions

For textile fabrics[1], the level of complexity of their structure on a mesoscopic scale strongly depends on their manufacturing process. This may lead to quite complicated load transfer mechanisms, which are responsible for their structural response on a macroscopic level. In general, these mechanisms are always a combination of the rovings's/yarn's elongation, friction between the single rovings/yarns and intrinsic rigid body motions of the meso-structure. Thus, a nonlinear relation between the strains and the stresses on a macroscopic level is generally observed. This chapter presents a novel approach for modeling textile fabrics within the framework of hyperelasticity (two families of fibers: warp and weft). In more detail, it introduces a representation of the strain-energy function which is based on a combination of so-called *Bézier surfaces* and *Bézier curves*. The data sets for these response surfaces/curves are directly generated out of experimental data obtained by velocity-driven biaxial tensile test.

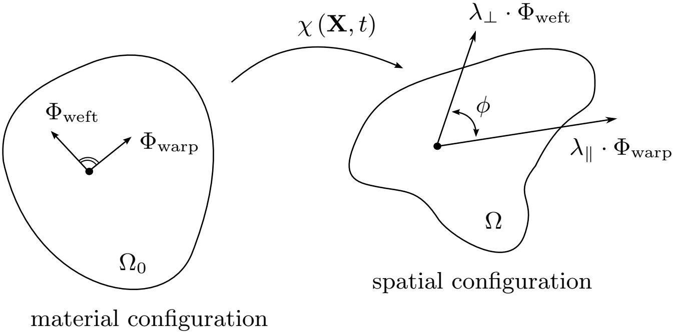

Figure 4.1: Schematic nonlinear orthotropic material composed of two families of fibers: Φ_{warp} and Φ_{weft}

As already mentioned in Section 3.3, the concept of hyperelasticty proves to be very powerful for modeling nonlinear elastic materials on a macroscopic level. In order to describe the structural response in terms of a strain-energy function some assumptions for the presented material model have to be made. First of all, the material is assumed to behave ideal elastically. Secondly, the material consists of two preferred directions Φ_{warp} and Φ_{weft} which are initially perpendicular[2] to each other, cf. Figure 4.1. The deformation behavior on a macroscopic level is reduced to three characteristic load transfer mechanisms, namely the fiber stretches $\lambda_\parallel$ and $\lambda_\perp$

---

[1] either non-crimp, woven, knitted or braided fabrics

[2] i.e. the material behavior is assumed to be orthotropic leading to a decoupling of normal strains and shear strains

and the fiber twist $\cos\phi$ (cf. Figure 4.1). According to Equation (3.57a), the fiber stretches in warp ($\|$: $i = 1$) and weft ($\perp$: $i = 2$) direction are expressed in terms of the fourth and sixth structural invariant $I_{\|}$ and $I_{\perp}$:

$$I_{\|} = I_4\left(\mathbf{C}, \mathbf{M}_{\|}\right) = \operatorname{tr}\left(\mathbf{C}\,\mathbf{M}_{\|}\right) = \lambda_{\|}^2 \tag{4.1a}$$

$$I_{\perp} = I_6\left(\mathbf{C}, \mathbf{M}_{\perp}\right) = \operatorname{tr}\left(\mathbf{C}\,\mathbf{M}_{\perp}\right) = \lambda_{\perp}^2 \tag{4.1b}$$

with $\mathbf{M}_{\|}$ and $\mathbf{M}_{\perp}$ being the corresponding structural tensors:

$$\mathbf{M}_{\|} = \Phi_{\text{warp}} \otimes \Phi_{\text{warp}} \quad \text{and} \quad \mathbf{M}_{\perp} = \Phi_{\text{weft}} \otimes \Phi_{\text{weft}} \tag{4.2}$$

The fiber twist is expressed in terms of a mixed invariant $I_{\sharp}$:

$$I_{\sharp} = I_{\sharp}\left(\mathbf{C}, \mathbf{M}_{\|}, \mathbf{M}_{\perp}\right) = \frac{\operatorname{tr}\left(\mathbf{C}\,\mathbf{M}_{\|}\,\mathbf{C}\,\mathbf{M}_{\perp}\right)}{\operatorname{tr}\left(\mathbf{C}\,\mathbf{M}_{\|}\right)\,\operatorname{tr}\left(\mathbf{C}\,\mathbf{M}_{\perp}\right)} = \cos^2\phi \tag{4.3}$$

The first and second derivative of the mixed invariant $I_{\sharp}$ w.r.t. the right Cauchy-Green tensor $\mathbf{C}$ are as follows:

$$\frac{\partial I_{\sharp}}{\partial \mathbf{C}} = -\frac{I_{\sharp}}{I_{\|}}\,\mathbf{M}_{\|} - \frac{I_{\sharp}}{I_{\perp}}\,\mathbf{M}_{\perp} + \sqrt{\frac{I_{\sharp}}{I_{\|}\,I_{\perp}}}\,\left(\mathbf{M}_{\|\perp} + \mathbf{M}_{\perp\|}\right) \tag{4.4}$$

$$\begin{aligned}
\frac{\partial^2 I_{\sharp}}{\partial \mathbf{C}\,\partial \mathbf{C}} = {} & 2\,\frac{I_{\sharp}}{I_{\|}^2}\,\mathbf{M}_{\|} \otimes \mathbf{M}_{\|} + \frac{I_{\sharp}}{I_{\|}\,I_{\perp}}\,\mathbf{M}_{\|} \otimes \mathbf{M}_{\perp} \\
& + \frac{I_{\sharp}}{I_{\|}\,I_{\perp}}\,\mathbf{M}_{\perp} \otimes \mathbf{M}_{\|} + 2\,\frac{I_{\sharp}}{I_{\perp}^2}\,\mathbf{M}_{\perp} \otimes \mathbf{M}_{\perp} \\
& - \frac{1}{I_{\|}}\sqrt{\frac{I_{\sharp}}{I_{\|}\,I_{\perp}}}\,\mathbf{M}_{\|} \otimes \left(\mathbf{M}_{\|\perp} + \mathbf{M}_{\perp\|}\right) \\
& - \frac{1}{I_{\perp}}\sqrt{\frac{I_{\sharp}}{I_{\|}\,I_{\perp}}}\,\mathbf{M}_{\perp} \otimes \left(\mathbf{M}_{\|\perp} + \mathbf{M}_{\perp\|}\right) \\
& - \frac{1}{I_{\|}}\sqrt{\frac{I_{\sharp}}{I_{\|}\,I_{\perp}}}\,\left(\mathbf{M}_{\|\perp} + \mathbf{M}_{\perp\|}\right) \otimes \mathbf{M}_{\|} \\
& - \frac{1}{I_{\perp}}\sqrt{\frac{I_{\sharp}}{I_{\|}\,I_{\perp}}}\,\left(\mathbf{M}_{\|\perp} + \mathbf{M}_{\perp\|}\right) \otimes \mathbf{M}_{\perp} \\
& + \frac{1}{2\,I_{\|}\,I_{\perp}}\,\left(\mathbf{M}_{\|\perp} + \mathbf{M}_{\perp\|}\right) \otimes \left(\mathbf{M}_{\|\perp} + \mathbf{M}_{\perp\|}\right)
\end{aligned} \tag{4.5}$$

with $\mathbf{M}_{\|\perp}$ and $\mathbf{M}_{\perp\|}$ being the mixed structural tensors:

$$\mathbf{M}_{\|\perp} = \Phi_{\text{warp}} \otimes \Phi_{\text{weft}} \quad \text{and} \quad \mathbf{M}_{\perp\|} = \Phi_{\text{weft}} \otimes \Phi_{\text{warp}} \tag{4.6}$$

Finally, the material shows an orthotropic behavior. This allows for a decoupling of normal strains and shear strains. Hence, the strain-energy function $\Psi\left(I_{\parallel}, I_{\perp}, I_{\sharp}\right)$ can be separated as follows:

$$\Psi\left(I_{\parallel}, I_{\perp}, I_{\sharp}\right) = \Psi_{\text{norm}}\left(I_{\parallel}, I_{\perp}\right) + \Psi_{\text{shear}}\left(I_{\sharp}\right) \tag{4.7}$$

According to Equation (3.61), the 2^{nd} Piola-Kirchhoff stress tensor $\mathbf{S}$ can be established by means of the first derivative of Equation (4.7) w.r.t. the right Cauchy-Green tensor $\mathbf{C}$:

$$\mathbf{S} = 2\,\frac{\partial\Psi\left(I_{\parallel}, I_{\perp}\right)}{\partial I_{\parallel}}\,\frac{\partial I_{\parallel}}{\partial\mathbf{C}} + 2\,\frac{\partial\Psi\left(I_{\parallel}, I_{\perp}\right)}{\partial I_{\perp}}\,\frac{\partial I_{\perp}}{\partial\mathbf{C}} + 2\,\frac{\partial\Psi\left(I_{\sharp}\right)}{\partial I_{\sharp}}\,\frac{\partial I_{\sharp}}{\partial\mathbf{C}} \tag{4.8}$$

According to Equation (3.66), the second derivative of Equation (4.7) w.r.t. the right Cauchy-Green tensor $\mathbf{C}$ leads to the elasticity tensor $\mathbb{D}$:

$$\begin{aligned}
\mathbb{D} = {} & 4\,\frac{\partial I_{\parallel}}{\partial\mathbf{C}} \otimes \frac{\partial^2\Psi\left(I_{\parallel}, I_{\perp}\right)}{\partial I_{\parallel}\,\partial I_{\parallel}}\,\frac{\partial I_{\parallel}}{\partial\mathbf{C}} + 4\,\frac{\partial I_{\parallel}}{\partial\mathbf{C}} \otimes \frac{\partial^2\Psi\left(I_{\parallel}, I_{\perp}\right)}{\partial I_{\parallel}\,\partial I_{\perp}}\,\frac{\partial I_{\perp}}{\partial\mathbf{C}} \\
& + 4\,\frac{\partial I_{\perp}}{\partial\mathbf{C}} \otimes \frac{\partial^2\Psi\left(I_{\parallel}, I_{\perp}\right)}{\partial I_{\perp}\,\partial I_{\parallel}}\,\frac{\partial I_{\parallel}}{\partial\mathbf{C}} + 4\,\frac{\partial I_{\perp}}{\partial\mathbf{C}} \otimes \frac{\partial^2\Psi\left(I_{\parallel}, I_{\perp}\right)}{\partial I_{\perp}\,\partial I_{\perp}}\,\frac{\partial I_{\perp}}{\partial\mathbf{C}} \\
& + 4\,\frac{\partial\Psi\left(I_{\parallel}, I_{\perp}\right)}{\partial I_{\parallel}}\,\frac{\partial^2 I_{\parallel}}{\partial\mathbf{C}\,\partial\mathbf{C}} + 4\,\frac{\partial\Psi\left(I_{\parallel}, I_{\perp}\right)}{\partial I_{\perp}}\,\frac{\partial^2 I_{\perp}}{\partial\mathbf{C}\,\partial\mathbf{C}} \\
& + 4\,\frac{\partial I_{\sharp}}{\partial\mathbf{C}} \otimes \frac{\partial^2\Psi\left(I_{\sharp}\right)}{\partial I_{\sharp}\,\partial I_{\sharp}} + 4\,\frac{\partial\Psi\left(I_{\sharp}\right)}{\partial I_{\sharp}}\,\frac{\partial^2 I_{\sharp}}{\partial\mathbf{C}\,\partial\mathbf{C}}
\end{aligned} \tag{4.9}$$

REMARK I: Due to the experimental set-up, the plane stress conditions (see Section 3.3.3) are automatically full-filled.

REMARK II: For further information on the mixed invariants (4.3) the author refers to Aimène et al. [1], Schröder and Neff [100], Vidal-Sallé et. al [107].

REMARK III: Due to the sum rule in differentiation, the decoupling between normal and shear strains is still maintained in the 2^{nd} Piola-Kirchhoff stress tensor (4.8) as well as in the elasticity tensor (4.9).

4.1.1 The concept behind: Bézier surfaces/curves

Consider an arbitrary curve $\mathcal{C}$ in parametric form embedded in an Euclidean space $\mathbb{R}^3$:

$$\mathcal{C} : \xi \in [0,1] \rightarrow \mathbb{R}^3 \ , \ \xi \rightarrow \mathbf{x}\left(\xi\right) = x_i\left(\xi\right)\ \mathbf{e}_i \tag{4.10}$$

In case of a Bézier representation, any point $\mathbf{x}\left(\xi\right)$ located on the curve $\mathcal{C}$ is defined as follows:

$$\mathbf{x}\left(\xi\right) = \sum_{i=0}^{p} B_{i,p}\left(\xi\right)\ \mathbf{P}_i \qquad \text{for} \quad 0 \leq \xi \leq 1 \tag{4.11}$$

where $\mathbf{P}_i$ are the so-called *control points* and $B_{i,p}(\xi)$ are the p-th degree *Bernstein polynomials* for the i-th control point:

$$B_{i,p}(\xi) = \frac{p!}{i!\,(p-i)!}\,\xi^i\,(1-\xi)^{p-i} \tag{4.12}$$

A closer look on the control points $\mathbf{P}_i$ reveals that the required number of control points n is directly linked to the polynomial degree p of the chosen Bernstein functions, i.e. $n = p + 1$. The polygon formed by the control points $\{\mathbf{P}_0 \ldots \mathbf{P}_p\}$ is called the *control polygon* of the curve, see Figure 4.2. Furthermore, the control points forms a *convex hull*, i.e. the Bézier curve is bounded by its control points (dotted gray box in Figure 4.2).

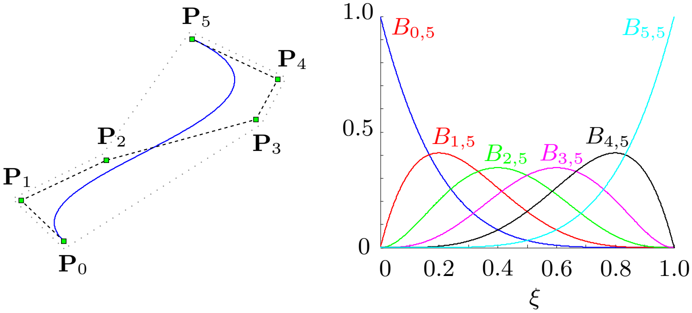

Figure 4.2: Bézier curve ($p = 5$): Curve (blue solid) and control polygon (dashed black) within $\mathbb{R}^3$ (left) and corresponding Bernstein functions (right)

Based on the exemplary Bézier curve shown in Figure 4.2, the following properties can be derived. The list may not be complete, only the properties relevant for this thesis are addressed:

- The Bernstein polynomials form a *partition of unity*:

$$\sum_{i=0}^{p} B_{i,p}(\xi) = 1 \quad \forall\, 0 \le \xi \le 1 \tag{4.13}$$

- Only the first and last control point show an interpolating character:

$$\mathbf{P}_0 = \mathbf{x}(\xi = 0) \quad \text{and} \quad \mathbf{P}_p = \mathbf{x}(\xi = 1) \tag{4.14}$$

- The derivative of a p-th degree Bézier curve will again result in a Bézier curve but of degree $p - 1$:

$$\frac{\mathrm{d}\mathbf{x}(\xi)}{\mathrm{d}\xi} = \sum_{i=0}^{p} \frac{\mathrm{d}}{\mathrm{d}\xi}\big(B_{i,p}(\xi)\big)\,\mathbf{P}_i = p\sum_{i=0}^{p-1} B_{i,p-1}(\xi)\,(\mathbf{P}_{i+1} - \mathbf{P}_i) \tag{4.15}$$

- → At $\xi = 0$ and $\xi = 1$ the Bézier curves are tangent to their control polygon

Consider an arbitrary surface $\mathcal{S}$ in parametric form embedded in an Euclidean space $\mathbb{R}^3$:

$$\mathcal{S} : (\xi, \eta) \in [0,1] \times [0,1] \rightarrow \mathbb{R}^3 \ , \ (\xi, \eta) \rightarrow \mathbf{x}(\xi, \eta) = x_i(\xi, \eta) \ \mathbf{e}_i \tag{4.16}$$

Applying the concept of *tensor product surfaces*, a Bézier surface is constructed by means of two independent Bernstein polynomials (4.12) $B_{i,p}(\xi)$ and $B_{j,q}(\eta)$ of degree p and q, respectively:

$$\mathbf{x}(\xi, \eta) = \sum_{i=0}^{p} \sum_{j=0}^{q} B_{i,p}(\xi) \ B_{j,q}(\eta) \ \mathbf{P}_{i,j} \quad \text{for} \quad 0 \leq \xi, \eta \leq 1 \tag{4.17}$$

with $\mathbf{P}_{i,j}$ being a $(p+1) \times (q+1)$ bidirectional net of control points, called *control mesh*, which in turn forms a convex hull. The overall number of control points is directly linked to the polynomial degree of the Bernstein polynomials. Due to the tensor product character of Bézier surfaces, the major properties are analog to those of Bézier curves. Again, only the relevant properties are listed:

- → The product of the Bernstein polynomials forms a *partition of unity*:

$$\sum_{i=0}^{p} \sum_{j=0}^{q} B_{i,p}(\xi) \ B_{j,p}(\eta) = 1 \quad \forall \, 0 \leq \xi, \eta \leq 1 \tag{4.18}$$

- → Only the vertexes of the control mesh show an interpolating character:

$$\mathbf{P}_{0,0} = \mathbf{x}(\xi = 0, \eta = 0) \quad \text{and} \quad \mathbf{P}_{p,0} = \mathbf{x}(\xi = 1, \eta = 0) \tag{4.19a}$$

$$\mathbf{P}_{1,0} = \mathbf{x}(\xi = 1, \eta = 0) \quad \text{and} \quad \mathbf{P}_{p,q} = \mathbf{x}(\xi = 1, \eta = 1) \tag{4.19b}$$

- → The partial derivatives of a Bézier surface of polynomial degree $p \times q$ w.r.t. either ξ or η will again result in a Bézier surface but of reduced polynomial degree, i.e. $p-1$ or $q-1$, respectively:

$$\frac{\partial \mathbf{x}(\xi, \eta)}{\partial \xi} = p \sum_{i=0}^{p-1} \sum_{j=0}^{q} B_{i,p-1}(\xi) \ B_{j,q}(\eta) \ (\mathbf{P}_{i+1,j} - \mathbf{P}_{i,j}) \tag{4.20a}$$

$$\frac{\partial \mathbf{x}(\xi, \eta)}{\partial \eta} = q \sum_{i=0}^{p} \sum_{j=0}^{q-1} B_{i,p}(\xi) \ B_{j,q-1}(\eta) \ (\mathbf{P}_{i,j+1} - \mathbf{P}_{i,j}) \tag{4.20b}$$

→ The mixed partial derivative of a Bézier surface of polynomial degree $p \times q$ result in a Bézier surface of polynomial degree $(p-1) \times (q-1)$:

$$\begin{aligned}\frac{\partial^2 \mathbf{x}(\xi,\eta)}{\partial\xi\,\partial\eta} &= p\,q \sum_{i=0}^{p-1}\sum_{j=0}^{q-1} B_{i,p-1}(\xi)\; B_{j,q-1}(\eta)\; \left(\mathbf{P}_{i+1,j+1} + \mathbf{P}_{i,j}\right) \\ &\quad - p\,q \sum_{i=0}^{p-1}\sum_{j=0}^{q-1} B_{i,p-1}(\xi)\; B_{j,q-1}(\eta)\; \left(\mathbf{P}_{i+1,j} + \mathbf{P}_{i,j+1}\right)\end{aligned} \tag{4.21}$$

→ The tangent planes at the vertexes of the control mesh are spanned by the tangent vectors of corresponding Bézier curves

REMARK IV: For further information on parameterized surfaces/curves based on either Bernstein polynomials or B-Spline/NURBS basis functions the author refers to PIEGL AND TILLER [92].

4.1.1.1 Strain-energy function: $\Psi_{\text{norm}}\left(I_\parallel, I_\perp\right)$

The goal is now to express the strain-energy function $\Psi_{\text{norm}}\left(I_\parallel, I_\perp\right)$ in terms of a Bézier surface. Therefore, let $\mathcal{V}_{\text{norm}} \subset \mathbb{R}^3$ be an Euclidean vector space over the body $\mathcal{K}^3$:

$$\mathcal{K}^3 \rightarrow \mathcal{V}_{\text{norm}}\,, \quad \left(I_\parallel, I_\perp, \Psi_{\text{norm}}\right) \rightarrow I_\parallel \mathbf{e}_1 + I_\perp \mathbf{e}_2 + \Psi_{\text{norm}} \mathbf{e}_3 \tag{4.22}$$

with $\mathcal{K}^3 = \{\left(I_\parallel, I_\perp, \Psi_{\text{norm}}\right) \big|\, I_\parallel, I_\perp, \Psi_{\text{norm}} \in \mathbb{R}\}$, and let $\mathcal{S}(\xi,\eta)$ be an arbitrary parameterized surface embedded in $\mathcal{V}_{\text{norm}}$:

$$\begin{aligned}\mathcal{S} : (\xi,\eta) \in [0,1]\times[0,1] &\rightarrow \mathcal{V}_{\text{norm}}\,, \\ (\xi,\eta) &\rightarrow \left[I_\parallel(\xi,\eta), I_\perp(\xi,\eta), \Psi_{\text{norm}}(\xi,\eta)\right]\end{aligned} \tag{4.23}$$

Applying the concept of tensor product surfaces (4.17) to (4.23), the desired Bézier surface is defined as follows:

$$\begin{bmatrix} I_\parallel(\xi,\eta) \\ I_\perp(\xi,\eta) \\ \Psi_{\text{norm}}(\xi,\eta) \end{bmatrix} = \sum_{i=0}^{p}\sum_{j=0}^{q} B_{i,p}(\xi)\; B_{j,q}(\eta) \begin{bmatrix} \hat{I}_\parallel(\xi,\eta) \\ \hat{I}_\perp(\xi,\eta) \\ \hat{\Psi}_{\text{norm}}(\xi,\eta) \end{bmatrix}_{i,j} \tag{4.24}$$

Considering Equation (4.8), the first partial derivatives of the strain-energy function Ψ_{norm} w.r.t. to the structural invariants $I_\parallel$ and $I_\perp$ are required for establishing the 2nd Piola-Kirchhoff stress tensor. For the sake of clarity, the arguments are skipped. Applying the chain rule of calculus to Equation (4.24) yields:

$$\frac{\partial \Psi_{\text{norm}}}{\partial I_\parallel} = \frac{\partial \Psi_{\text{norm}}}{\partial \xi}\frac{\partial \xi}{\partial I_\parallel} + \frac{\partial \Psi_{\text{norm}}}{\partial \eta}\frac{\partial \eta}{\partial I_\parallel} \tag{4.25a}$$

$$\frac{\partial \Psi_{\text{norm}}}{\partial I_\perp} = \frac{\partial \Psi_{\text{norm}}}{\partial \xi}\frac{\partial \xi}{\partial I_\perp} + \frac{\partial \Psi_{\text{norm}}}{\partial \eta}\frac{\partial \eta}{\partial I_\perp} \tag{4.25b}$$

with the *inverse Jacobian* $\mathbf{J}^{-1}$:

$$\begin{bmatrix} \dfrac{\partial \xi}{\partial I_{\|}} & \dfrac{\partial \xi}{\partial I_{\perp}} \\ \dfrac{\partial \eta}{\partial I_{\|}} & \dfrac{\partial \eta}{\partial I_{\perp}} \end{bmatrix} = \frac{1}{\dfrac{\partial I_{\|}}{\partial \xi}\dfrac{\partial I_{\perp}}{\partial \eta} - \dfrac{\partial I_{\perp}}{\partial \xi}\dfrac{\partial I_{\|}}{\partial \eta}} \begin{bmatrix} \dfrac{\partial I_{\perp}}{\partial \eta} & -\dfrac{\partial I_{\perp}}{\partial \xi} \\ -\dfrac{\partial I_{\|}}{\partial \eta} & \dfrac{\partial I_{\|}}{\partial \xi} \end{bmatrix} \tag{4.26}$$

The same strategy applies to the second partial derivatives of the strain-energy function Ψ_{norm} w.r.t. the structural invariants $I_{\|}$ and $I_{\perp}$. These derivatives are required for establishing the elasticity tensor defined by Equation (4.9). Therefore, applying the chain rule of calculus to Equation (4.25) yields:

$$\frac{\partial^2 \Psi_{\text{norm}}}{\partial I_{\|}\, \partial I_{\|}} = \frac{\partial^2 \Psi_{\text{norm}}}{\partial I_{\|}\, \partial \xi}\frac{\partial \xi}{\partial I_{\|}} + \frac{\partial^2 \Psi_{\text{norm}}}{\partial I_{\|}\, \partial \eta}\frac{\partial \eta}{\partial I_{\|}} \tag{4.27a}$$

$$\frac{\partial^2 \Psi_{\text{norm}}}{\partial I_{\perp}\, \partial I_{\perp}} = \frac{\partial^2 \Psi_{\text{norm}}}{\partial I_{\perp}\, \partial \xi}\frac{\partial \xi}{\partial I_{\perp}} + \frac{\partial^2 \Psi_{\text{norm}}}{\partial I_{\perp}\, \partial \eta}\frac{\partial \eta}{\partial I_{\perp}} \tag{4.27b}$$

$$\frac{\partial^2 \Psi_{\text{norm}}}{\partial I_{\|}\, \partial I_{\perp}} = \frac{\partial^2 \Psi_{\text{norm}}}{\partial I_{\|}\, \partial \xi}\frac{\partial \xi}{\partial I_{\perp}} + \frac{\partial^2 \Psi_{\text{norm}}}{\partial I_{\|}\, \partial \eta}\frac{\partial \eta}{\partial I_{\perp}} \tag{4.27c}$$

by means of the following relations:

$$\begin{aligned} \frac{\partial^2 \Psi_{\text{norm}}}{\partial I_{(\star)}\, \partial(\bullet)} = {} & \frac{\partial^2 \Psi_{\text{norm}}}{\partial \xi\, \partial(\bullet)}\frac{\partial \xi}{\partial I_{(\star)}} + \frac{\partial \Psi_{\text{norm}}}{\partial \xi}\frac{\partial^2 \xi}{\partial I_{(\star)} \partial(\bullet)} \\ & + \frac{\partial^2 \Psi_{\text{norm}}}{\partial \eta\, \partial(\bullet)}\frac{\partial \eta}{\partial I_{(\star)}} + \frac{\partial \Psi_{\text{norm}}}{\partial \eta}\frac{\partial^2 \eta}{\partial I_{(\star)} \partial(\bullet)} \end{aligned} \tag{4.28}$$

where $I_{(\star)} \in \begin{bmatrix} I_{\|} & I_{\perp} \end{bmatrix}$ and $(\bullet) \in [\xi \quad \eta]$. Applying Equation (A.19) to (4.26) leads to the second partial derivatives of the surface parameter $(\bullet)$ w.r.t. the structural invariant $I_{(\star)}$ and the surface parameter $(\bullet)$:

$$\frac{\partial \mathbf{J}^{-1}}{\partial(\bullet)} = \frac{-1}{\det \mathbf{J}^2}\frac{\partial \det \mathbf{J}}{\partial(\bullet)}\operatorname{adj}\mathbf{J} + \frac{1}{\det \mathbf{J}}\frac{\partial \operatorname{adj}\mathbf{J}}{\partial(\bullet)} \tag{4.29}$$

REMARK V: The presented strain-energy function (response surface) is based on sample points gained due to biaxial tensile tests where the specimen is mounted in a fiber parallel way - see Section 4.1.2.1.

4.1.1.2 Strain-energy function: $\Psi_{\text{shear}}(I_{\sharp})$

By analogy with the previous Section 4.1.1.1, the strain-energy function $\Psi_{\text{shear}}(I_{\sharp})$ is also based on a Bézier representation but in terms of a curve. Therefore, let $\mathcal{V}_{\text{shear}} \subset \mathbb{R}^3$ be an Euclidean vector space over the body $\mathcal{K}^2$:

$$\mathcal{K}^2 \to \mathcal{V}_{\text{shear}}\,, \quad (I_{\sharp}, \Psi_{\text{shear}}) \to I_{\sharp}\mathbf{e}_1 + \Psi_{\text{shear}}\mathbf{e}_2 \tag{4.30}$$

with $\mathcal{K}^2 = \{(I_\sharp, \Psi_{\text{shear}}) | \, I_\sharp, \Psi_{\text{shear}} \in \mathbb{R}\}$, and let $\mathcal{C}(\xi)$ be an arbitrary parameterized curve embedded in $\mathcal{V}_{\text{shear}}$:

$$\mathcal{C} : \xi \in [0,1] \to \mathbb{R}^2 \ , \ \xi \to \left[I_\sharp(\xi) \, , \Psi_{\text{shear}}(\xi) \right] \tag{4.31}$$

By means of Equation (4.11), the desired Bézier curve can be defined:

$$\begin{bmatrix} I_\sharp(\xi) \\ \Psi_{\text{shear}}(\xi) \end{bmatrix} = \sum_{i=0}^{p} B_{i,p}(\xi) \begin{bmatrix} \hat{I}_\sharp(\xi) \\ \hat{\Psi}_{\text{shear}}(\xi) \end{bmatrix}_i \tag{4.32}$$

Considering Equation (4.8), the first partial derivative of the strain-energy function Ψ_{shear} w.r.t. to the structural invariant $I_\sharp$ is required for establishing the 2nd Piola-Kirchhoff stress tensor. For the sake of clarity, the arguments are skipped. Applying the chain rule of calculus to Equation (4.32) yields:

$$\frac{\partial \Psi_{\text{shear}}}{\partial I_\sharp} = \frac{\partial \Psi_{\text{shear}}}{\partial \xi} \frac{\partial \xi}{\partial I_\sharp} = \frac{\partial \Psi_{\text{shear}}}{\partial \xi} \left[\frac{\partial I_\sharp}{\partial \xi} \right]^{-1} \tag{4.33}$$

The same strategy applies to the second partial derivative of the strain-energy function Ψ_{shear} w.r.t. to the structural invariant $I_\sharp$. This derivative is required for establishing the elasticity tensor defined by Equation (4.9). Therefore, applying the chain rule of calculus to Equation (4.33) yields:

$$\frac{\partial^2 \Psi_{\text{shear}}}{\partial I_\sharp \, \partial I_\sharp} = \frac{\partial^2 \Psi_{\text{shear}}}{\partial \xi \, \partial \xi} \left[\frac{\partial I_\sharp}{\partial \xi} \right]^{-2} + \frac{\partial \Psi_{\text{shear}}}{\partial \xi} \left[\frac{\partial^2 I_\sharp}{\partial \xi \, \partial \xi} \right]^{-1} \tag{4.34}$$

REMARK VI: The presented response curve method is based on sample points gained due to biaxial tensile tests where the specimen is mounted under 45° - see Section 4.1.2.2.

4.1.2 Data processing

As already mentioned in the introduction of this chapter, the presented material model is based on experimental data gathered during velocity-driven biaxial tensile tests. In general, biaxial tensile tests are capable of capturing the load-displacement relation for a specimen subjected to a biaxial stress state. Within the scope of this thesis, the displacements are measured by means of a *video extensiometer*. Thereby, each path of the four reference marks $M_1 \dots M_4$ is traced separately. The arising forces are measured by means of four load cells $K_1 \dots K_4$ located at each clamp of the biaxial testing machines. Figure 4.4 shows a schematic description of the used specimen. In addition, an artificial mark CM for calculating the corresponding right Cauchy-Green tensors (3.41) is introduced.

In order to provide an adequate set of data for the presented material response surfaces/curves (see 4.1.1.1 and 4.1.1.2), a *velocity-driven*[3] experimental set-up has to be chosen. This ensures a unique strain state for each

---

[3] i.e. each axis of the biaxial testing machine is driven with an individually preset velocity

sample point[4] and for each speed ratio (see Section 4.2). Hence, a unique biaxial stress state at each sample point is consistently captured[5]. Therefore, at each instant of time t_i the following quadruple (4-tuple), called *sample*, is achieved:

$$t_i \longrightarrow \{u_{\mathrm{M}_{13}}, u_{\mathrm{M}_{24}}, f_{\mathrm{K}_{13}}, f_{\mathrm{K}_{24}}\}_i \quad \text{for} \quad i \in [0,\ n_{\mathrm{exp}}] \tag{4.35}$$

with n_{exp} being the total number of samples per experiment, $u_{\mathrm{M}_{13}}$ and $u_{\mathrm{M}_{24}}$ being the arithmetic mean of the displacements and $f_{\mathrm{K}_{13}}$ and $f_{\mathrm{K}_{24}}$ being the arithmetic mean of the forces (cf. Figure 4.4):

$$u_{\mathrm{M}_{13}} = \frac{u_{\mathrm{M}_1} + u_{\mathrm{M}_3}}{2} \quad \text{and} \quad u_{\mathrm{M}_{24}} = \frac{u_{\mathrm{M}_2} + u_{\mathrm{M}_4}}{2} \tag{4.36a}$$

$$f_{\mathrm{K}_{13}} = \frac{f_{\mathrm{K}_1} + f_{\mathrm{K}_3}}{2} \quad \text{and} \quad f_{\mathrm{K}_{24}} = \frac{f_{\mathrm{K}_2} + f_{\mathrm{K}_4}}{2} \tag{4.36b}$$

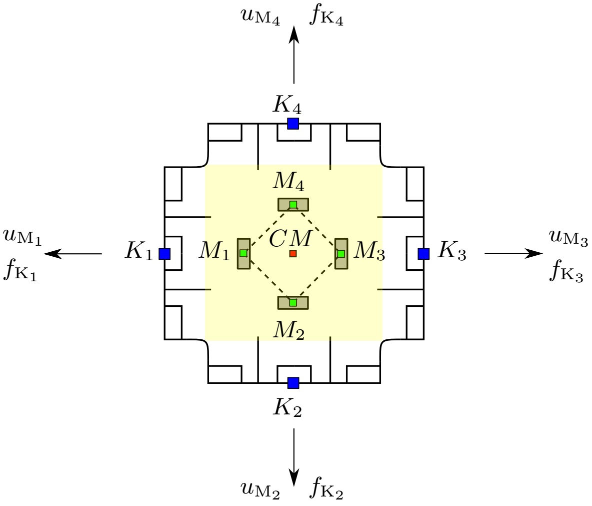

Figure 4.3: Schematic description: fabric specimen with reference marks ($M_1 \dots M_4$), load cells ($K_1 \dots K_4$) and artificial mark (CM)

REMARK VII: A detailed description of the experimental set-up is given in Wendt and Krzywinski [109], [110].

REMARK VIII: Depending on the experimental set-up, i.e. the fiber

---

[4] i.e. a set of displacements and forces captured at an instant of time t_i

[5] this will not be the case for a *displacement-driven* (i.e. each axis of the biaxial testing machine is driven with a constant velocity) experimental set-up where a biaxial stress state can only be captured at different instants of time

orientation within the specimen, the achieved sample points will either be called *normal-sample* (fiber-parallel) or *shear-sample* (under 45°).

REMARK IX: The set of normal-samples or shear-samples (4.35) collected within one experiment will either be called *normal-campaign* $\mathbb{V}_{\text{norm}}$ or *shear-campaign* $\mathbb{V}_{\text{shear}}$.

The sample points introduced by Equation (4.35) cannot be used directly for establishing the material response surfaces/curves. But each sample point provides the required information for computing the introduced structural invariants ($I_{\parallel}$, $I_{\perp}$ or $I_{\sharp}$) and strain-energies (Ψ_{norm} or Ψ_{shear}) at the corresponding instant of time t_i and depending on the experimental set-up. This leads to the following *triple* (4.37a) and *double* (4.37b) based on either a normal-sample or a shear-sample:

$$t_i \longrightarrow \left\{I_{\parallel}, I_{\perp}, \Psi_{\text{norm}}\right\}_i \quad \text{for} \quad i \in [0,\, n_{\text{exp}}] \tag{4.37a}$$

$$t_i \longrightarrow \left\{I_{\sharp}, \Psi_{\text{shear}}\right\}_i \quad \text{for} \quad i \in [0,\, n_{\text{exp}}] \tag{4.37b}$$

REMARK X: For the remainder of this thesis, the set of all triples defined by Equation (4.37a) is called *normal-set* $\mathbb{U}_{\text{norm}}$ and the set of all doubles defined by Equation (4.37b) is called *shear-set* $\mathbb{U}_{\text{shear}}$.

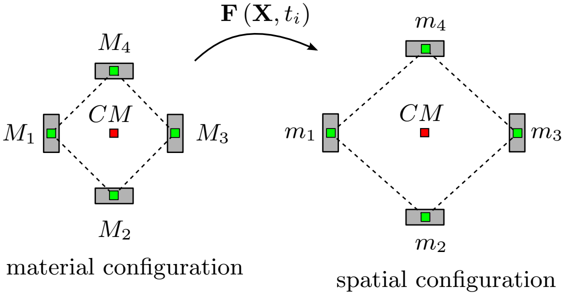

Figure 4.4: Description of motion: reference marks

According to Equation (4.1) and (4.3), the structural invariants ($I_{\parallel}$, $I_{\perp}$ and $I_{\sharp}$) only depend on the structural or mixed structural tensors and the right Cauchy-Green tensor. Since the structural tensors $\mathbf{M}_{\parallel}$ and $\mathbf{M}_{\perp}$ (4.2) and the mixed structural tensors $\mathbf{M}_{\parallel\perp}$ and $\mathbf{M}_{\perp\parallel}$ (4.6) only depend on the fiber direction within the material configuration, they are constant for each instant of time t_i. Thus, their computation is straightforward and has to be done only once per test campaign. The challenge is now to compute the right Cauchy-Green tensor $\mathbf{C}$ based on the measured displacements. Therefore, the motion of the specimen at the point CM is described in terms of material and spatial positions of the reference marks ($M_1 \dots M_4$), see Figure 4.4. By means of a bi-linear interpolation scheme, the material and spatial position of CM, $\mathbf{X}_{\mathrm{CM}}$ and $\mathbf{x}_{\mathrm{CM}} = \mathbf{x}_{\mathrm{CM}}\left(t_i\right)$, is defined as follows:

$$\mathbf{X}_{\mathrm{CM}} = \sum_{i=1}^{4} N_i \left(\theta^1, \theta^2\right)\Big|_{(0,0)} \mathbf{X}_{\mathrm{M_i}} \tag{4.38a}$$

$$\mathbf{x}_{\mathrm{CM}} = \sum_{i=1}^{4} N_i \left(\theta^1, \theta^2\right)\Big|_{(0,0)} \mathbf{x}_{\mathrm{m_i}} \tag{4.38b}$$

with $\mathrm{m_i}$ being the averaged spatial reference mark positions at an instant of time t_i:

$$m_1 = M_1 - u_{\mathrm{M}_{13}} \quad \text{and} \quad m_3 = M_3 + u_{\mathrm{M}_{13}} \tag{4.39a}$$

$$m_2 = M_2 - u_{\mathrm{M}_{24}} \quad \text{and} \quad m_4 = M_4 + u_{\mathrm{M}_{24}} \tag{4.39b}$$

and $N_1\left(\theta^1, \theta^2\right) \ldots N_4\left(\theta^1, \theta^2\right)$ being the standard bi-linear *Lagrangian* shape functions:

$$N_1\left(\theta^1, \theta^2\right) = \frac{1}{4}\left(1 - \theta^1\right)\left(1 - \theta^2\right) \qquad \text{for} \quad -1 \leq \theta^1, \theta^2 \leq 1 \tag{4.40a}$$

$$N_2\left(\theta^1, \theta^2\right) = \frac{1}{4}\left(1 + \theta^1\right)\left(1 - \theta^2\right) \qquad \text{for} \quad -1 \leq \theta^1, \theta^2 \leq 1 \tag{4.40b}$$

$$N_3\left(\theta^1, \theta^2\right) = \frac{1}{4}\left(1 + \theta^1\right)\left(1 + \theta^2\right) \qquad \text{for} \quad -1 \leq \theta^1, \theta^2 \leq 1 \tag{4.40c}$$

$$N_4\left(\theta^1, \theta^2\right) = \frac{1}{4}\left(1 - \theta^1\right)\left(1 + \theta^2\right) \qquad \text{for} \quad -1 \leq \theta^1, \theta^2 \leq 1 \tag{4.40d}$$

Applying Equation (2.28) to the parameterized material and spatial positions of CM (4.38) leads to the corresponding convective coordinate frames:

$$\mathbf{G}_i^{\mathrm{CM}} = \frac{\partial \mathbf{X}_{\mathrm{CM}}}{\partial \theta^i} \quad i = 1 \ldots 2 \quad \text{and} \quad \mathbf{G}_3^{\mathrm{CM}} = \frac{\mathbf{G}_1^{\mathrm{CM}} \times \mathbf{G}_2^{\mathrm{CM}}}{\left\|\mathbf{G}_1^{\mathrm{CM}} \times \mathbf{G}_2^{\mathrm{CM}}\right\|} \tag{4.41a}$$

$$\mathbf{g}_i^{\mathrm{CM}} = \frac{\partial \mathbf{x}_{\mathrm{CM}}}{\partial \theta^i} \quad i = 1 \ldots 2 \quad \text{and} \quad \mathbf{g}_3^{\mathrm{CM}} = \frac{\mathbf{g}_1^{\mathrm{CM}} \times \mathbf{g}_2^{\mathrm{CM}}}{\left\|\mathbf{g}_1^{\mathrm{CM}} \times \mathbf{g}_2^{\mathrm{CM}}\right\|} \tag{4.41b}$$

Equation (4.41a) and Equation (4.41b) serve the basis for the calculation of the deformation gradient $\mathbf{F}\left(\mathbf{X}_{\mathrm{CM}}, t_i\right)$ (3.22) and the corresponding right Cauchy-Green tensor $\mathbf{C}\left(\mathbf{X}_{\mathrm{CM}}, t_i\right)$ (3.40) at each instant of time t_i.

Finally, for each instant of time t_i all required information is provided for computing the structural invariants $I_{\|}$ and $I_{\perp}$ (4.1) or $I_{\sharp}$ (4.3) based on either the corresponding normal-sample or the corresponding shear-sample.

REMARK XI: Due to the experimental set-up, the in-plane normal and shear stresses are constantly distributed over the specimen's thickness. Hence, for the calculation of the deformation gradient and the right Cauchy-Green tensor the mid-surface of the specimen is chosen (i.e. $\theta^3 = 0$). Furthermore, the director is assumed to be inextensible (see 3-parameter formulation on page 36f).

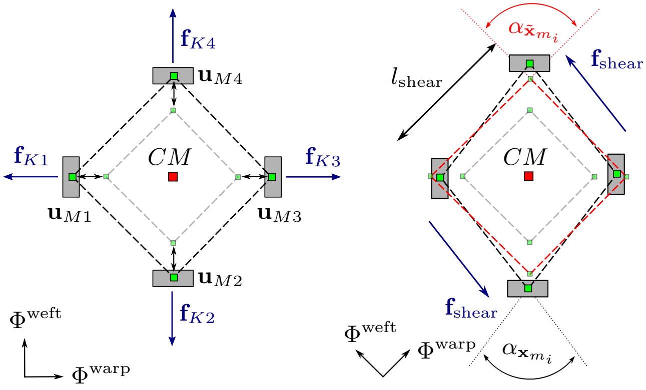

Figure 4.5: Schematic description: normal-sample (left) and shear-sample (right)

According to Equation (3.54), the strain-energy function describes the *elastic potential energy* of a continuum per unit volume[6], i.e. the *specific* elastic potential energy. By analogy with a simple spring, the specific elastic potential energy is directly linked to the *specific work* done by an external force. Thus, the strain-energy function can be interpreted as the area under a load-displacement curve per unit volume, i.e. the primitive of the load-displacement relation. The challenge is now to establish the mentioned integrals based on the discrete samples either belonging to a normal or shear campaign (a schematic description for both experimental set-ups is shown in Figure 4.5). For this purpose, the continuous parameter θ^1 is introduced representing the time span between two instants of time t_{i-1} and t_i. Applying a linear interpolation scheme leads to:

$$\{\bullet\}_{t_i}\left(\theta^1\right) = N_1\left(\theta^1\right)\{\bullet\}_{i-1} + N_2\left(\theta^1\right)\{\bullet\}_i \quad \text{for} \quad i \in [1,\, n_{\text{exp}}] \tag{4.42}$$

with

$$N_1\left(\theta^1\right) = \frac{1}{2}\left(1 - \theta^1\right) \qquad \text{for} \quad -1 \leq \theta^1 \leq 1 \tag{4.43a}$$

$$N_2\left(\theta^1\right) = \frac{1}{2}\left(1 + \theta^1\right) \qquad \text{for} \quad -1 \leq \theta^1 \leq 1 \tag{4.43b}$$

---

[6] for further information the author refers to Holzapfel [60] and Ogden [88].

being the the standard linear Lagrangian shape functions and $\{\bullet\}_{i-1}$, $\{\bullet\}_i$ being either a normal or a shear sample defined by Equation (4.35). Finally, the primitive $\Psi_{(\bullet)}$ of the load-displacement relation at an instant of time t_i can be established as a sum over integrals of the corresponding linearly interpolated segments $\{\bullet\}_k\left(\theta^1\right)$:

$$\Psi_{(\bullet)}\big|_{t_i} = \frac{1}{V}\sum_{k=t_1}^{t_i}\int_{-1}^{1}\{\bullet\}_k\left(\theta^1\right)\,\mathrm{d}\theta^1 = \frac{1}{V}\sum_{k=1}^{i}\{\bullet\}_{k-1}+\{\bullet\}_k \tag{4.44}$$

with V being the representative volume defined as the product of the considered surface area A (indicated by the yellowish area in Figure 4.3) and the specimen's thickness thk, i.e. $V = \mathrm{thk}\cdot A$. The structure of $\{\bullet\}_k\left(\theta^1\right)$ depends on the underlying campaign $(\bullet)$, see Section 4.1.2.1 and 4.1.2.2.

4.1.2.1 Strain-energy function: Ψ_{norm}

Consider data only arising out of a normal-campaign. By means of Equation (4.42) and (4.44) the specific elastic potential energy at each instant of time t_i can be established in terms of the specific work done by the biaxial tensioning:

$$\Psi_{\mathrm{norm}}\big|_{t_i} = \frac{1}{V}\sum_{k=t_1}^{t_i} 2\int_{-1}^{1}\mathbf{f}_k\left(\theta^1\right)\,\mathrm{d}\mathbf{u}_k\left(\theta^1\right) \quad \text{for} \quad t_i\in\left[t_1,\,t_{n_{\mathrm{exp}}}\right] \tag{4.45}$$

Due to the experimental set-up shown in Figure 4.4 (left), the measured forces and displacements are already representing the proper quantities. Therefore, the samples (4.35) can directly be used for establishing the force vector $\mathbf{f}_k\left(\theta^1\right)$ and the differential displacement vector $\mathrm{d}\mathbf{u}_k\left(\theta^1\right)$:

$$\mathbf{f}_k\left(\theta^1\right) = N_1\left(\theta^1\right)\begin{bmatrix} f_{\mathrm{K}_{13}}\\ f_{\mathrm{K}_{24}}\end{bmatrix}_{i-1} + N_2\left(\theta^1\right)\begin{bmatrix} f_{\mathrm{K}_{13}}\\ f_{\mathrm{K}_{24}}\end{bmatrix}_{i} \tag{4.46}$$

and

$$\mathrm{d}\mathbf{u}_k\left(\theta^1\right) = \frac{\partial}{\partial\theta^1}\left(N_1\left(\theta^1\right)\begin{bmatrix} u_{\mathrm{M}_{13}}\\ u_{\mathrm{M}_{24}}\end{bmatrix}_{i-1} + N_2\left(\theta^1\right)\begin{bmatrix} u_{\mathrm{M}_{13}}\\ u_{\mathrm{M}_{24}}\end{bmatrix}_{i}\right)\mathrm{d}\theta^1 \tag{4.47}$$

with

$$\left\{u_{\mathrm{M}_{13}}, u_{\mathrm{M}_{24}}, f_{\mathrm{K}_{13}}, f_{\mathrm{K}_{24}}\right\}_i \in \mathbb{V}_{\mathrm{norm}} \quad \text{for} \quad i\in[0,\,n_{exp}] \tag{4.48}$$

REMARK XII: According to Equation (4.36), each sample (4.48) represents the arithmetic mean of the measured data (i.e. displacements and forces). Due to the symmetry of the experimental set-up the following relations hold:

$$2\int f_{\mathrm{K}_{13}} \cdot \mathrm{d}u_{\mathrm{M}_{13}} = \int f_{\mathrm{K}_1} \cdot \mathrm{d}u_{\mathrm{M}_1} + \int f_{\mathrm{K}_3} \cdot \mathrm{d}u_{\mathrm{M}_3} \tag{4.49a}$$

$$2\int f_{\mathrm{K}_{24}} \cdot \mathrm{d}u_{\mathrm{M}_{24}} = \int f_{\mathrm{K}_2} \cdot \mathrm{d}u_{\mathrm{M}_2} + \int f_{\mathrm{K}_4} \cdot \mathrm{d}u_{\mathrm{M}_4} \tag{4.49b}$$

4.1.2.2 Strain-energy function: Ψ_{shear}

Consider data only arising out of a shear-campaign. By means of Equation (4.42) and (4.44) the specific elastic potential energy at each instant of time t_i can be establish in terms of the specific work done by the applied biaxial tensile loading:

$$\Psi_{\mathrm{shear}}\big|_{t_i} = \frac{1}{V}\sum_{k=t_1}^{t_i}\int_{-1}^{1} M_k\left(\theta^1\right)\,\mathrm{d}\alpha_k\left(\theta^1\right) \quad \text{for} \quad t_i \in \left[t_1,\, t_{n_{\exp}}\right] \tag{4.50}$$

with $M_k\left(\theta^1\right)$ being the shear moment and $\alpha_k\left(\theta^1\right)$ being the shear angle resulting from the experimental set-up, shown in Figure 4.5 (right). In more detail, in case of the specimen for a shear campaign, the warp and weft directions are not aligned with the axis of the biaxial testing machine but under 45° to it. Based on the fact that such an experimental set-up only generates shear loads, the corresponding shear forces f_{shear} at an instant of time t_i can be established by means of *Mohr's analogy*:

$$f_{\mathrm{shear}} = \frac{f_{\mathrm{K}_{13}i} - f_{\mathrm{K}_{24}i}}{2} \tag{4.51}$$

Unfortunately, the lever arms of the acting shear forces and the shear angles cannot directly be established by means of the measured marker positions $m_1 \dots m_4$. This is due to the description of the motion based on the convective coordinate frames (4.41) and the resulting deformation gradient. In contrast to the normal-campaign (see Section 4.1.2.1), only the shape-altering portions of the motion are responsible for the specific work representing the specific elastic potential Ψ_{shear}. By means of the so-called *multiplicative decomposition*, the deformation gradient can be rearranged in terms of an *isochoric* (volume-preserving or distortional) motion $\mathbf{F}_{\mathrm{iso}}$ and a *volumetric* (volume-changing or dilational) motion $\mathbf{F}_{\mathrm{vol}}$:

$$\mathbf{F} = \mathbf{F}_{\mathrm{iso}} \cdot \mathbf{F}_{\mathrm{vol}} \tag{4.52}$$

with

$$\mathbf{F}_{\mathrm{iso}} = J^{-\frac{1}{3}}\,\mathbf{F} \quad \text{and} \quad \mathbf{F}_{\mathrm{vol}} = J^{\frac{1}{3}}\,\mathbf{I} \tag{4.53}$$

Applying $(4.53)_2$ to the material positions of the reference marks $\mathbf{X}_{M_{(\bullet)}i}$ leads to their *hydrostatic* positions $\tilde{\mathbf{x}}_{m_{(\bullet)}i}$

$$\tilde{\mathbf{x}}_{m_{(\bullet)}i} = \mathbf{F}_{\mathrm{vol}} \cdot \mathbf{X}_{M_{(\bullet)}i} \quad \text{with} \quad (\bullet) = 1 \dots 4 \tag{4.54}$$

The resulting so-called *hydrostatic configuration* is represented by the red dashed square in Figure 4.5. Eventually, the arising shear moment $\mathbf{M}_i$ at an instant of time t_i can be interpreted as a *force couple* acting on the hydrostatic configuration (cf. Figure 4.5):

$$M_i = f_{\text{shear}} \cdot l_{\text{shear}} \tag{4.55}$$

with l_{shear} being the arithmetic mean of the descriptive square:

$$l_{\text{shear}} = \frac{\|\tilde{\mathbf{x}}_{\mathrm{m}_4 i} - \tilde{\mathbf{x}}_{\mathrm{m}_1 i}\| + \|\tilde{\mathbf{x}}_{\mathrm{m}_3 i} - \tilde{\mathbf{x}}_{\mathrm{m}_2 i}\|}{2} \tag{4.56}$$

At last, the shear angle α_i at an instant of time t_i can be established as the difference between the interior angles (cf. Figure 4.5):

$$\alpha_i = \left| \alpha_{\tilde{\mathbf{x}}_{\mathrm{m}_i}} - \alpha_{\mathbf{x}_{\mathrm{m}_i}} \right| \tag{4.57}$$

with

$$\alpha_{\tilde{\mathbf{x}}_{\mathrm{m}_i}} = \arccos\left(\frac{(\tilde{\mathbf{x}}_{\mathrm{m}_1 i} - \tilde{\mathbf{x}}_{\mathrm{m}_2 i}) \cdot (\tilde{\mathbf{x}}_{\mathrm{m}_3 i} - \tilde{\mathbf{x}}_{\mathrm{m}_2 i})}{\|\tilde{\mathbf{x}}_{\mathrm{m}_1 i} - \tilde{\mathbf{x}}_{\mathrm{m}_2 i}\| \cdot \|\tilde{\mathbf{x}}_{\mathrm{m}_3 i} - \tilde{\mathbf{x}}_{\mathrm{m}_2 i}\|} \right) \tag{4.58a}$$

$$\alpha_{\mathbf{x}_{\mathrm{m}_i}} = \arccos\left(\frac{(\mathbf{x}_{\mathrm{m}_1 i} - \mathbf{x}_{\mathrm{m}_2 i}) \cdot (\mathbf{x}_{\mathrm{m}_3 i} - \mathbf{x}_{\mathrm{m}_2 i})}{\|\mathbf{x}_{\mathrm{m}_1 i} - \mathbf{x}_{\mathrm{m}_2 i}\| \cdot \|\mathbf{x}_{\mathrm{m}_3 i} - \mathbf{x}_{\mathrm{m}_2 i}\|} \right) \tag{4.58b}$$

Finally, considering Equation (4.50) the required shear moment $\mathbf{M}_k\left(\theta^1\right)$ and the differential shear angle $\mathrm{d}\alpha_k\left(\theta^1\right)$ within a time span k result in:

$$\mathbf{M}_k\left(\theta^1\right) = N_1\left(\theta^1\right)\mathbf{M}_{i-1} + N_2\left(\theta^1\right)\mathbf{M}_i \tag{4.59}$$

and

$$\mathrm{d}\alpha_k\left(\theta^1\right) = \frac{\partial}{\partial\theta^1}\left(N_1\left(\theta^1\right)\alpha_{i-1} + N_2\left(\theta^1\right)\alpha_i\right)\mathrm{d}\theta^1 \tag{4.60}$$

with

$$\{u_{\mathrm{M}_{13}}, u_{\mathrm{M}_{24}}, f_{\mathrm{K}_{13}}, f_{\mathrm{K}_{24}}\}_i \in \mathbb{V}_{\text{shear}} \quad \text{for} \quad i \in [0,\, n_{\text{exp}}] \tag{4.61}$$

4.1.3 Data fitting

Consider the Bézier surface (4.24) and Bézier curve (4.32) introduced in Section 4.1.1. The goal is now to find that surface or curve such that the test data represented by either a normal-set $\mathbb{U}_{\text{norm}}$ or shear-set $\mathbb{U}_{\text{shear}}$ are approximated in the best way. For stability reasons only the control points $\mathbf{P}_{(\bullet)}$ are defined as design variables, i.e. for a given polynomial degree the shape of the control polygon is of interest. Applying the *concept of least squares* leads to a scalar vector-valued function $O\left(\mathbf{P}_{(\bullet)}\right)$ which minimizes the sum of the error squares between the surface/curve and the corresponding normal-samples (4.37a) or shear-samples (4.37b). Therefore, each normal-sample or shear-sample has to be assigned to a corresponding set of surface parameters (ξ_k, η_k) or curve parameter ξ_k, respectively. Several strategies for this task are given in Piegl and Tiller [92].

Furthermore, it is important to mention that the *stress-free state*[7] has to be preserved by the surface/curve. Therefore, additional so-called *equality constraints* $C_i\left(\mathbf{P}_{(\bullet)}\right)$ regarding the value of the surface/curve and the derivatives of the surface/curve at specific configurations have to be taken into account. Hence, according to the theory of *convex optimization* the following *Lagrangian function* $\mathcal{L}\left(\mathbf{P}_{(\bullet)}, \lambda_i\right)$ representing the constrained optimization problem can be stated as follows:

$$\min_{\mathbf{P}_{(\bullet)},\lambda_i} \rightarrow \mathcal{L}\left(\mathbf{P}_{(\bullet)}, \lambda_i\right) = O\left(\mathbf{P}_{(\bullet)}\right) + \sum_{i=1}^{n_C} \lambda_i \cdot C_i\left(\mathbf{P}_{(\bullet)}\right) \tag{4.62}$$

with C_i being the i-th constraint equation, λ_i being the corresponding i-th Lagrangian multiplier and n_C being the total number of constraint equations. By means of Equation (2.1) the well-known stationary conditions can be established:

$$\nabla_{\mathbf{P}_{(\bullet)}} \mathcal{L}\left(\mathbf{P}_{(\bullet)}, \lambda_i\right) = \mathbf{0} \tag{4.63a}$$

$$\nabla_{\lambda_i} \mathcal{L}\left(\mathbf{P}_{(\bullet)}, \lambda_i\right) = \mathbf{0} \tag{4.63b}$$

REMARK XIII: For further information on the method of least squares for curve/surface approximation and the method of Lagrange multipliers the author refers to Arora [3], Belytschko et al. [11], Gekeler [47], Myers and Montgomery [87], Piegl and Tiller [92].

4.1.3.1 Strain-energy function: $\Psi_{\text{norm}}\left(I_{\|}, I_{\perp}\right)$

Consider the samples (4.37a) belonging to the normal-set $\mathbb{U}_{\text{norm}}$. Due to the chosen experimental set-up (normal campaigns), only data representing the material response under tensile loading are available. In case of an iterative solution strategy[8], the corresponding predictor might point towards a compressive strain state. In order to increase the numerical stability, assumptions for the compressive region have to be made. Within the scope of this thesis the material behavior is assumed to be symmetric. Therefore, the same material response as for the tensile regime is assumed for the compressive regime:

$$\Psi_{\text{norm}}\left(I_{\|}, I_{\perp}\right) = \Psi_{\text{norm}}\left(I_{\|} - 1, I_{\perp} - 1\right) \tag{4.64}$$

---

[7] i.e. for $I_{\|} = 1$, $I_{\perp} = 1$ and $I_{\sharp} = 0$ the specific elastic potential energy Ψ and the 2nd Piola-Kirchhoff stresses $\mathbf{S}$ have to vanish

[8] e.g. Newton-Raphson, Method of steepest descent

Consequently, the normal-samples defined by Equation (4.37a) need to be extended as follows:

$$t_i \longrightarrow \left\{I_{\|}, I_{\perp}, \Psi_{\text{norm}}\right\}_i \in \mathbb{U}_{\text{norm}} \qquad \text{for } i \in [0,\ n_{\text{exp}}] \tag{4.65a}$$

$$t_i \longrightarrow \left\{I_{\|} - 1, I_{\perp} - 1, \Psi_{\text{norm}}\right\}_{n_{exp}+i} \in \mathbb{U}_{\text{sym}} \quad \text{for } i \in [1,\ n_{\text{exp}}] \tag{4.65b}$$

and

$$\tilde{\mathbb{U}}_{\text{norm}} = \mathbb{U}_{\text{norm}} \cup \mathbb{U}_{\text{sym}} \tag{4.66}$$

REMARK XIV: The assumption made in Equation (4.64) evidently contradicts with the underlying physics, i.e. the structural response of textile fabrics under compression. The reason for this is the fact that membrane-like structures in general are only capable of carrying tensile loads. However, the unphysical strain states are feasible during an analysis, since these are purely artificial and will show no influence on the converged solution.

Finally, the constrained optimization problem (4.62) can be stated as follows:

$$O\left(\mathbf{P}_{i,j}\right) = \sum_{k=1}^{\left|\tilde{\mathbb{U}}_{\text{norm}}\right|} \left\| \begin{bmatrix} I_{\|} \\ I_{\perp} \\ \Psi_{\text{norm}} \end{bmatrix}_k - \sum_{i=0}^{p} \sum_{j=0}^{q} B_{i,p}\left(\xi_k\right)\ B_{j,q}\left(\eta_k\right)\ \mathbf{P}_{i,j} \right\| \tag{4.67}$$

such that

$$C_1\left(\mathbf{P}_{i,j}\right) = \sum_{i=0}^{p} \sum_{j=0}^{q} B_{i,p}\left(\xi_{\text{SF}}\right)\ B_{j,q}\left(\eta_{\text{SF}}\right)\ \mathbf{P}_{i,j} = \mathbf{0} \tag{4.68a}$$

$$C_2\left(\mathbf{P}_{i,j}\right) = \sum_{i=0}^{p} \sum_{j=0}^{q} \left.\frac{\partial B_{i,p}\left(\xi\right)}{\partial \xi}\right|_{\xi_{\text{SF}}} B_{j,q}\left(\eta_{\text{SF}}\right)\ \hat{\Psi}_{\text{norm}\ i,j} = 0 \tag{4.68b}$$

$$C_3\left(\mathbf{P}_{i,j}\right) = \sum_{i=0}^{p} \sum_{j=0}^{q} B_{i,p}\left(\xi\right)\ \left.\frac{\partial B_{j,q}\left(\eta_{\text{SF}}\right)}{\partial \eta}\right|_{\eta_{\text{SF}}} \hat{\Psi}_{\text{norm}\ i,j} = 0 \tag{4.68c}$$

with the design variables $\mathbf{P}_{i,j}$ and the stress-free state $(\xi_{\text{SF}}, \eta_{\text{SF}})$:

$$\mathbf{P}_{i,j} = \begin{bmatrix} \hat{I}_{\|} & \hat{I}_{\perp} & \hat{\Psi}_{\text{norm}} \end{bmatrix}_{i,j}^{T} \quad \text{and} \quad \left(\xi_{\text{SF}}, \eta_{\text{SF}}\right) = (0.5, 0.5) \tag{4.69}$$

The stress-free state specified by equation $(4.69)_2$ is the result of the symmetry assumptions defined by Equation (4.65) in combination with the domain of the local parameters (4.18). In case of the undeformed state, Equation (4.68a) enforces that no work will be done. Furthermore, Equation (4.68b) and Equation (4.68c) enforce a horizontal tangential plane at the undeformed state which results in vanishing normal components of the 2^{nd} Piola-Kirchhoff stress tensor.

4.1.3.2 Strain-energy function: $\Psi_{\text{shear}}\left(I_{\sharp}\right)$

Consider the samples (4.37b) belonging to the shear-set $\mathbb{U}_{\text{shear}}$. In case of the shear campaigns, the full range is achieved by just switching the speed ratios[9]. Thus, the constrained optimization problem (4.62) can be stated as follows:

$$O\left(\mathbf{P}_i\right) = \sum_{k=1}^{|\mathbb{U}_{\text{shear}}|} \left\| \begin{bmatrix} I_{\sharp} \\ \Psi_{\text{shear}} \end{bmatrix}_k - \sum_{i=0}^{p} B_{i,p}\left(\xi_k\right)\,\mathbf{P}_i \right\| \tag{4.70}$$

such that

$$C_1\left(\mathbf{P}_i\right) = \sum_{i=0}^{p} B_{i,p}\left(\xi_{\text{SF}}\right)\,\mathbf{P}_i = \mathbf{0} \tag{4.71a}$$

$$C_2\left(\mathbf{P}_i\right) = \sum_{i=0}^{p} \left.\frac{\partial B_{i,p}\left(\xi\right)}{\partial \xi}\right|_{\xi_{\text{SF}}} \hat{\Psi}_{\text{shear}\,i} = 0 \tag{4.71b}$$

with the design variables $\mathbf{P}_i$ and the stress-free state ξ_{SF}:

$$\mathbf{P}_i = \begin{bmatrix} \hat{I}_{\sharp} & \hat{\Psi}_{\text{shear}} \end{bmatrix}_i^T \quad \text{and} \quad \xi_{\text{SF}} = 0 \tag{4.72}$$

The derivation of the specified stress-free state $(4.72)_2$ is quite trivial since it simply represents the starting point of the material response curve. In case of the undeformed state, Equation (4.71a) enforces that no work will be done. Furthermore, Equation (4.71b) enforces a horizontal tangent at the undeformed state which again results in a vanishing shear component of the 2nd Piola-Kirchhoff stress tensor.

4.2 Test campaign

The presented test campaign (i.e. the experiments and the subsequent material modeling) was part of the DFG founded project: *Experimentelle Analyse und numerische Modellierung der Deformation dehnfähiger Textilien und deren Wechselwirkung auf Tragkörper* [73]. Within the course of this project 3 different types of textile fabrics (sample I - III) were characterized by means of velocity-driven biaxial tension tests. The chosen materials are listed in Table 4.1. The experiments were carried out by the research group of Prof. Dr.-Ing. habil. S. Krzywinski[10]. These data were then used as a basis for the material model (Section 4.1.1) and processing workflow (Section 4.1.2 - 4.1.3) developed within the scope of this thesis. It is important to note that the chosen Bézier surfaces and curves act as filter smoothing the test data containing errors and noise due to the experimental setup.

---

[9] e.g. exchanging 10 : 1 with 1 : 10, see Table 4.2

[10] Institute of Textile Machinery and High Performance Material Technology (ITM) at the Dresden University of Technology

material	fabric type	Section
sample I	interlock jersey	4.2.1
sample II	twill weave	4.2.2
sample III	reinforced (stitch course) interlock jersey	4.2.3

Table 4.1: Test matrix: Materials

	speed ratio $\left[{}^{\mathrm{mm}}/_{\mathrm{min}}\right]$	
campaign	$M_1 - M_3$	$M_2 - M_4$
1	10	1
2	10	2.5
3	10	5
4	10	7.5
5	10	10
6	7.5	10
7	5	10
8	2.5	10
9	1	10

Table 4.2: Test matrix: Campaigns' speed ratios $\left[{}^{\mathrm{mm}}/_{\mathrm{min}}\right]$

Each textile fabric (sample I - III) has been tested under 9 different speed ratios between the $M_1 - M_3$ and $M_2 - M_4$ axis, see Figure 4.3. Furthermore 2 different fiber orientations namely the warp/weft direction aligned with the $M_1 - M_3$ and $M_2 - M_4$ axis and the warp/weft direction under 45° were applied. Hence, the raw data for each material consists of 9 normal-campaigns $\mathbb{V}^1_{\mathrm{norm}} \dots \mathbb{V}^9_{\mathrm{norm}}$ and 9 shear-campaigns $\mathbb{V}^1_{\mathrm{shear}} \dots \mathbb{V}^9_{\mathrm{shear}}$. The chosen speed ratios are listed in Table 4.2.

The gathered experimental data were processed as explained in Section 4.1.2 and led to the corresponding normal-sets $\tilde{\mathbb{U}}_{\mathrm{norm}}$ and shear-sets $\mathbb{U}_{\mathrm{shear}}$ for each textile fabric (sample I - III). Finally, the data fitting strategy introduced in Section 4.1.3 was applied. For each textile fabric (sample I - III), the chosen polynomial degrees of the corresponding material response surface/curve are listed in Table 4.3.

In the following Sections 4.2.1 - 4.2.3 the established material response surfaces and curves for each textile fabric (sample I - III) are presented, see Figure 4.7, Figure 4.10 and Figure 4.13, respectively. Additionally, the underlying normal-sets $\tilde{\mathbb{U}}_{\mathrm{norm}}$ and shear-sets $\mathbb{U}_{\mathrm{shear}}$ are shown in Figure 4.6, Figure 4.9 and Figure 4.12. Figure 4.8, Figure 4.11 and Figure 4.14 show a comparison between the normal-sets $\tilde{\mathbb{U}}_{\mathrm{norm}}$ and shear-sets $\mathbb{U}_{\mathrm{shear}}$ and the corresponding material response surfaces (sample I - III).

Material	Response surface p-th degree	 q-th degree	Response Curve p-th degree
sample I	2	2	6
sample II	2	2	4
sample III	2	2	4

Table 4.3: Test matrix: Polynomial degrees for surface/curve fitting

REMARK I: The set of polynomial degrees for each material response surface (p, q) and curve (p) has been determined in an empirical way. In more detail, a parameter study varying the polynomial degrees has been carried for each material response surface and curve.

REMARK II: For further information on the experimental set-up and the test data the author refers to WENDT AND KRZYWINSKI [109], [110].

4.2.1 Material: interlock jersey

The description of the tested material, the experimental procedures (fiber orientations and speed ratios) and the chosen polynomial degrees can be found on page 77ff.

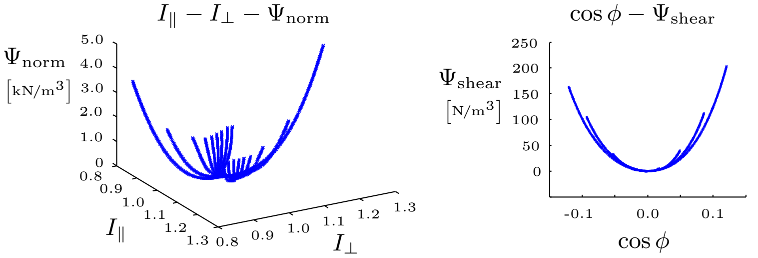

Figure 4.6: Sample I: normal-set $\tilde{\mathbb{U}}_{\text{norm}}$ vs. shear-set $\mathbb{U}_{\text{shear}}$

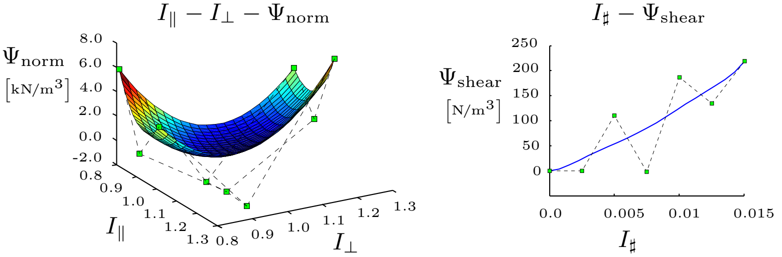

Figure 4.7: Sample I: Bézier surface and curve with control points

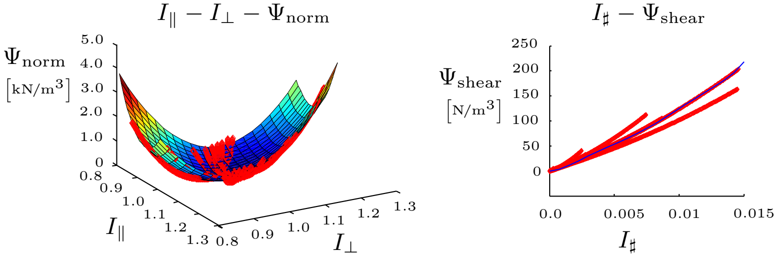

Figure 4.8: Sample I: Accordance of the established Bézier surface and curve to the processed sample points (red squares)

4.2.2 Material: twill weave

The description of the tested material, the experimental procedures (fiber orientations and speed ratios) and the chosen polynomial degrees can be found on page 77ff.

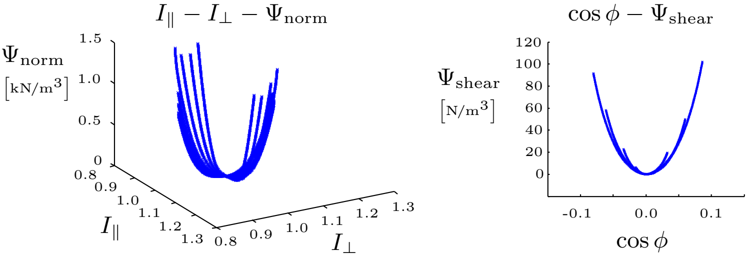

Figure 4.9: Sample II: normal-set $\tilde{\mathbb{U}}_{\text{norm}}$ vs. shear-set $\mathbb{U}_{\text{shear}}$

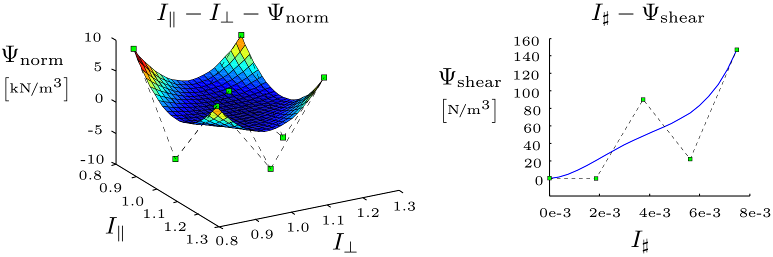

Figure 4.10: Sample II: Bézier surface and curve with control points

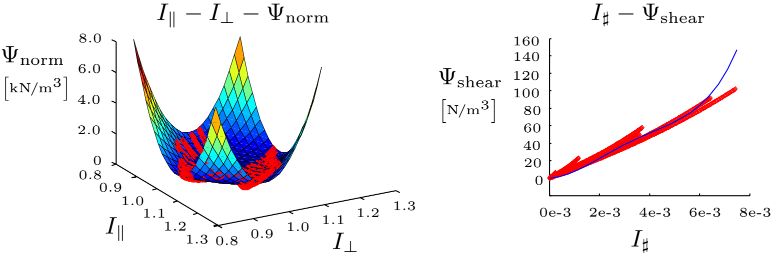

Figure 4.11: Sample II: Accordance of the established Bézier surface and curve to the processed sample points (red squares)

4.2.3 Material: reinforced (stitch course) interlock jersey

The description of the tested material, the experimental procedures (fiber orientations and speed ratios) and the chosen polynomial degrees can be found on page 77ff.

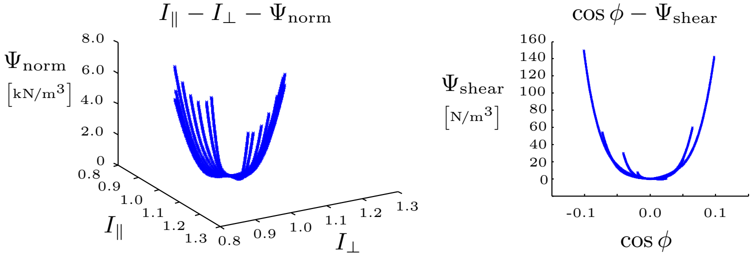

Figure 4.12: Sample III: normal-set $\tilde{\mathbb{U}}_{\text{norm}}$ vs. shear-set $\mathbb{U}_{\text{shear}}$

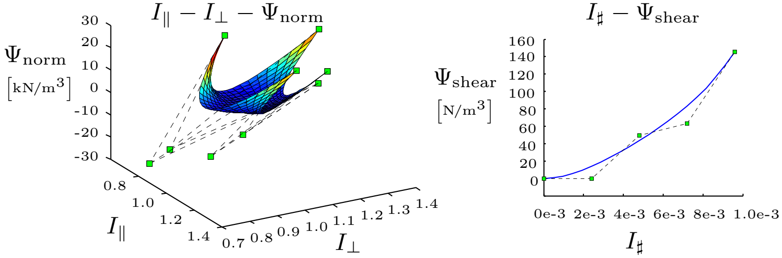

Figure 4.13: Sample III: Bézier surface and curve with control points

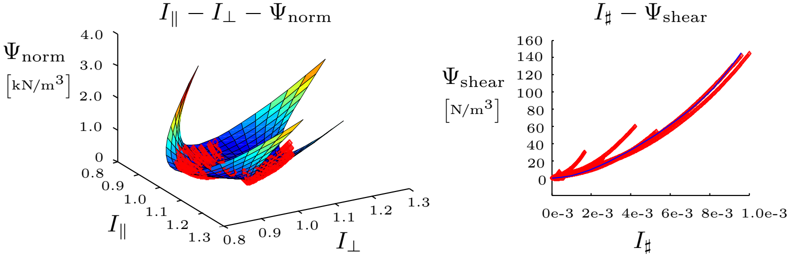

Figure 4.14: Sample III: Accordance of the established Bézier surface and curve to the processed sample points (red squares)

5

The Variation of Reference Strategy

"Sein Blick ist vom Vorübergehn der Stäbe so müd
geworden, dass er nichts mehr hält. Ihm ist, als ob es tausend
Stäbe gäbe und hinter tausend Stäben keine Welt."

— Rainer Maria Rilke, 1875 - 1926
Bohemian-Austrian poet and novelist

Each design engineer working in the field of lightweight design has to deal with this well-known issue: "How should the cutting pattern of the textile fabric be such that the final draped shape has minimal deviation from the desired product?" This chapter will show a novel approach for generating optimized cutting patterns taking into account the underlying material properties. The so-called *Variation of Reference Strategy* (VaReS) is based on a variational energy principle in combination with nonlinear kinematics from a Lagrangian perspective. But in contrast to a *Total Lagrangian Formulation*, the global positions of the nodes in the undeformed configuration are the design variables for the unconstrained optimization problem. This chapter presents two different strategies for solving the described unconstrained optimization problem, namely a second-order (Newton-Raphson) and a first-order (steepest descent) numerical scheme. Additionally, several numerical experiments are presented showing the power, robustness and stability of the developed *Variation of Reference Strategy.*

5.1 The concept behind: Varying reference

As already described in Section 1.1, modern lightweight designs are characterized due to a close interplay of complex surfaces[1] and high performance materials[2]. Keeping in mind that the wrought material is delivered in a plane fashion, one of the major challenges is to find that plane cutting pattern (i.e. $\kappa = 0$, see page 28) of such a non-developable (i.e. $\kappa \neq 0$, see page 28) surface which possesses the best compromise of all its design criteria[3], see Figure 5.1. In order to end up with an innovative numerical method for the generation of optimized cutting patterns especially the nonlinear and complex structural response of the chosen material has to be incorporated in the underlying mathematical model. Considering the *least squares optimization* approach and *minimization of stress difference energy* method published by LINHARD [74] and LINHARD ET AL. [75] [76], these numerical approaches work well for isotropic materials within the linear and moderately nonlinear regime. But they show severe deficiencies when it comes to anisotropic and/or highly nonlinear material models. The reasons for these deficiencies are the following: On the one hand, the chosen linearization of the *Euler-Almansi* strain measure within the least-squares approach. And on the other hand the chosen test function for the Galerkin approach within the stress difference energy method. Both lead to a violation of the *frame-indifference requirement* in nonlinear continuum mechanics. As a consequence, severe convergence problems may occur, if an anisotropic and/or highly nonlinear material model is applied.

It is obvious that the shape of the cutting pattern has a great influence on the draping process, i.e. on the residual stress field and in case of anisotropic materials on the final fiber orientation. In the following, a novel approach for generating optimized cutting patterns will be introduced. The so-called *Variation of Reference Strategy* (VaReS) circumvents the described drawbacks when it comes to nonlinearities induced by the constitutive relation. In more detail, VaReS can be seen as a reinterpretation of the *stress compensation method* published by MAURIN AND MOTRO [83]. The key idea of their approach was the minimization of the differences between the resulting residual stresses and a predefined stress state. But instead of directly working with stress states, VaReS is based on the elastic potential energies arising due to the mentioned stresses. Hence, the key idea of VaRes is the following:

Find the cutting pattern such that the total (elastic) potential energy of the final draped textile fabric is minimized.

In terms of mechanics, this approach leads to a shift of unknowns. Instead of computing the unknown displacements of a known (unloaded) structure exposed to a set of external loads, the unloaded structure itself is not known

---

[1] i.e. synclastic or anticlastic shapes, see Figure 2.3

[2] e.g. high-strength alloys, plastic films or textile fabrics (either non-crimp, knitted, woven or braided)

[3] e.g. predefined stress state, fiber orientation, etc. within the target structure

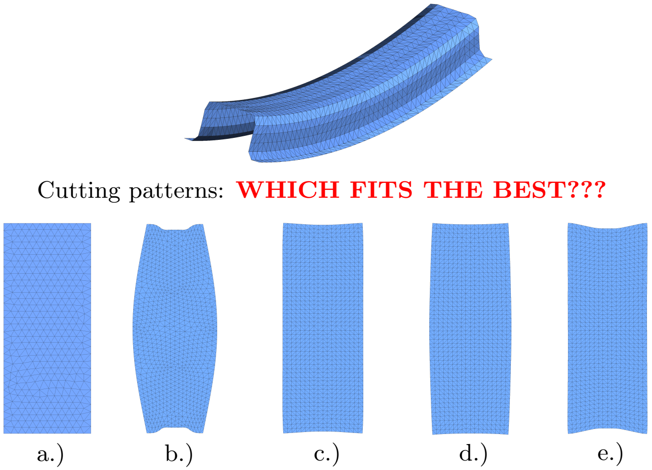

Figure 5.1: No unique (analytical) solution: a.) rectangular, b.) projected, c.) - e.) optimized (stress criteria)

but its deformed shape. Thus, instead of computing the unknown spatial configuration of a continuous body $\mathcal{B}$ for a given set of boundary conditions its material configuration is of interest. This so-called *concept of inverse mechanics* is exemplary applied to a simple cantilever beam pointing out the major differences compared to the well-known *standard mechanics*, see Figure 5.2.

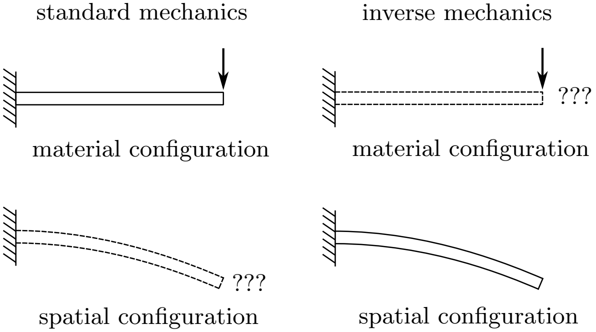

Figure 5.2: Standard mechanics (left) vs. inverse mechanics (right) - unknown (dashed) vs. known (solid) configuration

REMARK I: For further information on the *concept of objectivity* the author refers to Holzapfel [60].

REMARK II: For the remainder of this thesis only thin membrane-like structures, i.e. surfaces and trusses, are under investigation.

5.1.1 The (shape-) optimization problem

Consider a parameterized surface $\mathcal{S}$ embedded in an Euclidean space $\mathbb{R}^3$ representing the mid-plane of a continuous body $\mathcal{B}$ (i.e. $\theta^3 = 0$). According to Equation (3.16b), each point $P \in \mathcal{S}$ is described by its spatial position vector $\mathbf{x}$. The geometrical region occupied by all points $P \in \mathcal{S}$ within the spatial configuration is called Ω. Since the shape of Ω represents the final draped (non-developable) structure, it is held fixed in space:

$$\forall\, \mathbf{x} = \mathbf{r}\left(\theta^1, \theta^2, \theta^3 = 0\right) \in \Omega \;:\; \kappa \neq 0 \;\veebar\; \kappa = 0 \tag{5.1}$$

Consequently, for each $P \in \mathcal{S}$ a unique material position vector $\mathbf{X}$ can be defined as well (3.16a). The geometrical region occupied by all points $P \in \mathcal{S}$ within the material configuration is called Ω_0 representing the unknown plane cutting pattern:

$$\forall\, \mathbf{X} = \mathbf{R}\left(\theta^1, \theta^2, \theta^3 = 0\right) \in \Omega_0 \;:\; \mathrm{K}_1 = \mathrm{K}_2 = 0 \tag{5.2}$$

Due to the non-developable characteristics of $\mathcal{S}$ within its fixed spatial configuration, every motion $\chi(\mathbf{X}, t)$ will result in a residual stress field being non-zero. As already mentioned in the introduction of this section (see Figure 5.1), the residual stress field strongly depends on the chosen set of material position vectors $\mathbf{X} \in \Omega_0$ (i.e. the distribution of all points $P \in \mathcal{S}$ within Ω_0). Speaking in terms of energies, the total potential energy $\Pi_\chi(\mathbf{X})$ at each point $P \in \mathcal{S}$ generated by the motion $\chi(\mathbf{X}, t)$ is exclusively depending on its material position $\mathbf{X} \in \Omega_0$. Hence, the aim is now to find that set of material position vectors $\mathbf{X} \in \Omega_0$ such that the total potential energy $\Pi_\chi(\mathbf{X})$ is minimized:

$$\min_{\mathbf{X} \in \Omega_0} \rightarrow \Pi_{\text{total}}(\mathbf{X}) = \Pi_\chi(\mathbf{X}) - \Pi_{\text{pre}} \tag{5.3}$$

with Π_{pre} being the total elastic potential energy arising due to a predefined stress state[4]. It is important to note that the material position vectors $\mathbf{X} \in \Omega_0$ of all $P \in \mathcal{S}$ are the *design variables* of the stated optimization problem.

REMARK III: Compared to the principle of *Minimum Total Potential Energy*, Equation (5.3) describes exactly the inverse problem. Instead of seeking for the unknown spatial configuration of a given material configuration, the unknown material configuration for a given spatial configuration is now of interest.

REMARK IV: In case of a tensile structure, the stress state within the membrane is directly linked to its spatial shape. Thus, the predefined stress state is a powerful set-screw for each design engineer.

---

[4] defined by the design engineer

5.1.2 The variational principle

Consider the unconstrained optimization problem stated in Equation (5.3). Within the scope of this section, the natural variational principle introduced in Section 2.1.3 is applied to Equation (5.3) leading to its stationary point, i.e. $\delta\Pi_{\mathrm{total}} = 0$. This approach is similar to the principle of *Minimum Total Potential Energy* introduced in Section 3.4.2. But instead of considering a virtual displacement field $\delta\mathbf{u}(t)$, a field of *virtual material position vectors* $\delta\mathbf{X} = \delta\mathbf{X}(t=0)$ is introduced (cf. Figure 5.3).

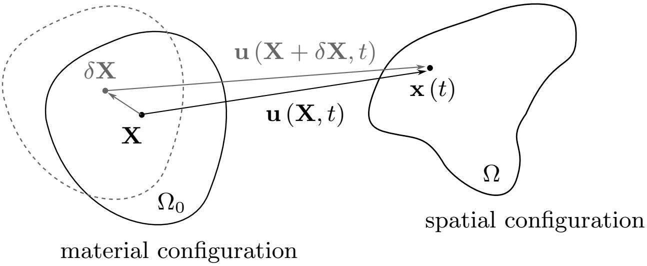

Figure 5.3: Variation of reference: virtual material position $\delta\mathbf{X}$

According to the laws of variational calculus, the minimum of a functional is located in its stationary point. Hence, the 1st Variation of Equation (5.3) has to vanish:

$$\delta\Pi_{\mathrm{total}}(\mathbf{X}) = D_{\delta\mathbf{X}}\Pi_{\mathrm{total}}(\mathbf{X}) = \frac{\mathrm{d}}{\mathrm{d}\epsilon}\left[\Pi_{\mathrm{total}}(\mathbf{X}+\epsilon\delta\mathbf{X})\right]\Big|_{\epsilon=0} \overset{!}{=} 0 \qquad (5.4)$$

Assuming hyperelastic material behavior, the total elastic potential energy can be expressed in terms of a material dependent strain-energy function. In contrast to Equation (3.54), the strain-energy function can be alternatively expressed in terms of the Green-Lagrange strain tensor $\mathbf{E}$ (see HOLZAPFEL [60]):

$$\Pi_{\mathrm{total}}(\mathbf{X}) = \int\limits_{\Omega_0} \Psi\big(\mathbf{E}(\mathbf{X})\big)\,\mathrm{d}\Omega_0 - \int\limits_{\Omega_0} \Psi(\mathbf{E}_{\mathrm{pre}})\,\mathrm{d}\Omega_0 \qquad (5.5)$$

with $\mathbf{E}(\mathbf{X}) = \mathbf{E}\big(\mathbf{C}(\mathbf{X})\big)$ being the Green-Lagrange strains arising due to the motion $\chi(\mathbf{X},t)$ and $\mathbf{E}_{\mathrm{pre}} = \mathbf{E}(\mathbf{C}_{\mathrm{pre}})$ being a physically meaningful Green-Lagrange strain tensor effectuating the desired stress state. Finally, inserting Equation (5.5) into (5.4) and applying the chain rule leads to the *governing equation of VaReS*:

$$\begin{aligned}\delta\Pi_{\mathrm{total}}(\mathbf{X}) = &\int\limits_{\Omega_0}\Big[\mathbf{S}\big(\mathbf{E}(\mathbf{X})\big) - \mathbf{S}(\mathbf{E}_{\mathrm{pre}})\Big] : \delta\mathbf{E}(\mathbf{X})\,\mathrm{d}\Omega_0 \\ &+ \int\limits_{\Omega_0}\Big[\Psi\big(\mathbf{E}(\mathbf{X})\big) - \Psi(\mathbf{E}_{\mathrm{pre}})\Big]\,\delta\,\mathrm{d}\Omega_0 \overset{!}{=} 0\end{aligned} \qquad (5.6)$$

with the 1st Variation of the Green-Lagrange strain tensor $\delta\mathbf{E}\left(\mathbf{X}\right)$

$$\delta\mathbf{E}\left(\mathbf{X}\right) = D_{\delta\mathbf{X}}\mathbf{E}\left(\mathbf{X}\right) = \frac{\mathrm{d}}{\mathrm{d}\epsilon}\left[\mathbf{E}\left(\mathbf{X}+\epsilon\delta\mathbf{X}\right)\right]\Big|_{\epsilon=0} \tag{5.7}$$

the strain-energy functions $\delta\Psi\big(\mathbf{E}\left(\mathbf{X}\right)\big)$ and $\delta\Psi\left(\mathbf{E}_{\mathrm{pre}}\right)$

$$\delta\Psi\big(\mathbf{E}\left(\mathbf{X}\right)\big) = \mathbf{S}\big(\mathbf{E}\left(\mathbf{X}\right)\big) : \delta\mathbf{E}\left(\mathbf{X}\right) \tag{5.8a}$$

$$\delta\Psi\left(\mathbf{E}_{\mathrm{pre}}\right) = \mathbf{S}\left(\mathbf{E}_{\mathrm{pre}}\right) : \delta\mathbf{E}\left(\mathbf{X}\right) \tag{5.8b}$$

and the differential domain $\delta\,\mathrm{d}\Omega_0$

$$\delta\,\mathrm{d}\Omega_0 = D_{\delta\mathbf{X}}\,\mathrm{d}\Omega_0\left(\mathbf{X}\right) = \frac{\mathrm{d}}{\mathrm{d}\epsilon}\left[\mathrm{d}\Omega_0\left(\mathbf{X}+\epsilon\delta\mathbf{X}\right)\right]\Big|_{\epsilon=0} \tag{5.9}$$

REMARK V: Equation (5.6) explicitly shows the major difference of VaReS compared to LINHARD's *minimization of stress difference method.* In the later, all stresses and strains are defined w.r.t. the spatial configuration, i.e. Cauchy stresses and Euler-Almansi strains are used. In case of a nonlinear material model, the Lie-time derivative (3.36) of the Euler-Almansi strain tensor may become quite cumbersome. The reason therefore is the choice of an adequate *stress rate*[5]. VaReS elegantly circumvents this problem by formulating the governing equations w.r.t. the material configuration, i.e. in terms of Green-Lagrange strains and 2nd Piola-Kirchhoff stresses.

5.1.3 Solution strategies

The nonlinear characteristics of the *governing equation of VaReS* (5.6) requires an iterative solution strategy. In the following sections, two different numerical approaches are introduced taking into account either the curvature (second-order approach - Section 5.1.3.1) or the gradient (first-order approach - Section 5.1.3.2) of the underlying unconstrained optimization problem (5.3).

5.1.3.1 Second-order approach: Linearization of the variational principle

The first solution strategy is based on a consistent linearization of the variational principle, introduced in Section 2.2.1. Applying a truncated Taylor-Series (2.19) to the *governing equation of VaReS* (5.6) leads to the *linearized governing equation of VaReS*:

$$\delta\Pi_{\mathrm{total}}\left(\mathbf{X}^{i+1}\right) = \delta\Pi_{\mathrm{total}}\left(\mathbf{X}^{i}\right) + \Delta\delta\Pi_{\mathrm{total}}\left(\mathbf{X}^{i},\Delta\mathbf{X}\right) + \mathcal{O}\left(\Delta\mathbf{X}^{2}\right) \tag{5.10}$$

---

[5] e.g. BADEL ET AL. [5], BELYTSCHKO [11], HOLZAPFEL [60], OGDEN [88]

with $\Delta\delta\Pi_{\text{total}}\left(\mathbf{X}^i, \Delta\mathbf{X}\right)$ being the Gâteaux derivatives in the direction of the design variables (2.17):

$$\begin{aligned}\Delta\delta\Pi_{\text{total}}\left(\mathbf{X}^i, \Delta\mathbf{X}\right) &= D_{\Delta\mathbf{X}}\,\delta\Pi_{\text{total}}\left(\mathbf{X}^i\right) \\ &= \frac{\mathrm{d}}{\mathrm{d}\epsilon}\left[\delta\Pi_{\text{total}}\left(\mathbf{X}^i + \epsilon\Delta\mathbf{X}\right)\right]\Bigg|_{\epsilon=0}\end{aligned} \tag{5.11}$$

with

$$\Delta\mathbf{X} = \mathbf{X}^{i+1} - \mathbf{X}^i \tag{5.12}$$

Considering the fact that Equation (5.6) stems from a hyperelastic potential, the linearization of the 2^{nd} Piola-Kirchhoff stress tensor (3.64) can be expressed in terms of the elasticity tensor and the linearized Green-Lagrange strain tensor:

$$\Delta\mathbf{S}\left(\mathbf{E}\left(\mathbf{X}\right)\right) = D_{\Delta\mathbf{X}}\mathbf{S}\left(\mathbf{E}\left(\mathbf{X}\right)\right) = \mathbb{D}\left(\mathbf{E}\left(\mathbf{X}\right)\right) : \Delta\mathbf{E}\left(\mathbf{X}\right) \tag{5.13}$$

with the linearization of the Green-Lagrange strain tensor $\Delta\mathbf{E}\left(\mathbf{X}\right)$

$$\Delta\mathbf{E}\left(\mathbf{X}\right) = D_{\Delta\mathbf{X}}\mathbf{E}\left(\mathbf{X}\right) = \frac{\mathrm{d}}{\mathrm{d}\epsilon}\left[\mathbf{E}\left(\mathbf{X} + \epsilon\Delta\mathbf{X}\right)\right]\Big|_{\epsilon=0} \tag{5.14}$$

Finally, the *linearized governing equation of VaReS* can be stated as follows:

$$\begin{aligned}\Delta\delta\Pi_{\text{total}}\left(\mathbf{X}, \Delta\mathbf{X}\right) = &\int_{\Omega_0}\left[\mathbf{S}\left(\mathbf{E}\left(\mathbf{X}\right)\right) - \mathbf{S}\left(\mathbf{E}_{\text{pre}}\right)\right] : \Delta\delta\mathbf{E}\left(\mathbf{X}\right)\,\mathrm{d}\Omega_0 \\ &+ \int_{\Omega_0}\left[\mathbb{D}\left(\mathbf{E}\left(\mathbf{X}\right)\right) - \mathbb{D}\left(\mathbf{E}_{\text{pre}}\right)\right] : \Delta\mathbf{E}\left(\mathbf{X}\right) : \delta\mathbf{E}\left(\mathbf{X}\right)\,\mathrm{d}\Omega_0 \\ &+ \int_{\Omega_0}\left[\mathbf{S}\left(\mathbf{E}\left(\mathbf{X}\right)\right) - \mathbf{S}\left(\mathbf{E}_{\text{pre}}\right)\right] : \Delta\delta\mathbf{E}\left(\mathbf{X}\right)\,\mathrm{d}\Omega_0 \\ &+ \int_{\Omega_0}\left[\mathbf{S}\left(\mathbf{E}\left(\mathbf{X}\right)\right) - \mathbf{S}\left(\mathbf{E}_{\text{pre}}\right)\right] : \delta\mathbf{E}\left(\mathbf{X}\right)\,\Delta\,\mathrm{d}\Omega_0 \\ &+ \int_{\Omega_0}\left[\mathbf{S}\left(\mathbf{E}\left(\mathbf{X}\right)\right) - \mathbf{S}\left(\mathbf{E}_{\text{pre}}\right)\right] : \Delta\mathbf{E}\left(\mathbf{X}\right)\,\delta\,\mathrm{d}\Omega_0 \\ &+ \int_{\Omega_0}\left[\Psi\left(\mathbf{E}\left(\mathbf{X}\right)\right) - \Psi\left(\mathbf{E}_{\text{pre}}\right)\right]\,\Delta\delta\,\mathrm{d}\Omega_0\end{aligned} \tag{5.15}$$

REMARK VI: More detailed information on the *linearized governing equation of VaReS* is given Section 5.2.3.

5.1.3.2 First-order approach: The method of steepest descent

An alternative solution strategy is based on the method of steepest descent, introduced in Section 2.2.2. Hence, applying Equation (2.24) and (2.25) to the objective function stated by Equation (5.3) leads to the update of the material position vector $\mathbf{X}^{i+1} \in \Omega_0$:

$$\mathbf{X}^{i+1} = \mathbf{X}^{i} - \alpha^{i} \cdot \nabla_{\mathbf{X}} \Pi_{\text{total}} \left(\mathbf{X}^{i} \right) \tag{5.16}$$

Assuming a hyperelastic material behavior, the total potential energy can be expressed in terms of a strain-energy function (5.5). Hence, by means of the chain rule the gradient of the total elastic potential (search direction $\mathbf{s}^{i}$) can then be expressed in terms of strains and stresses:

$$\begin{aligned} \nabla_{\mathbf{X}} \Pi_{\text{total}} \left(\mathbf{X}^{i} \right) = & \int_{\Omega_0} \left[\mathbf{S} \left(\mathbf{E} \left(\mathbf{X}^{i} \right) \right) - \mathbf{S} \left(\mathbf{E}_{\text{pre}} \right) \right] : \nabla_{\mathbf{X}} \mathbf{E} \left(\mathbf{X}^{i} \right) \, \mathrm{d}\Omega_0^{i} \\ & + \int_{\Omega_0} \left[\Psi \left(\mathbf{E} \left(\mathbf{X}^{i} \right) \right) - \Psi \left(\mathbf{E}_{\text{pre}} \right) \right] \nabla_{\mathbf{X}} \, \mathrm{d}\Omega_0^{i} \end{aligned} \tag{5.17}$$

with

$$\nabla_{\mathbf{X}} \Psi \left(\mathbf{E} \left(\mathbf{X} \right) \right) = \mathbf{S} \left(\mathbf{E} \left(\mathbf{X} \right) \right) : \nabla_{\mathbf{X}} \mathbf{E} \left(\mathbf{X} \right) \tag{5.18a}$$

$$\nabla_{\mathbf{X}} \Psi \left(\mathbf{E}_{\text{pre}} \right) = \mathbf{S} \left(\mathbf{E}_{\text{pre}} \right) : \nabla_{\mathbf{X}} \mathbf{E} \left(\mathbf{X} \right) \tag{5.18b}$$

and $\nabla_{\mathbf{X}} \mathbf{E} \left(\mathbf{X} \right)$ and $\nabla_{\mathbf{X}} \, \mathrm{d}\Omega_0$ being the gradients of the Green-Lagrange strains and the differential material domain, respectively.

5.2 Finite element formulation: 3 parameter membrane

Since there exists no closed form solution for the stated nonlinear optimization problem, a numerical approximation procedure has to be applied. This section presents a finite element based strategy for solving the governing equation of VaReS (5.6) (second-order scheme) as well as for establishing the gradient of the objective function (5.17) (first-order scheme). Therefore, a nonlinear finite element is presented in the following. Prior to that, the following assumptions have to be introduced:

All structures of investigation are considered as thin, see Figure 2.1, i.e. their geometrical description and kinematics can be reduced to the element's mid-surface Ω_0 assuming a constant thickness l_3 over the element (degenerated solid - see Section 3.1.1). According to BISCHOFF ET AL. [14], the Green-Lagrange strain tensor $\mathbf{E}$ (3.44) can be reduced to the element's mid-surface ($\theta^3 = 0$) by means of the curvature tensor $\mathbf{K}$ (2.39) in combination with the sets of material and spatial base vectors defined in Equation (3.17) and (3.18):

$$\begin{aligned}\mathbf{E} &= \bar{\mathbf{E}} + \theta^3\mathbf{K} + 2\tilde{\mathbf{E}} \\ &= E_{kl}\,\mathbf{A}^k \otimes \mathbf{A}^l + \theta^3 \mathrm{K}_{kl}\,\mathbf{A}^k \otimes \mathbf{A}^l + 2E_{k3}\,\mathbf{A}^k \otimes \mathbf{A}^3\end{aligned} \tag{5.19}$$

with $k, l = 1 \ldots 2$. The normal strain in thickness direction is assumed to be zero, i.e. $E_{33} = 0$.

A nonlinear 3-parameter formulation (see page 36f) is chosen for describing the geometry and the kinematics of the element's mid-surface. Thus, depending on the underlying strain-energy function, an additional treatment of the inextensible spatial director may be required (see plane stress conditions - chapter 3.3.3). Finally, only the so-called *membrane actions* will be considered. This leads to the following simplifications:

- → Only the normal and shear strains arising due to in-plane deformations are considered within the energy balance, i.e. the bending contributions are neglected: $\theta^3\mathbf{K} = \mathbf{0}$.
- → The cross-sections stay plane and perpendicular to the mid-surface, i.e. all out-of-plane shear contributions are neglected: $2\tilde{\mathbf{E}} = \mathbf{0}$.
- → The in-plane stress resultants are assumed to be constantly distributed over the thickness l_3. Therefore, the corresponding integrals can be reduced to the mid-surface: $\Omega_0\left(\theta^3 = 0\right) = \Omega_0^{\mathcal{S}} \cdot l_3$.

Incorporating the first two simplifications into Equation (5.19), the Green-Lagrange strain tensor $\mathbf{E}\left(\mathbf{X}\right)$ can be reformulated in terms of the covariant (3.2) and contra-variant (3.5) base vectors as follows:

$$\mathbf{E}\left(\mathbf{X}\right) = \frac{1}{2}\left(g_{kl} - G_{kl}\right)\,\mathbf{G}^k \otimes \mathbf{G}^l \quad \text{for} \quad k, l = 1 \ldots 3 \tag{5.20}$$

whereat the covariant in-plane ($i = 1 \ldots 2$) material (5.21a) and spatial (5.21b) base vectors are reduced to the mid-surface:

$$\mathbf{G}_i = \frac{\partial \mathbf{R}\left(\theta^1, \theta^2, \theta^3 = 0\right)}{\partial \theta^i} = \frac{\partial \mathbf{R}^{\text{mid}}\left(\theta^1, \theta^2\right)}{\partial \theta^i} = \mathbf{A}_i \tag{5.21a}$$

$$\mathbf{g}_i = \frac{\partial \mathbf{r}\left(\theta^1, \theta^2, \theta^3 = 0\right)}{\partial \theta^i} = \frac{\partial \mathbf{r}^{\text{mid}}\left(\theta^1, \theta^2\right)}{\partial \theta^i} = \mathbf{a}_i \tag{5.21b}$$

and the covariant out-of-plane material and spatial base vectors are equivalent to the material (3.4) and spatial (3.19) directors:

$$\mathbf{G}_3 = \mathbf{D}\left(\theta^1, \theta^2\right) = \mathbf{A}_3 \quad \text{and} \quad \mathbf{g}_3 = \mathbf{d}\left(\theta^1, \theta^2\right) = \mathbf{a}_3 \tag{5.22}$$

Finally, incorporating the third simplification and the plane stress requirement into both the governing equation of VaReS (5.6) as well as into the gradient of the objective function (5.17), leads to the so-called *residual force equation* of the developed membrane element (second-order approach):

$$\begin{aligned}\delta\Pi_{total}\left(\mathbf{X}\right) &= l_3 \int\limits_{\Omega_0^{\mathcal{S}}} \left(\mathbf{S}_\chi - \mathbf{S}_{\text{pre}}\right) : \delta\mathbf{E}\left(\mathbf{X}\right)\,\mathrm{d}\Omega_0^{\mathcal{S}} \\ &+ l_3 \int\limits_{\Omega_0^{\mathcal{S}}} \left(\Psi_\chi - \Psi_{\text{pre}}\right)\,\delta\,\mathrm{d}\Omega_0^{\mathcal{S}} \overset{!}{=} 0\end{aligned} \tag{5.23}$$

as well as to the search direction (first-order approach):

$$\begin{aligned}\nabla_{\mathbf{X}}\Pi_{total}\left(\mathbf{X}\right) &= l_3 \int\limits_{\Omega_0^{\mathcal{S}}} \left(\mathbf{S}_\chi - \mathbf{S}_{\text{pre}}\right) : \nabla_{\mathbf{X}}\mathbf{E}\left(\mathbf{X}\right)\,\mathrm{d}\Omega_0^{\mathcal{S}} \\ &+ l_3 \int\limits_{\Omega_0^{\mathcal{S}}} \left(\Psi_\chi - \Psi_{\text{pre}}\right)\,\nabla_{\mathbf{X}}\,\mathrm{d}\Omega_0^{\mathcal{S}}\end{aligned} \tag{5.24}$$

For the sake of clarity the indexes $(\bullet)_\chi$ and $(\bullet)_{\text{pre}}$ are introduced: $\mathbf{S}_\chi = \mathbf{S}_{\text{ps}}\big(\mathbf{E}\left(\mathbf{X}\right)\big)$, $\Psi_\chi = \Psi_{\text{ps}}\big(\mathbf{E}\left(\mathbf{X}\right)\big)$, $\mathbf{S}_{\text{pre}} = \mathbf{S}_{\text{ps}}\left(\mathbf{E}_{\text{pre}}\right)$ and $\Psi_{\text{pre}} = \Psi_{\text{ps}}\left(\mathbf{E}_{\text{pre}}\right)$. The subscript $(\bullet)_{\text{ps}}$ and $(\bullet)_{\text{pre}}$ indicates the enforced plane stress conditions and the predefined state, respectively.

REMARK I: Due to the 3-parameter formulation, the requirements made on the out-of-plane normal and shear strains are automatically full-filled (i.e. $E_{13} = E_{23} = E_{31} = E_{32} = E_{33} = 0$).

REMARK II: It is important to note that the out-of-plane base vectors are not required for computing the 1^{st} Variation of the total potential energy (5.23), but they have to be taken into account for establishing realistic stress and elasticity tensors as well as for computing the 1^{st} Variation of the strain tensor $\delta\mathbf{E}$.

REMARK III: The introduced *membrane theory* may be extended to the so-called *Kirchhoff-Love theory* by simply adding the bending contribution to the membrane contribution. Furthermore, if both the bending and shear contributions are added, the membrane may be extended to a *Reissner-Mindlin shell.*

5.2.1 3 parameter formulation: isoparametric concept

Consider an arbitrary point $P \in \mathcal{S}$ located on the mid-surface ($\theta^3 = 0$) of a thin continuous body $\mathcal{B}$ (cf. Figure 3.1). In order to describe the motion $\chi\left(\mathbf{X}, t\right)$ of the point $P \in \mathcal{S}$ a 3-node triangular shaped finite element is introduced (cf. Figure 5.4). Following the isoparametric concept, the material position vector $\mathbf{R}^{\text{LTE}}$ and spatial position vector $\mathbf{r}^{\text{LTE}}$ of $P \in \mathcal{S}$ are interpolated between the material vertexes $\hat{\mathbf{X}}_k$ and spatial vertexes $\hat{\mathbf{x}}_k$ of the linear triangular element (LTE), respectively:

$$\mathbf{R}^{\text{LTE}} = \mathbf{R}\left(\theta^1, \theta^2, \theta^3 = 0\right) = \sum_{k=1}^{3} N_k\left(\theta^1, \theta^2\right) \cdot \hat{\mathbf{X}}_k \tag{5.25a}$$

$$\mathbf{r}^{\text{LTE}} = \mathbf{r}\left(\theta^1, \theta^2, \theta^3 = 0\right) = \sum_{k=1}^{3} N_k\left(\theta^1, \theta^2\right) \cdot \hat{\mathbf{x}}_k \tag{5.25b}$$

with $N_1\left(\theta^1, \theta^2\right) \ldots N_3\left(\theta^1, \theta^2\right)$ being the linear triangular shape functions:

$$N_1\left(\theta^1, \theta^2\right) = 1 - \theta^1 - \theta^2 \qquad \text{for} \quad 0 \leq \theta^1, \theta^2 \leq 1 \tag{5.26a}$$

$$N_2\left(\theta^1, \theta^2\right) = \theta^1 \qquad \text{for} \quad 0 \leq \theta^1, \theta^2 \leq 1 \tag{5.26b}$$

$$N_3\left(\theta^1, \theta^2\right) = \theta^2 \qquad \text{for} \quad 0 \leq \theta^1, \theta^2 \leq 1 \tag{5.26c}$$

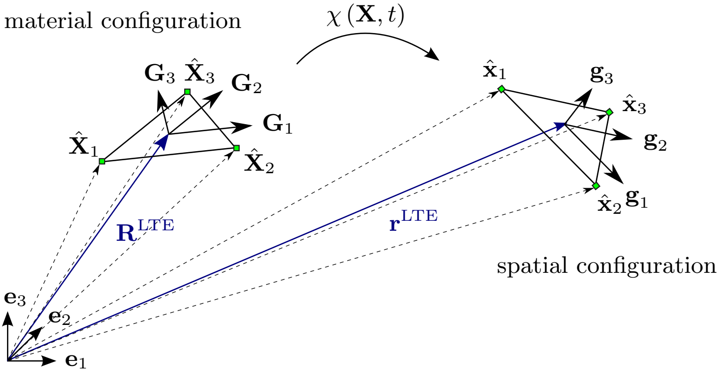

Figure 5.4: 3 parameter nonlinear membrane finite element

Applying the concept of a 3-parameter formulation (5.25), the covariant in-plane as well as the out-of-plane material (5.27a) and spatial (5.27b) base vectors are then defined as follows:

$$\mathbf{G}_i = \sum_{k=1}^{3} \frac{\partial N_k\left(\theta^1, \theta^2\right)}{\partial \theta^i} \cdot \hat{\mathbf{X}}_k \quad \text{and} \quad \mathbf{G}_3 = \frac{\mathbf{G}_1 \times \mathbf{G}_2}{\|\mathbf{G}_1 \times \mathbf{G}_2\|} \tag{5.27a}$$

$$\mathbf{g}_i = \sum_{k=1}^{3} \frac{\partial N_k\left(\theta^1, \theta^2\right)}{\partial \theta^i} \cdot \hat{\mathbf{x}}_k \quad \text{and} \quad \mathbf{g}_3 = \frac{\mathbf{g}_1 \times \mathbf{g}_2}{\|\mathbf{g}_1 \times \mathbf{g}_2\|} \tag{5.27b}$$

Furthermore, recalling Equation (2.33), the determinant of the Jacobian detJ defining the mapping between the triangular parametric space and the material mid-surface $\Omega_0^{\mathcal{S}}$ can be established as follows:

$$\mathrm{detJ}\left(\mathbf{X}\right) = \frac{1}{2} \left\| \mathbf{G}_1 \times \mathbf{G}_2 \right\| \tag{5.28}$$

REMARK IV: Throughout this thesis only triangular elements are considered. The proposed method can easily be applied to other types of 2D finite elements, e.g. a bi-linear quadrilateral element.

5.2.2 Discrete residual force equation

Applying the discrete geometry (5.25) to the stated shape optimization problem (5.3) leads to a finite set of design variables. Thus, based on the concept of VaReS each component X_a (DOF) of the material vertex $\hat{\mathbf{X}}_k = X_a \, \mathbf{e}_a$ is defined as design variable. More precisely, if the discrete mid-surface of the thin structure is embedded in an Euclidean space $\mathbb{R}^3$ each node consists of 3 DOFs which in turn results in a maximum amount of 3 design variables.

From a numerical perspective, the dependency of the material base vectors on the chosen design variables constitutes the major difference compared to the Total Lagrangian Formulation. In more detail, the partial derivatives of the covariant in-plane material base vectors (5.27a) w.r.t. the a-th DOF do not vanish:

$$\frac{\partial \mathbf{G}_1}{\partial X_a} = \sum_{k=1}^{3} \frac{\partial N_k\left(\theta^1, \theta^2\right)}{\partial \theta^1} \cdot \frac{\partial \hat{\mathbf{X}}_k}{\partial X_a} \tag{5.29}$$

$$\frac{\partial \mathbf{G}_2}{\partial X_a} = \sum_{k=1}^{3} \frac{\partial N_k\left(\theta^1, \theta^2\right)}{\partial \theta^2} \cdot \frac{\partial \hat{\mathbf{X}}_k}{\partial X_a} \tag{5.30}$$

Hence, the first derivative of the covariant out-of-plane base vector $(5.27\mathrm{a})_2$ w.r.t. to the a-th DOF results in:

$$\frac{\partial \mathbf{G}_3}{\partial X_a} = \frac{\left\| \mathbf{G}_1 \times \mathbf{G}_2 \right\| \dfrac{\partial \left(\mathbf{G}_1 \times \mathbf{G}_2\right)}{\partial X_a} - \dfrac{\partial \left\| \mathbf{G}_1 \times \mathbf{G}_2 \right\|}{\partial X_a} \left(\mathbf{G}_1 \times \mathbf{G}_2\right)}{\left\| \mathbf{G}_1 \times \mathbf{G}_2 \right\| \left\| \mathbf{G}_1 \times \mathbf{G}_2 \right\|} \tag{5.31}$$

with

$$\frac{\partial \left(\mathbf{G}_1 \times \mathbf{G}_2\right)}{\partial X_a} = \frac{\partial \mathbf{G}_1}{\partial X_a} \times \mathbf{G}_2 + \mathbf{G}_1 \times \frac{\partial \mathbf{G}_2}{\partial X_a} \tag{5.32a}$$

$$\frac{\partial \left\| \mathbf{G}_1 \times \mathbf{G}_2 \right\|}{\partial X_a} = \frac{\left(\mathbf{G}_1 \times \mathbf{G}_2\right) \cdot \left(\dfrac{\partial \mathbf{G}_1}{\partial X_a} \times \mathbf{G}_2 + \mathbf{G}_1 \times \dfrac{\partial \mathbf{G}_2}{\partial X_a}\right)}{\left\| \mathbf{G}_1 \times \mathbf{G}_2 \right\|} \tag{5.32b}$$

Consider the modified Green-Lagrange strain tensor $\mathbf{E}\left(\mathbf{X}\right)$ defined in Equation (5.20). In case of a discrete geometry description, its 1st Variation w.r.t. the a-th DOF can be established by applying Equation (5.25) and (5.20) to Equation (5.7):

$$\delta\mathbf{E}\left(\mathbf{X}\right) = D_{\delta X_a}\mathbf{E}\left(\mathbf{X}\right) = \frac{\mathrm{d}}{\mathrm{d}\epsilon}\left[\mathbf{E}\left(\mathbf{X}+\epsilon\delta X_a\right)\right]\Big|_{\epsilon=0} = \frac{\partial\mathbf{E}\left(\mathbf{X}\right)}{\partial X_a}\delta X_a \tag{5.33}$$

In more detail, the last term of (5.33) can be expressed in terms of the set of in-plane base vectors:

$$\frac{\partial\mathbf{E}\left(\mathbf{X}\right)}{\partial X_a}\delta X_a = \left[\left(E_{kl,a} - E_{rl}\Gamma^r_{ka} - E_{ks}\Gamma^s_{la}\right)\,\mathbf{G}^k\otimes\mathbf{G}^l\right]\,\delta X_a \tag{5.34}$$

with $E_{kl,a}$ being the first derivative of the covariant modified Green-Lagrange strain tensor w.r.t. the a-th DOF:

$$E_{kl,a} = -\frac{1}{2}\left(\frac{\partial\mathbf{G}_k}{\partial X_a}\cdot\mathbf{G}_l + \mathbf{G}_k\cdot\frac{\partial\mathbf{G}_l}{\partial X_a}\right) \quad \text{with} \quad k,l = 1\dots3 \tag{5.35}$$

and Γ^r_{ka} and Γ^s_{la} being the so-called *Christoffel symbols* associated with the a-th DOF:

$$\Gamma^r_{ka} = \frac{\partial\mathbf{G}_k}{\partial X_a}\cdot\mathbf{G}^r = -\frac{\partial\mathbf{G}^r}{\partial X_a}\cdot\mathbf{G}_k \quad \text{with} \quad r = 1\dots3 \tag{5.36a}$$

$$\Gamma^s_{la} = \frac{\partial\mathbf{G}_l}{\partial X_a}\cdot\mathbf{G}^s = -\frac{\partial\mathbf{G}^s}{\partial X_a}\cdot\mathbf{G}_l \quad \text{with} \quad s = 1\dots3 \tag{5.36b}$$

Consider the differential material domain $\mathrm{d}\Omega_0^{\mathcal{S}}$. The occurring integrals are evaluated by means of the so-called *Gaussian quadrature*[6]. Therefore, a mapping of the differential domain from the material space to the triangular parametric space is required. Applying Equation (5.28) to (2.32) yields:

$$\mathrm{d}\Omega_0^{\mathcal{S}} = \det\mathrm{J}\left(\mathbf{X}\right)\,\mathrm{d}\theta^1\,\mathrm{d}\theta^2 = \frac{1}{2}\left\|\mathbf{G}_1\times\mathbf{G}_2\right\|\,\mathrm{d}\theta^1\,\mathrm{d}\theta^2 \tag{5.37}$$

Due to the dependency of the determinant of the Jacobian $\det\mathrm{J}\left(\mathbf{X}\right)$ on the chosen design variables, the 1st Variation of the differential material domain w.r.t. the a-th DOF does not vanish:

$$\delta\,\mathrm{d}\Omega_0^{\mathcal{S}} = D_{\delta X_a}\det\mathrm{J}\left(\mathbf{X}\right)\,\mathrm{d}\theta^1\,\mathrm{d}\theta^2 \tag{5.38}$$

with

$$D_{\delta X_a}\det\mathrm{J}\left(\mathbf{X}\right) = \frac{\mathrm{d}}{\mathrm{d}\epsilon}\left[\det\mathrm{J}\left(\mathbf{X}+\epsilon\delta X_a\right)\right]\Big|_{\epsilon=0} = \frac{\partial\det\mathrm{J}\left(\mathbf{X}\right)}{\partial X_a}\delta X_a \tag{5.39}$$

---

[6] for further information the author refers to Belytschko et al. [11], Hughes [61], Zienkiewicz [113], etc.

In more detail, the last term of (5.39) can be expressed in terms of the covariant in-plane base vectors:

$$\frac{\partial \mathrm{detJ}}{\partial X_a}\delta X_a = \frac{(\mathbf{G}_1 \times \mathbf{G}_2) \cdot \left(\dfrac{\partial \mathbf{G}_1}{\partial X_a} \times \mathbf{G}_2 + \mathbf{G}_1 \times \dfrac{\partial \mathbf{G}_2}{\partial X_a} \right)}{2 \, \| \mathbf{G}_1 \times \mathbf{G}_2 \|} \, \delta X_a \tag{5.40}$$

Finally, inserting Equation (5.33), (5.38) and (5.39) into Equation (5.23) leads to the *discrete residual force equation*:

$$\delta \Pi_{\mathrm{total}} (\mathbf{X}) = \boldsymbol{\mathcal{R}} \cdot \delta \mathbf{X} \tag{5.41}$$

By means of the 1^{st} *Fundamental Lemma of Variational Calculus* (i.e. $\delta X_a \neq 0$) the a-th coefficient of the residual vector $\mathcal{R}_a$ can be established as follows:

$$\begin{aligned} \mathcal{R}_a = l_3 \int_0^1 \int_0^1 \mathrm{detJ} \; (\mathbf{S}_\chi - \mathbf{S}_{\mathrm{pre}}) : \frac{\partial \mathbf{E}(\mathbf{X})}{\partial X_a} \; \mathrm{d}\theta^1 \; \mathrm{d}\theta^2 \\ + \, l_3 \int_0^1 \int_0^1 \frac{\partial \mathrm{detJ}}{\partial X_a} \; (\Psi_\chi - \Psi_{\mathrm{pre}}) \; \mathrm{d}\theta^1 \; \mathrm{d}\theta^2 = 0 \end{aligned} \tag{5.42}$$

5.2.3 Linearized discrete residual force equation: Tangential stiffness matrix

The nonlinear characteristics of the residual force Equation (5.42) requires an iterative solution scheme. The method of choice is the *Newton-Raphson scheme*, introduced in Section 2.1.5. By means of a truncated Taylor-Series (2.19), the required linearized residual force equation can be established as follows:

$$\boldsymbol{\mathcal{R}}\left(\mathbf{X}^{i+1}\right) = \boldsymbol{\mathcal{R}}\left(\mathbf{X}^{i}\right) + \Delta\boldsymbol{\mathcal{R}}\left(\mathbf{X}^{i}, \Delta\mathbf{X}\right) + \mathcal{O}\left(\Delta\mathbf{X}^2\right) \tag{5.43}$$

with $\Delta\boldsymbol{\mathcal{R}}(\mathbf{X}, \Delta\mathbf{X})$ being the Gâteaux derivatives in the direction of the design variables, i.e. the *linearized governing equation of VaReS* stated in Equation (5.15). A closer look reveals that the Gâteaux derivatives of the a-th residual force w.r.t. the b-th DOF directly yield the coefficients of the well-known *consistent tangential stiffness matrix* $\boldsymbol{\mathcal{K}}$:

$$\begin{aligned} \Delta\mathcal{R}_a (\mathbf{X}, \Delta X_b) = D_{\Delta X_b} \mathcal{R}_a (\mathbf{X}) = \left. \frac{\mathrm{d}}{\mathrm{d}\epsilon} \left(\mathcal{R}_a (\mathbf{X} + \epsilon \, \Delta X_b) \right) \right|_{\epsilon = 0} \\ = \frac{\partial \mathcal{R}_a (\mathbf{X})}{\partial X_b} \, \Delta X_b = \mathcal{K}_{ab} \, \Delta X_b \end{aligned} \tag{5.44}$$

Consider the differential material domain $\mathrm{d}\Omega_0^{\mathcal{S}}$. Due to the concept of the directional derivative, the linearization of the differential material domain w.r.t. the b-th DOF is similar to its 1$^{\text{st}}$ Variation (5.38), i.e.:

$$\Delta\, \mathrm{d}\Omega_0^{\mathcal{S}} = D_{\delta X_b} \mathrm{detJ}\left(\mathbf{X}\right)\ \mathrm{d}\theta^1\ \mathrm{d}\theta^2 \tag{5.45}$$

with

$$D_{\delta X_b} \mathrm{detJ}\left(\mathbf{X}\right) = \frac{\mathrm{d}}{\mathrm{d}\epsilon}\ \left[\mathrm{detJ}\left(\mathbf{X} + \epsilon \delta X_b\right)\right]\Big|_{\epsilon=0} = \frac{\partial \mathrm{detJ}\left(\mathbf{X}\right)}{\partial X_b} \Delta X_b \tag{5.46}$$

Furthermore, the linearization of the 1$^{\text{st}}$ Variation of the differential material domain $\delta\, \mathrm{d}\Omega_0^{\mathcal{S}}$ is required:

$$\Delta\, \delta\, \mathrm{d}\Omega_0^{\mathcal{S}} = D_{\Delta X_b} \frac{\partial \mathrm{detJ}\left(\mathbf{X}\right)}{\partial X_a}\ \delta X_a\ \mathrm{d}\theta^1\ \mathrm{d}\theta^2 \tag{5.47}$$

with

$$D_{\Delta X_b} \frac{\partial \mathrm{detJ}\left(\mathbf{X}\right)}{\partial X_a} = \frac{\mathrm{d}}{\mathrm{d}\epsilon}\left[\frac{\partial \mathrm{detJ}\left(\mathbf{X} + \epsilon \Delta X_b\right)}{\partial X_a}\right]\Bigg|_{\epsilon=0} = \frac{\partial^2 \mathrm{detJ}\left(\mathbf{X}\right)}{\partial X_a \partial X_b} \Delta X_b \tag{5.48}$$

Finally, the second derivative of detJ w.r.t. the a-th DOF and b-th DOF can be expressed in terms of the covariant in-plane base vectors:

$$\begin{aligned} \frac{\partial^2 \mathrm{detJ}\left(\mathbf{X}\right)}{\partial X_a \partial X_b} = & -\frac{\left[\dfrac{\partial\left(\mathbf{G}_1 \times \mathbf{G}_2\right)}{\partial X_a} \cdot \left(\mathbf{G}_1 \times \mathbf{G}_2\right)\right]\left[\dfrac{\partial\left(\mathbf{G}_1 \times \mathbf{G}_2\right)}{\partial X_b} \cdot \left(\mathbf{G}_1 \times \mathbf{G}_2\right)\right]}{2\ \left\|\mathbf{G}_1 \times \mathbf{G}_2\right\|^3} \\ & + \frac{\dfrac{\partial\left(\mathbf{G}_1 \times \mathbf{G}_2\right)}{\partial X_a} \cdot \dfrac{\partial\left(\mathbf{G}_1 \times \mathbf{G}_2\right)}{\partial X_b}}{2\ \left\|\mathbf{G}_1 \times \mathbf{G}_2\right\|} \end{aligned} \tag{5.49}$$

Consider the modified Green-Lagrange strain tensor $\mathbf{E}\left(\mathbf{X}\right)$. Again, due to the concept of the directional derivative, the linearization of the Green-Lagrange strain tensor w.r.t the b-th DOF is similar to its 1$^{\text{st}}$ Variation (5.33), i.e.:

$$\Delta \mathbf{E}\left(\mathbf{X}\right) = D_{\Delta X_b} \mathbf{E}\left(\mathbf{X}\right) = \frac{\mathrm{d}}{\mathrm{d}\epsilon}\ \left[\mathbf{E}\left(\mathbf{X} + \epsilon \Delta X_b\right)\right]\Big|_{\epsilon=0} = \frac{\partial \mathbf{E}\left(\mathbf{X}\right)}{\partial X_b} \Delta X_b \tag{5.50}$$

In more detail, the last term of (5.50) can be expressed in terms of the covariant in-plane base vectors:

$$\frac{\partial \mathbf{E}\left(\mathbf{X}\right)}{\partial X_b} \Delta X_b = \left[\left(E_{kl,b} - E_{rl} \Gamma_{kb}^r - E_{ks} \Gamma_{lb}^s\right)\ \mathbf{G}^k \otimes \mathbf{G}^l\right]\ \Delta X_b \tag{5.51}$$

with $E_{kl,b}$ being the first derivatives of the covariant modified Green-Lagrange strain tensor w.r.t. the b-th DOF:

$$E_{kl,b} = -\frac{1}{2}\left(\frac{\partial \mathbf{G}_k}{\partial X_b} \cdot \mathbf{G}_l + \mathbf{G}_k \cdot \frac{\partial \mathbf{G}_l}{\partial X_b}\right) \quad \text{with} \quad k,l = 1 \ldots 3 \tag{5.52}$$

and Γ^r_{kb} and Γ^s_{lb} being the *Christoffel symbols* associated with the b-th DOF:

$$\Gamma^r_{kb} = \frac{\partial \mathbf{G}_k}{\partial X_b} \cdot \mathbf{G}^r = -\frac{\partial \mathbf{G}^r}{\partial X_b} \cdot \mathbf{G}_k \quad \text{with} \quad r = 1 \ldots 3 \tag{5.53a}$$

$$\Gamma^s_{lb} = \frac{\partial \mathbf{G}_l}{\partial X_b} \cdot \mathbf{G}^s = -\frac{\partial \mathbf{G}^s}{\partial X_b} \cdot \mathbf{G}_l \quad \text{with} \quad s = 1 \ldots 3 \tag{5.53b}$$

Furthermore, the linearization of the 1$^{\text{st}}$ Variation of the modified Green-Lagrange strain tensor $\delta \mathbf{E}(\mathbf{X})$ is required:

$$\begin{aligned} \Delta\, \delta \mathbf{E}(\mathbf{X}) &= D_{\Delta X_b} \frac{\partial \mathbf{E}(\mathbf{X})}{\partial X_a}\, \delta X_a = \frac{\mathrm{d}}{\mathrm{d}\epsilon} \left[\frac{\partial \mathbf{E}(\mathbf{X} + \epsilon \Delta X_b)}{\partial X_a} \right] \Bigg|_{\epsilon=0} \delta X_a \\ &= \frac{\partial^2 \mathbf{E}(\mathbf{X})}{\partial X_a\, \partial X_b}\, \delta X_a\, \Delta X_b \end{aligned} \tag{5.54}$$

Finally, the second derivative of the modified Green-Lagrange strain tensor $\mathbf{E}(\mathbf{X})$ w.r.t. the a-th DOF and b-th DOF can be expressed in terms of the covariant in-plane base vectors:

$$\begin{aligned} \frac{\partial^2 \mathbf{E}(\mathbf{X})}{\partial X_a \partial X_b} &= E_{kl,a,b}\, \mathbf{G}^k \otimes \mathbf{G}^l \\ &\quad - \left(E_{rl,b} \Gamma^r_{ka} + E_{rl} \Gamma^r_{ka,b} \right) \mathbf{G}^k \otimes \mathbf{G}^l \\ &\quad - \left(E_{ks,b} \Gamma^s_{la} + E_{ks} \Gamma^s_{la,b} \right) \mathbf{G}^k \otimes \mathbf{G}^l \\ &\quad - \left(E_{ml,a} - E_{rl} \Gamma^r_{ma} - E_{ms} \Gamma^s_{la} \right) \Gamma^m_{kb}\, \mathbf{G}^k \otimes \mathbf{G}^l \\ &\quad - \left(E_{kn,a} - E_{rn} \Gamma^r_{ka} - E_{ks} \Gamma^s_{na} \right) \Gamma^n_{lb}\, \mathbf{G}^k \otimes \mathbf{G}^l \end{aligned} \tag{5.55}$$

with $E_{kl,a,b}$ being the second derivative of the modified covariant Green-Lagrange strain tensor w.r.t. the a-th and b-th DOF:

$$E_{kl,a,b} = -\frac{1}{2} \left(\frac{\partial \mathbf{G}_k}{\partial X_a} \cdot \frac{\partial \mathbf{G}_l}{\partial X_b} + \frac{\partial \mathbf{G}_k}{\partial X_b} \cdot \frac{\partial \mathbf{G}_l}{\partial X_a} \right) \quad \text{with} \quad k,l = 1 \ldots 3 \tag{5.56}$$

The *Christoffel symbols* $\Gamma^r_{ka} = \Gamma^r_{ma}$, $\Gamma^s_{la} = \Gamma^s_{na}$, Γ^r_{kb}, Γ^s_{lb} have already been defined in Equation (5.36) and (5.53), respectively. Furthermore, the *Christoffel symbols* Γ^m_{kb} and Γ^n_{lb} are associated with the partial derivatives of the 1$^{\text{st}}$ Variation of the Green-Lagrange strain tensor $\delta \mathbf{E}(\mathbf{X})$ w.r.t. the b-th DOF:

$$\Gamma^m_{kb} = \frac{\partial \mathbf{G}_k}{\partial X_b} \cdot \mathbf{G}^m = -\frac{\partial \mathbf{G}^m}{\partial X_b} \cdot \mathbf{G}_k \quad \text{with} \quad m = 1 \ldots 3 \tag{5.57a}$$

$$\Gamma^n_{lb} = \frac{\partial \mathbf{G}_l}{\partial X_b} \cdot \mathbf{G}^n = -\frac{\partial \mathbf{G}^n}{\partial X_b} \cdot \mathbf{G}_l \quad \text{with} \quad n = 1 \ldots 3 \tag{5.57b}$$

Additionally, the first derivatives of the *Christoffel symbols* associated with the a-th DOF w.r.t. the b-th DOF $\Gamma^r_{ka,b}$ and $\Gamma^s_{la,b}$ are defined as:

$$\Gamma^r_{ka,b} = \frac{\partial \mathbf{G}_k}{\partial X_a} \cdot \frac{\partial \mathbf{G}^r}{\partial X_b} = -\frac{\partial \mathbf{G}^r}{\partial X_a} \cdot \frac{\partial \mathbf{G}_k}{\partial X_b} \quad \text{with} \quad r = 1 \ldots 3 \tag{5.58a}$$

$$\Gamma^s_{la,b} = \frac{\partial \mathbf{G}_l}{\partial X_a} \cdot \frac{\partial \mathbf{G}^s}{\partial X_b} = -\frac{\partial \mathbf{G}^s}{\partial X_a} \cdot \frac{\partial \mathbf{G}_l}{\partial X_b} \quad \text{with} \quad s = 1 \ldots 3 \tag{5.58b}$$

Finally, inserting Equation (5.13), (5.45), (5.47), (5.50) and (5.54) into Equation (5.44) leads to the a-th b-th coefficients $\mathcal{K}_{ab}$ of the consistent tangential stiffness matrix:

$$\mathcal{K}_{ab}\, \Delta X_b = \left[\boldsymbol{\mathcal{K}}_\chi\right]_{ab}\, \Delta X_b + \left[\boldsymbol{\mathcal{K}}_{\text{pre}}\right]_{ab}\, \Delta X_b \tag{5.59}$$

with

$$\begin{aligned}
\left[\boldsymbol{\mathcal{K}}_\chi\right]_{ab} = {} & l_3 \int_0^1 \int_0^1 \det\mathrm{J}\; \mathbf{S}_\chi : \frac{\partial^2 \mathbf{E}(\mathbf{X})}{\partial X_a \partial X_b}\; \mathrm{d}\theta^1\, \mathrm{d}\theta^2 \\
& + l_3 \int_0^1 \int_0^1 \det\mathrm{J}\; \mathbb{D}_\chi : \frac{\partial \mathbf{E}(\mathbf{X})}{\partial X_b} : \frac{\partial \mathbf{E}(\mathbf{X})}{\partial X_a}\; \mathrm{d}\theta^1\, \mathrm{d}\theta^2 \\
& + l_3 \int_0^1 \int_0^1 \frac{\partial \det\mathrm{J}}{\partial X_b}\; \mathbf{S}_\chi : \frac{\partial \mathbf{E}(\mathbf{X})}{\partial X_a}\; \mathrm{d}\theta^1\, \mathrm{d}\theta^2 \\
& + l_3 \int_0^1 \int_0^1 \frac{\partial \det\mathrm{J}}{\partial X_a}\; \mathbf{S}_\chi : \frac{\partial \mathbf{E}(\mathbf{X})}{\partial X_b}\; \mathrm{d}\theta^1\, \mathrm{d}\theta^2 \\
& + l_3 \int_0^1 \int_0^1 \frac{\partial^2 \det\mathrm{J}}{\partial X_a \partial X_b}\; \Psi_\chi\; \mathrm{d}\theta^1\, \mathrm{d}\theta^2
\end{aligned} \tag{5.60}$$

and

$$\begin{aligned}
\left[\boldsymbol{\mathcal{K}}_{\text{pre}}\right]_{ab} = {} & l_3 \int_0^1 \int_0^1 \det\mathrm{J}\; \mathbf{S}_{\text{pre}} : \frac{\partial^2 \mathbf{E}(\mathbf{X})}{\partial X_a \partial X_b}\; \mathrm{d}\theta^1\, \mathrm{d}\theta^2 \\
& + l_3 \int_0^1 \int_0^1 \det\mathrm{J}\; \mathbb{D}|_{\mathbf{S}_{\text{pre}}} : \frac{\partial \mathbf{E}(\mathbf{X})}{\partial X_b} : \frac{\partial \mathbf{E}(\mathbf{X})}{\partial X_a}\; \mathrm{d}\theta^1\, \mathrm{d}\theta^2 \\
& + l_3 \int_0^1 \int_0^1 \frac{\partial \det\mathrm{J}}{\partial X_b}\; \mathbf{S}_{\text{pre}} : \frac{\partial \mathbf{E}(\mathbf{X})}{\partial X_a}\; \mathrm{d}\theta^1\, \mathrm{d}\theta^2 \\
& + l_3 \int_0^1 \int_0^1 \frac{\partial \det\mathrm{J}}{\partial X_a}\; \mathbf{S}_{\text{pre}} : \frac{\partial \mathbf{E}(\mathbf{X})}{\partial X_b}\; \mathrm{d}\theta^1\, \mathrm{d}\theta^2 \\
& + l_3 \int_0^1 \int_0^1 \frac{\partial^2 \det\mathrm{J}}{\partial X_a \partial X_b}\; \Psi_{\text{pre}}\; \mathrm{d}\theta^1\, \mathrm{d}\theta^2
\end{aligned} \tag{5.61}$$

REMARK V: A closer look on Equation (5.60) and (5.61) reveals that the resulting consistent tangential stiffness matrix $\boldsymbol{\mathcal{K}}$ is symmetric. This property is essential for choosing an adequate numerical solver for the established linear system of equation (5.43).

REMARK VI: In various literature for standard finite elements (e.g. PARISCH [89], RAMM[96]) the tangential stiffness matrix is split into an elastic part $\boldsymbol{\mathcal{K}}_{\text{elast}}$ and geometric part $\boldsymbol{\mathcal{K}}_{\text{geo}}$. In analogy, the developed consistent tangential stiffness matrix $\boldsymbol{\mathcal{K}}$ can be split as follows:

$$\boldsymbol{\mathcal{K}} = \boldsymbol{\mathcal{K}}_{\text{elast}} + \boldsymbol{\mathcal{K}}_{\text{geo}} + \boldsymbol{\mathcal{K}}_{\text{VaReS}} \tag{5.62}$$

with the elastic part $\boldsymbol{\mathcal{K}}_{\text{elast}}$

$$\begin{aligned}
\left[\boldsymbol{\mathcal{K}}_{\text{elast}}\right]_{ab} &= l_3 \int_0^1 \int_0^1 \det\mathrm{J}\ \mathbb{D}_\chi : \frac{\partial \mathbf{E}(\mathbf{X})}{\partial X_b} : \frac{\partial \mathbf{E}(\mathbf{X})}{\partial X_a}\ \mathrm{d}\theta^1\,\mathrm{d}\theta^2 \\
&+ l_3 \int_0^1 \int_0^1 \det\mathrm{J}\ \ \mathbb{D}|_{\mathbf{S}_{\text{pre}}} : \frac{\partial \mathbf{E}(\mathbf{X})}{\partial X_b} : \frac{\partial \mathbf{E}(\mathbf{X})}{\partial X_a}\ \mathrm{d}\theta^1\,\mathrm{d}\theta^2
\end{aligned} \tag{5.63}$$

the geometric part $\boldsymbol{\mathcal{K}}_{\text{geo}}$

$$\begin{aligned}
\left[\boldsymbol{\mathcal{K}}_{\text{geo}}\right]_{ab} &= l_3 \int_0^1 \int_0^1 \det\mathrm{J}\ \mathbf{S}_\chi : \frac{\partial^2 \mathbf{E}(\mathbf{X})}{\partial X_a \partial X_b}\ \mathrm{d}\theta^1\,\mathrm{d}\theta^2 \\
&+ l_3 \int_0^1 \int_0^1 \det\mathrm{J}\ \mathbf{S}_{\text{pre}} : \frac{\partial^2 \mathbf{E}(\mathbf{X})}{\partial X_a \partial X_b}\ \mathrm{d}\theta^1\,\mathrm{d}\theta^2
\end{aligned} \tag{5.64}$$

and the additional terms resulting from the presented *Variation of Reference Strategy* $\boldsymbol{\mathcal{K}}_{\text{VaReS}}$

$$\begin{aligned}
\left[\boldsymbol{\mathcal{K}}_{\text{VaReS}}\right]_{ab} &= l_3 \int_0^1 \int_0^1 \frac{\partial \det\mathrm{J}}{\partial X_b}\ \mathbf{S}_\chi : \frac{\partial \mathbf{E}(\mathbf{X})}{\partial X_a}\ \mathrm{d}\theta^1\,\mathrm{d}\theta^2 \\
&+ l_3 \int_0^1 \int_0^1 \frac{\partial \det\mathrm{J}}{\partial X_b}\ \mathbf{S}_{\text{pre}} : \frac{\partial \mathbf{E}(\mathbf{X})}{\partial X_a}\ \mathrm{d}\theta^1\,\mathrm{d}\theta^2 \\
&+ l_3 \int_0^1 \int_0^1 \frac{\partial \det\mathrm{J}}{\partial X_a}\ \mathbf{S}_\chi : \frac{\partial \mathbf{E}(\mathbf{X})}{\partial X_b}\ \mathrm{d}\theta^1\,\mathrm{d}\theta^2 \\
&+ l_3 \int_0^1 \int_0^1 \frac{\partial \det\mathrm{J}}{\partial X_a}\ \mathbf{S}_{\text{pre}} : \frac{\partial \mathbf{E}(\mathbf{X})}{\partial X_b}\ \mathrm{d}\theta^1\,\mathrm{d}\theta^2 \\
&+ l_3 \int_0^1 \int_0^1 \frac{\partial^2 \det\mathrm{J}}{\partial X_a \partial X_b}\ \Psi_\chi\ \mathrm{d}\theta^1\,\mathrm{d}\theta^2 \\
&+ l_3 \int_0^1 \int_0^1 \frac{\partial^2 \det\mathrm{J}}{\partial X_a \partial X_b}\ \Psi_{\text{pre}}\ \mathrm{d}\theta^1\,\mathrm{d}\theta^2
\end{aligned} \tag{5.65}$$

REMARK VII: In order to validate the resulting consistent tangential stiffness matrix $\boldsymbol{\mathcal{K}}$ (5.59), a quadratic convergence rate within the so-called *convergence radius* has to be shown. The following *single truss problem* is designed for investigating its characteristics and behavior until convergence is achieved. For the sake of clarity, the concept of VaReS is applied to a

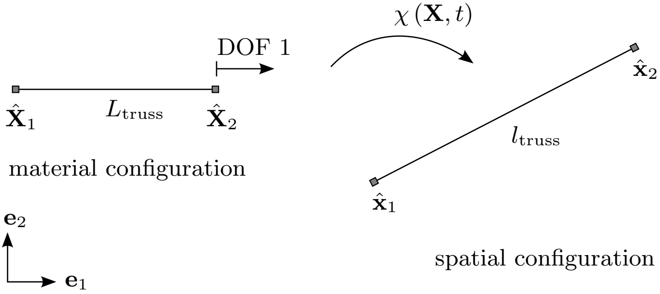

Figure 5.5: Single truss problem: set-up

truss element embedded in a 2 dimensional Euclidean space $\mathbb{R}^2$. Thus, the truss element consists of 2 nodes and 4 DOFs.

The concept of the numerical experiment is the following. Consider a single VaReS formulated truss element undergoing a motion $\chi(\mathbf{X},t)$ (cf. Figure 5.5). As initial material configuration (i.e. at iteration step n = 0), a horizontal alignment of the truss with $L_{\text{truss}}^{\text{n=0}} = 1.00$ is chosen. Additionally, a set of Dirichlet BCs is applied restraining the horizontal and vertical motion of $\hat{\mathbf{X}}_1$ and the vertical motion of $\hat{\mathbf{X}}_2$. Thus, the problem consists of only one DOF, namely the horizontal component of $\hat{\mathbf{X}}_2$ (indicated as DOF 1 in Figure 5.5). The goal is now to find that material nodal position $\hat{\mathbf{X}}_2$ which results in a stress-free mapping. More precisely, in case of convergence (n = conv) the truss element is exclusively subjected to a rigid body motion, i.e. $L_{\text{truss}}^{\text{n=con}} = l_{\text{truss}} = 1.4142$. The convergence behavior of the Newton-Raphson scheme is shown in Figure 5.6. A solution was achieved within 7 iteration steps ($\text{error}_{\text{abs}} = 1.133\text{E}-12$). Furthermore, a quadratic decay of the dynamic residual $\|\boldsymbol{\mathcal{R}}\|$ can be observed after the fourth iteration step (n = 4), i.e. the *quadratic convergence rate* requirement of a second-order Newton-method is met.

The outcome of the presented convergence study raises the following question: *What is the reason for the poor convergence behavior in the beginning?* In order to understand this effect, a closer look on the evolution of the Eigenvalues of the unconstrained tangential stiffness matrix $\boldsymbol{\mathcal{K}}_{\text{truss}}$ needs to be taken (cf. Figure 5.7):

$$\begin{aligned}
[\boldsymbol{\mathcal{K}}_{\text{truss}}]_{ab} = {} & \frac{E\,A}{16} \cdot \frac{\left(L_{\text{truss}}^2 + l_{\text{truss}}^2\right)^2 - 4\,l_{\text{truss}}^4}{L_{\text{truss}}^4} \cdot \frac{\partial^2 L_{\text{truss}}}{\partial X_a \partial X_b} \\
& + \frac{E\,A}{4} \cdot \frac{\left(3\,l_{\text{truss}}^2 - L_{\text{truss}}^2\right) \cdot l_{\text{truss}}^2}{L_{\text{truss}}^5} \cdot \frac{\partial L_{\text{truss}}}{\partial X_a} \cdot \frac{\partial L_{\text{truss}}}{\partial X_b}
\end{aligned} \tag{5.66}$$

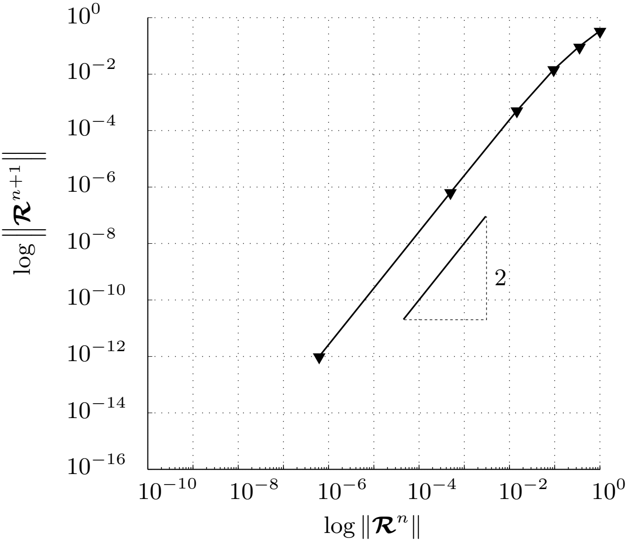

Figure 5.6: Single truss problem: convergence plot

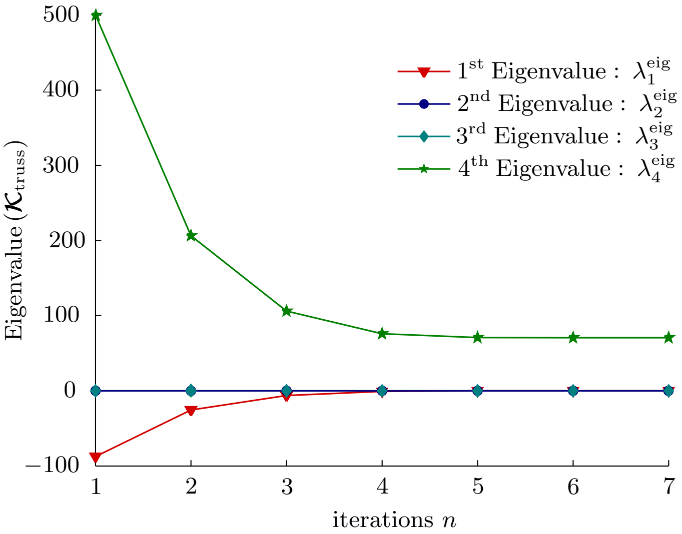

Figure 5.7: Single truss problem: Eigenvalues of $\boldsymbol{\mathcal{K}}_{\text{truss}}$ vs. number of Newton-Raphson iterations n

with $a, b = 1 \dots 4$, i.e.

$$\hat{\mathbf{X}}_1 = \begin{bmatrix} X_1 & X_2 \end{bmatrix}^{\mathrm{T}} \quad \text{and} \quad \hat{\mathbf{X}}_2 = \begin{bmatrix} X_3 & X_4 \end{bmatrix}^{\mathrm{T}} \tag{5.67}$$

and the well-known Eigenvalue problem:

$$\left(\boldsymbol{\mathcal{K}}_{\text{truss}} - \lambda_i^{\text{eig}} \, \mathbf{I} \right) \cdot \mathbf{u}_i^{\text{eig}} = 0 \quad \text{with} \quad i = 1 \dots 4 \tag{5.68}$$

Considering the last iteration step (n = 7), the 1st, 2nd and 3rd Eigenvalue λ_i^{eig} are vanishing. In terms of structural mechanics, all three rigid body modes (2 translations and 1 rotation) are preserved by $\boldsymbol{\mathcal{K}}_{\text{truss}}^{\text{n=7}}$. A comparison between the convergence speed (see Figure 5.6) and the corresponding Eigenvalues λ_i^{eig} (see Figure 5.7) reveals an interesting correlation. Up to the fourth iteration (n < 4), not even a linear convergence rate is achieved. Instead of three only two rigid body modes are preserved, which is indicated by only two of the four corresponding Eigenvalues being zero ($\lambda_2^{\text{eig}} = \lambda_3^{\text{eig}} = 0$). After that (n ≥ 4), the behavior changes completely. All three rigid body modes ($\lambda_1^{\text{eig}} = \lambda_2^{\text{eig}} = \lambda_3^{\text{eig}} = 0$) are activated and the expected quadratic convergence rate can be observed. The missing rigid body mode in the beginning of the iterative scheme indicates a lack in the underlying physics. In more detail, the arbitrarily chosen initial material configuration was purely based on geometric facets which in turn results in a physically meaningless stress field [7]. After a certain iteration (in this case n = 4), the deformation field is eventually able to produce a sensible material response resulting in a correct rank deficiency of the unconstrained consistent tangential stiffness matrix.

CONCLUSION: The presented numerical experiment underlines the sensitivity of the convergence behavior w.r.t. the chosen initial material configuration.

5.2.4 Discrete gradient of the objective function

As already mentioned in Section 5.2.2, applying the discrete geometry (5.25) to the stated shape optimization problem (5.3) leads to a finite set of design variables. Hence, the gradient of the objective function is defined as the vector of partial derivatives w.r.t. the components of the material vertexes $\hat{\mathbf{X}}_k = X_a \, \mathbf{e}_a$:

$$\begin{aligned} \left[\nabla_{\mathbf{X}} \Pi_{\text{total}} \left(\mathbf{X} \right) \right]_a = {} & l_3 \int\limits_{\Omega_0^{\mathcal{S}}} \left(\mathbf{S}_\chi - \mathbf{S}_{\text{pre}} \right) : \frac{\partial \mathbf{E} \left(\mathbf{X} \right)}{\partial X_a} \, \mathrm{d}\Omega_0^{\mathcal{S}} \\ & + l_3 \int\limits_{\Omega_0^{\mathcal{S}}} \left(\Psi_\chi - \Psi_{\text{pre}} \right) \frac{\partial}{\partial X_a} \, \mathrm{d}\Omega_0^{\mathcal{S}} \end{aligned} \tag{5.69}$$

---

[7] due to either unrealistic strain states or non-suitable material models

Consider the partial derivatives of the modified Green-Lagrange strain tensor $\mathbf{E}(\mathbf{X})$ defined in Equation (5.20). By means of the partial derivatives of the covariant material base vectors (5.29) - (5.31), they can be established as follows:

$$\frac{\partial \mathbf{E}(\mathbf{X})}{\partial X_a} = \left(E_{kl,a} - E_{rl}\Gamma^r_{ka} - E_{ks}\Gamma^s_{la}\right) \mathbf{G}^k \otimes \mathbf{G}^l \tag{5.70}$$

with $E_{kl,a}$ being the first derivatives of the covariant modified Green-Lagrange strain tensor w.r.t. the a-th DOF:

$$E_{kl,a} = -\frac{1}{2}\left(\frac{\partial \mathbf{G}_k}{\partial X_a} \cdot \mathbf{G}_l + \mathbf{G}_k \cdot \frac{\partial \mathbf{G}_l}{\partial X_a}\right) \quad \text{with} \quad k,l = 1\dots3 \tag{5.71}$$

and Γ^r_{ka} and Γ^s_{la} being the *Christoffel symbols* associated with the a-th DOF:

$$\Gamma^r_{ka} = \frac{\partial \mathbf{G}_k}{\partial X_a} \cdot \mathbf{G}^r = -\frac{\partial \mathbf{G}^r}{\partial X_a} \cdot \mathbf{G}_k \quad \text{with} \quad r = 1\dots3 \tag{5.72a}$$

$$\Gamma^s_{la} = \frac{\partial \mathbf{G}_l}{\partial X_a} \cdot \mathbf{G}^s = -\frac{\partial \mathbf{G}^s}{\partial X_a} \cdot \mathbf{G}_l \quad \text{with} \quad s = 1\dots3 \tag{5.72b}$$

Consider the partial derivatives of the differential material domain. Recalling Equation (5.37), they can be expressed in terms of the covariant in-plane material base vectors:

$$\frac{\partial}{\partial X_a}\,\mathrm{d}\Omega_0 = \frac{(\mathbf{G}_1 \times \mathbf{G}_2) \cdot \left(\dfrac{\partial \mathbf{G}_1}{\partial X_a} \times \mathbf{G}_2 + \mathbf{G}_1 \times \dfrac{\partial \mathbf{G}_2}{\partial X_a}\right)}{2\,\left\|\mathbf{G}_1 \times \mathbf{G}_2\right\|}\,\mathrm{d}\theta^1\,\mathrm{d}\theta^2 \tag{5.73}$$

5.3 Assessment of the convergence and robustness

Consider the unconstrained optimization problem stated in Equation (5.5). Upon closer investigations, a strong link between the underlying strain-energy function and convergence behavior of the stated optimization problem can be observed. This section will discuss several numerical aspects regarding the robustness and convergence behavior of VaReS subjected to three different types of material models (see test matrix Table 5.1).

Therefore, a numerical experiment is designed, investigating the behavior of a single triangular finite element embedded in 3 dimensional Euclidean space $\mathbb{R}^3$. Both the material $\hat{\mathbf{X}}_i$ and spatial $\hat{\mathbf{x}}_i$ coordinates of the i-th nodes are listed in Table 5.2.

The concept of the numerical experiment is the following. Consider the material nodal position $\hat{X}_3 = X_a\,\mathbf{e}_a$. Its vertical component X_{DOF1} is varied within the range $0.35 \leq X_{\mathrm{DOF1}} \leq 3.5$, leading to a prescribed motion $\chi(\mathbf{X}, t)$ mapping the material configuration to its fixed spatial configuration (cf. Figure 5.8). Additionally, no prescribed stresses are considered

	divergence	overshooting predictor	relative fiber orientation
Ψ_{StVenKir}	x	x	
Ψ_{NeoHook}	x	x	
Ψ_{woven}	x	x	x

Table 5.1: Test matrix: Investigated numerical aspects vs. strain-energy functions Ψ

node		$\hat{\mathbf{X}}_i$			$\hat{\mathbf{x}}_i$	
	X_1	X_2	X_3	x_1	x_2	x_3
1	0.00	0.00	0.00	0.00	0.00	5.00
2	2.00	0.00	0.00	2.00	0.00	5.00
1	1.00	X_{DOF1}	0.00	1.00	1.00	5.00

Table 5.2: Experimental set-up: material $\hat{\mathbf{X}}_i$ and spatial $\hat{\mathbf{x}}_i$ coordinates of the i-th node

(i.e. $\Pi_{\text{pre}} = 0$). It is important to note that no system of equation needs to be solved here. For each prescribed motion $\chi(\mathbf{X}, t)$ the corresponding total potential energy $\Pi(\mathbf{C}_\chi)$ and the residual force $\mathcal{R}_{X_{\text{DOF1}}}$ is calculated. This leads to the solution space (*potential energy curve* and *residual force curve*) of the numerical experiment. The experiment is designed in a way that for $X_{\text{DOF1}} = 1.0$ the corresponding motion $\chi(\mathbf{X}, t)$ results in a pure rigid body motion (cf. Table 5.2), i.e. a stress-free mapping is preserved leading to $\mathcal{R}_{X_{\text{DOF1}}} = 0.00$.

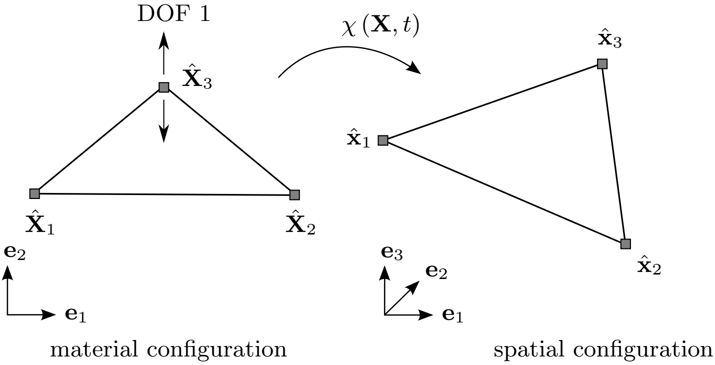

Figure 5.8: Single triangle problem: set-up

The goal is now to investigate the influence of different strain-energy functions on the solution space. The following three strain-energy functions namely a Neo-Hookean (5.74), a St. Venant-Kirchhoff (5.75) and a material model describing an orthoropic woven fabric[8] (5.76) exhibiting a low shear resistance are chosen for the presented study:

$$\Psi_{\mathrm{NeoHook}} = \frac{1}{2}\,\lambda\,\ln(\sqrt{I_3})^2 - \mu\,\ln(\sqrt{I_3}) + \frac{1}{2}\,\mu\,(I_1 - 3) \tag{5.74}$$

$$\Psi_{\mathrm{StVenKir}} = \frac{1}{2}\,\lambda\,(tr(\mathbf{E}))^2 + \mu\,tr(\mathbf{E}^2) \tag{5.75}$$

$$\begin{aligned}\Psi_{\mathrm{woven}}\,(\mathbf{C}) = \sum_{i=0}^{r} \frac{1}{i+1}\,A_i\,\left(I_4^{i+1} - 1\right) + \sum_{j=0}^{s} \frac{1}{j+1}\,B_j\,\left(I_6^{j+1} - 1\right) \\ + \sum_{k=1}^{t} \frac{1}{k}\,C_k\,\left(\frac{1}{I_4\,I_6} tr\left(\mathbf{C}\mathbf{M}^1\mathbf{C}\mathbf{M}^2\right)\right)^k\end{aligned} \tag{5.76}$$

In case of the orthotropic[9] woven fabric, two different fiber orientations (0°/90° and −45°/45°) are investigated. The resulting potential energy curves and residual force curves are shown in Figure 5.9 and Figure 5.10, respectively. It is important to note that all curves meet the stress-free mapping at $X_{\mathrm{DOF1}} = 1.0$, i.e. for all cases the pure rigid body motion is preserved in both the potential energies and the residual forces (see black arrows).

Despite the fact, that the solution of the optimization problem is quite trivial[10], the chosen set-up allows a deep insight in the characteristics of the presented solution strategies (second-order and first-order approach). In the following, the presented curves are discussed in more detail - see test matrix Table 5.1.

REMARK I: The choice of the strain-energy functions is not arbitrary. Each strain-energy function represents a specific group of hyperelastic models, namely material models based on polyconvex strain-energy functions (5.74), material models based on general strain-energy functions (5.75) and transversely isotropic/orthotropic materials exhibiting low shear resistance based on general strain-energy functions (5.76).

5.3.1 Divergence

Consider the regime of tensile strains, i.e. $X_{\mathrm{DOF1}} > 1.0$. After passing certain points (dashed circles in Figure 5.11), the residual force curves representing the St. Venant-Kirchhoff strain-energy function (red dashed/dotted

---

[8] the applied material model and material data (plain weave) have been published by Aimène et al. [1]

[9] i.e. the material fiber directions (warp/weft) are orthotropic

[10] i.e. there exists a unique analytical solution which results in a stress-free mapping into the respective fixed spatial configuration

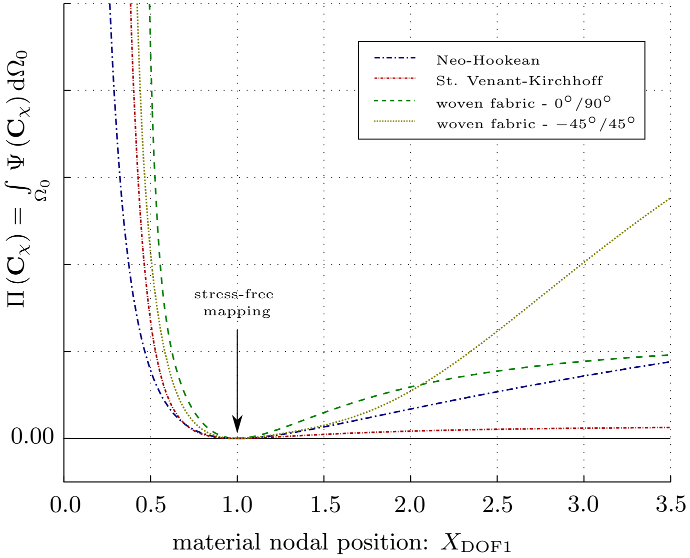

Figure 5.9: Single triangle problem: total potential energy $\Pi\left(\mathbf{C}_\chi\right)$ vs. material nodal position X_{DOF1}

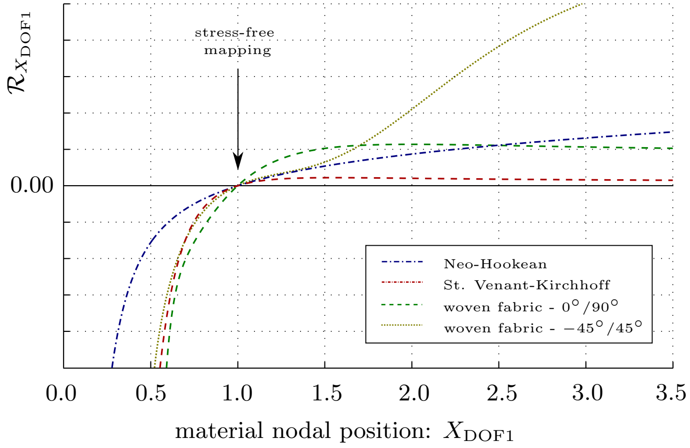

Figure 5.10: Single triangle problem: residual force $\mathcal{R}_{X_{\mathrm{DOF1}}}$ vs. material nodal position X_{DOF1}

line in Figure 5.11) and the strain-energy function for the woven fabric under 0°/90° (green dashed line in Figure 5.11) start to decline again. This declining behavior may lead to additional roots, i.e. points where the residual force vanishes. Such artificial roots exhibit absolutely no physical meaning, since they result exclusively from the lack of polyconvexity[11] of the underlying strain-energy function.

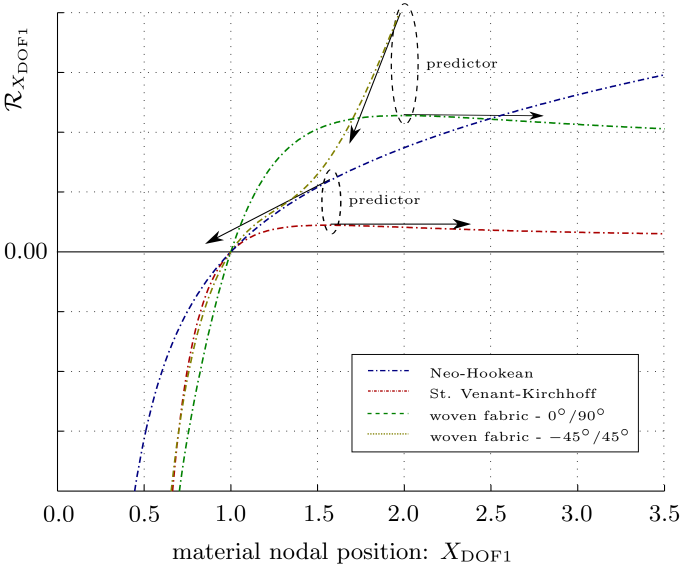

Figure 5.11: Divergence: residual force $\mathcal{R}_{X_{\mathrm{DOF1}}}$ vs. material nodal position X_{DOF1}

If such a critical point is passed towards the wrong direction, the corresponding director of the applied Newton-Raphson scheme (second-order approach) may get distracted (indicated by solid black arrows in Figure 5.11). In such a case, the Newton-Raphson scheme will result in an artificial root. This numerical effect is called *divergence*.

In order to circumvent the diverging behavior, a strategy based on so-called *time steps* is proposed. The key idea behind the introduced time-stepping strategy is analogous to the well-known load-stepping strategy in standard statics (structural mechanics). However, instead of modifying the right-hand side of the equilibrium equation[12], several *homotopic* intermediate geometries (time steps) between a plane initial guess and the target structure are generated (cf. Figure 5.12). In more detail, instead of directly

---

[11] see Schröder and Neff [100]

[12] i.e. external virtual work δW_{ext} (3.100) or (3.107), respectively

solving for the target structure (time step n), several intermediate geometries ($0 < i < n$) are generated a priori to the analysis (cutting pattern generation). Thus, the converged solution (intermediate cutting pattern) of the time step i is then used as the initialization of time step $i + 1$. It is important to mention that the quadratic convergence rate of the Newton-Raphson scheme is preserved within each subproblem.

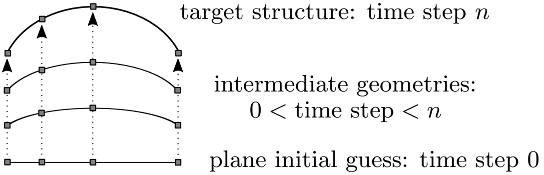

Figure 5.12: Time-stepping strategy: homotopic intermediate geometries

CONCLUSION: In case of a second-order approach, non-polyconvex strain-energy functions may suffer from severe convergence problems after passing a critical strain state within the tensile regime. These critical points strongly depend on both the applied material model itself and on the fiber orientation. Such critical strain states can be circumvented by applying a certain number of time steps.

5.3.2 Overshooting predictor

In case of certain tensile deformation states (dashed circles in Figure 5.13), another numerical effect called *overshooting* of the predictor can be observed. More precisely, an overshooting predictor points towards either a singular or a physically meaningless point within the solution space. The reason for this effect is the *local convergence* of the Newton-Raphson scheme. Hence, the initialization of the underlying nonlinear system of equations has to meet the corresponding *convergence radius*, i.e. that region of the solution space, for which convergence is guaranteed. Figure 5.13 clearly shows the influence of the chosen strain-energy function Ψ on the convergence radius of the presented second-order approach (see Section 5.1.3.1).

In order to circumvent the overshooting behavior (solid black line in Figure 5.13), a strategy directly working on the predictor is proposed. In more detail, the update of the iterative scheme is modified by means of a damping factor:

$$\boldsymbol{\mathcal{R}}\left(\mathbf{X}^{i+1}\right) = \boldsymbol{\mathcal{R}}\left(\mathbf{X}^{i}\right) + \alpha \cdot \Delta\boldsymbol{\mathcal{R}}\left(\mathbf{X}^{i}, \Delta\mathbf{X}\right) + \mathcal{O}\left(\Delta\mathbf{X}^{2}\right) \tag{5.77}$$

This additional parameter ($0.0 \leq \alpha \leq 1.0$) shortens the predictor and thereby avoids an overshooting. The choice of an appropriate damping

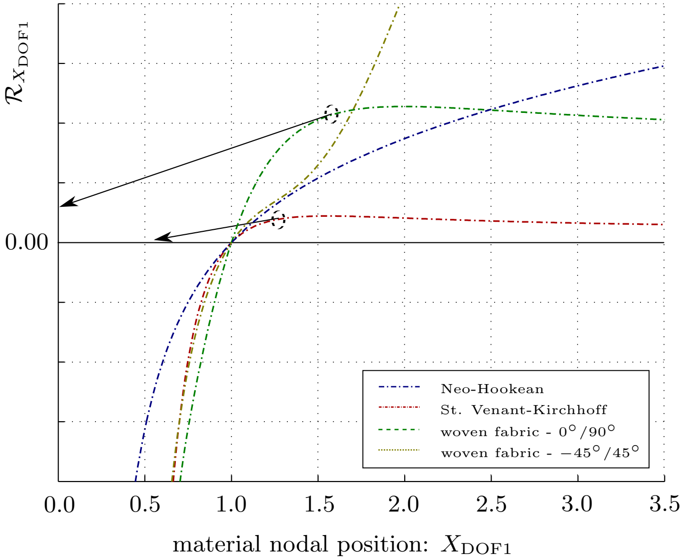

Figure 5.13: Overshooting predictor: residual force $\mathcal{R}_{X_{\text{DOF1}}}$ vs. material nodal position X_{DOF1}

factor that is either constant or adaptive strongly depends on the characteristics of the problem which is to be solved. This strategy is also known as *damped Newton-Raphson scheme*, see DEUFLHARD [35]. Its major drawback is the loss of the quadratic convergence rate of the Newton-Raphson scheme.

CONCLUSION: Depending on the underlying strain-energy function, certain deformation states result in an overshooting of the predictors. These critical deformation states can be circumvented by either modifying the length of the predictor or introducing a certain number of time steps (see Section 5.3.1). A combination of both strategies is also possible, i.e. using a damped predictor within each time step.

5.3.3 Relative fiber orientation

In contrast to a *Total Lagrangian Formulation*, the angle, called relative *fiber orientation*, between the warp/weft direction and an element edge does not stay constant during the solution process. The reason for that is the choice of design variables. In more detail, each design update leads to a new material mesh, whereas the global fiber orientation within the cutting pattern does not change. In order to investigate the effect of the relative fiber orientation on the solution space, the numerical experiment described above needs to be extended. Therefore, two more fiber orientations (−75°/15° and −60°/30°) are examined. The residual force curves representing the orthotropic woven fabric are shown in Figure 5.14.

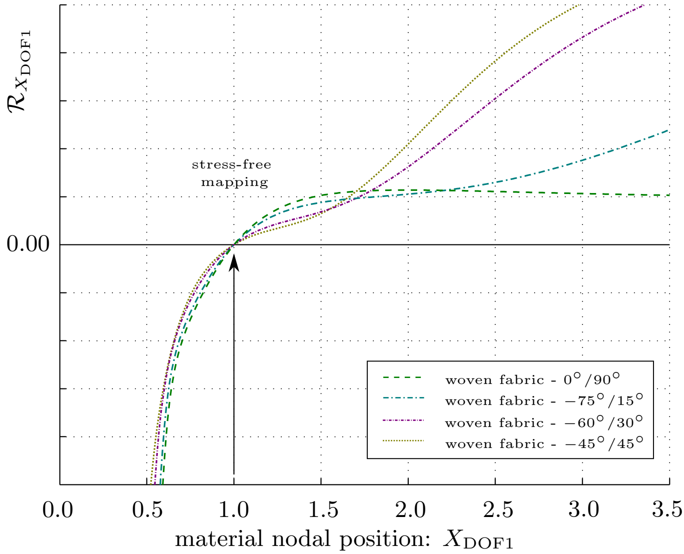

Figure 5.14: Relative fiber orientations: residual force $\mathcal{R}_{X_{\mathrm{DOF1}}}$ vs. material nodal position X_{DOF1}

Consider the regime of tensile strains ($X_{\mathrm{DOF1}} > 1.0$). A significant relation between the relative fiber orientation and the curvature of the residual force curve can be observed. In more detail, the point of inflection is significantly shifted in each case. In case of a Newton-Raphson scheme (second-order approach), such an inflection point results in a singular tangential stiffness matrix which in turn leads to an unsolvable system of equation. Hence, the convergence radius of the Newton-Raphson scheme is not only effected by the initialization of the optimization problem but also by the relative fiber orientation.

Consider the corresponding potential energy curves shown in Figure 5.15. The influence of the relative fiber orientation is still observable but less prominent. In order to overcome the described drawback of the second-oder approach, an alternative solution strategy namely the method of steepest descent (first-order approach) is preferred. Due to the fact that the method of steepest descent directly acts on the energy level, its convergence radius is less effected by the relative fiber orientation (cf. Figure 5.15).

CONCLUSION: The characteristics of the residual forces strongly depend on the relative fiber orientation. The method of steepest descent

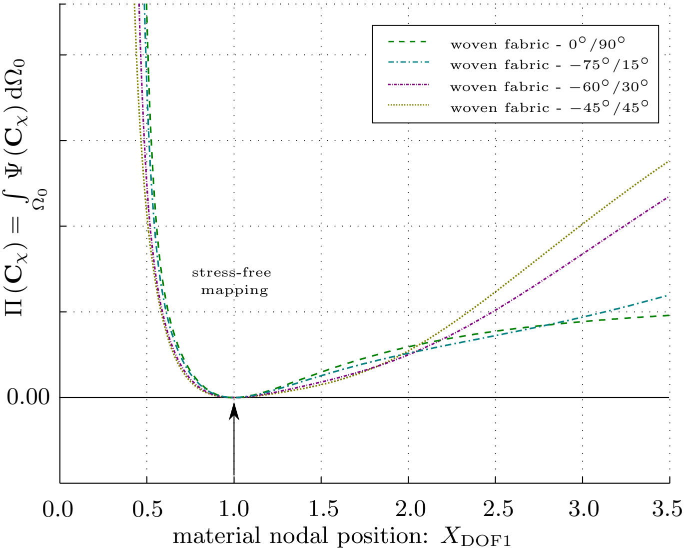

Figure 5.15: Relative fiber orientations: total potential energy $\Pi\left(\mathbf{C}_\chi\right)$ vs. material nodal position X_{DOF1}

(first-order approach) circumvents this somewhat awkward behavior by directly acting on the potential energies. In order to enhance its performance, the evaluation of the step size α^i by means of an adaptive scheme (3-point rule) is proposed. Thereby, the total potential energy is approximated in terms of a quadratic function between a specified range:

$$\Pi_{\text{total}}^{i+1}(\alpha) = A\,\alpha^2 + B\,\alpha + C \quad \text{for} \quad \alpha_{\text{min}} \leq \alpha \leq \alpha_{\text{max}} \tag{5.78}$$

The corresponding coefficients (A, B, C) are determined by solving the following linear system of equation:

$$\begin{bmatrix} \alpha_{\text{min}}^2 & \alpha_{\text{min}} & 1.00 \\ \alpha_{0.5}^2 & \alpha_{0.5} & 1.00 \\ \alpha_{\text{max}}^2 & \alpha_{\text{max}} & 1.00 \end{bmatrix} \cdot \begin{bmatrix} A \\ B \\ C \end{bmatrix} = \begin{bmatrix} \Pi_{\text{total}}\left(\mathbf{X}^{i+1}, \alpha_{\text{min}}\right) \\ \Pi_{\text{total}}\left(\mathbf{X}^{i+1}, \alpha_{0.5}\right) \\ \Pi_{\text{total}}\left(\mathbf{X}^{i+1}, \alpha_{\text{max}}\right) \end{bmatrix} \tag{5.79}$$

whith $\alpha_{0.5}$ being the arithmetic mean of the specified range

$$\alpha_{0.5} = \alpha_{\text{min}} + \frac{\alpha_{\text{max}} - \alpha_{\text{min}}}{2} \tag{5.80}$$

The optimal step size α_{opt} is located at the extreme value of Equation (5.78):

$$\frac{\mathrm{d}\Pi_{\text{total}}^{i+1}(\alpha)}{\mathrm{d}\alpha} = 2A\,\alpha + B \overset{!}{=} 0 \quad \Longrightarrow \quad \alpha_{\text{opt}} = -\frac{A}{2\,B} \tag{5.81}$$

Finally, the step size α^i is established as follows:

$$\alpha^i = \frac{1}{\left\| \nabla_{\mathbf{X}} \Pi_{\text{total}} \left(\mathbf{X}^i \right) \right\|_\infty} \cdot \begin{cases} \alpha_{\text{min}} & \text{for} \quad \alpha_{\text{opt}} < \alpha_{\text{min}} \\ \alpha_{\text{opt}} & \text{for} \quad \alpha_{\text{min}} \leq \alpha \leq \alpha_{\text{max}} \\ \alpha_{\text{max}} & \text{for} \quad \alpha_{\text{opt}} > \alpha_{\text{max}} \end{cases} \tag{5.82}$$

For further information on alternative line search techniques (e.g. fixed step size, *Armijo step-size rule*, etc.) the author refers to Baldick [6] or Gekeler [47].

5.3.4 Summary

The outcome of the presented numerical experiment (single triangle problem) is summarized in Table 5.3.

	approach	line search	time stepping	damping
Group 1	NR		x	x
Group 2	NR /SD	x	x	x
Group 3	SD	x	x	

Table 5.3: Single triangle problem: summary (NR: Newton-Raphson scheme - SD: method of steepest descent)

Based on the identified issues (divergence - overshooting predictor - relative fiber orientation), Table 5.3 correlates the examined strain-energy functions (Group 1: material models based on polyconvex strain-energy functions - Group 2: material models based on general strain-energy functions - Group 3: transversely isotropic/orthotropic materials exhibiting low shear resistance based on general strain-energy functions) to an adequate solution strategy (NR: Newton-Raphson scheme - SD: method of steepest descent). Therefore, this table serves as a guideline for all upcoming problems/examples within the scope of this thesis.

5.4 Benchmarks and Validation

The following examples are presented underlining the capabilities and generality of VaReS (see test matrix Table 5.4). In more detail, three different types of geometries (ruled: cylindrical shell - synclastic: spherical shell - anticlastic: generic rib) and two different types of strain-energy functions (Neo-Hookean: Equation (5.74) - balanced plain weave made of fiber-glass: Equation (5.76)) are chosen. Furthermore, scenarios with multiple plies exhibiting different fiber orientations and taking into account their off-set to the structure's mid-surface (called stack) are shown.

	NeoHook	glass plain weave
cylindrical shell	NR / SD	
spherical shell	NR	SD
generic rib	NR	SD

Table 5.4: Test matrix: numerical examples

REMARK I: In all examples no additional predefined stress-states are considered. The effect of a predefined stress-state on the resulting cutting patterns is discussed in chapter 6.1.

5.4.1 Ruled surfaces: cylindrical shell

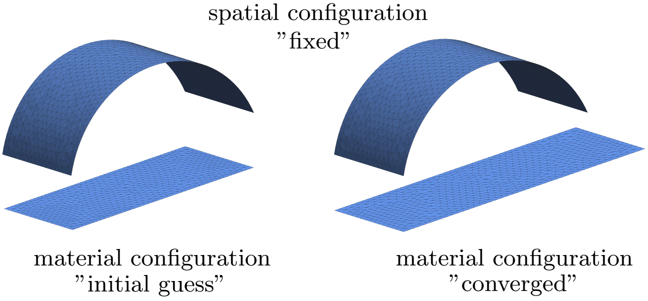

Figure 5.16: Cylindrical shell: initial (left) vs. converged (right) material configuration

Consider a 160° section of a cylindrical shell with radius $r = 0.5\text{m}$ (cf. Figure 5.16). Due to the fact that a cylindrical shell is a ruled surface (cf. Figure 2.3), there exists an analytical solution for the cutting pattern problem. Thus, the optimized cutting pattern (converged solution) has to be identical to the congruent rectangle. Hence, the cylindrical shell can be used as a *benchmark* for both the second-order approach (Section 5.4.1.1) and the first-order approach (Section 5.4.1.2). As depicted in Figure 5.16

(left), the problem is initialized with an *orthogonal projection* of each element onto the x-y-plane. This initialization strategy (cf. Figure 5.17) yields heavily distorted elements on both front edges of the initial material configuration. In order to circumvent problems arising from these locally extremely large strain states, a Laplace operator based in-plane mesh regularization technique[13] is applied.

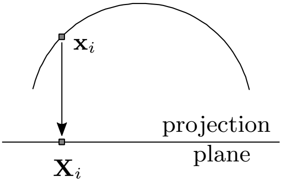

Figure 5.17: Initialization strategy: orthogonal projection onto a plane

A Neo-Hookean strain-energy function (5.74) is applied. The chosen Poisson's ratio and Young's modulus of elasticity are listed in Table 5.5.

Young's modulus E [Pa]	Poisson's ratio ν [$-$]
$1.0\text{E}+03$	0.10

Table 5.5: Cylindrical shell: material parameters

5.4.1.1 Benchmark: Newton-Raphson scheme

Consider the second-order approach (see Section 5.1.2). Due to the applied Newton-Raphson scheme, the tangential stiffness matrix (5.60) has to exhibit a so-called *full rank*[14]. In terms of mechanics this means that all rigid body motions have to be suppressed through a set of adequate Dirichlet BCs. In order to keep the restrictions as low as possible, a so-called *statically determinate support* is chosen. In more detail, all translatory DOFs of node #2 and the translatory DOF in global x-direction of node #14 are held fixed (as depicted in Figure 5.18).

The analytical solution is met within 5 time steps (cf. Figure 5.12)) and a total number of $n_{\text{total}} = 25$ iterations steps ($n_1 = 5$, $n_2 = 5$, $n_3 = 5$, $n_4 = 5$, $n_5 = 5$). For each time step, the optimized cutting patterns and the resulting von Mises stresses within the target structure are visualized in Figure 5.19.

---

[13] see Firl [41]

[14] i.e. the number of linearly independent equations has to be identical to the number of DOFs

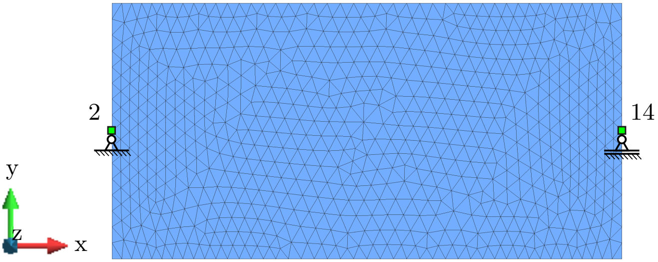

Figure 5.18: Boundary conditions: statically determinate support

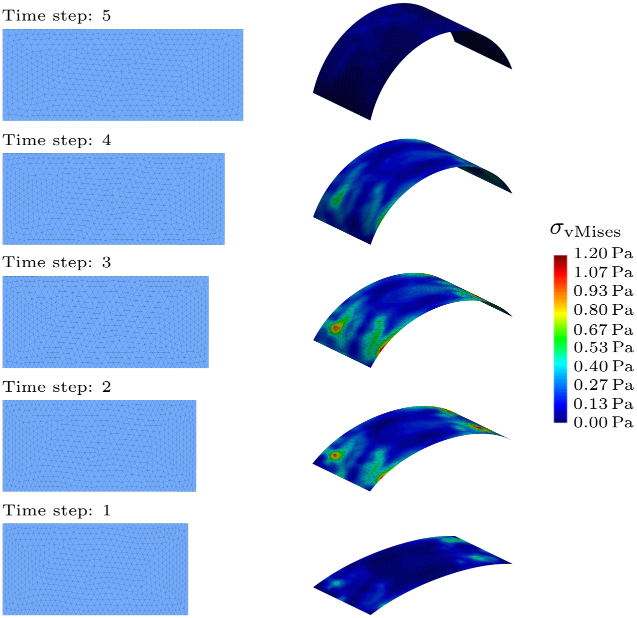

Figure 5.19: Cylindrical shell: cutting pattern vs. von Mises stresses (5 time steps - see page 109)

Furthermore, Figure 5.20 illustrates the evolution of the relative residual norm $\mathcal{R}^n_{\text{rel}}$ (5.83) for each time step (convergence behavior).

$$\mathcal{R}^n_{\text{rel}} = \frac{\|\boldsymbol{\mathcal{R}}^n_{\text{abs}}\|}{\|\boldsymbol{\mathcal{R}}^1_{\text{abs}}\|} \tag{5.83}$$

The evolution of the relative error $\text{Error}_{\text{rel}}$ w.r.t. the surface area of the congruent rectangle $\Omega^{\mathcal{S}}_{0\,\text{exact}}$ for each iteration step is shown in Figure 5.21.

$$\text{Error}_{\text{rel}} = \frac{\left|\Omega^{\mathcal{S}}_{0\,\text{exact}} - \Omega^{\mathcal{S}}_{0\,\text{iter}}\right|}{\Omega^{\mathcal{S}}_{0\,\text{exact}}} \tag{5.84}$$

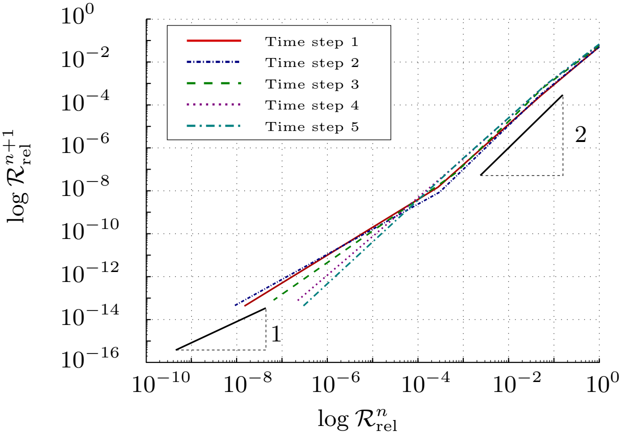

Figure 5.20: Cylindrical shell: convergence plot (5 time steps)

A comparison of both plots reveals a correlation between the relative error $\text{Error}_{\text{rel}}$ and the convergence behavior for each time step. In more detail, in the beginning a quadratic convergence rate can be observed. As soon as the analytical solution[15] for each subproblem is reached (i.e. the relative error almost vanishes), the corresponding convergence rates slow down to a linear behavior. The reason of this effect is the well-known issue with the *numerical zero*. This directly contradicts with the fact that in numerics a mathematical zero cannot be accomplished but only approximated by a very small number, the so-called *machine accuracy*. However, if the relative error drops below machine accuracy, the results are still very small[16] but random (*numerical noise*).

---

[15] i.e. the total elastic potential energy has to be exactly zero (ruled surfaces)

[16] i.e. less than machine accuracy

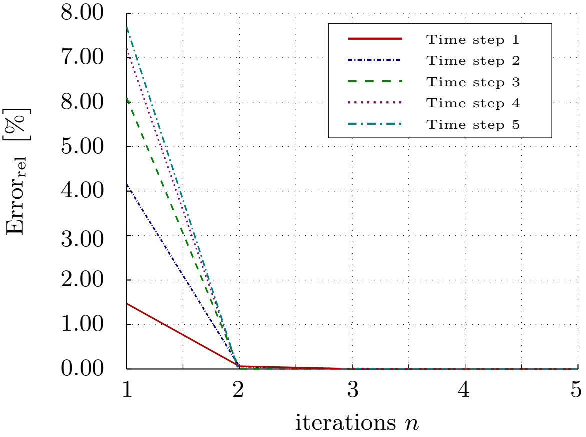

Figure 5.21: Cylindrical shell: $\mathrm{Error}_{\mathrm{rel}}$ [%] vs. iterations n (5 time steps)

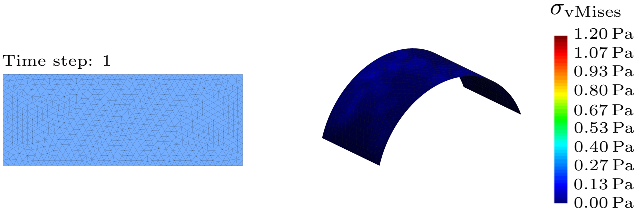

Figure 5.22: Cylindrical shell: cutting pattern vs. von Mises stresses (1 time step)

Consider only one time step. In order to achieve convergence a damping factor $\alpha = 0.1$ needs to be applied to Equation (5.77). The analytical solution is met after a total number of $n = 196$ iterations. The optimized cutting pattern and the resulting von Mises stresses within the target structure are visualized in Figure 5.22. The convergence behavior is illustrated in Figure 5.23. Figure 5.24 shows the evolution of the relative error $\mathrm{Error}_{\mathrm{rel}}$ (5.84). Due to the applied damping factor only a linear convergence rate can be observed. Comparing both computational runs clearly shows that the loss of the quadratic convergence rate leads to a noticeable increase of iteration steps (Newton-Raphson scheme) even though the total number of time steps has been decreased.

CONCLUSION: The preserved quadratic convergence rate of the Newton-Raphson scheme underlines the strength of the *time step strategy* for sta-

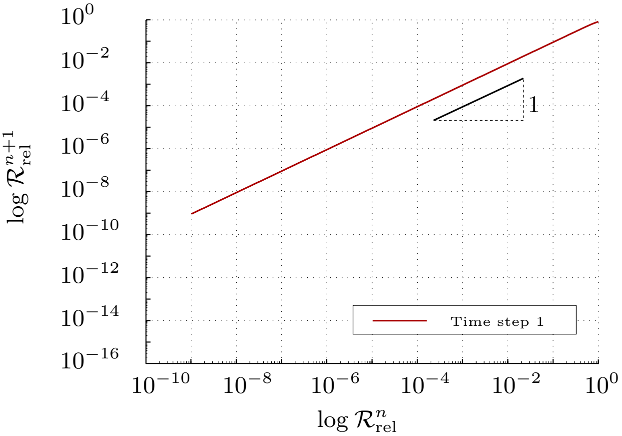

Figure 5.23: Cylindrical shell: convergence plot (1 time step)

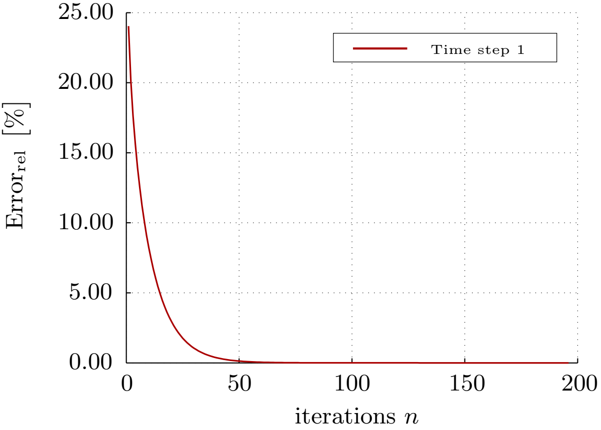

Figure 5.24: Cylindrical shell: $\mathrm{Error}_{\mathrm{rel}}$ $[\%]$ vs. iterations n (1 time step)

bilization. In general, the choice of boundary conditions is arbitrary, but one has to keep in mind that they directly affect the resulting shape of the cutting pattern and the residual stresses.

5.4.1.2 Benchmark: Method of steepest descent

Consider the first-order approach (see Section 5.1.3.2). Due to the fact that there is no system of equations which needs to be solved (i.e. there exists no tangential stiffness matrix), Dirichlet BCs are not mandatory. Thus, the problem is initialized as explained but without any restrictions on node #2 and node #14 (cf. Figure 5.18). The analytical solution is met within 1 time step (step size: $1.0\mathrm{E}-06 \leq \alpha_{\mathrm{opt}} \leq 1.0\mathrm{E}-02$) and a total number of $n_{\mathrm{total}} = 3886$ iterations steps. The optimized cutting pattern and the resulting von Mises stresses are visualized in Figure 5.25.

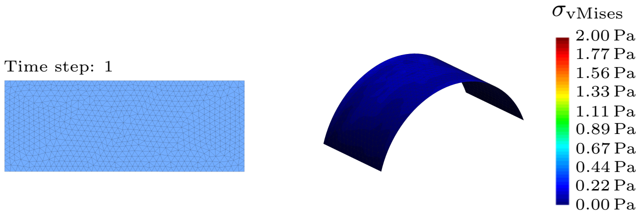

Figure 5.25: Cylindrical shell: cutting pattern (left) vs. von Mises stresses (right)

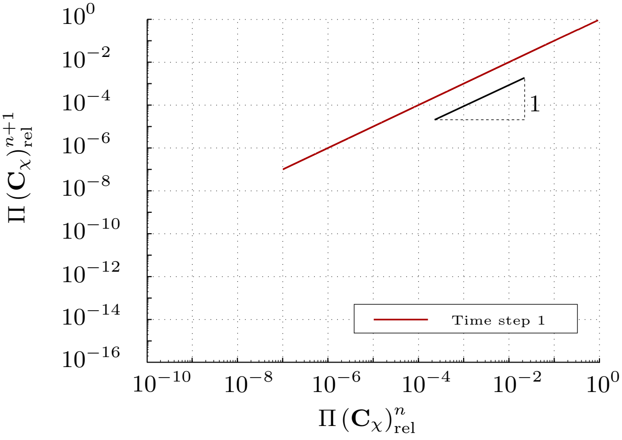

Figure 5.26: Cylindrical shell: convergence plot

Furthermore, Figure 5.26 illustrates the evolution of the relative objective function $\Pi\left(\mathbf{C}_\chi\right)^n_{\text{rel}}$ (5.85) (convergence behavior). Figure 5.27 shows the evolution of the relative error $\text{Error}_{\text{rel}}$ (5.84).

$$\Pi\left(\mathbf{C}_\chi\right)^n_{\text{rel}} = \frac{\Pi\left(\mathbf{C}_\chi\right)^n}{\Pi\left(\mathbf{C}_\chi\right)^0} \tag{5.85}$$

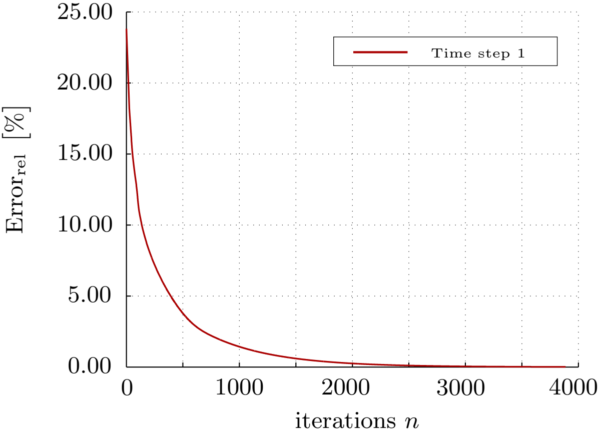

Figure 5.27: Cylindrical shell: $\text{Error}_{\text{rel}}$ [%] vs. iterations n

CONCLUSION: The method of steepest descent exhibits a linear convergence rate. The adaptive line search technique (3-point rule) proves to be quite powerful, since it allows large design updates in the beginning. When the iterative scheme approaches the analytical solution, an overshooting is prevented by significantly smaller step sizes. Furthermore, no Dirichlet BCs are required which may negatively affect the resulting shape of the cutting pattern.

5.4.2 Synclastic surfaces: spherical shell

Consider a 160° section of a hemispherical shell with radius $r = 0.5$m (cf. Figure 5.28). Again, the problem is initialized with an orthogonal projection (cf. Figure 5.17) of each element onto the x-y-plane in combination with the mentioned in-plane mesh regularization technique. Due to the synclastic characteristics of the (rotationally symmetrical) target structure (cf. Figure 2.3), only an optimized[17] but not unique cutting pattern can be found (i.e. there exists no analytical solution). The aim of the

---

[17] according to the concept of VaReS the minimization of total elastic potential energy is chosen as governing criteria

following study is to get a deeper understanding of the impact of preferred material directions on the shape of the resulting cutting patterns for synclastic target structures. Hence, in addition to the isotropic Neo-Hookean strain-energy function (5.74), the nonlinear material model[18] describing a glass plain weave (5.76) is applied.

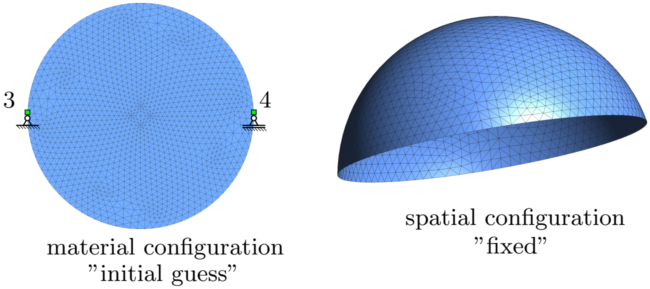

Figure 5.28: Spherical shell: orthogonal projection (left) vs. target geometry (right)

5.4.2.1 Neo-Hookean material

Consider the isotropic case. The applied material parameters (Young's modulus, Poisson's ratio) are listed in Table 5.5. Choosing the second-order approach for solving the optimization problem requires an adequate set of Dirichlet BCs. Hence a statically determinate support is realized by restraining node #3 and node #4 (cf. Figure 5.28).

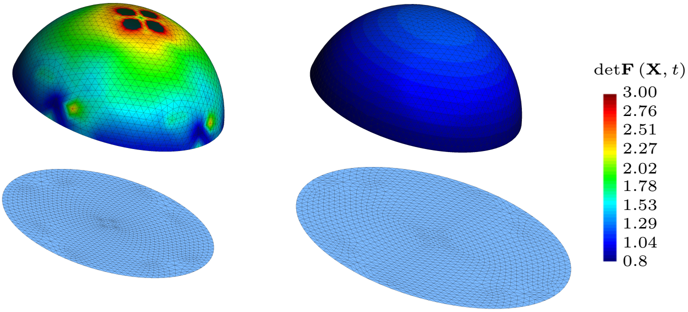

Figure 5.29: Spherical shell (Neo-Hookean): volume ratio $\det\mathbf{F}(\mathbf{X},t)$ resulting from an initial motion $\chi(\mathbf{X}_{\text{init}},t)$ (left) and the converged motion $\chi(\mathbf{X}_{\text{conv}},t)$ (right)

---

[18] Aimène et al. [1]

A converged solution is achieved within a total number of $n_{\text{total}} = 47$ iterations split into 5 time steps ($n_1 = 6$, $n_2 = 6$, $n_3 = 8$, $n_4 = 11$, $n_5 = 16$). The distortion of each element arising due to the motion $\chi(\mathbf{X}, t)$ is quantified by means of the volume ratio $\det\mathbf{F}(\mathbf{X}, t)$ (see page 38), i.e. it serves as a quality check with $\det\mathbf{F}(\mathbf{X}, t) = 1.00$ being the reference value. Figure 5.29 shows a significant improvement compared to the initial guess. The optimized cutting pattern (the red dashed line indicates the initial guess) and the resulting von Mises stresses within the target structure are illustrated in Figure 5.30.

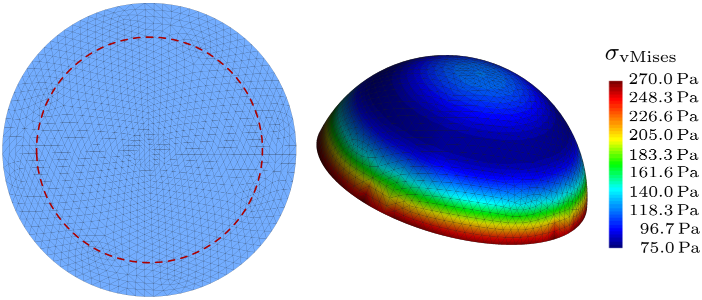

Figure 5.30: Spherical shell (Neo-Hookean): initial guess (red dashed) vs. optimized cutting pattern (left) and resulting von Mises stresses (right)

CONCLUSION: Due to the isotropic material model, the shape of the optimized cutting pattern remains rotationally symmetric.

5.4.2.2 Glass plain weave

A_0 [kPa] B_0 [kPa]	A_1 [kPa] B_1 [kPa]	A_2 [kPa] B_2 [kPa]	A_3 [kPa] B_3 [kPa]
−14.495	23.482	−10.818	1.831
−14.495	23.482	−10.818	1.831

Table 5.6: Glass plain weave: tensile material coefficients (see table 1 in Aimène et al. [1])

Consider the anisotropic (more precisely orthotropic) case. The coefficients of the corresponding polynomials (5.76) are published in Aimène et al. [1] and summarized in Table 5.6 and Table 5.7. It can clearly be seen that the chosen fabric exhibits the same material behavior for both the warp and weft direction. In order to investigate the effect of anisotropy on the resulting shape of the cutting pattern two different scenarios are defined

C_1 [kPa] C_6 [kPa]	C_2 [kPa] C_7 [kPa]	C_3 [kPa] C_8 [kPa]	C_4 [kPa] C_9 [kPa]	C_5 [kPa]
0.0045 −4.593	−0.00801 5.637	95.314 −3.722	−0.605 1.023	2.177

Table 5.7: Glass plain weave: shear material coefficients (see table 2 in Aimène et al. [1])

(cf. Figure 5.31). Both optimization problems (scenarios) are then solved by applying the method of steepest descent. Hence, no additional Dirichlet BCs are required.

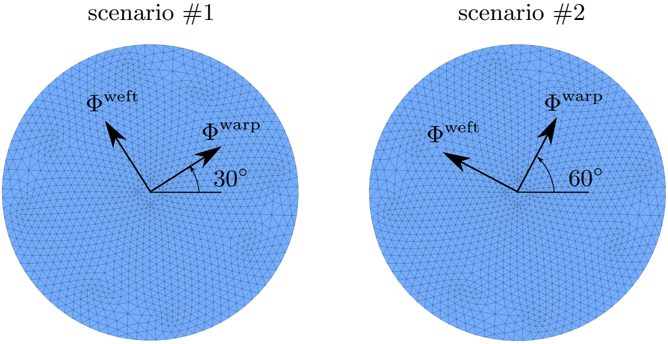

Figure 5.31: Spherical shell (plain weave): material fiber orientation (initial guess) for scenario #1 (left) and scenario #2 (right)

Applying 1 time step, a converged solution for the respective scenario is achieved within $n_{\#1} = 2572$ and $n_{\#2} = 2565$ iterations. For both scenarios, the optimized cutting patterns (the red dashed lines indicate the initial guess) as well as the improvements in terms of the volume ratio $\det\mathbf{F}\,(\mathbf{X}, t)$ are illustrated in Figure 5.32 and Figure 5.33, respectively. Furthermore, the occurring fiber twists (i.e. the deviation of the initially orthogonal fibers arising due to the motion $\chi\,(\mathbf{X}, t)$) are shown in Figure 5.34.

$$\text{Fiber twist} = \arccos\left(\frac{\mathbf{F}\;\Phi^{\text{warp}} \cdot \mathbf{F}\;\Phi^{\text{weft}}}{\left\|\mathbf{F}\;\Phi^{\text{warp}}\right\| \cdot \left\|\mathbf{F}\;\Phi^{\text{weft}}\right\|}\right) \tag{5.86}$$

CONCLUSION: Due to the anisotropic (more precisely orthotropic) material model, the shape of the optimized cutting pattern does not remain rotationally symmetric but axially symmetric w.r.t. the warp/weft directions.

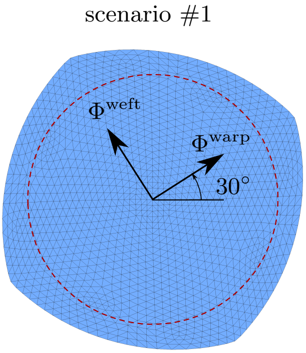

Figure 5.32: Spherical shell (plain weave): initial guess (red dashed) vs. optimized cutting pattern for scenario #1 (left) and scenario #2 (right)

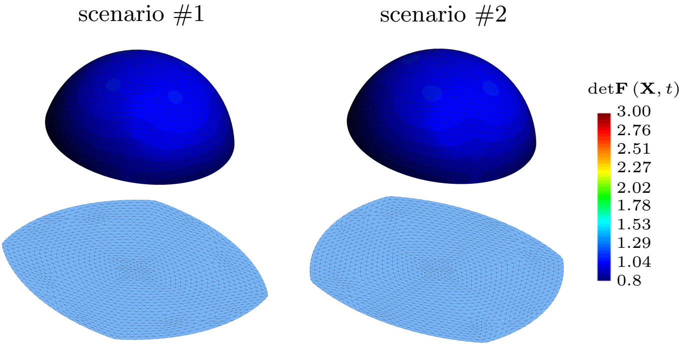

Figure 5.33: Spherical shell (plain weave): volume ratio $\det \mathbf{F}(\mathbf{X}, t)$ resulting from the converged motion $\chi(\mathbf{X}_{\text{conv}}, t)$ for scenario #1 (left) and scenario #2 (right)

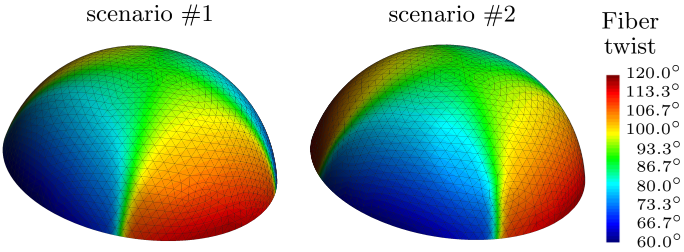

Figure 5.34: Spherical shell (plain weave): fiber twist (5.86) resulting from the converged motion $\chi(\mathbf{X}_{\text{conv}}, t)$ for scenario #1 (left) and scenario #2 (right)

5.4.3 Anticlastic surface: generic rib

Consider a 30° segment of a generic rib (cf. Figure 5.35). Similarly to the previous synclastic structure (Section 5.4.2), there exists only an optimized[19] but non-unique cutting pattern for this anticlastic (axially symmetric) target structure. In contrast to the cylindrical and spherical shell, the rib segment is initialized by means of a *cylindrical projection*. More precisely, each node is projected onto a surrounding cylindrical shell. Considering the parabolic characteristics of a cylinder (ruled surface - cf. Figure 2.3), the projected nodes can then easily be transfered into the desired projection plane (see Figure 5.36).

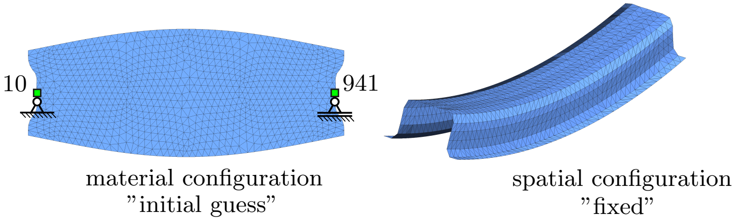

Figure 5.35: Generic rib: cylindrical projection (left) vs. target geometry (right)

Again, the aim of the following study is to obtain a deeper understanding of the impact of preferred material directions on the shape of the resulting cutting patterns for anticlastic target structures. Hence, in addition to the isotropic Neo-Hookean strain-energy function (5.74), the nonlinear material model[20] describing a glass plain weave (5.76) is applied.

---

[19] according to the concept of VaReS the minimization of total elastic potential energy is chosen as governing criterion

[20] Aimène et al. [1]

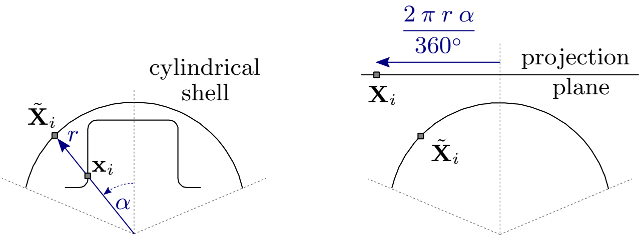

Figure 5.36: Initialization strategy: projection onto surrounding cylinder (left) and transfer to projection plane (right)

5.4.3.1 Neo-Hookean material

Considering the isotropic case, the applied material parameters (Young's modulus, Poisson's ratio) are listed in Table 5.5. Choosing the second-order approach for solving the optimization problem requires an adequate set of Dirichlet BCs. Hence a statically determinate support is realized by restraining node #10 and node #941 (cf. Figure 5.35 (left)).

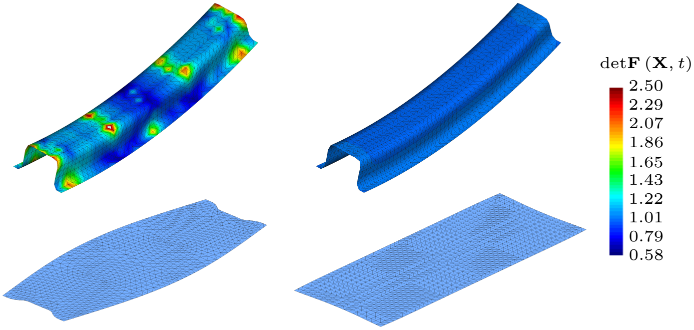

Figure 5.37: Generic rib (Neo-Hookean): volume ratio det$\mathbf{F}\,(\mathbf{X},t)$ resulting from an initial motion $\chi\,(\mathbf{X}_{\text{init}},t)$ (left) and the converged motion $\chi\,(\mathbf{X}_{\text{conv}},t)$ (right)

A converged solution is achieved within a total number of $n_{\text{total}} = 24$ iterations split into 5 time steps ($n_1 = 5$, $n_2 = 5$, $n_3 = 4$, $n_4 = 5$, $n_5 = 5$). As illustrated in Figure 5.37, in case of an optimized cutting pattern a significant improvement in the volume ratio can be observed. The optimized cutting pattern and the resulting von Mises stresses within the target structure are shown in Figure 5.38 and Figure 5.39, respectively.

CONCLUSION: Due to the isotropic material model, the shape of the optimized cutting pattern remains axially symmetric.

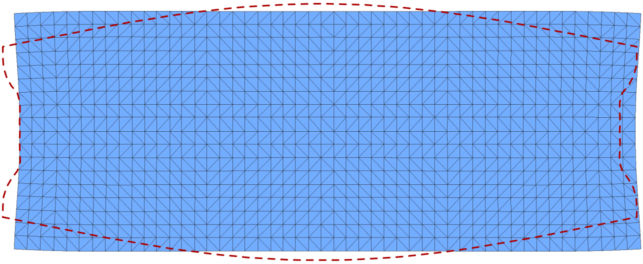

Figure 5.38: Generic rib (Neo-Hookean): initial guess by cylindrical projection (red dashed) vs. optimized cutting pattern

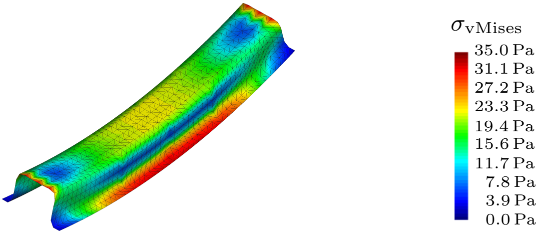

Figure 5.39: Generic rib (Neo-Hookean): resulting von Mises stresses

5.4.3.2 Glass plain weave

Consider the anisotropic (more precisely orthotropic) case. Again, the same strain-energy function (5.76) describing a balanced plain weave made of glass fibers is applied - see Table 5.6 and Table 5.7. Two different scenarios are defined (cf. Figure 5.40) showing the effect of anisotropy on the resulting shape of the cutting pattern. Both optimization problems (scenarios) are then solved by applying the method of steepest descent. Hence, no additional Dirichlet BCs are required.

Applying 1 time step, a converged solution for the respective scenario is achieved within $n_{\#1} = 2059$ and $n_{\#2} = 45855$ iterations. For both scenarios, the optimized cutting patterns (the red dashed lines indicate the initial guess) as well as the improvements in terms of the volume ratio $\det\mathbf{F}(\mathbf{X}, t)$ are illustrated in Figure 5.41 and Figure 5.42, respectively. Furthermore, the occurring fiber twists (i.e. the deviation of the primary orthogonal fibers arising due to the motion $\chi(\mathbf{X}, t)$) are shown in Figure 5.43, respectively.

CONCLUSION: Due to the orthotropic material behavior, the shape of the optimized cutting patterns remain axially symmetric w.r.t. the structure's symmetry axes. The low shear stiffness of the applied material

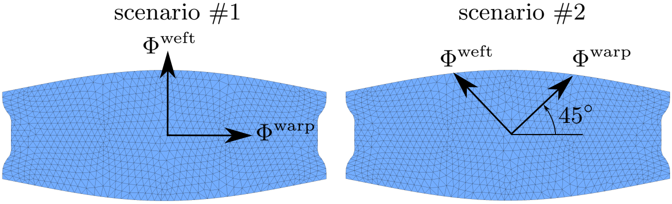

Figure 5.40: Generic rib (plain weave): material fiber orientation (initial guess by cylindrical projection) for scenario #1 (left) and scenario #2 (right)

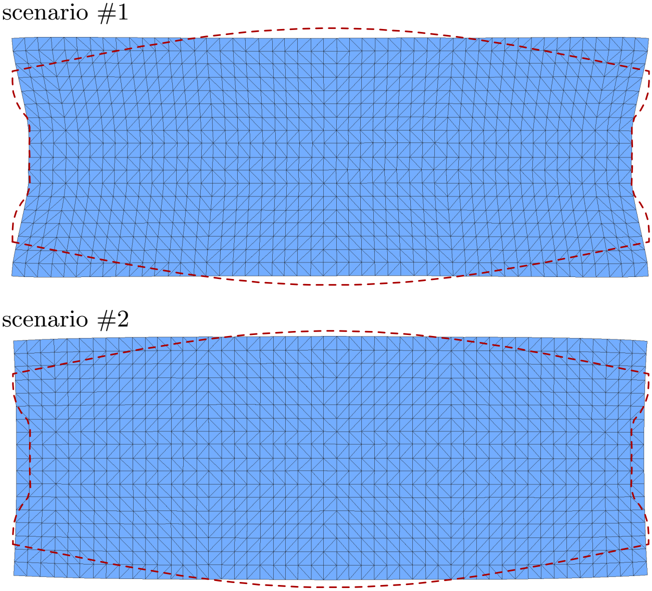

Figure 5.41: Generic rib (plain weave): initial guess by cylindrical projection (red dashed) vs. optimized cutting pattern

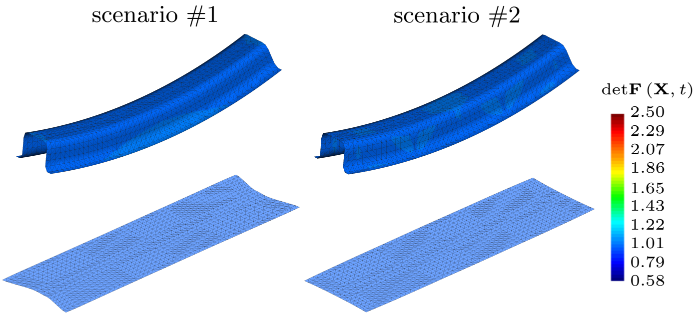

Figure 5.42: Generic rib (plain weave): volume ratio $\det\mathbf{F}(\mathbf{X}, t)$ resulting from the converged motion $\chi(\mathbf{X}_{\text{conv}}, t)$ for scenario #1 (left) and scenario #2 (right)

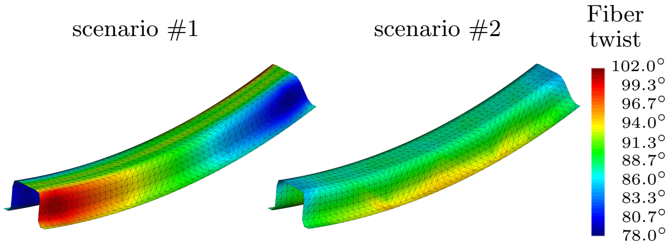

Figure 5.43: Generic rib (plain weave): fiber twist (5.86) resulting from the converged motion $\chi(\mathbf{X}_{\text{conv}}, t)$ for scenario #1 (left) and scenario #2 (right)

leads to an almost rectangular cutting pattern, if the fiber directions are not aligned with the structure's symmetry axis.

5.4.4 Summary

The outcome of the presented examples (cylindrical shell, spherical shell and generic rib) underline the general applicability, robustness and potential of the developed *Variation of Reference Strategy*.

The cylindrical shell serves as a benchmark verifying both the introduced second-order as well as the first-order approach. Within that scope, the discussed strategies, namely the time stepping strategy - Section 5.3.1, the damped Newton-Raphson - Section 5.3.2 and the adaptive line search for the method of steepest descent - Section 5.3.3, have been applied and their impacts on the convergence behavior have been verified. For all cases, the congruent rectangle (analytical solution) has been met. In case of the undamped Newton-Raphson scheme (the second-order approach), the expected quadratic convergence rate was obtained. In case of the damped Newton-Raphson scheme (the second-order approach) as well as the method of steepest descent, the expected linear convergence rate was obtained.

The numerical experiments based on the spherical shell and the generic rib show a significant influence of preferred material directions (anisotropy) on the shape of the resulting cutting patterns. It is important to mention that in case of an underlying isotropic strain-energy function, the (rotational or axial) symmetry of the target structure is preserved within the optimized cutting pattern. If an orthotropic material model is applied to a rotationally symmetric target structure, an axial symmetry w.r.t. the preferred material direction within the optimized cutting pattern can be observed. In contrast, for axially symmetric target structures the optimized cutting patterns remain axially symmetric w.r.t. the target structure's symmetry axes.

6

Applications / projects

"Der Worte sind genug gewechselt,
Laßt mich auch endlich Taten sehen!"

— Johann Wolfgang von Goethe, 1749 - 1832
German poet and politician

Leaving an academic environment, this chapter focuses on industrial applications of the developed *response surface based material model* as well as the *Variation of Reference Strategy.* In the following, two different projects are presented and their outcome is discussed. The first project deals with the generation of optimized cutting patterns for selected parts of a textile car seat cover. The presented results show the capabilities of the introduced *Variation of Reference Strategy* (see Chapter 5) in combination with the introduced material model (see Chapter 4). Furthermore, the effect of a predefined stress state on the shape of the cutting pattern and the underlying foam structure (frame) of the car seat is addressed. The second project focuses on the generation of optimized cutting patterns for structures made of carbon fiber reinforced plastics (CFRPs). In general, such structures consist of several layers (plies) exhibiting different preferred material directions. The presented results show the capabilities of the *Variation of Reference Strategy* in combination with highly anisotropic material models. Furthermore, the offset of each ply to the mid-surface of the structure of investigation is also taken into account.

6.1 Car seat (DFG BL 306 20-2)

The presented results are based on the outcome of the research project *DFG BL 306 20-2* funded by the *German Research Foundation*. The project was part of a cooperation between the Institute of Textile Machinery and High Performance Material Technology (ITM) at the Dresden University of Technology, the Institute of Textile Technology and Process Engineering (ITV) Denkendorf and the Chair of Structural Analysis at the Technische Universität München.

6.1.1 Numerical model

The aim of this application is the generation of optimized cutting patterns for selected parts of a textile car seat cover. Figure 6.1 illustrates the full CAD (surface-) model of the target structure. In order to show the capability of the presented *Variation of Reference Strategy* (see Chapter 5) in combination with the material model for textile fabrics (see Chapter 4), the knee support (green), side flange (magenta) and rear flange (blue) are chosen for further investigation (see Figure 6.1).

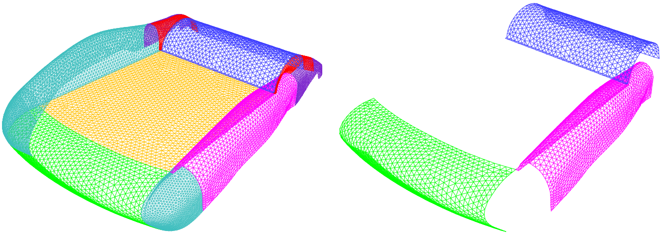

Figure 6.1: Car seat: full CAD model (left) vs. selected parts (right): knee support (green), side flange (magenta) and rear flange (blue)

For all simulations, the response surface based strain-energy function of an interlock jersey is applied to the respective part. The corresponding material response surfaces/curves are discussed in Section 4.2.1 in very detail.

A closer look on the design of the car seat reveals that in contrast to architectural membranes the textile covers are supported by an elastic foam structure. From a manufacturing point of view a so-called *compensation* of the optimized cutting pattern is requested. The resulting shrinkage of the cutting pattern ensures a better fit of the textile cover on the underlying foam structure of the car seat. Recalling Equation (5.3), the effect of compensation is incorporated in VaReS and can be controlled by means of an elastic potential representing a predefined stress state. In textile engineering the specification of these normal stresses in terms of compensation forces is very common. Keeping in mind that the material behavior of the applied textile fabric is defined by means of a surface based strain-energy function, these compensation forces need to be expressed in terms of a set of structural invariants - see Section 6.1.1.1. The predefined compensation forces as well as the corresponding Cauchy stresses and structural invariants for the applied interlock jersey are summarized in Table 6.1.

	warp $(\bullet)_{\|}$			weft $(\bullet)_{\perp}$	
$f_{\|}$ $\left[{}^{\mathrm{N}}/_{\mathrm{m}}\right]$	$\sigma_{\|}^{\mathrm{pre}}$ [Pa]	$I_{\|}^{\mathrm{pre}}$ $[-]$	$f_{\perp}$ $\left[{}^{\mathrm{N}}/_{\mathrm{m}}\right]$	$\sigma_{\perp}^{\mathrm{pre}}$ [Pa]	$I_{\perp}^{\mathrm{pre}}$ $[-]$
18.0	6000.0	0.986	88.0	29333.0	1.1179

Table 6.1: Predefined stress state: Compensation forces, Cauchy stresses and structural invariants in warp and weft direction

It is well known for architectural membranes that the stresses within the membrane are directly linked to its shape (*equilibrium surface*). However, in case of supported structures, the residual stresses arising due to the draping process and/or compensation of the cutting pattern generate pressure-like forces acting on the underlying frame. These so-called *effective forces* are directly linked to the geometry of the target structure - see Section 6.1.1.2. Within the scope of this example (car seat) the textile fabric is supported by an underlying foam structure and therefore the effective forces acting on the underlying foam structure are of interest as well.

REMARK I: The correlation between the effective forces, Cauchy stresses and structural invariants stated in Table 6.1 strongly depends on the considered material. In case of a response surface based strain-energy function this correlation is not quite trivial and is therefore explained in more detail in Section 6.1.1.1.

6.1.1.1 Predefined stress state

Consider a response surface based strain-energy function introduced in Chapter 4. In case of predefined normal stresses, the desired compensation forces ($f_{\|}^{\mathrm{pre}}$ and $f_{\perp}^{\mathrm{pre}}$) need to be expressed in terms of a set of associated structural invariants ($I_{\|}^{\mathrm{pre}}$ and $I_{\perp}^{\mathrm{pre}}$). Therefore, additional response surfaces, called *stress surfaces*, representing the in-plane normal Cauchy stresses (σ_{11} and σ_{22}) need to be established (see Section 4.1.1.1):

$$\begin{aligned} \mathcal{S}_{\|} : (\xi,\eta) \in [0,1] \times [0,1] \rightarrow \mathcal{V}_{\|} \, , \\ (\xi,\eta) \rightarrow \left[I_{\|}(\xi,\eta) \, , I_{\perp}(\xi,\eta) \, , \sigma_{11}(\xi,\eta) \right] \end{aligned} \tag{6.1a}$$

$$\begin{aligned} \mathcal{S}_{\perp} : (\xi,\eta) \in [0,1] \times [0,1] \rightarrow \mathcal{V}_{\perp} \, , \\ (\xi,\eta) \rightarrow \left[I_{\|}(\xi,\eta) \, , I_{\perp}(\xi,\eta) \, , \sigma_{22}(\xi,\eta) \right] \end{aligned} \tag{6.1b}$$

with $\mathcal{V}_{\|} \subset \mathbb{R}^3$ and $\mathcal{V}_{\perp} \subset \mathbb{R}^3$ being Euclidean vector spaces over the bodies $\mathcal{K}^3_{\|}$ and $\mathcal{K}^3_{\perp}$, respectively:

$$\mathcal{K}^3_{\|} \to \mathcal{V}_{\|}\,, \quad \left(I_{\|}, I_{\perp}, \sigma_{11}\right) \to I_{\|}\mathbf{e}_1 + I_{\perp}\mathbf{e}_2 + \sigma_{11}\mathbf{e}_3 \tag{6.2a}$$

$$\mathcal{K}^3_{\perp} \to \mathcal{V}_{\perp}\,, \quad \left(I_{\|}, I_{\perp}, \sigma_{22}\right) \to I_{\|}\mathbf{e}_1 + I_{\perp}\mathbf{e}_2 + \sigma_{22}\mathbf{e}_3 \tag{6.2b}$$

and

$$\boldsymbol{\sigma} = J^{-1}\chi_*\left(2\frac{\partial \Psi_{\text{norm}}}{\partial \mathbf{C}}\right) = \sigma_{ij}\,\frac{\Phi_i}{\|\Phi_i\|} \otimes \frac{\Phi_j}{\|\Phi_j\|} \quad \text{with} \quad i,j = 1\ldots2 \tag{6.3}$$

Due to the experimental setup (see Section 4.1.2), the principal directions are equivalent to the fiber directions, i.e. the coefficients σ_{ij} in Equation (6.3) represent the true principal Cauchy stresses. Hence, the compensation forces can easily be converted into the in-plane normal coefficients of the Cauchy stress tensor defined by Equation (6.3):

$$\sigma^{\text{pre}}_{\|} = \sigma^{\text{pre}}_{11} = \frac{f^{\text{pre}}_{\|}}{\text{thk}} \quad \text{and} \quad \sigma^{\text{pre}}_{\perp} = \sigma^{\text{pre}}_{22} = \frac{f^{\text{pre}}_{\perp}}{\text{thk}} \tag{6.4}$$

Figure 6.2 illustrates the stress surfaces defined in Equation (6.1) based on the experimental data of an interlock jersey. The specified compensation forces expressed in terms of Cauchy stresses $\sigma^{\text{pre}}_{\|}$ and $\sigma^{\text{pre}}_{\perp}$ (see Table 6.1) are highlighted as isolines (solid black lines in Figure 6.2) in the respective stress surfaces $\mathcal{S}_{\|}$ and $\mathcal{S}_{\perp}$.

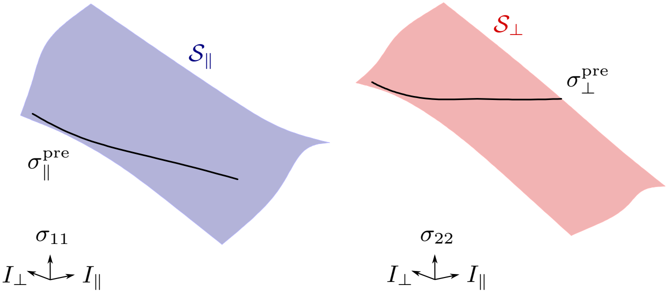

Figure 6.2: Predefined normal stress state $\sigma^{\text{pre}}_{\|}$ and $\sigma^{\text{pre}}_{\perp}$ (solid black lines) for an interlock jersey: stress surface $\mathcal{S}_{\|}$ (left) vs. stress surface $\mathcal{S}_{\perp}$ (right)

As stated in the assumptions made for the *response surface based material model* introduced in Section 4.1 (orthotropic material - Equation (4.7)), the normal and shear stresses are decoupled. In case of predefined normal stresses, the shear stresses are not affected by these stresses and can be neglected ($\sigma^{\text{pre}}_{\sharp} = 0$). Hence, the set of structural invariants representing

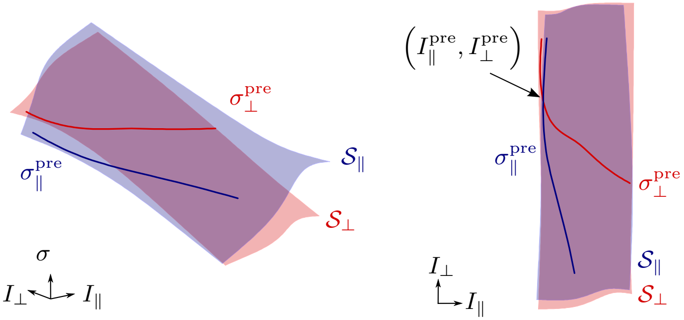

Figure 6.3: Predefined normal stress state $\sigma_{\|}^{\text{pre}}$ (solid blue line) and $\sigma_{\perp}^{\text{pre}}$ (solid red line) for an interlock jersey: skew isolines (left) vs. orthogonal projection of isolines (right)

the specified compensation forces can be interpreted as a point belonging to both isolines of the stress surface $\mathcal{S}_{\|}$ and $\mathcal{S}_{\perp}$. More precisely, the intersection $\left(I_{\|}^{\text{pre}}, I_{\perp}^{\text{pre}}\right)$ between the orthogonal projections of both isolines onto the $I_{\|} - I_{\perp} -$ plane. Figure 6.3 illustrates the described strategy for the mentioned interlock jersey and compensation forces.

6.1.1.2 Effective forces on the frame

In case of a syncalstic or anticlastic membrane structure, certain stresses are still remaining within the target geometry, i.e. after deforming the cutting pattern into its final 3 dimensional shape (draping process). If the membrane structure is supported (car seat), the effect of these residual stresses on the underlying frame can be expressed in terms of pressure-like *effective forces* ($\mathbf{f}_{\text{eff}} = p_{\text{surf}} \cdot \mathbf{n}$). Assuming plane stress conditions, the magnitude p_{surf} of such an effective force is equivalent to the surface pressure resulting from the interaction of curvature and residual stresses within the membrane. By means of *Barlow's formula* the following relation can be established:

$$\mathbf{f}_{\text{eff}} = \left(\frac{t \cdot \hat{\sigma}_{11}}{\mathrm{R}_1} + \frac{t \cdot \hat{\sigma}_{22}}{\mathrm{R}_2} \right) \cdot \mathbf{n} \tag{6.5}$$

with R_1 and R_2 being the principal radii of curvature (see Equation (2.41)) and $\mathbf{n}$ being the surface normal vector. The stress components $\hat{\sigma}_{11}$ and $\hat{\sigma}_{22}$ are the normal coefficients of the Cauchy stress tensor in the principal directions $\hat{\mathbf{n}}_1$ and $\hat{\mathbf{n}}_2$ (see Equation (2.40)), respectively:

$$\boldsymbol{\sigma} = \hat{\sigma}_{ij}\, \hat{\mathbf{n}}_i \otimes \hat{\mathbf{n}}_j \tag{6.6}$$

It is important to mention that the sign of the surface pressure indicates the direction of action of the effective force in terms of the surface normal vector, see Equation (6.5). Thus, if $p_{\text{surf}} > 0$ the resulting force is aligned with the surface normal $\mathbf{n}$, else against the direction of $\mathbf{n}$.

6.1.2 Results

Besides the generation of optimized cutting patterns, the effect of a prescribed stress state on the underlying foam structure is in the focus of this research project. Therefore, for each selected part (see Figure 6.1) two scenarios - one *unstressed* and one *pre-stressed* - have been investigated. The corresponding predefined stress state is listed in Table 6.1. Below, the optimized cutting patterns for each part and scenario (knee support (see Section 6.1.2.1), rear flange (see Section 6.1.2.2), side flange (see Section 6.1.2.3)) are presented and compared against each other. Due to the chosen interlock jersey (rrk), the resulting fiber distortions are of minor interest and will not be discussed here.

Recalling Equation (6.5), the predefined stress state will lead to nonconstant effective forces strongly depending on the curvature of the target geometry. In order to asses the quality of the optimized cutting patterns (regular and compensated), the relative error Error_{rel} of the *surface pressure* p_{surf} (i.e. the magnitude of the effective forces - see Section 6.1.1.2) acting on the underlying foam structure is defined as follows:

$$\text{Error}_{rel} = \frac{p_{\text{surf}} - p_{\text{surf}}^{\text{pre}}}{p_{\text{surf}}^{\text{pre}}} \tag{6.7}$$

with p_{surf} being the surface pressure arising due to the residual stresses within the textile fabric and $p_{\text{surf}}^{\text{pre}}$ being the target surface pressure which is corresponding to the predefined stress state $\sigma_{\parallel}^{\text{pre}}$ and $\sigma_{\perp}^{\text{pre}}$.

6.1.2.1 Results: knee support

Figure 6.4 illustrates the optimized cutting patterns for both scenarios, the regular (dashed blue) and the pre-stressed (solid green). The chosen material directions are indicated by the fiber coordinate system in the lower left. Figure 6.5 illustrates the resulting strain-energies $\Psi_{\text{rrk}}(\mathbf{C})$ for both scenarios. Figure 6.6 shows the target surface pressure field and the averaged normal directions defining its direction of action. Figure 6.7 shows the resulting surface pressure field for both scenarios. The relative error for both scenarios is visualized in Figure 6.8.

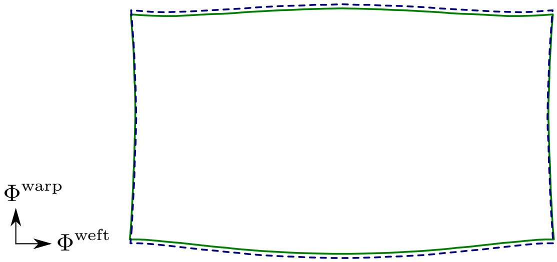

Figure 6.4: Cutting patterns for the knee support: compensated (solid green) vs. regular (dashed blue)

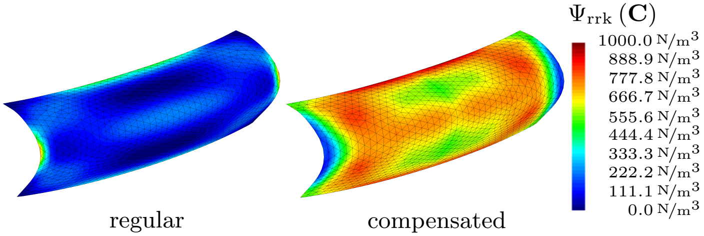

Figure 6.5: Strain-energy $\Psi_{\text{rrk}}(\mathbf{C})$ for the knee support: regular (left) vs. compensated (right)

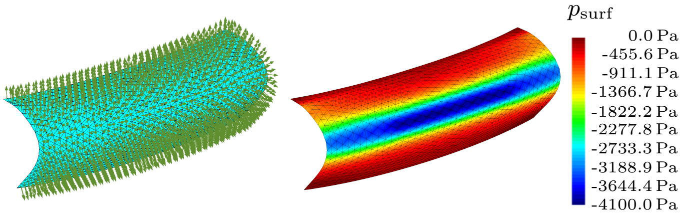

Figure 6.6: Surface pressure $p_{\text{surf}}^{\text{pre}}$ for the knee support: averaged normal directions of the target geometry (left) vs. target surface pressure due to the predefined stress state (right)

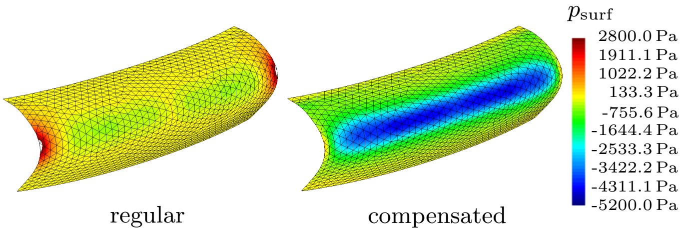

Figure 6.7: Surface pressure p_{surf} for the knee support: regular (left) vs. compensated (right)

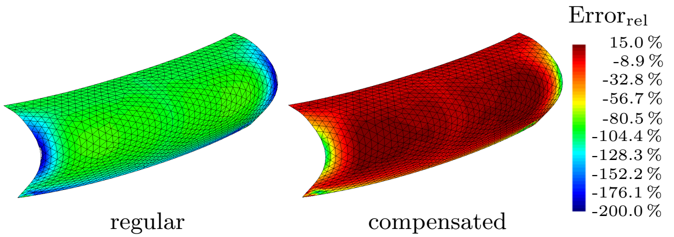

Figure 6.8: Relative error $\mathrm{Error}_{\mathrm{rel}}$ for the knee support: regular (left) vs. compensated (right)

6.1.2.2 Results: rear flange

Figure 6.9 illustrates the optimized cutting patterns for both scenarios, the regular (dashed blue) and the pre-stressed (solid green). The chosen material directions are indicated by the fiber coordinate system in the lower left. Figure 6.10 illustrates the resulting strain-energies $\Psi_{\mathrm{rrk}}\left(\mathbf{C}\right)$ for both scenarios.

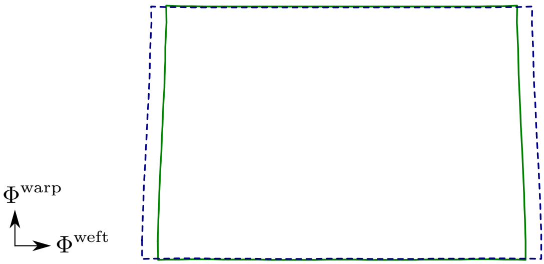

Figure 6.9: Cutting patterns for the rear flange: compensated (solid green) vs. regular (dashed blue)

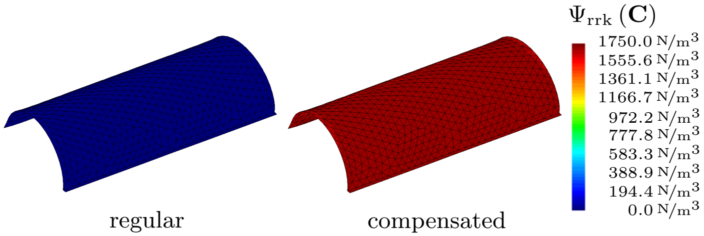

Figure 6.10: Strain-energy $\Psi_{\mathrm{rrk}}(\mathbf{C})$ for the rear flange: regular (left) vs. compensated (right)

Figure 6.11 shows the target surface pressure field and the averaged normal directions defining its direction of action. Figure 6.12 shows the resulting surface pressure field for both scenarios. The relative error for both scenarios is visualized in Figure 6.13.

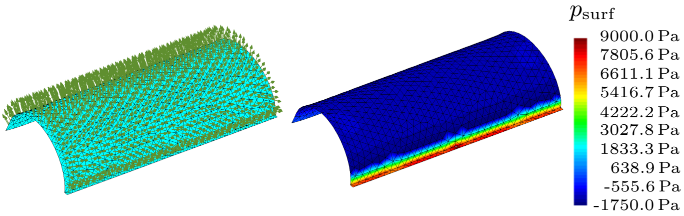

Figure 6.11: Surface pressure $p_{\mathrm{surf}}^{\mathrm{pre}}$ for the rear flange: averaged normal directions of the target geometry (left) vs. target surface pressure due to the predefined stress state (right)

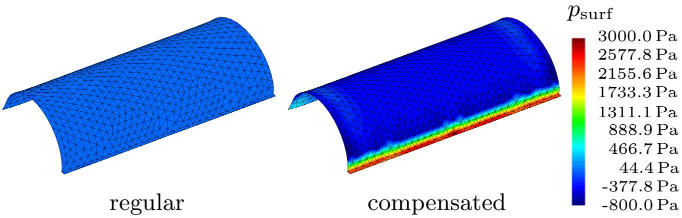

Figure 6.12: Surface pressure p_{surf} for the rear flange: regular (left) vs. compensated (right)

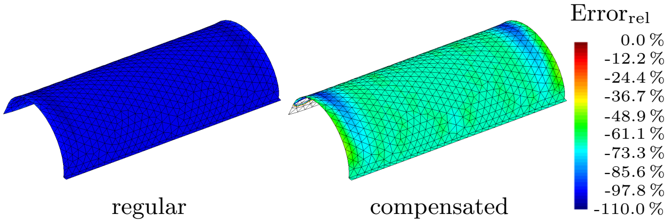

regular compensated

Figure 6.13: Relative error $\mathrm{Error}_{\mathrm{rel}}$ for the rear flange: regular (left) vs. compensated (right)

6.1.2.3 Results: side flange

Figure 6.14 illustrates the optimized cutting patterns for both scenarios, the regular (dashed blue) and the pre-stressed (solid green). The chosen material directions are indicated by the fiber coordinate system in the lower left. Figure 6.15 illustrates the resulting strain-energies $\Psi_{\mathrm{rrk}}(\mathbf{C})$ for both scenarios.

Figure 6.14: Cutting patterns for the side flange: compensated (solid green) vs. regular (dashed blue)

Figure 6.16 shows the target surface pressure field and the averaged normal directions defining its direction of action. Figure 6.17 shows the resulting surface pressure field for both scenarios. The relative error for both scenarios is visualized in Figure 6.18.

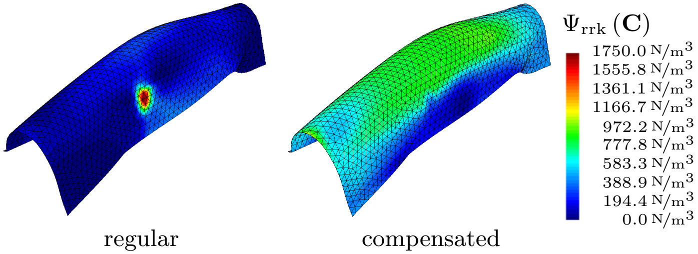

regular compensated

Figure 6.15: Strain-energy $\Psi_{\mathrm{rrk}}\,(\mathbf{C})$ for the side flange: regular (left) vs. compensated (right)

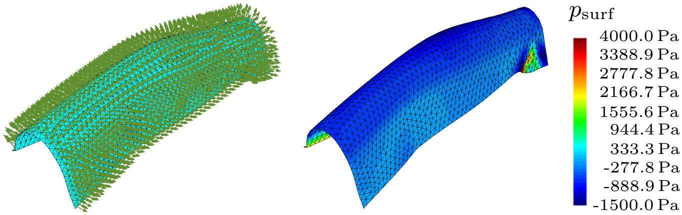

Figure 6.16: Surface pressure $p_{\mathrm{surf}}^{\mathrm{pre}}$ for the side flange: averaged normal directions of the target geometry (left) vs. target surface pressure due to the predefined stress state (right)

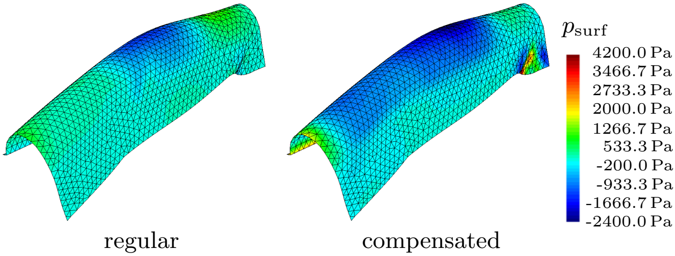

regular compensated

Figure 6.17: Surface pressure p_{surf} for the side flange: regular (left) vs. compensated (right)

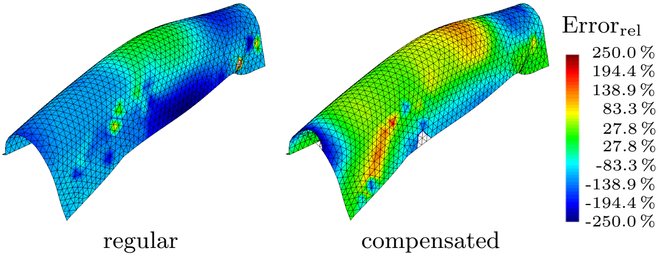

Figure 6.18: Relative error Error$_{\mathrm{rel}}$ for the side flange: regular (left) vs. compensated (right)

6.1.3 Summary and Discussion

As shown in the previous Sections 6.1.2.1 - 6.1.2.3, for all selected parts the developed *Variation of Reference Strategy* (VaReS) proves to be capable of finding a regular as well as a compensated cutting pattern.

Consider the cutting patterns resulting from the unstressed scenario. All these cutting patterns still lead to certain levels of total elastic potential energy within the target structure, which are low but distinctly not zero (see Figure 6.5, Figure 6.10 and Figure 6.15). This outcome is to be expected since all three target structures are either described as synclastic (knee support) or anticlastic surfaces (side flange and rear flange). But it is important to note that the numbers itself are of less interest since they are directly related to the underlying material model. Thus, using the magnitude of the resulting strain-energy function as a quality criterion is not appropriate.

	target $[\mathrm{m}^2]$	regular $[\mathrm{m}^2]$	compensated $[\mathrm{m}^2]$
KS	79050.07 E-06	79312.25 E-06	76925.38 E-06
RF	61827.64 E-06	61828.87 E-06	57345.05 E-06
SF	72340.76 E-06	72767.84 E-06	70089.46 E-06

Table 6.2: Surface areas: knee support (KS), rear flange (RF), side flange (SF)

Consider the cutting patterns resulting from the pre-stressed scenario. For all parts the compensated cutting pattern is clearly smaller than the respective regular one. This leads to a noticeable increase of the total elastic potential energy (see Figure 6.5, Figure 6.10 and Figure 6.15). The surface areas of the each target structure (target) and of the corresponding cutting patterns resulting from both the unstressed (regular) and pre-stressed (compensated) scenario are summarized in Table 6.2. This outcome is to be expected, since these shrinkages are the mechanisms that realize stress states shifted from the energetic optimum, i.e. the minimum of the total elastic potential energy. In order to judge about the quality of the compensated cutting patterns the relative error $\text{Error}_{\text{rel}}$ of the resulting surface pressure fields are shown in Figure 6.8, Figure 6.13 and Figure 6.18. Especially in case of the rear flange and the side flange remarkable deviations of the corresponding target surface pressure field can be observed. The reason for this is the geometry of the target structure (car seat). In contrast to architectural membranes, where its geometry is characterized by an equilibrium between the stresses and the boundary conditions (*form-found surface*[1]), the shape of the selected parts (knee support, rear flange, side flange) is defined by its underlying frame (supported structure). Consequently, the prescribed stress state within the textile fabric is not necessary in equilibrium with the curvature defined by the underlying frame (additional constraints) and therefore a desired constantly distributed stress state (predefined stress state) might be non-physical.

CONCLUSION: Due to the fact that each target structure is not a form-found surface, a constant prescribed stress field leads to a nonconstant pressure field strongly depending on the local curvature, see Figure 6.6, Figure 6.11 and Figure 6.16. Especially for elastically supported structures, a constant effective force acting on the underlying frame is of more interest. Thus, instead of prescribing the stress state a predefined surface pressure would be a more adequate criterion controlling the compensation of the cutting pattern.

---

[1] for further information the author refers to DIERINGER ET. AL [36], DIERINGER [37], LINHARD [74] and LINHARD ET AL. [75] [76]

6.2 Structures made of CFRP

The presented results are based on the outcome of a research project funded by the *BMW Group*. The project was part of a cooperation between the division Prozessgestaltung, Simulation, Entwicklung CAE at the BMW Group and the Chair of Structural Analysis at the Technische Universität München.

6.2.1 Material model for a carbon UD-ply

Consider a non-crimp fabric (UD-ply) made of carbon fibers (cf. Figure 1.2). In order to describe its highly anisotropic behavior on a macroscopic level an additional strain-energy function based on the structural invariants (3.57) in direction of the rovings needs to be introduced. Within that course, Bonet and Burton [22] extended the Neo-Hookean strain-energy function (5.74) in their work as follows:

$$\Psi_{\mathrm{Bonet}} = \left[\alpha + \beta \ln \sqrt{I_3} + \gamma \left(I_4 - 1\right)\right] \left(I_4 - 1\right) - 0.5\alpha \left(I_5 + 1\right) \tag{6.8}$$

with $\alpha = \alpha\left(E, \nu, G_\phi\right)$, $\beta = \beta\left(E_\phi, E, \nu\right)$ and $\gamma = \gamma\left(E_\phi, E, \nu, G_\phi\right)$ being coefficients[2] depending on the Young's modulus in direction of the rovings E_ϕ, the shear modulus in direction of the rovings G_ϕ, the Young's modulus E and the Poisson's ratio ν of the isotopic part. Finally, Equation (6.8) is simply added:

$$\Psi_{\mathrm{UD-Ply}} = \Psi_{\mathrm{NeoHook}} + \Psi_{\mathrm{Bonet}} \tag{6.9}$$

The corresponding material parameters for a single UD-ply made of carbon fibers are listed in Table 6.3.

thk [m]	E_ϕ [Pa]	G_ϕ [Pa]	E [Pa]	ν [−]
0.25E − 03	75.0E + 09	0.3E + 09	0.3E + 09	0.0

Table 6.3: Material parameter: carbon UD-ply

6.2.2 Cutting pattern for stacks

In general, lightweight structures made of glass/carbon fiber reinforced plastics (aeronautic, aerospace and automotive applications) consist of several plies exhibiting different fiber orientations which are stacked atop each other. The pile of different plies is called stack. Its internal texture is called stacking sequence or lay-up. As already shown in Section 5.4, a preferred material direction directly effects the shape of the resulting cutting pattern. Hence, a common cutting pattern for a stack would lead to areas within each single ply where the resulting stresses are not optimized. The following thought experiment will underline this effect.

---

[2] explained in more detail in Appendix C.3

Figure 6.19: Manufacturing of a BMW M3 CFRP rooftop: automated stacking of the single UD-plies (left) and preforming of the stack (right) [93]

Consider the generated cutting patterns of the generic rib (cf. Figure 5.41). Now, the cutting pattern of scenario #2 is subjected to the fiber orientation of scenario #1. The resulting stresses in warp and weft direction for both cutting patterns (optimized and disadvantageous) are illustrated and compared in Figure 6.20 and Figure 6.21, respectively.

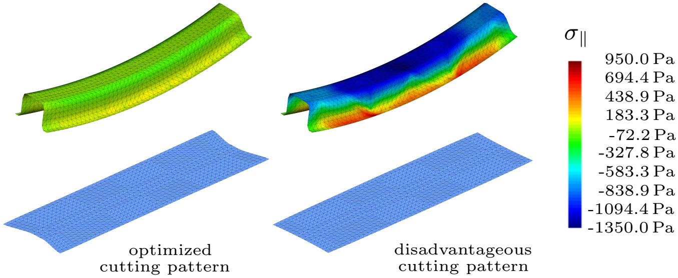

Figure 6.20: Generic rib (plain weave): resulting Cauchy-stresses (warp) within the target geometry - optimized cutting pattern (left) vs. disadvantageous cutting pattern (right)

Especially areas exhibiting high compressive stresses are of interest for a design engineer since they posses a higher vulnerability for the occurrence of wrinkles. In the presented example, a heavy increase of compressive stresses in warp direction can be observed, if a disadvantageous cutting pattern is applied. In order to understand this effect one has to take a closer look on the fiber twist defined by Equation (5.86). Figure 6.22 illustrates the resulting fiber twist for both cutting patterns (optimized and disadvantageous). In the case of a disadvantageous cutting pattern almost no fiber distortions can be observed, i.e. almost no shear deformations are occurring. However, this directly contradicts with the major advantage of textile fabrics compared to sheet metals which is based on the fabrics' shear

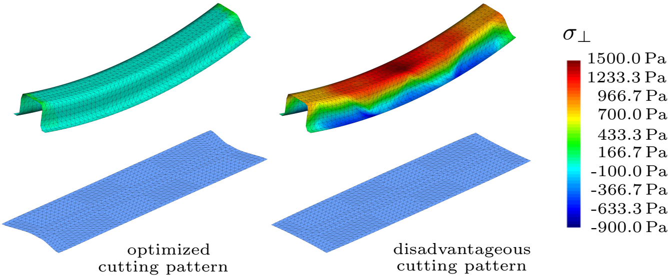

Figure 6.21: Generic rib (plain weave): resulting Cauchy-stresses (weft) within the target geometry - optimized cutting pattern (left) vs. disadvantageous cutting pattern (right)

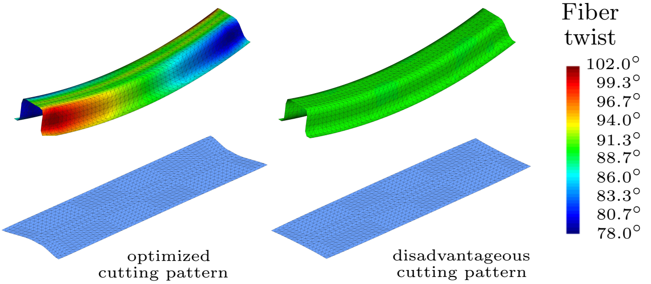

Figure 6.22: Generic rib (plain weave): resulting fiber twist within the target geometry - optimized cutting pattern (left) vs. disadvantageous cutting pattern (right)

flexibility. More precisely, the high shear flexibility of textile fabrics leads to a reduction of the undesired normal stresses (either tensile or compressive) which in turn enables a broader range of applications when it comes to synclastic or anticlastic structures. Hence, in order to take advantage of this effect, the optimized cutting pattern should preferably lead to almost only shear deformations. In oder to circumvent the shown complications, the optimized cutting patterns for each ply within the stack are created independently. Additionally, the offset of each ply to the mid-surface of the structure of investigation is taken into account. A very common stacking sequence is the so-called *quasi-isotropic* lay-up:

$$\phi_\alpha = \left[\, 0^\circ \,/\, 90^\circ \,/\, 45^\circ \,/\, -45^\circ \,/\, -45^\circ \,/\, 45^\circ \,/\, 90^\circ \,/\, 0^\circ \,\right]$$

In the following, this stacking sequence is applied to a synclastic (spherical shell - Section 6.2.3) and to an anticlastic (roof crossrail - Section 6.2.4) structure.

6.2.3 Spherical shell

Consider the 160° section of a hemispherical shell ($r = 0.5\text{m}$) already introduced in Section 5.4.2. Within the context of this example, the structure consists of 8 UD-plies made of carbon fibers which are arranged in a quasi-isotropic lay-up (cf. Figure 6.23).

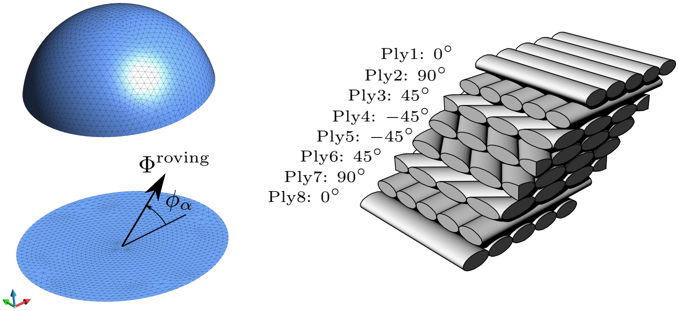

Figure 6.23: Spherical shell (stack): initial guess (orthogonal projection) vs. target structure (left) and quasi-isotropic stacking sequence (right)

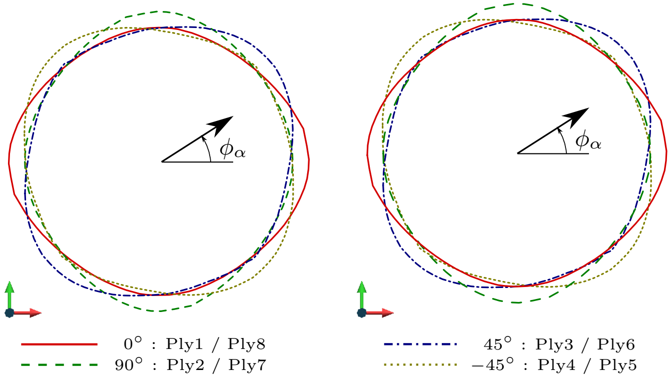

Figure 6.24: Spherical shell (stack): optimized cutting patterns for Ply1 - Ply4 (left) and Ply5 - Ply8 (right)

Therefore, the strain-energy function describing an UD-ply made of carbon fibers (6.9) is applied (see Table 6.3). As indicated in Section 5.4.2.2, the problem is initialized with an orthogonal projection and solved by means of the first-order approach (method of steepest descent). Thus, no additional Dirichlet BCs are mandatory. The goal is now to find the individual optimized cutting pattern for each ply within the stack, i.e. taking into

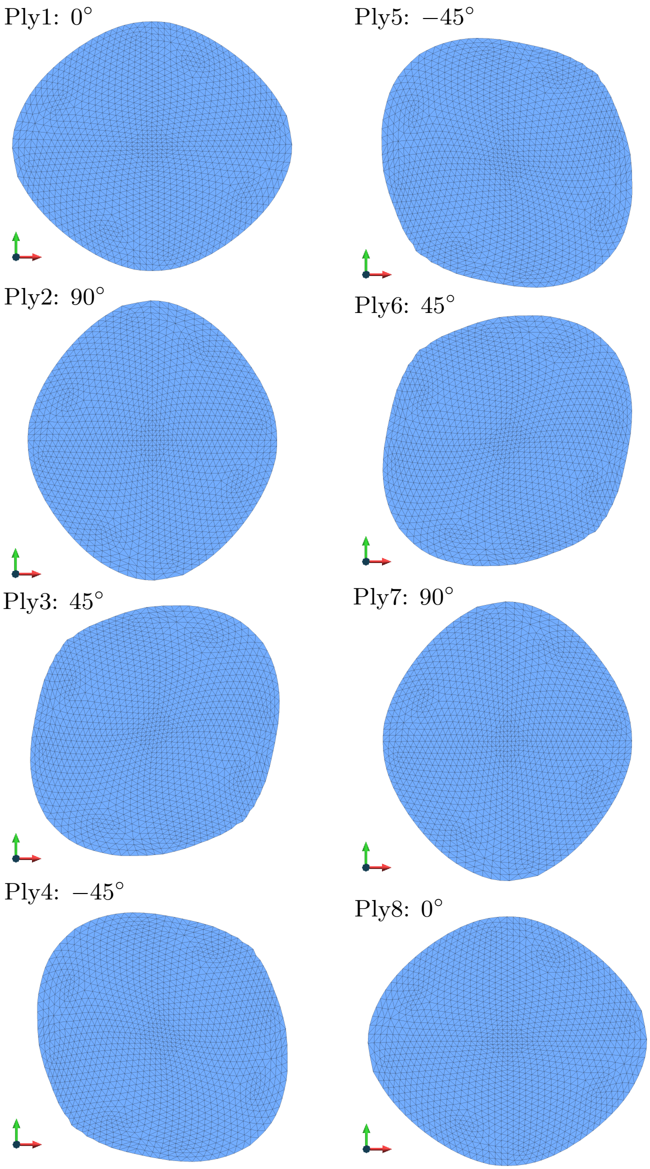

Ply1: 0°

Ply2: 90°

Ply3: 45°

Ply4: −45°

Ply5: −45°

Ply6: 45°

Ply7: 90°

Ply8: 0°

Figure 6.25: Spherical shell (stack): optimized cutting patterns Ply1 - Ply4 (left) and Ply5 - Ply8 (right)

account the fiber orientation within the ply and its off-set from the mid-surface. The optimized cutting patterns are illustrated in Figure 6.24 and Figure 6.25.

REMARK I: During the entire manufacturing process (i.e. draping, infiltration and curing) the stack is supported by the mold. Due to its construction the structural behavior of the mold is considered as rigid compared to stack. Therefore, the effective forces acting on the mold (underlying frame) are of less interest.

REMARK II: Due to the manufacturing process and the high tensile stiffness of the carbon rovings, no predefined stress-state needs to be taken into account.

6.2.4 Roof crossrail

Consider a car roof crossrail made of carbon fibers (cf. Figure 6.26). The chosen stack consists of 8 UD-plies in a quasi-isotropic lay-up. Similar to the previous example (spherical shell - Section 6.2.3), the goal is to find the individual optimized cutting pattern for each ply within the stack, i.e. taking into account the fiber orientation within the ply and its offset from the mid-surface. But in contrast to a rotationally symmetric target structure, now an axially symmetric one is under investigation.

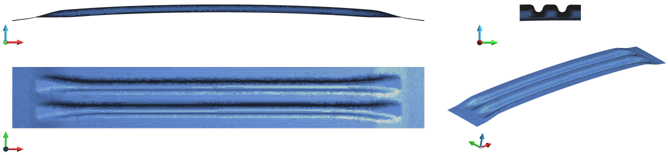

Figure 6.26: Roof crossrail: target structure

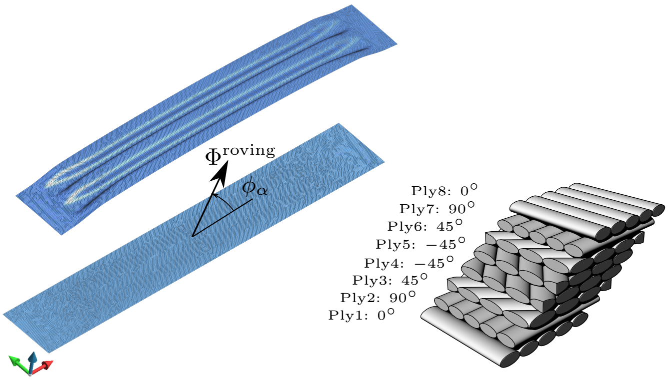

Figure 6.27: Roof crossrail (stack): initial guess (orthogonal projection) vs. target structure (left) and quasi-isotropic stacking sequence (right)

Furthermore, the strain-energy function defined by Equation (6.9) is applied for describing the behavior of each UD-ply (see Table 6.3). The problem is initialized with an orthogonal projection (cf. Figure 6.27) and solved by means of the first-order approach (method of steepest descent). Thus, no additional Dirichlet BCs are mandatory. The optimized cutting patterns are illustrated in Figure 6.28 and Figure 6.29.

REMARK III: During the entire manufacturing process (i.e. draping, infiltration and curing) the stack is supported by the mold. Due to its construction the structural behavior of the mold is considered as rigid

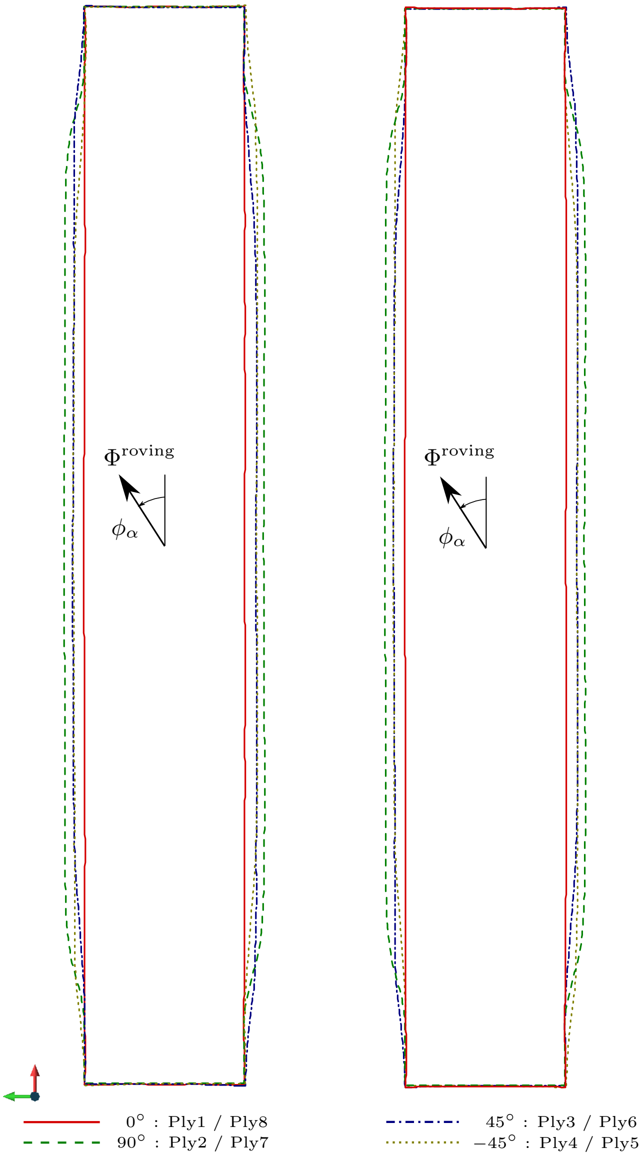

Figure 6.28: Roof crossrail (stack): optimized cutting patterns for Ply1 - Ply4 (left) and Ply5 - Ply8 (right)

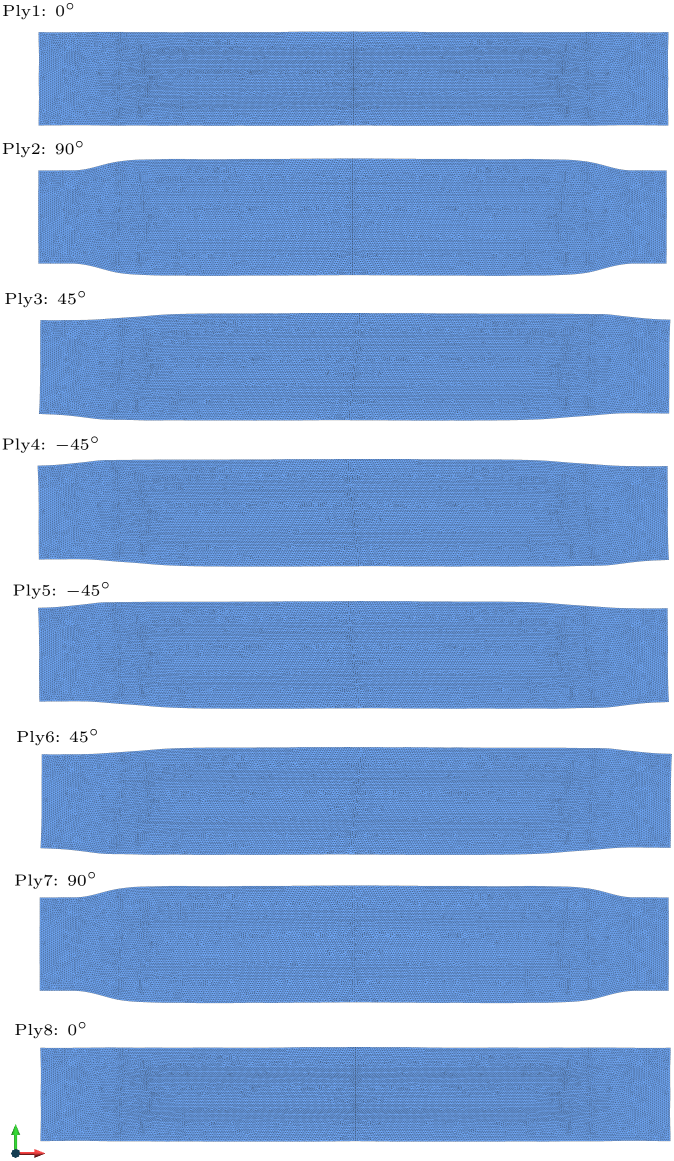

Figure 6.29: Roof crossrail (stack): optimized cutting patterns (individual UD-ply)

compared to stack. Therefore, the effective forces acting on the mold (underlying frame) are of less interest.

REMARK IV: Due to the manufacturing process and the high tensile stiffness of the carbon rovings, no predefined stress-state needs to be taken into account.

6.2.5 Summary and Discussion

The previous sections (6.2.3 - 6.2.4) have shown the capabilities of the developed *Variation of Reference Strategy* applied to supported structures in combination with highly anisotropic nonlinear materials. Furthermore, different fiber orientations within the target structure have been dealt with. For both structures, the spherical shell (synclastic) as well as the roof crossrail (anticlastic), a set of optimized cutting patterns has been found taking into account both the preferred material directions as well as the offset of each UD-ply to the structure's mid-surface.

For all cases, a strong dependency between the orientation of the UD-ply (preferred material direction) and the shape of the optimized cutting pattern can be observed. The offset of each UD-ply to the structure's mid-surface is reflected by a difference in the surface area of two corresponding[3] UD-plies. For each target structure, spherical shell and car roof crossrail, the corresponding UD-plies are compared with each other in Table 6.4 and Table 6.5, respectively.

	upper UD-ply		lower UD-ply	
ϕ_{alpha}	#	area 2D $\left[\mathrm{m}^2\right]$	area 2D $\left[\mathrm{m}^2\right]$	#
0°	Ply1	$1.289310\mathrm{E}+00$	$1.280477\mathrm{E}+00$	Ply8
90°	Ply2	$1.288171\mathrm{E}+00$	$1.281777\mathrm{E}+00$	Ply7
45°	Ply3	$1.277991\mathrm{E}+00$	$1.274177\mathrm{E}+00$	Ply6
−45°	Ply4	$1.276666\mathrm{E}+00$	$1.275411\mathrm{E}+00$	Ply5

Table 6.4: Spherical shell: comparison of the cutting patterns' surface areas (area 2D) for identically aligned UD-plies

	lower UD-ply		upper UD-ply	
ϕ_{alpha}	#	area 2D $\left[\mathrm{mm}^2\right]$	area 2D $\left[\mathrm{mm}^2\right]$	#
0°	Ply1	$1.735625\mathrm{E}+05$	$1.740449\mathrm{E}+05$	Ply8
90°	Ply2	$2.068691\mathrm{E}+05$	$2.069949\mathrm{E}+05$	Ply7
45°	Ply3	$1.928220\mathrm{E}+05$	$1.929827\mathrm{E}+05$	Ply6
−45°	Ply4	$1.928926\mathrm{E}+05$	$1.929443\mathrm{E}+05$	Ply5

Table 6.5: Roof crossrail: comparison of the cutting patterns' surface areas (area 2D) for identically aligned UD-plies

Consider the spherical shell. Due to the rotational symmetry of the target structure, each of the optimized cutting patterns exhibit an axial symme-

---

[3] i.e. identically aligned UD-plies

try w.r.t. the respective fiber orientation. A similar correlation has been observed for orthotropic materials (see Section 5.4.2.2)

Consider the car roof crossrail. Due to the axial symmetry of the target structure, each of the optimized cutting patterns exhibits at least a point wise symmetry w.r.t. the center of the respective area. This outcome contradicts with the correlation which has been observed for orthotropic materials (see Section 5.4.3.2).

CONCLUSION: This observation (i.e. a highly anisotropic material in combination with an axially symmetric target structure) underlines the importance of taking into account the material properties for the generation of optimized cutting patterns.

7

Conclusions and Outlook

"Das also war des Pudels Kern!"

— Johann Wolfgang von Goethe, 1749 - 1832
German poet and politician

The *generation of optimized cutting patterns* for *textile fabrics* has been in the focus of this thesis. Within that scope, a novel approach for solving the optimization problem and a novel material model capturing the structural response of textile fabrics on a macroscopic level has been developed, implemented and evaluated.

Generation of optimized cutting patterns
A novel numerical strategy for generating optimized cutting patterns, the so-called *Variation of Reference Strategy* (VaReS), is elaborated in Chapter 5. Its key idea is based on an unconstrained optimization problem minimizing the total potential energy within the target structure (*energy principle*). The core concept of VaReS is the definition of the design variables. In contrast to the well-known principles in structural analysis (*Minimum of Total Potential Energy* or *Principle of Virtual Work*), the material nodal positions are defined as unknowns. Consequently, the primary variables are anchored within the material (or reference) configuration, where the target structure represents the spatial configuration and is held fixed. This setup guarantees the required[1] stress-free state in the (optimized) cutting pattern. Two different solution strategies, namely the *linearization of the variational principle* (second-order approach) and the *method of steepest descent* (first-order approach), are presented for solving the underlying partial differential equation. Both strategies are based on an isoparametric finite element approach. The core innovation of the developed *3-parameter VaReS-membrane element* is the *Gâteaux derivative* of the underlying strain-energy function. More precisely, the *Gâteaux derivative* results in the directional derivatives of both the Green-Lagrange strain tensor and the differential material domain in direction of the material nodal positions. The scope of each approach is directly linked to the underlying strain-energy function. A guideline concerning this matter is given in Table 5.3. Furthermore, two different strategies for increasing the robustness - namely *time-stepping strategy* and *damped predictor* - have been tested and discussed.

Material model for textile fabrics
A novel approach for modeling the structural response of either knitted, braided or woven fabrics based on a nonlinear (hyperelastic) surrogate model is developed in Chapter 4. The key idea is the representation of the fabric's strain-energy function in terms of response surfaces and/or curves spanned over a set of structural invariants. The presented surrogate model is based on a pair consisting of a *Bézier surface* and a *Bézier curve* describing the fabric's in-plane normal and in-plane shear behavior. The workflow for generating the developed response surfaces/curves is established as follows. A series of velocity-driven biaxial tensile tests provide the raw data for the required sampling points of the Bézier surfaces/curves. Then, the gained raw data have to be transformed into adequate continuum mechanical quantities (strain-energy and structural invariants). This

---

[1] Considering the manufacturing process (draping), the stress-free cutting pattern is deformed to its final shape exhibiting residual stresses due to its double-curved characteristics.

step is called *data processing.* Finally, the corresponding control points of the Bézier surfaces/curves are established by means of a constrained least squares approach. This step is called *data fitting.*

The developed solution strategies have been benchmarked by means of a section of a cylindrical shell[2]. In case of the *linearized variational principle*, a quadratic convergence rate of the applied Newton-Raphson scheme has been observed. In case of the *method of steepest descent* a linear convergence rate has been observed. Additionally, several numerical experiments on anticlastic (generic rib) and synclastic (spherical shell) structures in combination with isotropic (Neo-Hook) and orthotropic (glass plain weave) material behavior has been performed. (Section 5.4). The established workflow for generating the underlying strain-energy function of the *response surface based material model* has been applied to three different types of textile fabrics, namely an interlock jersey, a twill weave and a reinforced interlock jersey (Section 4.2). Finally, the presented *Variation of Reference Strategy* and the *response surface based material model* have been applied to two different industrial applications, namely a textile car seat cover and a CFRP roof crossrail (Chapter 6).

The presented numerical experiments and industrial applications show the generality and potential of both the *Variation of Reference Strategy* and the *response surface based material model.* Based on the gained knowledge and experience the following conclusions can be drawn.

Variation of Reference Strategy
The applied strain-energy function shows a strong influence on the characteristics of the residual force equation and therefore on the characteristics of the optimization problem.

In case of polyconvex strain-energy functions, the linearization of the variational approach (second-order approach) proves to be effective. The reason for this is the quadratic rate of convergence of the Newton-Raphson scheme due to convex properties of the optimization problem. It is important to note that the overall convergence behavior is highly sensitive w.r.t. the initialization strategy and the applied set of Dirichlet BCs.

The method of steepest descent (first-order approach) proves very useful for finding the cutting patterns for orthotropic and anisotropic materials. In order to reduce the number of iterations an adaptive line search technique (3-point rule) is proposed. It is important to note that no further Dirichlet BCs are required which might have a negative effect on the resulting shape of the cutting pattern.

Critical strain states and overshooting predictors may cause severe convergence problems. The *time-stepping strategy* turns out to be quite powerful, since it increases the robustness and stability of the underlying optimization problem.

---

[2] For ruled surfaces there exists an analytical solution - namely the congruent rectangle.

The resulting symmetry of the optimized cutting pattern is directly linked to both the symmetry of the target structure (rotational or axial) and the preferred material directions. In case of an isotropic material, the symmetry of the target structure is preserved within the optimized cutting pattern.

An important property of the *Variation of Reference Strategy* is that it guarantees a stress-free state in the cutting pattern at each optimization step. In terms of mechanics, the unknown cutting pattern is defined as *material configuration*. Hence, the motion mapping the cutting pattern (material configuration) to the target structure (spatial configuration) is consistent with the physics of the underlying problem.

The major distinction between the presented *Variation of Reference Strategy* and the existing methods for the generation of cutting patterns (see Section 1.3.2) is the choice of the description of motion. In more detail, the *Variation of Reference Strategy* is based on a *Total Lagrangian Formulation* allowing for a direct incorporation of nonlinear anisotropic material models based on the concept of hyperealsticity.

Response surface based material model
Considering the experimental set-up of the velocity driven biaxial tensile tests, the structural response of the underlying micro-structure is automatically captured on a macroscopic level (experimental raw data). Therefore, the presented material model is applicable to a wide range of textile fabrics.

The presented workflow (data processing and data fitting) allows an easy and straight-forward identification of the required material parameters represented by the control points of the corresponding Bézier surface/curve.

The achieved cutting patterns for selected parts of a car seat cover made of an interlock jersey (see Section 6.1) underline the capability of the *response surface based material model* in combination with the developed *Variation of Reference Strategy.*

Outlook
In case of supported structures (e.g. car seat cover), the application of a constant prescribed stress field for compensation purposes turned out to be less suitable. The reason for that is the fact that for non-form-found surfaces, a constant stress field leads to a nonconstant pressure field which is strongly depending on the underlying curvature. Especially for elastically supported structures, a constant effective force acting on the underlying foam core is of more interest. Thus, instead of a constant prescribed stress field, a constant predefined effective force is proposed as a more adequate criterion for controlling the compensation of the cutting pattern. Due to the fact that the stress field within a double-curved tensile structure is directly linked to the underlying curvature of the target structure and the predefined effective force (6.5), the incorporation of the proposed criterion into the *Variation of Reference Strategy* is straight-forward.

In case of structures made of carbon fibers, a strong dependency between the orientation of the UD-ply and the shape of the optimized cutting pattern has been observed. Therefore, the application of an optimized cutting pattern for each ply within a stack (instead of a common cutting pattern for the entire stack) reduces the overall material consumption of the structure and yields a draped stack with significantly higher quality.

So far, the presented *Variation of Reference Strategy* is based on an unconstrained optimization problem. Especially the presented first-order approach is ideal for further enhancements. The following additional constraints may lead to an even more sophisticated method for the design of structures made of carbon or glass fibers:

→ predefining the fiber orientation within the target structure

→ considering the interaction between the plies

→ adding additional manufacturing constraints

List of Figures

List of Tables

Bibliography

[1] Y. Aimène, E. Vidal-Sallé, B. Hagège, F. Sidoroff, and P. Boisse. A hyperelastic approach for compostie reinforced large deformation analysis. *Journal of Composite Materials*, 44 (1):5–26, 2010.

[2] H. Altenbach. *Kontinuumsmechanik.* Springer, Berlin, Heidelberg, New York, Hongkong, London, Mailand, Paris, Tokio, 2012.

[3] J. S. Arora. *Introduction to optimum design.* AP - Elsevier, Amsterdam, Bosten, Heidelberg, London, New York, Oxford, Paris, San Diego, San Francisco, Singapore, Sydney, Tokyo, 2012.

[4] Y. Başar and W.B. Krätzig. *Mechanik der Flächentragwerken.* Friedr. Vieweg & Sohn, Braunschweig, Wiesbaden, 1985.

[5] P. Badel, S. Gauthier, E. Vidal-Sallé, and P. Boisse. Rate constitutive equations for computational analyses for textile composite reinforced mechanical behaviour during forming. *Composites: Part A*, 40:997–1007, 2009.

[6] R. Baldick. *Applied Optimization - Formulation and Algorithms for Engineering Systems.* Cambridge University Press, Cambridge, New York, Melbourne, Madrid, Cape Town, Singapore, São Paulo, 2006.

[7] D. Ballhause. *Diskrete Modellierung des Verformungs- und Versagensverhaltens von Gewebemembranen.* PhD thesis, Institut für Statik und Dynamik der Luft- und Raumfahrtkonstruktionen, Universität Stuttgart, 2007.

[8] D. Ballhause, M. König, and Bernd Kröplin. A microstructure model for fabric-reinforced membranes based on discrete element modelling. In E. O nate and B. Kröplin, editors, *Textile Composites and Inflatabel Structures II - Structural Membranes*, Barcelona, 2005. CIMNE.

[9] D. Balzani, F. Gruttmann, and J. Schröder. Analysis of thin shells using anisotropic polyconvex energy densities. *Comput. Methods Appl. Mech. Engrg.*, 197:1015–1032, 2008.

[10] B. A. Bednarcyk, B. Stier, J.-W. Simon, S. Reese, and E. J. Pineda. Meso- and micro-scale modeling of damage in plain weave composites. *Composite Structures*, 121:285–270, 2015.

[11] T. Belytschko, W.K. Liu, and B. Moran. *Nonlinear Finite Elements for Continua and Structures.* John Wiley & Sons LTD, Chichester, Weinheim, New York, Brisbane, Singapore, Toronto, 2000.

[12] A. Beutelspacher. *Lineare Algebra.* Springer Spektrum, Wiesbaden, 2014.

[13] M. Bischoff. *Theorie und Numerik einer dreidimensionalen Schalenformulierung.* PhD thesis, Institut für Baustatik, Universität Stuttgart, 1999.

[14] M. Bischoff, W.A. Wall, K.-U. Bletzinger, and E. Ramm. Models and finite elements of thin-walled structures (chapter 3). *Encyclopedia of Computational Mechanics - Volume 2: Solids and Structures*, 2:59–137, 2004.

[15] K.-U. Bletzinger and J. Linhard. Tracing the equilibrium - recent advances in numerical form finding. *International Journal of Space Structures*, 25 (2):107–116, 2010.

[16] K.-U. Bletzinger, J. Linhard, and R. Wüchner. Extended and integrated numerical form finding and cutting patterning of membrane structures. *Journal of the International Association for Shell and Spatial Structures*, 50 (3):35–49, 2009.

[17] R. Blum. Beitrag zur nichtlinearen Mebrantheorie. *Sonderforschungsbereich 64 (SFB 64): Weitgespannte Flächentragwerke*, Mitteilungen 73:1–112, 1985.

[18] R. Blum and W. Bidmon. Spannungs-Dehnungs-Verhalten von Bautextilien. *Sonderforschungsbereich 64 (SFB 64): Weitgespannte Flächentragwerke*, Mitteilungen 74:1–120, 1987.

[19] R. Blum, H. Bögner, and G. Némoz. Material testing and properties. In D. Foster and M. Mollaert, editors, *European Design Guide for Tensile Surface Structures*, Brussel, 2004. TensiNet.

[20] R. Blum, H. Bögner, and G. Némoz. Testing methods and standards. In D. Foster and M. Mollaert, editors, *European Design Guide for Tesile Surface Structures*, Brussel, 2004. TensiNet.

[21] H. Bögner. *Vorgespannte Konstruktionen aus beschichteten Geweben und die Rolle des Schubverhaltens bei der Bildung von zweifach gekrümmten Flächen aus ebenen Streifen.* PhD thesis, Institut fü Werkstoffe im Bauwesen der Universität Stuttgart, 2004.

[22] J. Bonet and A.J. Burton. A simple orthotropic, transversely isotropic hyperelastic constitutive equation for large strain computations. *Comp. Methods Appl. Mech. Engrg.*, 162:151–164, 1998.

[23] B. N. Bridgens and P. D. Gosling. Biaxial fabric testing to determine in-situ material properties. In *Textile Composites and Inflatable Structres*, Barcelona,, 2003.

[24] B. N. Bridgens and P. D. Gosling. Membrane material behaviour: concepts, practice & developments. *Structural Engineer*, 20:28–33, 2004.

[25] B. N. Bridgens and P. D. Gosling. Tensile fabric structures: concepts, practice & developments. *Structural Engineer*, 20:21–27, 2004.

[26] B. N. Bridgens and P. D. Gosling. A predictive fabric model for membrane structure design. In E. O nate and B. Kröplin, editors, *Textile Composites and Inflatabel Structures II - Structural Membranes*, Barcelona, 2005. CIMNE.

[27] B. N. Bridgens and P. D. Gosling. New developments in fabric structural analysis. In *HKIE/IStructE Joint Structural Division Annual Seminar 2008 - Inovative Light-Weight Structures and Sustainable Facades*, Hong Kong - China,, 2008.

[28] B.N. Bridgens and P.D. Gosling. A new biaxial test protocol for architectural fabrics. *Journal of the International Association for Shell and Spatial Structures*, 45-3:175–181, 2004.

[29] I.N. Bronstein, K.A. Semendjajew, G. Musiol, and M. Mühlig. *Taschenbuch der Mathematik*. Verlag Harri Dutsch, Thun und Frankfurt am Main, 2001.

[30] D. Chapelle and K.J. Bathe. *The Finite Element Analysis of Shells - Fundamentals*. Springer, Berlin, Heidelberg, New York, Hongkong, London, Milan, Paris, Tokio, 2003.

[31] A. Charmetant, E. Vidal-Sallé, and P. Boisse. Hyperelastic modelling for mesoscopic analyses of composite reinforcements. *Composite Science and Technology*, 71:1623–1631, 2011.

[32] E.W.V. Chaves. *Notes on Continuum Mechanics*. Springer, Berlin, Heidelberg, New York, Hongkong, London, Milan, Paris, Tokio, 2013.

[33] Ch. Cherif, Ch. Freudenberg, B. Lehmann, C. Kowtsch, W. Trümper, J. Hausding, E. Laourine, K. Pietsch, M. Schade, O. Diestel, H. Rödel, H. Hund, T. Pusch, and G. Girdauskaite. *Textile Werkstoffe für den Leichtbau*. Springer, Berlin, Heidelberg, New York, Barcelona, Hongkong, London, Mailand, Paris, Tokio, 2011.

[34] M. Coelho, D. Roehl, and K.-U. Bletzinger. Using nurbs as response surface for membrane material behavior. In E. O nate and B. Kröplin, editors, *Textile Composites and Inflatabel Structures VI - Structural Membranes*, Barcelona, 2013. CIMNE.

[35] P. Deuflhard. *Newton Methods for Nonlinear Problems.* Springer, Berlin, Heidelberg, New York, Hongkong, London, Milan, Paris, Tokyo, 2004.

[36] F. Dieringer, R. Wüchner, and K.-U. Bletzinger. Practical advances in numerical form finding and cutting pattern generation for membrane structures. *Journal of the International Association for Shell and Spatial Structures*, 53 (3):147–156, 2012.

[37] F. H. Dieringer. *Numerical Methods for the Analysis and Design of Tensile Structures.* PhD thesis, Lehrstuhl für Statik, Technische Universität München, 2014.

[38] European Space Agency (ESA). Solar array and sunshield deployment. http://sci.esa.int/gaia/39230-solar-array-and-sunshield-deployment/. download: 28.07.2015.

[39] S. Fillep, J. Mergheim, and P. Steinmann. Computational modelling and homogenization of technical textiles. *Engineering Structures*, 50:68–73, 2013.

[40] S. Fillep, J. Orlik, Z. Bare, and P. Steinmann. Homogenization in periodically heterogeneous elastic bodies with multiple micro-contact. *Mathematics and Mechanics of Solids*, 19-8:1011–1021, 2014.

[41] M. Firl. *Optimal Shape Design of Shell Structures.* PhD thesis, Lehrstuhl für Statik, Technische Universität München, 2010.

[42] M. Flemming, G. Ziegmann, and S. Rothf. *Faserverbundbauweisen: Halbzeuge und Bauweisen.* Springer, Berlin, Heidelberg, New York, 1996.

[43] Institute for Carbon Composites TU München. Radial braiding machine with handling robot. http://www.lcc.mw.tum.de/en/research-groups/process-technology-for-fibers-and-textiles/braiding-technology/. download: 02.02.2015.

[44] DYNAmore (Gesellschaft für FEM Ingenieurdienstleistungen mbH). http://www.dynamore.de/de. download: 10.06.2015.

[45] S. Gatouillat, A. Bareggi, E. Vidal-Sallé, and P. Boisse. Meso modelling for composite preform shaping simulation of the loss of cohesion of the woven fibre network. *Composites Part A: Applied Science and Manufacturing*, 54:135–144, 2013.

[46] M.W. Gee, C. Reeps, E.H. Eckstein, and W.A. Wall. Prestressing in finite deformation abdominal aoritic aneurysm simulation. *Journal of Biomechanics*, 42:1732–1739, 2009.

[47] E.W. Gekeler. *Mathematische Methoden zur Mechanik.* Springer, Berlin, Heidelberg, New York, 2006.

[48] S. Germain, M. Scherer, and P. Steinmann. On inverse form finding for anisotropic hyperelasticity in logarithmic strain space. *International Journal of Structural Changes in Solids - Mechanics and Applications*, 2:1–16, 2010.

[49] ESI GmbH. https://www.esi-group.com/de. download: 10.06.2015.

[50] P. D. Gosling and B. N. Bridgens. Material testing & computational machanics - a new philosophy for architectural fabrics. *International Journal of Space Structures*, 23-4:215–232, 2008.

[51] S. Govindjee and P.A. Mihalic. Computational methods for inverse finite elastostatics. *Comp. Methods Appl. Mech. Engrg.*, 136:47–57, 1996.

[52] S. Govindjee and P.A. Mihalic. Computational methods for inverse deformations in quasi-incompressible finite elasticity. *Int. J. Numer. Meth. Engng.*, 43:821–838, 1998.

[53] L. Gründig, E. Moncrieff, P. Singer, and D. Ströbel. High performance cutting pattern generation of architectural textile structures. In *Fourth International Colloquium on Computation of Shell and Spatial Structures*, pages 1–15, Chania-Crete, Greece, June 5-7 2000.

[54] T. G. Gutowski, editor. *Advanced Composites Manufacturing*. John Wiley & Sons LTD, Chichester, Weinheim, New York, Brisbane, Singapore, Toronto, 1997.

[55] E. Haug, P. De Kermel, B. Gawenat, and A. Michalski. Industrial design and analysis of structual membranes. In *International Conference on Textile Composites and Inflatable Structures - STRUCTURAL MEMBRANES*, 2007.

[56] E. Haug, P. De Kermel, B. Gawenat, and A. Michalski. Industrial design and analysis of structual membranes. *International Journal of Space Structures*, 24 (4):191–204, 2009.

[57] P. Haupt. *Continuum Mechanics and Theory of Materials*. Springer, Berlin, Heidelberg, New York, Hongkong, London, Mailand, Paris, Tokio, 2000.

[58] Minami Hirokazu. A multi-step linear approximation method for non-linear analysis of stress and deformation of coated plane-weav fabric. *Journal of Textile Engineering*, 52-5:189–195, 2006.

[59] G. A. Holzapfel and R. W. Ogden. On planar biaxial tests for anisotropic nonlinearly elastic solids. a continuum mechanical framework. *Mathematics and Mechanics of Solids*, 14:474–489, 2009.

[60] G.A. Holzapfel. *Nonlinear Solid Mechanics - A continuum approach for engineering*. John Wiley & Sons LTD, Chichester, Weinheim, New York, Brisbane, Singapore, Toronto, 2000.

[61] T.J.R. Hughes. *The Finie Element Method - Linear Static and Dynamic Finite Element Analysis.* Dover Publication Inc., Mineola, 2000.

[62] M. Itskov. *Tensor Algebra and Tensor Analysis for Engineers.* Springer, Berlin, Heidelberg, New York, Hongkong, London, Mailand, Paris, Tokio, 2013.

[63] Michael Karwath, Rosemarie Wagner, and Bernd Kröplin. Ein orthotropes Werkstoffgesetz für Folien. *Stahlbau*, 76-5:297–304, 2007.

[64] S. Kawabata, M. Niwa, and H. Kawai. The finite deformation theory of plain-weave fabrics part I: The biaxial-deformation theory. *The Journal of The Textile Institute*, 64-1:21–46, 1973.

[65] S. Kawabata, M. Niwa, and H. Kawai. The finite deformation theory of plain-weave fabrics part II: The uniaxial-deformation theory. *The Journal of The Textile Institute*, 64-2:47–61, 1973.

[66] S. Kawabata, M. Niwa, and H. Kawai. The finite deformation theory of plain-weave fabrics part III: The shear-deformation theory. *The Journal of The Textile Institute*, 64-2:62–85, 1973.

[67] H. Kielhöfer. *Variationsrechnung.* Vieweg + Teubner Verlag, Wiesbaden, 2010.

[68] J.-Y. Kim and J.-B. Lee. A new technique for optimum cutting pattern generation of membrane structures. *Engineering Structures*, 24:745–756, 2002.

[69] S. Klinkel and S. Govindjee. Using finite strain 3d-material models in beam and shell elements. *Engineering Computations*, 19 (3):254–271, 2003.

[70] S. Klinkel, F. Gruttmann, and W. Wagner. A continuum based three-dimensional shell element for laminated structures. *Computers & Structures*, 71:43–62, 1999.

[71] F. Koschnick. *Geometrische Locking-Effekte bei Finiten Elementen und ein allgemeines Konzept zu ihrer Vermeidung.* PhD thesis, Lehrstuhl für Statik, Technische Universität München, 2004.

[72] W.B. Krätzig and Y. Başar. *Tragwerke 3 - Theorie und Anwendung der Methode der Finiten Elemente.* Springer, Berlin, Heidelberg, New York, Barcelona, Budapest, Hongkong, London, Mailand, Paris, Santa Clare, Singapur, Tokio, 1997.

[73] S. Krzywinski, H. Planck, and K.-U. Bletzinger. Abschlussbericht: Experimentelle Analyse und numerische Modellierung der Deformation dehnfähiger Textilien und deren Wechselwirkung auf Tragkörper (DFG BL 306 20-2, KR 3487/3-2, PL 120/19-2). Technical report, DFG, Dresden - Denkendorf - München, 2013.

[74] J. Linhard. *Numerisch-mechanische Betrachtung des Entwurfsprozesses von Membrantragwerken.* PhD thesis, Lehrstuhl für Statik, Technische Universität München, 2010.

[75] J. Linhard, R. Wüchner, and K.-U. Bletzinger. Introducing cutting patterns in form finding and structual analysis. *Computational Methods in Applied Sciences*, 8:69–84, 2008.

[76] J. Linhard, R. Wüchner, and K.-U. Bletzinger. Extended and integrated numerical form finding and cutting patterning of membrane structures. *Journal of the International Association for Shell and Spatial Structures*, 50 (3):35–49, 2009.

[77] K. Linkwitz. New methods for the determination of cutting pattern of prestressed cable nets and their application to the olympic roof munich. *Special lecture, delivered in Tokyo, Reprint from "The Proceedings IASS Symposium" Tokyo October 1971*, pages 551–555, 1971.

[78] K. Linkwitz. New methods for the determination of cutting pattern of prestressed cable nets and their application to the olympic roofs munich. *Proc. 1971 IASS Pacific Symposium Part II on TENSION STRUCTURES and SPACE FRAMES, Tokyo and Kyoto*, pages 13–26, 1972.

[79] K. Linkwitz and H. D. Preuss. Jahresbericht F - Geodäsie (Teilprojekt F2: Rechnerische Methoden und Abbildugen). *Sonderforschungsbereich 64 (SFB 64): Weitgespannte Flächentragwerke*, Mitteilungen 23:92–98, 1974.

[80] K. Linkwitz and H.-J. Schek. Einige Bemerkungen zur Berechnung von vorgespannten Seilnetzkonstruktionen. *Ingenieur-Archiv*, 40:145–158, 1971.

[81] K. Linkwitz, J.-J. Schek, and L. Gründig. Die Gleichgewichtsberechnung von Seilnetzen unter Zusatzbedingungen. *Ingenieur-Archiv*, 43:183–192, 1974.

[82] D. Lürding, Y. Başar, and U. Hanskötter. Application of transversely isotropic materials to multi-layer shell elements undergoing finte rotations and large strains. *International Journal of Solids and Structures*, 38:9493–9503, 2001.

[83] B. Maurin and R. Motro. Cutting pattern of fabric membranes with the stress compensation method. *International Journal of Spatial Structures*, 14 (2):121–129, 1999.

[84] J. McCartney, B. K. Hinds, and K. W. Chong. Pattern flattening for orthotropic materials. *Computer-Aided Design*, 37:631–644, 2005.

[85] J. McCartney, B. K. Hinds, and B. L. Seow. The flattening of triangulated surfaces incorporating darts and gussets. *Computer-Aided Design*, 31:249–260, 1999.

[86] R. Münsch and H.-W. Reinhardt. Zur Berechnung von Membrantragwerken aus beschichteten Geweben mit Hilfe genäherter elastischer Parameter. *Bauingenieur*, 70:271–275, 1995.

[87] R.H. Myers and D.C. Montgomery. *Response Surface Methodology.* John Wiley & Sons LTD, Chichester, Weinheim, New York, Brisbane, Singapore, Toronto, 2002.

[88] R.W. Ogden. *Non-linear Elastic Deformation.* Dover Publications, Inc., Mineola, 1984.

[89] H. Parisch. *Festkörper-Kontinuumsmechanik.* B.G. Teubner, Stuttgart, Leipzig, Wiesbaden, 2003.

[90] E. Parsons, T. Weerasooriya, S. Sarva, and S. Socrate. Impact of woven fabric: Experimental and mesostructure-based continuum-level simulations. *Journal of the Mechanics and Physics of Solids*, 58:1995–2021, 2010.

[91] B. Philipp, F. Dieringer, A. Michalski, R. Wüchner, and K.-U. Bletzinger. Form finding and structual analysis for hybrid structures in the desing process. In *Proceedings of the TensiNet Symposium 2013*, 2013.

[92] L. Piegl and W. Tiller. *The NURBS Book.* Springer Berlin Heidelberg New York Barcelona Hongkong London Milan Paris Tokyo, 1997.

[93] BMW Group PressClub. Pressemappe Innovationstage Mobilität der Zukunft. www.press.bmwgroup.com/global/startpage.html, Jul. 2010. download: 02.09.2015.

[94] BMW Group PressClub. Bmw i Innovation Days (Leipzig). www.press.bmwgroup.com/global/startpage.html, Apr. 2013. download: 23.01.2015.

[95] T. Raible, S. Reese, and P. Wriggers. Finite element modelling of orthotropic material behaviour in pneumatic membranes. *Z. Angew. Math. Mech*, 80:409–410, 2000.

[96] Ekkehard Ramm. Geometirsche nichtlineare Elastostatik und Finite Elemente. *Bericht Nr. 76 - 2 aus dem Institut für Baustatik der Universität Stuttgart*, pages 1–174, 1976.

[97] S. Reese, T. Raible, and P. Wriggers. Finite element modelling of orthotropic material behaviour in pneumatic membranes. *International Journal of Solids and Structures*, 38:9525–9544, 2001.

[98] M. J. G. Ruiz and L. Y. S. Gonzáles. Comparison of hyperelastic material models in the analysis of fabrics. *International Journal of Clothing Science and Technology*, 18-5:314–325, 2006.

[99] J. Schröder, D. Balzani, N. Stranghöner, J. Uhlemann, F. Gruttmann, and K. Saxe. Membranstrukturen mit nichtlinearem anisotropen Materialverhalten - Aspekte der Materialprüfung und der numerischen Simualtion. *Bauingenieur*, 86:381–389, 2011.

[100] J. Schröder and P. Neff. Invariant formulation of hyperelastic transverse isotropy based on polyconvex free energy functions. *International Journal of Solids and Structures*, 40:401–445, 2003.

[101] A. Sheffer and E. de Sturler. Parameterization of faceted surfaces for meshing using angle-based flattening. *Engineering with Computers*, 17:326–337, 2001.

[102] J.-W. Simon, D. Höwer, B. Siier, and S. Reese. Meso-mechanically motivated modeling of layered fiber reinforced composites accounting for delamination. *Composite Structures*, 122:477–487, 2015.

[103] B. Sonon and T. J. Massart. A level-set based representative volume element generator and xfem simulations for textile and 3d-reinforced composites. *Materials*, 6:5568–5592, 2013.

[104] 3DS Dassault Systèmes. http://www.3ds.com/. download: 10.06.2015.

[105] B.H.V. Topping and P. Iványi. *Computer Aided Design of Cable Membrane Structures.* Saxe-Coburg Publications, Kippen, Stirlingshire, 2007.

[106] M. Vaillant and J. Glaunés. Surface matching via currents. *Inf Process Med Imaging.*, 3565:381–392, 2005.

[107] E. Vidal-Sallé, Y. Aimène, and P. Boisse. Use of a hyperelastic constitutive law for dry woven forming simulations. In *The 14th International Conference on Material Forming: ESAFORM 2011 Proceedings*, pages 883–888, 2011.

[108] Ch. C. L. Wang, S. S.-F. Smith, and M. M. F. Yuen. Surface flattening based on energy model. *Computer-Aided Design*, 34:823–833, 2002.

[109] E. Wendt and S. Krzywinski. Uniaxial and biaxial tensile tests to determine the deformation behaviour of technical textiles. *Technical Textiles*, 54 (5-6):220–223, 2011.

[110] E. Wendt and S. Krzywinski. Virtual development of patterns for car seats by taking into account the deformation behaviour of the cover materials. In *12th World Textile Conference AUTEX 2012 - June 13-15*, 2012.

[111] VDI Wissensforum. Press release: Faserverbundbauteile wirtschaftlich herstellen. http://www.vdi.de/presse/artikel/faserverbundbauteile-wirtschaftlich-herstellen/, Feb. 2014. download: 23.01.2015.

[112] P. Wriggers. *Nichtlineare Finite-Elemente-Methoden.* Springer, Berlin, Heidelberg, New York, Hongkong, London, Mailand, Paris, Tokio, 2001.

[113] O.C. Zienkiewicz and R.L. Taylor. *The Finite Element Method - Volume 1: The Basis.* Butterworh Heinemann, Oxford, Auckland, Boston, Johannesburg, Melbourne, New Delhi, 2000.

A

Tensor Analysis

The following list summarizes the most important formulas and definitions addressed in this thesis. All formulas and definitions are based on the work of CHAVES [32], HOLZAPFEL [60], ITSKOV [62] and WRIGGERS [112].

A.1 Notation

Einstein notation:

$$a_i b^i = \sum_{i=1}^{n} a_i b^i = a_1 b^1 + a_2 b^2 + \ldots + a_n b^n \tag{A.1}$$

Euclidean base vectors:

$$\mathbf{e}_i \quad \text{with} \quad i = 1, 2, 3 \tag{A.2}$$

Covariant convective base vectors $(\bullet)^\flat$:

$$\mathbf{g}^\flat = g_i \mathbf{e}_i \quad \text{with} \quad i = 1, 2, 3 \tag{A.3}$$

Contra-variant convective base vectors $(\bullet)^\sharp$:

$$\mathbf{g}^\sharp = g^i \mathbf{e}_i \quad \text{with} \quad i = 1, 2, 3 \tag{A.4}$$

First order tensors:

$$\mathbf{a} = a_i \mathbf{g}^i = a^i \mathbf{g}_i = \tilde{a}_i \mathbf{e}_i \tag{A.5}$$

Second order tensors:

$$\mathbf{A} = A_{ij} \mathbf{g}^i \otimes \mathbf{g}^j = A^{ij} \mathbf{g}_i \otimes \mathbf{g}_j = \tilde{A}_{ij} \mathbf{e}_i \otimes \mathbf{e}_j \tag{A.6}$$

Fourth order tensors:

$$\begin{aligned} \mathbb{A} &= \mathbb{A}_{ijkl} \mathbf{g}^i \otimes \mathbf{g}^j \otimes \mathbf{g}^k \otimes \mathbf{g}^l \\ &= \mathbb{A}^{ijkl} \mathbf{g}_i \otimes \mathbf{g}_j \otimes \mathbf{g}_k \otimes \mathbf{g}_l \\ &= \tilde{\mathbb{A}}_{ijkl} \mathbf{e}_i \otimes \mathbf{e}_j \otimes \mathbf{e}_k \otimes \mathbf{e}_l \end{aligned} \tag{A.7}$$

According to HOLZAPFEL [60] the nomenclature of a tensor is based on its coefficients, i.e. a tensor with covariant or contra-variant coefficients is called covariant or contra-variant tensor, respectively.

A.2 Operators and Symbols

Kronecker delta:

$$\delta^{ij} = \delta^i_j = \delta^j_i = \begin{cases} 1 & \text{if} \quad i = j \\ 0 & \text{if} \quad i \neq j \end{cases} \tag{A.8}$$

with

$$\delta^{ij} = \mathbf{e}_i \cdot \mathbf{e}_j \quad \text{or} \quad \delta^i_j = \mathbf{g}^i \cdot \mathbf{g}_j \quad \text{or} \quad \delta^j_i = \mathbf{g}_i \cdot \mathbf{g}^j \tag{A.9}$$

Levi-Civita symbol:

$$\epsilon_{ijk} = \frac{1}{2} \left(i - j\right) \left(j - k\right) \left(k - i\right) \tag{A.10}$$

for $i, j, k = 1 \ldots 3$:

$$\epsilon_{ijk} = \begin{cases} 1 & \text{if} \quad (i, j, k) \in \left\{(1,2,3), (2,3,1), (3,1,2)\right\} \\ -1 & \text{if} \quad (i, j, k) \in \left\{(1,3,2), (3,2,1), (2,1,3)\right\} \\ 0 & \quad\quad \text{otherwise} : (i = j), (j = k), (i = k) \end{cases} \tag{A.11}$$

Christoffel symbols:

$$\frac{\partial \mathbf{G}_i \left(\bullet\right)}{\partial \left(\bullet\right)_j} = \Gamma_{ijk} \mathbf{G}^k \left(\bullet\right) = \Gamma^k_{ij} \mathbf{G}_k \left(\bullet\right) \tag{A.12}$$

with

$$\Gamma_{ijk} = \frac{\partial \mathbf{G}_i \left(\bullet\right)}{\partial \left(\bullet\right)_j} \mathbf{G}_k \left(\bullet\right) \tag{A.13a}$$

$$\Gamma^k_{ij} = \frac{\partial \mathbf{G}_i \left(\bullet\right)}{\partial \left(\bullet\right)_j} \mathbf{G}^k \left(\bullet\right) = -\frac{\partial \mathbf{G}^k \left(\bullet\right)}{\partial \left(\bullet\right)_j} \mathbf{G}_i \left(\bullet\right) \tag{A.13b}$$

Inner product:

$$< \left(\bullet\right) \ , \ \left(\bullet\right) >= \left(\bullet\right) \cdot \left(\bullet\right) \tag{A.14}$$

Outer product:

$$\left(\left(\bullet\right) \otimes \left(\bullet\right)\right)_{ij} = \left(\bullet\right)_i \left(\bullet\right)_j \tag{A.15}$$

$$\left(\left(\bullet\right) \odot \left(\bullet\right)\right)_{ijkl} = \frac{1}{2} \Big(\left(\bullet\right)_{ik} \left(\bullet\right)_{jl} + \left(\bullet\right)_{il} \left(\bullet\right)_{jk} \Big) \tag{A.16}$$

Euclidean norm (L2-norm):

$$\left\| \left(\bullet\right) \right\| = \left(< \left(\bullet\right) \ , \ \left(\bullet\right) >\right)^{\frac{1}{2}} = \sqrt{\left(\bullet\right) \cdot \left(\bullet\right)} \tag{A.17}$$

Permutability property:

$$\delta \int_{\Omega} (\bullet)\ \mathrm{d}\Omega = \int_{\Omega} \delta\ (\bullet)\ \mathrm{d}\Omega \tag{A.18}$$

Inverse of a regular matrix:

$$\mathbf{A}^{-1} = \frac{1}{\det \mathbf{A}}\, \mathrm{adj}\mathbf{A} = \frac{1}{\det \mathbf{A}}\, \mathrm{cof}\mathbf{A}^{T} \tag{A.19}$$

A.3 Tensor Algebra

First order tensors

Dot product:

$$\mathbf{a} \cdot \mathbf{b} = a_i\ \mathbf{e}_i \cdot b_j\ \mathbf{e}_j = a_i \delta^{ij} b_j = a_i b^i \tag{A.20}$$

$$\mathbf{a} \cdot \mathbf{b} = a_i\ \mathbf{g}^i \cdot b^j\ \mathbf{g}_j = a_i \delta^i_j b^j = a_i b^i \tag{A.21a}$$

$$\mathbf{a} \cdot \mathbf{b} = a^i\ \mathbf{g}_i \cdot b^j\ \mathbf{g}_j = a^i \delta^j_i b_j = a_i b^i \tag{A.21b}$$

$$\mathbf{a} \cdot \mathbf{b} = a_i\ \mathbf{g}^i \cdot b_j\ \mathbf{g}^j = a_i g^{ij} b_j \tag{A.21c}$$

$$\mathbf{a} \cdot \mathbf{b} = a^i\ \mathbf{g}_i \cdot b^j\ \mathbf{g}_j = a^i g_{ij} b^j \tag{A.21d}$$

Tensor product:

$$\mathbf{a} \otimes \mathbf{b} = a_i\ \mathbf{e}_i \otimes b_j\ \mathbf{e}_j = (\mathbf{a} \otimes \mathbf{b})_{ij}\ \mathbf{e}_i \otimes \mathbf{e}_j \tag{A.22}$$

with the outer product (A.15)

$$(\mathbf{a} \otimes \mathbf{b})_{ij} = \begin{bmatrix} a_1 \\ a_2 \\ a_3 \end{bmatrix} \begin{bmatrix} b_1 & b_2 & b_3 \end{bmatrix} = \begin{bmatrix} a_1 b_1 & a_1 b_2 & a_1 b_3 \\ a_2 b_1 & a_2 b_2 & a_2 b_3 \\ a_3 b_1 & a_3 b_2 & a_3 b_3 \end{bmatrix} \tag{A.23}$$

$$\mathbf{a} \otimes \mathbf{b} = a_i\ \mathbf{g}^i \otimes b_j\ \mathbf{g}^j = (\mathbf{a} \otimes \mathbf{b})_{ij}\ \mathbf{g}^i \otimes \mathbf{g}^j \tag{A.24a}$$

$$\mathbf{a} \otimes \mathbf{b} = a^i\ \mathbf{g}_i \otimes b^j\ \mathbf{g}_j = (\mathbf{a} \otimes \mathbf{b})^{ij}\ \mathbf{g}_i \otimes \mathbf{g}_j \tag{A.24b}$$

$$\mathbf{a} \otimes \mathbf{b} = a_i\ \mathbf{g}^i \otimes b^j\ \mathbf{g}_j = (\mathbf{a} \otimes \mathbf{b})_i^{\,j}\ \mathbf{g}^i \otimes \mathbf{g}_j \tag{A.24c}$$

$$\mathbf{a} \otimes \mathbf{b} = a^i\ \mathbf{g}_i \otimes b_j\ \mathbf{g}^j = (\mathbf{a} \otimes \mathbf{b})^i_{\,j}\ \mathbf{g}_i \otimes \mathbf{g}^j \tag{A.24d}$$

$$(\mathbf{a} \otimes \mathbf{b})\, \mathbf{c} = \mathbf{a}\, (\mathbf{b} \cdot \mathbf{c}) = (\mathbf{b} \cdot \mathbf{c})\, \mathbf{a} \tag{A.25a}$$

$$\mathbf{a}\, (\mathbf{b} \otimes \mathbf{c}) = (\mathbf{a} \cdot \mathbf{b})\, \mathbf{c} = \mathbf{c}\, (\mathbf{a} \cdot \mathbf{b}) \tag{A.25b}$$

$$(\mathbf{a} \otimes \mathbf{b})\, (\mathbf{c} \otimes \mathbf{d}) = (\mathbf{b} \cdot \mathbf{c})\, \mathbf{a} \otimes \mathbf{d} = \mathbf{a} \otimes \mathbf{d}\, (\mathbf{b} \cdot \mathbf{c}) \tag{A.25c}$$

$$\mathbf{A}\, (\mathbf{b} \otimes \mathbf{c}) = (\mathbf{A}\mathbf{b}) \otimes \mathbf{c} \tag{A.25d}$$

Higher order tensors
Dot product:

$$\mathbf{A}\cdot\mathbf{b} = A_{ij}\ \mathbf{e}_i\otimes\mathbf{e}_j\cdot b_k\ \mathbf{e}_k = A_{ij}\delta^{jk}b_k\ \mathbf{e}_i = A_{ij}b^j\ \mathbf{e}_i \tag{A.26}$$

$$\mathbf{A}\cdot\mathbf{b} = A_{ij}\ \mathbf{g}^i\otimes\mathbf{g}^j\cdot b^k\ \mathbf{g}_k = A_{ij}\delta^j_k b^k\ \mathbf{g}^i = A_{ij}b^j\ \mathbf{g}^i \tag{A.27a}$$

$$\mathbf{A}\cdot\mathbf{b} = A^{ij}\ \mathbf{g}_i\otimes\mathbf{g}_j\cdot b_k\ \mathbf{g}^k = A^{ij}\delta^k_j b_k\ \mathbf{g}_i = A^{ij}b_j\ \mathbf{g}_i \tag{A.27b}$$

$$\mathbf{A}\cdot\mathbf{b} = A_{ij}\ \mathbf{g}^i\otimes\mathbf{g}^j\cdot b_k\ \mathbf{g}^k = A_{ij}g^{jk}b_k\ \mathbf{g}^i \tag{A.27c}$$

$$\mathbf{A}\cdot\mathbf{b} = A^{ij}\ \mathbf{g}_i\otimes\mathbf{g}_j\cdot b^k\ \mathbf{g}_k = A^{ij}g_{jk}b^k\ \mathbf{g}_i \tag{A.27d}$$

Double contradiction:

$$\mathbf{A}:\mathbf{B} = A_{ij}B_{kl}\ (\mathbf{e}_i\otimes\mathbf{e}_j):(\mathbf{e}_k\otimes\mathbf{e}_l) = A_{ij}\delta^{ik}B_{kl}\delta^{jl} = A_{ij}B^{ij} \tag{A.28}$$

$$\mathbf{A}:\mathbf{B} = A^{ij}B_{kl}\ \left(\mathbf{g}_i\otimes\mathbf{g}_j\right):\left(\mathbf{g}^k\otimes\mathbf{g}^l\right) = A^{ij}\delta^k_i\delta^l_j B_{kl} = A^{ij}B_{ij} \tag{A.29a}$$

$$\mathbf{A}:\mathbf{B} = A_{ij}B^{kl}\ \left(\mathbf{g}^i\otimes\mathbf{g}^j\right):(\mathbf{g}_k\otimes\mathbf{g}_l) = A_{ij}\delta^i_k\delta^j_l B^{kl} = A_{ij}B^{ij} \tag{A.29b}$$

$$\mathbf{A}:\mathbf{B} = A_{ij}B_{kl}\ \left(\mathbf{g}^i\otimes\mathbf{g}^j\right):\left(\mathbf{g}^k\otimes\mathbf{g}^l\right) = A_{ij}g^{ik}g^{jl}B_{kl} \tag{A.29c}$$

$$\mathbf{A}:\mathbf{B} = A^{ij}B^{kl}\ \left(\mathbf{g}_i\otimes\mathbf{g}_j\right):(\mathbf{g}_k\otimes\mathbf{g}_l) = A^{ij}g_{ik}g_{jl}B^{kl} \tag{A.29d}$$

Tensor product:

$$(\mathbf{a}\otimes\mathbf{b})\otimes\mathbf{c} = \mathbf{a}\otimes\mathbf{b}\otimes\mathbf{c} \tag{A.30a}$$

$$(\mathbf{a}\otimes\mathbf{b}\otimes\mathbf{c})\,\mathbf{d} = (\mathbf{c}\cdot\mathbf{d})\,\mathbf{a}\otimes\mathbf{b} \tag{A.30b}$$

$$(\mathbf{a}\otimes\mathbf{b}\otimes\mathbf{c}):(\mathbf{d}\otimes\mathbf{e}) = (\mathbf{b}\cdot\mathbf{d})\,(\mathbf{c}\cdot\mathbf{e})\,\mathbf{a} \tag{A.30c}$$

$$(\mathbf{a}\otimes\mathbf{b})\otimes(\mathbf{c}\otimes\mathbf{d}) = \mathbf{a}\otimes\mathbf{b}\otimes\mathbf{c}\otimes\mathbf{d} \tag{A.31a}$$

$$(\mathbf{a}\otimes\mathbf{b}\otimes\mathbf{c}\otimes\mathbf{d}):(\mathbf{e}\otimes\mathbf{f}) = (\mathbf{c}\cdot\mathbf{e})\,(\mathbf{d}\cdot\mathbf{f})\,(\mathbf{a}\otimes\mathbf{b}) \tag{A.31b}$$

$$(\mathbf{A}\otimes\mathbf{B}):\mathbf{C} = \mathbf{A}\,(\mathbf{B}:\mathbf{C}) = (\mathbf{B}:\mathbf{C})\,\mathbf{A} \tag{A.32a}$$

$$\mathbf{A}:(\mathbf{B}\otimes\mathbf{C}) = (\mathbf{A}:\mathbf{B})\,\mathbf{C} = \mathbf{C}\,(\mathbf{A}:\mathbf{B}) \tag{A.32b}$$

$$(\mathbf{A}\otimes\mathbf{B}):(\mathbf{C}\otimes\mathbf{D}) = (\mathbf{B}:\mathbf{C})\,(\mathbf{A}\otimes\mathbf{D}) = (\mathbf{A}\otimes\mathbf{D})\,(\mathbf{B}:\mathbf{C}) \tag{A.32c}$$

$$\begin{aligned}\mathbb{A}:\mathbf{B} &= A^{ijkl}B_{mn}\,\left(\mathbf{g}_i\otimes\mathbf{g}_j\otimes\mathbf{g}_k\otimes\mathbf{g}_l\right):\left(\mathbf{g}^m\otimes\mathbf{g}^n\right)\\ &= A^{ijkl}\delta_k^m\delta_l^n B_{mn}\,\left(\mathbf{g}_i\otimes\mathbf{g}_j\right)\\ &= A^{ijkl}B_{kl}\,\left(\mathbf{g}_i\otimes\mathbf{g}_j\right)\end{aligned}\tag{A.33}$$

$$\begin{aligned}\mathbb{A}:\mathbf{B} &= A_{ijkl}B^{mn}\,\left(\mathbf{g}^i\otimes\mathbf{g}^j\otimes\mathbf{g}^k\otimes\mathbf{g}^l\right):\left(\mathbf{g}_m\otimes\mathbf{g}_n\right)\\ &= A_{ijkl}\delta_m^k\delta_{ln}^l B^{mn}\,\left(\mathbf{g}^i\otimes\mathbf{g}^j\right)\\ &= A_{ijkl}B^{kl}\,\left(\mathbf{g}^i\otimes\mathbf{g}^j\right)\end{aligned}\tag{A.34}$$

$$\begin{aligned}\mathbb{A}:\mathbf{B} &= A^{ijkl}B^{mn}\,\left(\mathbf{g}_i\otimes\mathbf{g}_j\otimes\mathbf{g}_k\otimes\mathbf{g}_l\right):\left(\mathbf{g}_m\otimes\mathbf{g}_n\right)\\ &= A^{ijkl}\;g_{km}\;g_{ln}B^{mn}\,\left(\mathbf{g}_i\otimes\mathbf{g}_j\right)\end{aligned}\tag{A.35}$$

$$\begin{aligned}\mathbb{A}:\mathbf{B} &= A_{ijkl}B_{mn}\,\left(\mathbf{g}^i\otimes\mathbf{g}^j\otimes\mathbf{g}^k\otimes\mathbf{g}^l\right):\left(\mathbf{g}^m\otimes\mathbf{g}^n\right)\\ &= A_{ijkl}\;g^{km}\;g^{ln}B_{mn}\,\left(\mathbf{g}^i\otimes\mathbf{g}^j\right)\end{aligned}\tag{A.36}$$

Trace of a tensor:

$$\begin{aligned}\mathrm{tr}\mathbf{A} &= \mathrm{tr}\left(A_{ij}\;\mathbf{e}_i\otimes\mathbf{e}_j\right) = A_{ij}\;\mathrm{tr}\left(\mathbf{e}_i\otimes\mathbf{e}_j\right) = A_{ij}\delta^{ij}\\ &= A_{11}+A_{22}+\ldots+A_{nn}\end{aligned}\tag{A.37}$$

$$\mathrm{tr}\mathbf{A} = \mathrm{tr}\left(A_{ij}\;\mathbf{g}^i\otimes\mathbf{g}^j\right) = A_{ij}\;\mathrm{tr}\left(\mathbf{g}^i\otimes\mathbf{g}^j\right) = A_{ij}g^{ij}\tag{A.38a}$$

$$\mathrm{tr}\mathbf{A} = \mathrm{tr}\left(A^{ij}\;\mathbf{g}_i\otimes\mathbf{g}_j\right) = A^{ij}\;\mathrm{tr}\left(\mathbf{g}_i\otimes\mathbf{g}_j\right) = A^{ij}g_{ij}\tag{A.38b}$$

Determinant of a tensor:

$$\det\mathbf{A} = \epsilon_{ijk}A_{i1}A_{j2}A_{k3}\tag{A.39}$$

Various operations:

$$\mathbf{c}=\mathbf{a}\times\mathbf{b}\quad\text{with}\quad c_i=\epsilon_{ijk}\;a_j\;b_k\tag{A.40}$$

$$(\mathbf{a}\times\mathbf{b})\cdot\mathbf{c}=\epsilon_{ijk}\;a_i\;b_j\;c_k\tag{A.41}$$

Divergence and related operations:

$$\mathrm{div}\mathbf{A}=\nabla\cdot\mathbf{A}=\frac{\partial A_{ij}}{\partial x_j}\mathbf{e}_i\tag{A.42}$$

$$\operatorname{div}\left(\mathbf{A}^T\mathbf{b}\right) = \operatorname{div}\mathbf{A}\cdot\mathbf{b} + \mathbf{A} : (\nabla\otimes\mathbf{b}) \tag{A.43}$$

Divergence theorem - Gauss's theorem

$$\int\limits_{\Omega} \operatorname{div}\left(\mathbf{A}^T\mathbf{b}\right)\,\mathrm{d}\Omega = \int\limits_{\Gamma} \mathbf{b}\cdot\mathbf{A}\,\mathbf{n}\,\mathrm{d}\Gamma \tag{A.44}$$

A.4 Tensor Calculus

In the following a selection of the most important rules of tensor calculus is given (see Belytschko et al. [11], Holzapfel [60] and Wriggers [112]):

$$\frac{\partial \mathrm{tr}\mathbf{A}}{\partial \mathbf{A}} = \mathbf{I} \tag{A.45}$$

$$\frac{\partial \mathrm{tr}\mathbf{A}^2}{\partial \mathbf{A}} = 2\mathbf{A}^T \tag{A.46}$$

$$\frac{\partial \det\mathbf{A}}{\partial \mathbf{A}} = \det\mathbf{A}\,\mathbf{A}^{-T} \tag{A.47}$$

$$\frac{\partial \mathbf{A}}{\partial \mathbf{A}} = \mathbf{I}\odot\mathbf{I} \tag{A.48}$$

$$\frac{\partial \mathbf{A}^{-1}}{\partial \mathbf{A}} = -\mathbf{A}^{-1}\odot\mathbf{A}^{-1} \tag{A.49}$$

$$\frac{\partial\left(\mathbf{A}:\mathbf{B}\right)}{\partial \mathbf{C}} = \mathbf{A}:\frac{\partial\mathbf{B}}{\partial\mathbf{C}} + \mathbf{B}:\frac{\partial\mathbf{A}}{\partial\mathbf{C}} \tag{A.50}$$

$$\frac{\partial\left(\Phi\mathbf{A}\right)}{\partial \mathbf{C}} = \mathbf{A}\otimes\frac{\partial\Phi}{\partial\mathbf{C}} + \Phi\,\frac{\partial\mathbf{A}}{\partial\mathbf{C}} \tag{A.51}$$

A.5 Tensor Operations

First order tensors
Push-forward:

$$\chi_*\left(\bullet\right)^\flat = \mathbf{F}^{-T}\left(\bullet\right)^\flat \quad \text{and} \quad \chi_*\left(\bullet\right)^\sharp = \mathbf{F}\left(\bullet\right)^\sharp \tag{A.52}$$

Pull-back:

$$\chi_*^{-1}\left(\bullet\right)^\flat = \mathbf{F}^{T}\left(\bullet\right)^\flat \quad \text{and} \quad \chi_*^{-1}\left(\bullet\right)^\sharp = \mathbf{F}^{-1}\left(\bullet\right)^\sharp \tag{A.53}$$

Second order tensors
Push-forward:

$$\chi_* \left(\bullet\right)^\flat = \mathbf{F}^{-T} \left(\bullet\right)^\flat \mathbf{F}^{-1} \quad \text{and} \quad \chi_* \left(\bullet\right)^\sharp = \mathbf{F} \left(\bullet\right)^\sharp \mathbf{F}^T \tag{A.54}$$

Pull-back:

$$\chi_*^{-1} \left(\bullet\right)^\flat = \mathbf{F}^{T} \left(\bullet\right)^\flat \mathbf{F} \quad \text{and} \quad \chi_*^{-1} \left(\bullet\right)^\sharp = \mathbf{F}^{-1} \left(\bullet\right)^\sharp \mathbf{F}^{-T} \tag{A.55}$$

B

Vectors/matrices for static condensation

B.1 Voigt notation

By means of utilizing the symmetry conditions of the strain, stress and elasticity tensors a vector/matrix representation known as *Voigt notation* can be established. It is important to note that only the coefficients of the tensors are considered, i.e. the information on the base vectors is lost. For further information the author refers to BELYTSCHKO [11].

Covariant Green-Lagrange strain tensor: $\mathbf{E} = E_{ij}\mathbf{G}^i \otimes \mathbf{G}^j$

$$\mathbf{E}^{\mathrm{V}} = [E_{11} \quad E_{22} \quad E_{33} \quad 2E_{23} \quad 2E_{13} \quad 2E_{12}]^T \tag{B.1}$$

Contra-variant 2nd Piola-Kirchhoff stress tensor: $\mathbf{S} = S^{ij}\mathbf{G}_i \otimes \mathbf{G}_j$

$$\mathbf{S}^{\mathrm{V}} = \left[S^{11} \quad S^{22} \quad S^{33} \quad S^{23} \quad S^{13} \quad S^{12}\right]^T \tag{B.2}$$

Contra-variant elasticity tensor: $\mathbb{D} = D^{ijkl}\mathbf{G}_i \otimes \mathbf{G}_j \otimes \mathbf{G}_k \otimes \mathbf{G}_l$:

$$\mathbb{D}^{\mathrm{V}} = \begin{bmatrix} D^{1111} & D^{1122} & D^{1133} & D^{1123} & D^{1113} & D^{1112} \\ D^{2211} & D^{2222} & D^{2233} & D^{2223} & D^{2213} & D^{2212} \\ D^{3311} & D^{3322} & D^{3333} & D^{3323} & D^{3313} & D^{3312} \\ D^{2311} & D^{2322} & D^{2333} & D^{2323} & D^{2313} & D^{2312} \\ D^{1311} & D^{1322} & D^{1333} & D^{1323} & D^{1313} & D^{1312} \\ D^{1211} & D^{1222} & D^{1233} & D^{1223} & D^{1213} & D^{1212} \end{bmatrix} \tag{B.3}$$

B.2 Static condensation

In-plane ($k = 11, 22, 12$) and out-of-plane ($o = 33, 13, 23$) proportions of the covariant Green-Lagrange strain tensor:

$$\mathbf{E}_k^{\mathrm{V}} = [E_{11} \quad E_{22} \quad 2E_{12}]^T \tag{B.4a}$$

$$\mathbf{E}_o^{\mathrm{V}} = [E_{33} \quad 2E_{23} \quad 2E_{13}]^T \tag{B.4b}$$

In-plane ($k = 11, 22, 12$) and out-of-plane ($o = 33, 13, 23$) proportions of the contra-variant 2nd Piola-Krichhoff stress tensor:

$$\mathbf{S}_k^{\mathrm{V}} = \begin{bmatrix} S^{11} & S^{22} & S^{12} \end{bmatrix}^T \tag{B.5a}$$

$$\mathbf{S}_o^{\mathrm{V}} = \begin{bmatrix} S^{33} & S^{23} & S^{13} \end{bmatrix}^T = 0 \tag{B.5b}$$

In-plane ($k = 11, 22, 12$) and out-of-plane ($o = 33, 13, 23$) proportions of the contra-variant elasticity tensor:

$$\mathbb{D}_{kk}^{\mathrm{V}} = \begin{bmatrix} D^{1111} & D^{1122} & D^{1112} \\ D^{2211} & D^{2222} & D^{2212} \\ D^{1211} & D^{1222} & D^{1212} \end{bmatrix} \tag{B.6a}$$

$$\mathbb{D}_{ko}^{\mathrm{V}} = \begin{bmatrix} D^{1133} & D^{1123} & D^{1113} \\ D^{2233} & D^{2223} & D^{2213} \\ D^{1233} & D^{1223} & D^{1213} \end{bmatrix} \tag{B.6b}$$

$$\mathbb{D}_{ok}^{\mathrm{V}} = \begin{bmatrix} D^{3311} & D^{3322} & D^{3312} \\ D^{2311} & D^{2322} & D^{2312} \\ D^{1311} & D^{1322} & D^{1312} \end{bmatrix} \tag{B.6c}$$

$$\mathbb{D}_{oo}^{\mathrm{V}} = \begin{bmatrix} D^{3333} & D^{3323} & D^{3313} \\ D^{2333} & D^{2323} & D^{2313} \\ D^{1333} & D^{1323} & D^{1313} \end{bmatrix} \tag{B.6d}$$

C

Hyperelastic material models

C.1 St. Venant-Kirchhoff

According to HOLZAPFEL [60], the corresponding strain-energy function is stated as follows:

$$\Psi_{\mathrm{StVenKir}} = \frac{1}{2}\,\lambda\,\left(tr\left(\mathbf{E}\right)\right)^2 + \mu\,tr\left(\mathbf{E}^2\right) \tag{C.1}$$

with λ and μ being the Lamé parameters

$$\mu = \frac{E}{2\left(1+\nu\right)} \tag{C.2a}$$

$$\lambda = \frac{\nu E}{\left(1+\nu\right)\left(1-2\nu\right)} \tag{C.2b}$$

Applying Equation (3.60) leads to the 2$^{\mathrm{nd}}$ Piola-Kirchhoff stress tensor:

$$\mathbf{S}_{\mathrm{StVenKir}} = \lambda\,tr\left(\mathbf{E}\right)\,\mathbf{I} + 2\,\mu\,\mathbf{E} \tag{C.3}$$

Applying Equation (3.65) leads to the elasticity tensor:

$$\mathbb{D}_{\mathrm{StVenKir}} = \lambda\,\mathbf{I}\otimes\mathbf{I} + 2\,\mu\,\mathbf{I}\odot\mathbf{I} \tag{C.4}$$

with $\mathbf{I}\odot\mathbf{I}$ defined as (see HOLZAPFEL [60])

$$\left(\mathbf{I}\odot\mathbf{I}\right)_{ijkl} = \frac{\partial E_{ij}}{\partial E_{kl}} = \frac{1}{2}\left(I_{ik}I_{jl} + I_{il}I_{jk}\right) \tag{C.5}$$

C.2 Neo-Hookean

According to BELYTSCHKO ET AL. [11], the corresponding strain-energy function is stated as follows:

$$\Psi_{\mathrm{NeoHook}} = \frac{1}{2}\,\lambda\,\ln\left(\sqrt{I_3}\right)^2 - \mu\,\ln\left(\sqrt{I_3}\right) + \frac{1}{2}\,\mu\,\left(I_1 - 3\right) \tag{C.6}$$

with λ and μ being the Lamé parameters defined in Equation (C.2a) and (C.2b), respectively. Applying Equation (3.60) leads to the 2nd Piola-Krichhoff stress tensor:

$$\mathbf{S}_{\text{NeoHook}} = \mu \left(\mathbf{I} - \mathbf{C}^{-1}\right) + \lambda \ln \sqrt{I_3}\, \mathbf{C}^{-1} \tag{C.7}$$

Applying Equation (3.65) leads to the elasticity tensor:

$$\mathbb{D}_{\text{NeoHook}} = \lambda\, \mathbf{C}^{-1} \otimes \mathbf{C}^{-1} + 2 \left(\mu - \lambda \ln \sqrt{I_3}\right) \mathbf{C}^{-1} \odot \mathbf{C}^{-1} \tag{C.8}$$

with $\mathbf{C}^{-1} \odot \mathbf{C}^{-1}$ defined as (see HOLZAPFEL [60])

$$\left(\mathbf{C}^{-1} \odot \mathbf{C}^{-1}\right)_{ijkl} = \frac{\partial C_{ij}^{-1}}{\partial C_{kl}} = \frac{1}{2} \left(C_{ik}^{-1} C_{jl}^{-1} + C_{il}^{-1} C_{jk}^{-1}\right) \tag{C.9}$$

C.3 Material model: simple transversely isotropic

In their work, BONET AND BURTON [22] presented the following nonlinear transversely isotropic material model. In more detail, the Neo-Hookean strain-energy function (C.6) is extended by simply adding an additional strain-energy function capturing the directional properties (i.e. the characteristics of the preferred material direction Φ):

$$\Psi_{\text{Bonet}} = \left[\alpha + \beta \ln \sqrt{I_3} + \gamma \left(I_4 - 1\right)\right] \left(I_4 - 1\right) - 0.5\alpha \left(I_5 + 1\right) \tag{C.10}$$

with

$$n = \frac{E}{E_\phi} \tag{C.11a}$$

$$m = 1 - \nu - 2n\nu^2 \tag{C.11b}$$

$$\lambda = \frac{E\left(\nu + n\nu^2\right)}{m\left(1+\nu\right)} \tag{C.11c}$$

$$\mu = \frac{E}{2\left(1+\nu\right)} \tag{C.11d}$$

$$\alpha\left(E, \nu, G_\phi\right) = \mu - G_\phi \tag{C.11e}$$

$$\beta\left(E_\phi, E, \nu\right) = \frac{E\nu^2\left(1-n\right)}{4m\left(1+\nu\right)} \tag{C.11f}$$

$$\gamma\left(E_\phi, E, \nu, G_\phi\right) = \frac{E_\phi\left(1-\nu\right)}{8m} - \frac{\lambda + 2\mu}{8} + \frac{\alpha}{2} - \beta \tag{C.11g}$$

Applying Equation (3.60) leads to the transversely isotropic proportion of the 2nd Piola-Kirchhoff stress tensor:

$$\begin{aligned} \mathbf{S}_{\text{Bonet}} &= \beta\left(I_4 - 1\right)\mathbf{C}^{-1} - \alpha\left(\mathbf{C}\,\mathbf{M} + \mathbf{M}\,\mathbf{C}\right) \\ &\quad + \left[2\alpha + \beta \ln \sqrt{I_3} + 4\gamma(I_4 - 1)\right] \mathbf{M} \end{aligned} \tag{C.12}$$

Applying Equation (3.65) leads to the transversely isotropic proportion of the elasticity tensor:

$$\begin{aligned}\mathbb{D}_{\text{Bonet}} &= 8\,\gamma\,\mathbf{M}\otimes\mathbf{M} - 2\,\beta\ (I_4 - 1)\ \mathbf{C}^{-1}\odot\mathbf{C}^{-1} \\ &\quad + 2\,\beta\left(\mathbf{C}^{-1}\otimes\mathbf{M} + \mathbf{M}\otimes\mathbf{C}^{-1}\right) - 2\,\alpha\ (\mathbf{I}\odot\mathbf{M} + \mathbf{I}\odot\mathbf{M})\end{aligned} \tag{C.13}$$

with $\mathbf{C}^{-1}\odot\mathbf{C}^{-1}$, $\mathbf{M}\odot\mathbf{I}$ and $\mathbf{I}\odot\mathbf{M}$ defined as

$$\left(\mathbf{C}^{-1}\odot\mathbf{C}^{-1}\right)_{ijkl} = \frac{1}{2}\left(C^{-1}_{ik}C^{-1}_{jl} + C^{-1}_{il}C^{-1}_{jk}\right) \tag{C.14a}$$

$$(\mathbf{M}\odot\mathbf{I})_{ijkl} = \frac{1}{2}\left(M^{-1}_{ik}I^{-1}_{jl} + M^{-1}_{il}I^{-1}_{jk}\right) \tag{C.14b}$$

$$(\mathbf{I}\odot\mathbf{M})_{ijkl} = \frac{1}{2}\left(I^{-1}_{ik}M^{-1}_{jl} + I^{-1}_{il}M^{-1}_{jk}\right) \tag{C.14c}$$

C.4 Material model: plain weave

In their work, AIMÈNE ET AL. [1] presented the following nonlinear orthotropic material model for describing the structural response of either a non-crimp or woven fabric. It is based on a sum of polynomials which are representing the strain-energies w.r.t. each fiber direction (Φ_1 and Φ_2) as well as its shear characteristics:

$$\begin{aligned}\Psi_{\text{woven}}(\mathbf{C}) &= \sum_{i=0}^{r}\frac{1}{i+1}\,A_i\,\left(I_4^{i+1} - 1\right) \\ &\quad + \sum_{j=0}^{s}\frac{1}{j+1}\,B_j\,\left(I_6^{j+1} - 1\right) \\ &\quad + \sum_{k=1}^{t}\frac{1}{k}\,C_k\,I_{46}^{k}\end{aligned} \tag{C.15}$$

with the mixed structural invariant $I_{46} = I_{46}(I_4, I_6)$

$$I_{46} = \frac{1}{I_4\,I_6}tr\left(\mathbf{C}\mathbf{M}_1\mathbf{C}\mathbf{M}_2\right) \tag{C.16}$$

Applying Equation (3.60) leads to the 2$^{\text{nd}}$ Piola-Kirchhoff stress tensor:

$$\begin{aligned}\mathbf{S}_{\text{woven}} &= 2\left(\sum_{i=0}^{r}A_i\,I_4^{i} + \frac{1}{I_4}\sum_{k=1}^{t}C_k\,I_{46}^{k}\right)\mathbf{M}_1 \\ &\quad + 2\left(\sum_{j=0}^{s}B_j\,I_6^{j} + \frac{1}{I_6}\sum_{k=1}^{t}C_k\,I_{46}^{k}\right)\mathbf{M}_2 \\ &\quad + 2\left(\frac{1}{\sqrt{I_4 I_6}}\sum_{k=1}^{t}\frac{1}{k}\,C_k\,I_{46}^{k-\frac{1}{2}}\right)(\mathbf{M}_{12} + \mathbf{M}_{21})\end{aligned} \tag{C.17}$$

with the mixed structural tensors $\mathbf{M}_{12}$ and $\mathbf{M}_{21}$

$$\mathbf{M}_{12} = \Phi_1 \otimes \Phi_2 \quad \text{and} \quad \mathbf{M}_{21} = \Phi_2 \otimes \Phi_1 \tag{C.18}$$

Applying Equation (3.65) leads to the elasticity tensor:

$$\begin{aligned}
\mathbb{D}_{\text{woven}} = {} & 4 \left(\sum_{i=0}^{r} i\, A_i\, I_4^{(i-1)} + \frac{1}{I_4^2} \sum_{k=1}^{t} (k+1)\ C_k\, I_{46}^{k} \right) \mathbf{M}_1 \otimes \mathbf{M}_1 \\
& + 4 \left(\frac{1}{I_4 I_6} \sum_{k=1}^{t} k\, C_k\, I_{46}^{k} \right) \mathbf{M}_1 \otimes \mathbf{M}_2 \\
& - 4 \left(\frac{1}{I_4} \sqrt{\frac{I_{46}}{I_4 I_6}} \sum_{k=1}^{t} k\, C_k\, I_{46}^{k-1} \right) \mathbf{M}_1 \otimes (\mathbf{M}_{12} + \mathbf{M}_{21}) \\
& + 4 \left(\frac{1}{I_4 I_6} \sum_{k=1}^{t} k\, C_k\, I_{46}^{k} \right) \mathbf{M}_2 \otimes \mathbf{M}_1 \\
& + 4 \left(\sum_{j=0}^{s} j\, B_j\, I_6^{(j-1)} + \frac{1}{I_6^2} \sum_{k=1}^{t} (k+1)\ C_k\, I_{46}^{k} \right) \mathbf{M}_2 \otimes \mathbf{M}_2 \\
& - 4 \left(\frac{1}{I_6} \sqrt{\frac{I_{46}}{I_4 I_6}} \sum_{k=1}^{t} k\, C_k\, I_{46}^{k-1} \right) \mathbf{M}_2 \otimes (\mathbf{M}_{12} + \mathbf{M}_{21}) \\
& - 4 \left(\frac{1}{I_4} \sqrt{\frac{I_{46}}{I_4 I_6}} \sum_{k=1}^{t} k\, C_k\, I_{46}^{k-1} \right) (\mathbf{M}_{12} + \mathbf{M}_{21}) \otimes \mathbf{M}_1 \\
& - 4 \left(\frac{1}{I_6} \sqrt{\frac{I_{46}}{I_4 I_6}} \sum_{k=1}^{t} k\, C_k\, I_{46}^{k-1} \right) (\mathbf{M}_{12} + \mathbf{M}_{21}) \otimes \mathbf{M}_2 \\
& + 4 \left(\frac{1}{I_4 I_6} \sum_{k=1}^{t} \left(k - \frac{1}{2} \right) C_k\, I_{46}^{k-1} \right) (\mathbf{M}_{12} + \mathbf{M}_{21}) \otimes (\mathbf{M}_{12} + \mathbf{M}_{21})
\end{aligned} \tag{C.19}$$